

Syracuse University

SURFACE

Dissertations - ALL

SURFACE

6-1-2015

Integration of EVs and DGs into the Electric Power System for Grid Modernization

Mohammad Nikkhah Mojdehi
Syracuse University

Follow this and additional works at: <https://surface.syr.edu/etd>



Part of the [Engineering Commons](#)

Recommended Citation

Nikkhah Mojdehi, Mohammad, "Integration of EVs and DGs into the Electric Power System for Grid Modernization" (2015). *Dissertations - ALL*. 267.
<https://surface.syr.edu/etd/267>

This Dissertation is brought to you for free and open access by the SURFACE at SURFACE. It has been accepted for inclusion in Dissertations - ALL by an authorized administrator of SURFACE. For more information, please contact surface@syr.edu.

Abstract

Electric power systems (EPSs) are rapidly becoming more complex. Penetration of distributed generators (DGs) are increasing rapidly. Among them, DG units with intermittent renewables resources, such as solar or wind, are attracting more attention. Moreover, plug-in electric vehicles (EVs) are expected to be deployed in large numbers over the next decade. These changes present opportunities as well as challenges for reliable and efficient operation of EPS.

Integrating EVs in large scale, would result in over-loading of EPS. Interconnection of DGs could impact adversely on the system operation including power quality and safety of the EPS. However, due to the growing number of EVs in the system, faster charging, shorter battery reaction time, and vehicle-to-grid services, EVs could be attractive sources for system operators (SOs) to improve system reliability while creating opportunity for EV owners to gain monetary benefits. In addition, the potential benefits of DG could be sustained in avoiding or shifting investment in transmission lines and/or transformers, minimizing ohmic losses, and protecting the environment.

In this dissertation, potential benefits and challenges of EVs and DGs are explored. For some potential benefits, the dissertation develops systematic frameworks, in order to facilitate integration of EVs and DGs into the EPS. Also for some challenges, the dissertation presents solutions to analyze and overcome related difficulties.

To study consequences of integrating EVs, a comprehensive model of EV operation is presented. The model covers different modes of operation and includes impact of battery degradation during the operation. The model is then extended to control a large group of EVs efficiently. Several possible ancillary services which could be offered by EVs, including voltage and frequency regulation services, are discussed. Several

systematic frameworks are developed to engage EVs in provision of ancillary services, from economical and technical view points. Simulation results clearly indicate EVs ability to participate in ancillary services and possible revenue stream for EV owners.

In terms of DGs, the dissertation addresses a common issue in most of utility companies and that is the risk of unintentional islanding of interconnected DGs. A systematic procedure is presented in this dissertation which can detect any possible operating conditions leading to an unintentional islanding of DGs. The developed procedure can serve utility companies as an analytical tool for any interconnection study, in a timely and costly efficient manner. The procedure is not dependent on the anti-islanding schemes nor DG technologies. Simulation results of different real case studies prove the generality and practicality of the procedure.

**Integration of EVs and DGs into the Electric Power System
for Grid Modernization**

by

Mohammad Nikkhah Mojdehi

B.S. University of Guilan, Iran, 2006

M.S. Iran University of Science and Technology, Iran, 2009

DISSERTATION

Submitted in partial fulfillment of the requirements for the
degree of Doctor of Philosophy in Electrical Engineering
in the Graduate School of Syracuse University

June 2015

Copyright ©Mohammad Nikkhah Mojdehi 2015

All Rights Reserved

This dissertation is dedicated to my mother, Mahnaz, and my father, Mohammad-Reza. Their support, encouragement, and constant love have sustained me throughout my life.

Acknowledgement

There are a lot of people without whom this dissertation could not have been written and to whom I am deeply indebted.

To my advisor, Prof. Prasanta K. Ghosh, who has steered me from the early stage of problem formulation to the clarification and carefulness of ideas in this dissertation, a very special thank for his profound knowledge and brilliant mind, which have allowed me to build a strong foundation in the field of smart grid through academic training and industrial practice. This dissertation would have been impossible without his mentorship.

I want to express my great appreciation to National Grid USA for their support. During my internship, I gained valuable knowledge and experiences on unintentional islanding of distribution electric power system. Field data and real case studies provided by National Grid made this dissertation attractive and practical.

I would like to thank Dr. Makan Fardad for insightful discussions, which enlightened me with ideas in the development of system models and optimization methodologies used in this dissertation. A very special thank for his effort and time in helping me to improve the content of this dissertation through many revisions.

All of my professors that I have encountered as teachers and as advisers have been brilliant and excited about sharing their understanding. My friends and classmates have always been around to encourage me to work and support me through hard times.

Contents

List of Tables	xi
List of Figures	xiii
1 Introduction	1
1.1 Background	1
1.2 Problem Definition	4
1.2.1 EV Related Challenge	4
1.2.2 DG Related Challenge	4
1.3 Claims of Originality	5
1.3.1 Chapter 2	5
1.3.2 Chapter 3	6
1.3.3 Chapter 4	6
1.3.4 Chapter 5	7
1.3.5 Chapter 6	7
1.4 Dissertation Outline	8
1.4.1 Chapter 2: Integration of DERs into the Micro-Grid	8
1.4.2 Chapter 3: EV Modeling	8
1.4.3 Chapter 4: Reactive Power Service from EVs	9

1.4.4	Chapter 5: Frequency Regulation Service from EVs	9
1.4.5	Chapter 6: DGs Integration and Micro-Grid	9
1.4.6	Chapter 7: Conclusion and Future Work	10
2	Integration of DERs into the Micro-Grid	11
2.1	Introduction	11
2.2	Carbon Emission	13
2.3	OPF Formulation	14
2.4	Numerical Results	16
2.5	Wind Energy Production	24
2.6	Integration of EVs	26
2.7	Stochastic Nature of EV Usage	28
2.8	Stochastic Optimal Scheduling of Micro-Grid	31
2.9	Numerical Results	32
2.9.1	Simulation Using Two Points Estimation	33
2.9.2	Monte-Carlo Simulation	41
2.10	Conclusion	48
3	EV Modeling	50
3.1	Introduction	50
3.2	Optimization Horizon	51
3.3	Battery Degradation	52
3.4	EV Operating Model	54
3.5	Aggregator Modeling and Optimization	59
3.6	Numerical Results	63
3.6.1	Single EV	65
3.6.2	EV Usage Pattern Generation	67

3.6.3	A Group of EVs	68
3.7	Conclusion	69
4	Reactive Power Service from EVs	70
4.1	Introduction	70
4.2	Reactive Power Market: A Review	72
4.3	EV's Characteristics for Reactive Power Service	76
4.3.1	Inverter Maximum Power	78
4.3.2	Power Ripple in Charger	78
4.4	Reactive Power Capability of EV	83
4.4.1	Nonlinear Approach	85
4.4.2	Linear Approach	86
4.5	Perturbation in Optimal Solutions	90
4.5.1	Nonlinear Approach	92
4.5.2	Linear Approach	93
4.6	Calculation of Reactive Power Supply Function	94
4.6.1	$p_k^* \geq 0$	98
4.6.2	$p_k^* < 0$	98
4.6.3	Nonlinear Approach	102
4.6.4	Linear Approach	102
4.7	Numerical Results	103
4.7.1	Nonlinear Approach	104
4.7.1.1	Scenario 1	105
4.7.1.2	Scenario 2	109
4.7.2	Linear Approach	114
4.7.2.1	Scenario 1	114

4.7.2.2	Scenario 2	118
4.8	Conclusion	123
5	Frequency Regulation Service from EVs	124
5.1	Introduction	124
5.2	Frequency Regulation: A Review	126
5.3	EV's Capability for Regulation Service	129
5.3.1	Perturbation in Optimal Solutions due to Regulation-Up Service	130
5.3.2	Perturbation in Optimal Solutions due to Regulation-Down Ser- vice	131
5.4	Bidding Strategy for Single EV	132
5.4.1	Regulation-Up	135
5.4.2	Regulation-Down	136
5.5	Bidding Strategy for an Aggregator	140
5.5.1	Upper Optimization Level	141
5.5.2	Lower Optimization Level	141
5.5.3	Post-process Optimization Level	141
5.6	Numerical Results	142
5.6.1	Scenario 1	142
5.6.2	Scenario 2	148
5.6.2.1	Upper Optimization Level	149
5.6.2.2	Lower Optimization Level	149
5.6.2.3	Post-Process Optimization Level	150
5.7	Conclusion	152
6	DGs Integration and Micro-Grid	153
6.1	Introduction	153

6.2	Screening Procedure: A Review	157
6.3	Distribution Feeder Modeling	160
6.4	PV Modeling	167
6.4.1	Real and Reactive Power Control Scheme	170
6.5	Islanding Conditions	174
6.6	Study Procedure	177
6.7	Numerical Results	178
6.7.1	Case 1	179
6.7.2	Case 2	181
6.8	Conclusion	189
7	Conclusion and Future Work	192
	Glossary	195

List of Tables

2.1	CO_2 Emission of Top Ten States (Metric Tons).	14
2.2	Simulation Settings	17
2.3	Simulation Settings	35
2.4	Emission Factors (lbs/MWh).	36
2.5	System Cost of Each Scenario.	43
2.6	Simulation Settings for Monte-Carlo Simulation.	43
3.1	Lithium-Ion battery cell degradation specifications.	64
3.2	EVs battery and charger specifications.	65
3.3	Normal Distribution Function Settings for EVs Usage Patterns.	67
4.1	Potential Markets for V2G Services Offered by EV	77
4.2	Operating Regions of EV Charger	78
4.3	Change in Operation Cost of EV due to Change in Active Power Flow Rate.	91
4.4	Marginal Cost of Deviation Caused by Δp_k in \$/kW.	92
4.5	Rescheduling Active Power Flow Rates in Receding Horizon Due to Perturbation in the Optimal Solution.	96
4.6	Maximum decrease in charging/discharging power at current time pe- riod k	101

4.7	Simulation settings in each scenario.	105
4.8	EVs specifications.	119
4.9	Normal Distribution Function Settings for EV's Usage Patterns.	120
5.1	Change in Operation Cost of EV due to Provision of Regulation-Up Service.	130
5.2	Marginal Cost of Deviation Caused by Δp_k During Regulation Up Service (\$/kW).	131
5.3	Change in Operation Cost of EV due to Provision of Regulation-Down Service.	131
5.4	Marginal Cost of Deviation Caused by Δp_k During Regulation Down Service (\$/kW).	132
5.5	Reschedulable deviation in the SOC of the battery.	133
5.6	Reschedulable power during time interval r of receding horizon.	134
5.7	Subsets R , R' , and R'' of receding horizon in Scenario 1 and Case 1.	144
5.8	Subsets R , R' , and R'' of receding horizon in Scenario 1 and Case 2.	144
5.9	EVs specifications.	148
5.10	Post-process optimization results for assigning AGC signal at 10 a.m.	151
5.11	Post-process optimization results for assigning AGC signal at 2:15 p.m.	152
6.1	Voltage and frequency trip set-points of the PV plants.	179
6.2	Transformers specifications of feeder in Case 2.	186
6.3	Capacitor banks specifications of feeder in Case 2.	186

List of Figures

1.1	Timeline of major events in the U.S. electric grid [3].	2
1.2	Smart grid features.	3
2.1	U.S. greenhouse gas emission by sectors.	14
2.2	33-bus Test system.	17
2.3	The daily electricity retail price	18
2.4	The daily base load	18
2.5	PV and WT daily availability.	19
2.6	Applied CO_2 emission tax in Scenario 4.	19
2.7	Operating cost of the network in Scenario 1.	20
2.8	Active power loss in Scenario 1.	20
2.9	Injected power from the main grid in different scenarios.	21
2.10	Generation scheduling of PVs on buses 4 and 25 in different scenarios.	21
2.11	Generation scheduling of WTs on buses 7 and 30 in different scenarios.	22
2.12	Operating cost reduction in different scenarios in comparison to scenario 1.	22
2.13	CO_2 emission tax in scenario 4.	23
2.14	Active power loss reduction in different scenarios in comparison to scenario 1.	23

2.15	Weibull probability distribution function for wind speed.	25
2.16	Typical power curve of WT.	26
2.17	Flow of power in proposed algorithm.	31
2.18	34-bus Test system	34
2.19	The WT energy generation.	36
2.20	Generation scheduling of DGs	37
2.21	EV group 1 scheduling: (a) Mean value of charging flow rates; (b) Mean value of actual charging time.	38
2.22	EV group 2 scheduling: (a) Mean value of charging flow rates; (b) Mean value of actual charging time.	39
2.23	EV group 3 scheduling: (a) Mean value of charging flow rates; (b) Mean value of actual charging time.	40
2.24	EV group 4 scheduling: (a) Mean value of charging flow rates; (b) Mean value of actual charging time.	41
2.25	EV group 5 scheduling: (a) Mean value of charging flow rates; (b) Mean value of actual charging time.	42
2.26	Flowchart of Monte-carlo simulation.	44
2.27	Mean value of daily charging flow rate of EVs.	45
2.28	Mean value of daily discharging flow rate of EVs.	45
2.29	Mean value of daily actual charging time of EVs.	46
2.30	Mean value of daily actual discharging time of EVs.	46
2.31	Mean value of daily DGs scheduling.	47
2.32	Standard deviation of daily DGs scheduling.	47
2.33	Mean value of daily voltage profile.	48
2.34	Standard deviation of daily voltage profile.	48

3.1	Degradation cost of a 16 kWh battery pack used in the Mitsubishi's i MiEV.	54
3.2	Operating regions of the EV.	55
3.3	Associated cost of active power flow of an EV.	57
3.4	Control and operation levels of the EPS including EVs.	60
3.5	NYISO daily price of charging/dischrging electrical power.	64
3.6	Charging/discharging schedule of a single EV ignoring the battery degradation effect.	66
3.7	Charging/discharging schedule of a single EV including the battery degradation effect.	66
3.8	Number of connected EVs.	67
3.9	Percentage of different EVs in simulations.	68
3.10	Aggregated charging/discharging schedule of a group of 1000 EVs. . .	68
4.1	Short-term dispatch of reactive power services.	75
4.2	The information exchange between different entities in the short-term dispatch of reactive power services.	76
4.3	A typical circuit of EV charger.	77
4.4	Operating limit of EV charger.	83
4.5	Reactive power capability of the EV: nonlinear approach.	84
4.6	Perturbation in operating point due to a change in reactive power service for: (a) Region I; (b) Region II; (c) Region III; and (d) Region IV.	86
4.7	Linear cuts for constraint (4.23).	87
4.8	perpendicular distance to the i^{th} linear cut at time interval k	88

4.9	Reactive power capability curve of the EV at time interval k in linear approach.	89
4.10	Perturbation in scheduled operating point by increase in reactive power service for (a) Region I; (b) Region II ; (c) Region III; and (d) Region IV.	90
4.11	Scheduled SOC of the EV battery.	95
4.12	Reschedulable active power flow rate at current time period k and during receding horizon.	97
4.13	Classifying time intervals of the receding horizon when $p_k^* \geq 0$	99
4.14	Classifying time intervals of the receding horizon when $p_k^* < 0$	100
4.15	Flowchart of rescheduling of the receding horizon.	101
4.16	Optimal scheduled charging/discharging activities in scenario 1.	105
4.17	Scheduled SOC of the EV battery in scenario 1.	106
4.18	Reactive power supply function of the EV in scenario 1 and time interval $k=2, 3, \dots, 13$	106
4.19	Reschedulable active power in receding horizon of time interval $k=1$	107
4.20	Reactive power supply function during time interval $k=1$ in scenario 1.	108
4.21	Optimal scheduled charging/discharging activities in scenario 2.	109
4.22	Scheduled SOC of the EV battery in scenario 2.	110
4.23	Reschedulable active power in receding horizon of time interval $k=1$	111
4.24	Reactive power supply function during time interval $k=1$ in scenario 2.	111
4.25	Reactive power supply function during time interval $k=17$ in scenario 2.	113
4.26	Optimal scheduled charging/discharging activities in scenario 1.	114
4.27	Reschedulable active power in receding horizon of time interval $k=4$, in scenario 1 considering the battery degradation factor.	116

4.28	Reactive power supply function during time interval $k=4$ in scenario 1 considering the battery degradation factor.	117
4.29	Reactive power supply function during time interval $k=4$ in scenario 1 neglecting the battery degradation factor.	118
4.30	Reactive power supply function during time interval $k=9$ in scenario 1 neglecting the battery degradation factor.	119
4.31	Optimal aggregated scheduled charging/discharging activities in scenario 2.	120
4.32	Reactive power supply function of the aggregator during time interval $k=24$ in scenario 2.	121
4.33	Reactive power supply function of the aggregator during time interval $k=26$ in scenario 2.	121
4.34	Reactive power supply function of the aggregator during time interval $k=30$ in scenario 2.	122
4.35	Reactive power supply function of the aggregator during time interval $k=34$ in scenario 2.	122
5.1	Sequential phases in power system operation.	127
5.2	Schematic of optimal allocation of AGC signal.	128
5.3	Frequency regulation service from EV in time step k	129
5.4	Reschedulable active power flow rate at current time period k and during receding horizon.	134
5.5	Classifying time intervals of the receding horizon for provision of regulation-up service.	135
5.6	Classifying time intervals of the receding horizon for provision of regulation-down service.	137

5.7	Flowchart of rescheduling during the receding horizon for providing regulation-up service.	138
5.8	Flowchart of rescheduling during the receding horizon for providing regulation-down service.	139
5.9	Flowchart of the aggregator’s bidding strategy calculation for regulation service.	140
5.10	Post-process optimization level.	142
5.11	Optimal scheduled charging/discharging activities in scenario 1. . . .	143
5.12	Regulation services in Scenario 1 during time interval $k=4$ for (a) Case 1 and (b) Case 2	146
5.13	Regulation services in Scenario 1 during time interval $k=9$ for (a) Case 1 and (b) Case 2	147
5.14	Regulation services in Scenario 1 during time interval $k=18$ for Case 1. . . .	147
5.15	Regulation services in Scenario 1 during time interval $k=14$ for Case 2. . . .	148
5.16	Optimal aggregated scheduled charging/discharging activities in scenario 2.	149
5.17	Regulation services in Scenario 2 at 10 a.m.	150
5.18	Regulation services in Scenario 2 at 2:15 p.m.	151
6.1	Anti-islanding schemes.	155
6.2	SANDIA screening procedure.	160
6.3	Flowchart of assigning color to each node.	163
6.4	Levelized graph using proposed algorithm.	164
6.5	Flowchart of tracking all paths from each end node to the source node.	165
6.6	Finding path in a graph using proposed algorithm.	166
6.7	Diagram of a grid-connected PV system.	168

6.8	The VSC averaged model.	169
6.9	Schematic diagram of a current-controlled real/reactive power controller in dq -frame.	171
6.10	Control block diagram of a current-controlled VSC system.	173
6.11	Schematic diagram of the distribution feeder under study.	174
6.12	Mapping of the NDZ in LF-PF space.	176
6.13	Feeder single line diagram in Case 1.	181
6.14	Run-on time in Case 1.	182
6.15	NDZ of PV plants in Case 1.	182
6.16	Frequency at PCC of PV plants in Case 1, with $LF=0.6$ and $PF=0.9802$	183
6.17	Three-phase voltage (phase A with blue, phase B with green, and phase C with red) at PCC of PV plant 1 in Case 1, with $LF=0.6$ and $PF=0.9802$: (a) For time window form 0 to 0.5 second; (b) For time window form 1.7 to 2.2 second	184
6.18	Three-phase voltage (phase A with blue, phase B with green, and phase C with red) at PCC of PV plant 2 in Case 1, with $LF=0.6$ and $PF=0.9802$: (a) For time window form 0 to 0.5 second; (b) For time window form 1.7 to 2.2 second	185
6.19	Feeder single line diagram in Case 2.	187
6.20	Run-on time in Case 2.	187
6.21	NDZ of PV plants in Case 2.	188
6.22	Frequency at PCC of PV plants in Case 2, with $LF=0.4$ and $PF=0.9848$	189
6.23	Three-phase voltage (phase A with blue, phase B with green, and phase C with red) at PCC of PV plant 1 in Case 2, with $LF=0.4$ and $PF=0.9848$: (a) For time window form 0 to 0.4 second; (b) For time window form 1.7 to 2.025 second	190

6.24 Three-phase voltage (phase A with blue, phase B with green, and phase C with red) at PCC of PV plant 2 in Case 2, with $LF=0.4$ and $PF=0.9848$: (a) For time window form 0 to 0.4 second; (b) For time window form 1.7 to 2.025 second 191

Chapter 1

Introduction

1.1 Background

The electrification of our society has empowered countless advances in other fields such that the U.S. National Academy of Engineering ranked it as the greatest engineering achievement of the last century [1]. Electricity consumption per capita has a strong correlation to social development indices and especially to economic indices (such as gross domestic product per capita). Increasing electricity consumption per capita can directly stimulate faster economic growth and indirectly achieve enhanced social development [2]. Therefore, existing power systems must be able to accommodate increasing demand of electricity. However, due to limited capacity and aging of the infrastructure, the present-day power system is not able to keep up with fast growth of electricity consumption. That means several events can lead the power system to major blackouts. Figure 1.1 shows a timeline of some events related to the electricity grid in the U.S. that have served as harbingers to important changes via mandates and legislations [3]. PJM in the figure stands for Pennsylvania-New Jersey-Maryland Interconnection. Several legislative mandates have been put in place to transform the

existing power system to modernized power system so called *Smart Grid*.

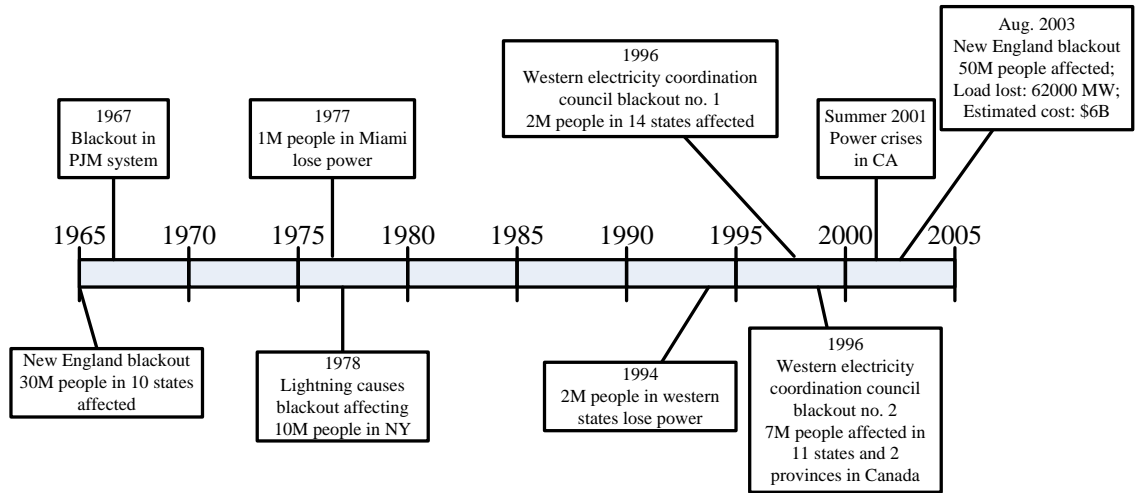


Figure 1.1: Timeline of major events in the U.S. electric grid [3].

Although there is no generally accepted definition for smart grid, the U.S. Department of Energy defines it as “an electric grid that uses information and communication technology to gather and act on information, such as information about the behavior of suppliers and consumers in an automated fashion to improve the efficiency, economics, and sustainability of the production and distribution of electricity.” Based on this definition, it can be inferred that efficiency, economics, and sustainability are the main goals to move from current power system toward smart grid.

Since smart grid can gather real-time information and provide close to real-time information of the system, new options have been proposed in the literature to improve the efficiency, economics, and sustainability of the grid [4]- [7]. These options could include generation, power delivery, and load part of power system. Figure 1.2 demonstrates some possible features of smart grid and their improved area.

In terms of generation, distributed generator (DG) is an attractive option. By

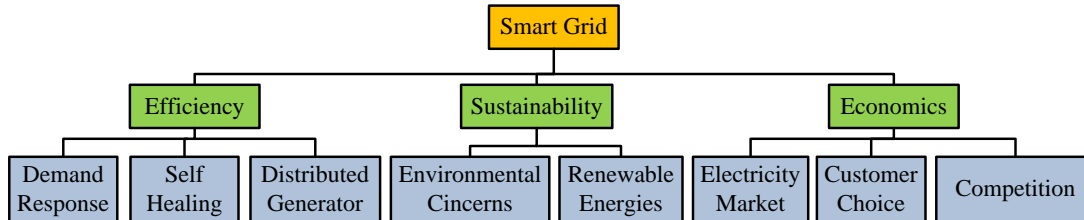


Figure 1.2: Smart grid features.

the Electric Reliability Council of Texas (ERCOT)’s definition, a DG resource is an electrical generating facility located at a customer’s point of common coupling (PCC), of ten MW or less and connected at a voltage less than 60 kV which may be connected in parallel operation to the utility system. Wind turbine (WT), micro-turbine, and photovoltaic (PV) are examples of DGs. In terms of power delivery, smart grid and management system enables a system operator (SO) to monitor and control electric power system (EPS) and interconnected DGs. The better measuring and communication technology, the more close to real-time control could be applied by the SO. In terms of load, demand response (DR), and load management systems are popular solutions to contribute in the smart grid concept. Electric vehicle (EV) is an attractive tool to facilitate DR.

However, there are also challenges with those above mentioned approaches. The productions of renewable energy, strongly influenced by weather conditions, are intermittent and cannot be forecasted accurately. That results in difficulties in power system planning and operation. In order to mitigate the adverse impact of those intermittencies, the stochastic characteristics and the dynamic interplay between renewable energy generation and load demand should be carefully considered. Integrating EVs into the power grid is also very challenging. The unregulated charging of EVs with fast charging flow rates can results in a heavy load burden on the already

stressful EPS and may even cause system to break down.

1.2 Problem Definition

1.2.1 EV Related Challenge

As mentioned in Section 1.1, unscheduled charging of EVs would impose heavy load on the already stressful EPS. Therefore controlled charging of EVs is inevitable. In order to control a large group of EVs, a simple operating model of EV is needed. The model should be accurate to consider different technical and economical aspects of the EV operation. The model must be comprehensive in order to study EV capabilities to provide different possible ancillary services.

To engage EVs in different activities, rather than just charging, one should evaluate the economic values of those activities. Those activities could be several ancillary services including voltage and frequency regulation services. A systematic framework to evaluate economic values of the services provided by EVs is necessary. Since those services have to be provided in a real-time or close to real-time basis, the framework should be easy to implement and scalable to be applied for a large group of EVs.

1.2.2 DG Related Challenge

As addressed in the IEEE 1547 standard, unplanned islanding of the distribution EPS must be prevented. According to the standard, loss of grid connection must be detected by DGs within 2 seconds and must lead to immediate trip of the DGs from the EPS. Hence it is crucial for the utility companies to ensure that connected DGs preclude any unintentional island risk to the grid. To perform this task, grid operating conditions in which interconnected DG's anti-islanding schemes may not

satisfy the requirements of the standard must be calculated. Although the number and penetration of DGs are increasing rapidly, a systematic and efficient procedure for utility companies to evaluate risk of unintentional islanding of interconnected DGs is missing.

1.3 Claims of Originality

This dissertation builds on the works of many previous research contributions and adapts well-established theories for EVs operating strategies to participate in energy and ancillary markets, as well as analyzing the risk of unintentional islanding of integrated DGs. Nonetheless, the following can be highlighted as contributions, in each chapter, that are original and distinct.

1.3.1 Chapter 2

1. Development of a deterministic optimal power flow (OPF) in distribution power system to analyze the effect of CO_2 emission cost on distribution system scheduling with PV and WT as power sources.
2. Development of a stochastic model of the distribution system considering uncertainties for renewable resources and EVs availabilities for charging and discharging. The model includes:
 - Stochastic optimal power flow (SOPF) based on two points estimation method for calculation of optimal scheduling of DGs along with optimal scheduling of EVs charging to minimize the operating cost of the system.
 - SOPF based on Monte-Carlo simulation to analyze the effects of operation of distributed energy resources (DERs) on social welfare considering

emission taxes.

1.3.2 Chapter 3

1. Development of the scheduling algorithms for an EV aggregator to minimize aggregator's operating cost including:

- Rigorous modeling of the EV which includes charging/discharging modes of operation and battery degradation cost;
- Approximating of the EV model with a linear program which improves the efficiency and scalability of the approach;
- Extending formulations for a large group of EVs under the aggregator's control.

1.3.3 Chapter 4

1. Development of a structure to calculate the reactive power supply function of EVs and that includes:

- Analyzing EV's capability to provide reactive power service.
- Modeling EV as a reactive power service provider (RPSP).
- Inclusion of current ripple limitation of the DC-link capacitor as a constraint on optimal EV operation.
- Calculation of the the EV's reactive power supply function as a step-wise ascending function, in real-time manner.

1.3.4 Chapter 5

1. Development of a multi-level optimization algorithm to strategize optimal participation of the aggregator in the frequency regulation market. The algorithm includes:
 - Upper optimization level: calculation of optimal charging/discharging schedules of EVs under the aggregator's control using linear programming;
 - Lower optimization level: calculation of optimal aggregator's bidding component, capacity, and ascending step-wise energy cost functions, to participate in regulation market and comply with Federal Energy Regulatory Commission (FERC) Order 755;
 - Post-process optimization level: optimal assignment of EV battery capacity to satisfy received automatic generation control (AGC) signal from the SO.

1.3.5 Chapter 6

1. Development of a procedure to evaluate the risk of unintentional islanding of integrated DGs and that includes:
 - Detection of distribution feeder topology and node connectivities, in a systematic way, from the data that can be obtained from softwares commonly used by utilities;
 - Using generic models of different types of DGs.
 - Finding operating regions which results in unintentional islanding, violating the IEEE 1547 standard.

1.4 Dissertation Outline

1.4.1 Chapter 2: Integration of DERs into the Micro-Grid

This chapter presents a model based on an OPF, to solve the micro-grid generation scheduling problem. The objective function of the OPF is to minimize the operating cost of the micro-grid, considering air pollutants emission cost, retail electricity price of the grid, price of generated power by DGs, and the weather conditions (including the wind speed and sun radiation characteristics). The OPF model is then extended to an SOPF which considers the uncertainty of EV usage pattern. Potential suppliers in the developed SOPF are the main grid supply, a range of different DG technologies within the micro-grid, and EVs operated in vehicle-to-grid mode. Solving SOPF based on two different methods, two points estimation and monte-carlo simulation, we analyze the effects of operating DERs on social welfare considering emission taxes. Based on the simulation results, it can be inferred that the three key features of smart grid (efficiency, economics, and sustainability) are improved through optimal coordination of EVs charging/discharging and DGs dispatching.

1.4.2 Chapter 3: EV Modeling

After proving the significant impact of EVs on efficiency, economics, and sustainability of EPS in Chapter 2, we provide a comprehensive EV model in this chapter. To develop an EV model, the characteristics of the EV charger and battery, the duration of time over which the EV is connected to EPS, the initial and the owners desired state of charge (SOC), and the battery degradation factor are discussed in this chapter. We present a procedure to linearize the EV model that includes charging/discharging modes of operation as well as battery degradation cost. The model is developed to

generate the aggregator's model, capable of controlling a large group of EVs.

1.4.3 Chapter 4: Reactive Power Service from EVs

In this chapter we study the possibility of the EV serving as RPSP. We start with analyzing technical constraints of the EV to provide reactive power service. Using the developed model of the EV in Chapter 3, we present a framework to calculate the reactive power supply function of the EV. The framework can serve the aggregator, representing the participant EVs in the reactive power service, to provide the aggregated reactive power supply function. The framework is scalable, efficient, and can be used to calculate the reactive power supply function as a step-wise ascending order function in real-time basis.

1.4.4 Chapter 5: Frequency Regulation Service from EVs

Capability of EV's battery to participate in frequency regulation service is investigated in this chapter. Using the EV model presented in Chapter 3, a framework is presented to accommodate EVs, as distributed energy storages, in FERC Order 755 requirement. That means the service provided by EVs must have appropriate bidding components, including the available power capacity for the regulation service along with a step-wise ascending energy cost function. The framework developed in this chapter can serve the aggregator to participate in frequency regulation market, without lowering the EV owners comfort level.

1.4.5 Chapter 6: DGs Integration and Micro-Grid

As addressed in the IEEE 1547 standard, unplanned islanding of the distribution EPS must be prevented. According to the standard, loss of grid connection must

be detected by DGs within 2 seconds and must lead to immediate trip of the DGs from the EPS. Hence it is crucial for the utility companies to ensure that connected DGs preclude any unintentional island risk to the grid. In this chapter, a procedure is developed that can be used by the utility companies to analyze the risk of occurring unintentional islanding due to integrated DG unit(s), in an efficient and systematic fashion. The developed procedure is not dependent on the DG's anti-islanding schemes (active or passive) and can be used as a tool for studying the risk of islanding in any radial distribution feeder.

1.4.6 Chapter 7: Conclusion and Future Work

This chapter summarizes the researcher's main contributions and discusses future research topics in the area, including problems regarding incorporation of EVs in reactive power service and frequency regulation, at EPS level and from the SO stand point. Also future research topics related to concerns of DGs interconnections are discussed. Those topics include possible improvement in the developed procedure, in order to take into account intermittent nature of renewable energy resources.

Chapter 2

Integration of DERs into the Micro-Grid

2.1 Introduction

Nowadays increasing demand of electricity forces power system SOs to operate their systems close to thermal, mechanical, and electrical limits. Several solutions could be considered to alleviate those operational conditions like increasing generation, transmission and distribution capacity, decreasing energy consumption by increasing equipment efficiency, and demand management. These scenarios have their own advantages and disadvantages. Introducing smart grids as next generation energy systems provides new capabilities for regulators, utilities, and customers. Those capabilities cover needs of bi-directional power flow, advanced metering infrastructure, real-time pricing or more broadly, time-variable pricing, smart devices and in-home energy management systems, peak load curtailment, demand side management, DR, demand for high power quality, increased concerns about global climate changes associated with conventional means of power generation, and integration of DGs.

Developments in DG technologies and restructuring of power system encourage using DGs in power system. Several definitions for DG have been presented in the literature [8]- [9]. This chapter engages in the following definition: DG is an electric power source connected directly to the distribution network or the customer [10]. The potential benefits of DG is sustained in the following factors: increasing power quality requirements, avoiding or shifting investment in transmission lines and/or transformers, minimizing ohmic losses, and protecting the environment [11]- [12].

In terms of environmental concerns, using renewable resources can decrease the amount of greenhouse gases, such as CO_2 . Operating PV and WT in a micro-grid, close to load centers, can help the SO to minimize greenhouse gases emission of EPS. Achieving this objective concludes optimal power generation scheduling of the micro-grid. Generation scheduling of the micro-grid is regulating the input power from the main grid and output power of DGs, meeting the power balance, the limits of output power of each DG, the bus voltage and the line capacity of the micro-grid, and minimizing the sum of generation cost and greenhouse gases emission cost [13]- [17]. Hence the micro-grid scheduling problem can be categorized as an optimization problem.

DR and load management systems are also popular options to contribute in the smart grid concept. EVs are an attractive option to facilitate DR programs. Implementing any methodologies in optimal micro-grid operation, considering DGs and EVs separately, would not be reliable. Considering one facet of the problem, might not give us the total picture of the system. In addition, evaluating feasibility of the micro-grid operation (technically and economically) is a crucial part of planning future smart grid.

This chapter presents a novel model based on an OPF, to solve the micro-grid generation scheduling problem. We start developing the OPF, first considering DGs

and CO_2 emission. We then extend the proposed OPF formulation to include EVs in the system operation. Then we add uncertainty of DG output, for renewable energies, and EV usage pattern into the OPF and upgrade it to a SOPF.

The main contribution of the research in this chapter is summarized as follows:

1. Development of a deterministic OPF to analyze the effect of greenhouse gas emission on distribution system scheduling with PV and WT.
2. Development of a SOPF considering uncertainties for renewable resources and EV usage patterns.
3. Analyzing the SOPF with two stochastic methodologies: Two point estimation; and Monte-Carlo simulation.

2.2 Carbon Emission

CO_2 and greenhouse gases emission are usually associated with burning of fossil fuels in different applications such as transportation, electricity, and etc. Figure 2.1 shows the U.S. energy-related CO_2 emissions by sector from 1990 to 2008 [18]. It can be seen that in the U.S., electric power sector has the most share in greenhouse gases emission. Therefore any reduction in greenhouse gases emission in this sector causes remarkable reduction in the whole amount. Table 2.1 lists CO_2 emission from the top ten states produced by power plants [19].

In this chapter, the focus is on using DGs with renewable resources (WT and PV) in order to decrease the power generation of conventional remote power plants (fossil fuels burning) and show its affects on greenhouse gases emission reduction. Next we develop an optimization problem to define optimal dispatch of DGs.

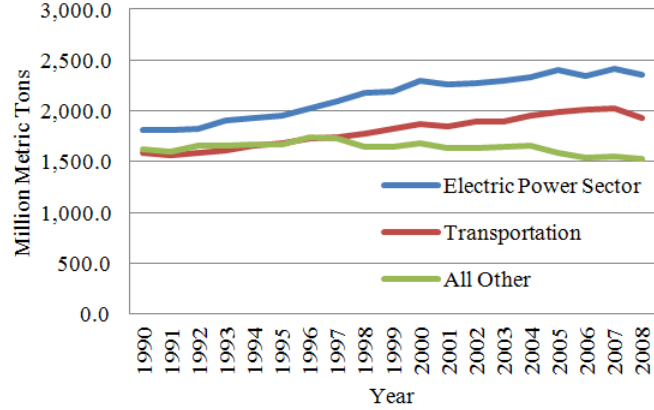


Figure 2.1: U.S. greenhouse gas emission by sectors.

Table 2.1: CO_2 Emission of Top Ten States (Metric Tons).

State	2009 Emission	2010 Emission
Texas	244,248,050	256,903,967
Florida	119,960,137	130,324,532
Ohio	119,793,429	124,966,156
Indiana	117,544,009	123,695,438
Pennsylvania	114,331,904	123,345,741
Illinois	102,752,939	107,082,729
Kentucky	92,614,351	99,246,065
Georgia	81,906,514	86,826,424
Alabama	74,033,748	84,734,388
Missouri	75,774,756	83,279,658

2.3 OPF Formulation

The SO is responsible for operation of the micro-grid. SO must operate the micro-grid in a way to minimize its operation cost. The operation cost includes several terms. These terms may vary with different policies. The operation cost of the micro-grid, considering power generation and CO_2 emission cost terms, can be expressed as

equation (2.1).

$$\sum_{t=1}^T [p_t^{grid} \times pr_t^r + \sum_{i=1}^M p_t^{DG_i} \times pr_{DG_i}] + \sum_{t=1}^T CEF \times CCE \times (p_t^{grid}), \quad (2.1)$$

where T is the number of time intervals for a day and t is an index for time interval, M represents number of DGs in the micro-grid and i is an index for DGs, p_t^{grid} and $p_t^{DG_i}$ are injected active power to the micro-grid from main grid and DG respectively. pr_t^r is retail price of electricity in the micro-grid, pr_{DG_i} is price of electricity generated by each DG. CEF and CCE stand for Carbon Emission Factor (kg/kWh) and Cost of Carbon Emission (\$/kg), respectively. First term in the equation is for power generation cost and the second term calculates the emission cost of network. It is assumed that in the micro-grid, only PV and WT are operated. Hence the emission cost associated with these kinds of DGs is zero.

The objective function of the OPF is to minimize the operating cost of the micro-grid. Therefore the purpose of the proposed OPF, is minimizing equation (2.1), subject to the following constraints.

$$p_t^{grid} + \sum_{i=1}^M p_t^{DG_i} = p_t^{load} + p_t^{loss}, \quad (2.2)$$

$$p_{min}^{DG_i} \leq p_t^{DG_i} \leq p_{max}^{DG_i}, \quad (2.3)$$

$$V_{min}^j \leq |V_t^j| \leq V_{max}^j, \quad (2.4)$$

$$P_t^{inj_j} = \sum_{k=1}^B |V_t^j| |V_t^k| |Y_{jk}| \cos(\theta_{jk} - \delta_t^j + \delta_t^k), \quad (2.5)$$

$$Q_t^{inj_j} = - \sum_{k=1}^B |V_t^j| |V_t^k| |Y_{jk}| \sin(\theta_{jk} - \delta_t^j + \delta_t^k), \quad (2.6)$$

$$|S_t^{jk}| \leq |S_{max}^{jk}|, \quad (2.7)$$

for all $t = 1, \dots, T$, $i = 1, \dots, M$, $l = 1, \dots, N$ and $j = 1, \dots, B$, where N is the number of lines in the micro-grid, l is an index for line, B is the number of

buses in the micro-grid, j and k are indexes for bus, V_t^j is bus voltage with phase δ_t^j (in radian), V_{min}^j and V_{max}^j are minimum and maximum values for amplitude of bus voltage, respectively. Y_{jk} is the element in row j and column k of the bus admittance matrix of the micro-grid with angle θ^{jk} (in radian). p_t^{loss} shows active power loss at time interval t . $P_t^{inj_j}$ and $Q_t^{inj_j}$ are the net active and reactive power injected to bus j . Injected power includes generated power from grid and DGs. S_t^{jk} is the transmitted apparent power (in VA) on the line between bus j and k and its maximum value is presented by S_{max}^{jk} . Constraints (2.2), (2.3), and (2.4) represent the load balance constraint of the micro-grid, voltage constraint on each bus of the micro-grid, and generation constraint which are specified as upper and lower limits for the real power outputs of DG units, respectively. Constraints (2.5) and (2.6) express active and reactive power flow equations of the micro-grid. Transmitted power of each line is restricted by equation (2.7). Optimization variables of the proposed OPF are p_t^{grid} and $p_t^{DG_i}$ which are the micro-grid scheduling solutions. The following section provides some numerical results of developed OPF.

2.4 Numerical Results

The following assumptions are considered in this section:

- The OPF is run for 24 hours a day. It means that the number of time interval is 24.
- Constant CCE (flat rate) is used.
- Storage devices in operation of renewable energy are not considered.
- V_{min}^j and V_{max}^j are assumed 0.9 and 1 pu respectively, for all buses.

Figure 2.2 shows a micro-grid [20]. From the figure, it can be seen that four DGs are installed. Two PV on buses 4 and 25 (G_1 and G_3), and two WTs on buses 7 and 30 (G_2 and G_4). Bus 1 is connected to the main grid.

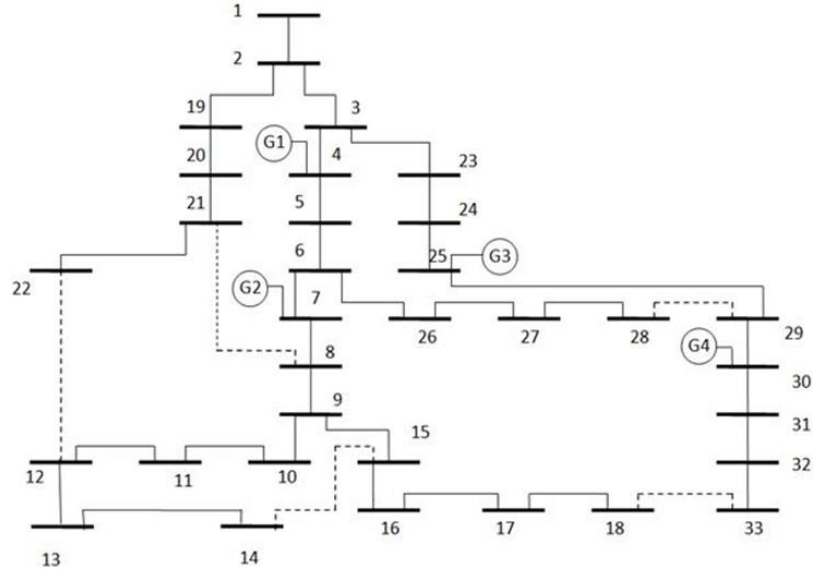


Figure 2.2: 33-bus Test system.

Table 2.2 shows the DGs characteristics used in this simulation. The prices of generated electricity by DGs are taken from reference [21].

Table 2.2: Simulation Settings

DG Unit	Minimum output power (kW)	Maximum output power (kW)	Electricity price (\$/kWh)
PV	0	200	0.21
WT	0	700	0.097

To have realistic solutions, we have used published data on the electricity retail price and daily base load. The data used in our simulations are shown in Figure 2.3 and 2.4 [22].

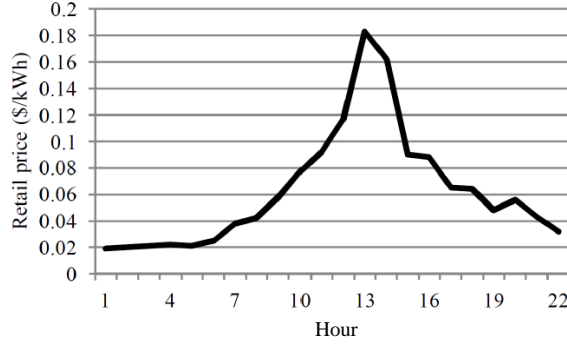


Figure 2.3: The daily electricity retail price

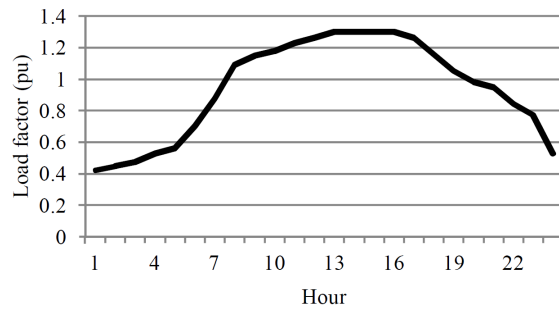


Figure 2.4: The daily base load

PV and WT generations vary with changes in sun irradiation and wind speed, respectively. These variations are assumed to be according to Figure 2.5. It is worth noting that the uncertainty in renewable energy resources will be considered when the SOPF framework is developed. It is also assumed that the fuel used to generate the imported electricity from the main grid is coal. CEF of burned coal is 95.52 (kg CO_2 per MMBtu) [23].

To have a better insight, four scenarios are considered for simulation. In the first scenario, DG units are not connected to the micro-grid. In second and third scenarios, DG units are connected to the micro-grid and constant CCE is applied, without and with considering price of generated electricity by DGs (fourth column of Table 2.2). The constant CCE in Scenario 2 and 3 is 28.24 (\$ per ton CO_2) [24]. In scenario

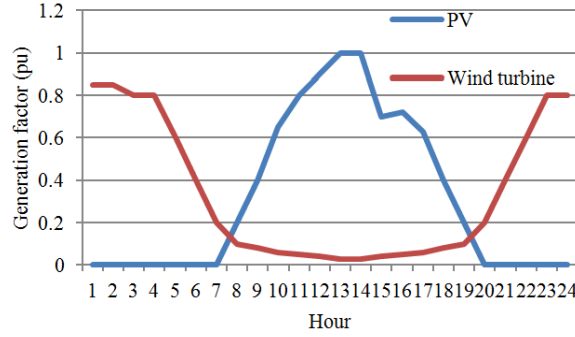


Figure 2.5: PV and WT daily availability.

4, we generate a linear function representing CO_2 emission tax to calculate emission cost, and also consider the price of generated electricity by DGs. Figure 2.6 shows the variations of CO_2 emission tax in terms of injected power from the grid, used in scenario 4. The optimization problems of defined scenarios are solved using MINOS to achieve optimum solutions.

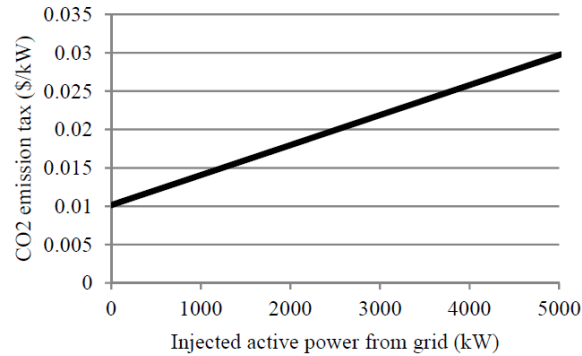


Figure 2.6: Applied CO_2 emission tax in Scenario 4.

Figure 2.7 and 2.8 show the operating cost and power loss of the micro-grid for Scenario 1. From now on, Scenario 1 will be considered as a base case for operating cost and power loss of the micro-grid under different scenarios.

In the first scenario, total load of the micro-grid is supplied by the power purchased from the main grid. Figure 2.9–2.11 show the generation scheduling in different

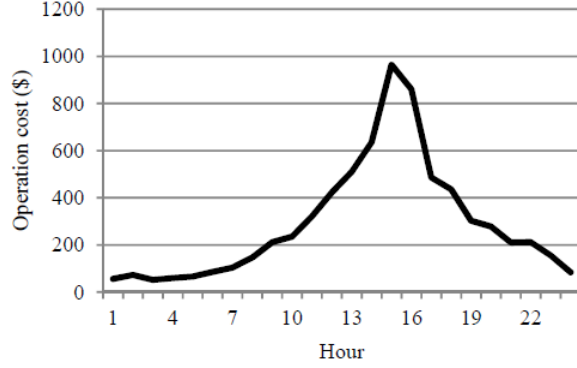


Figure 2.7: Operating cost of the network in Scenario 1.

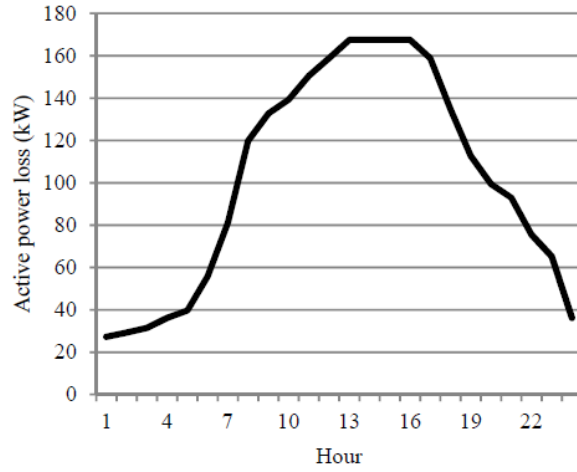


Figure 2.8: Active power loss in Scenario 1.

scenarios. Since PVs and WTs are assumed to have similar characteristics, their generation scheduling are the same. As expected, in Scenario 1, the micro-grid is fed by the injected power from the main grid. In Scenario 2, all DG units are scheduled at their maximum output. The rational is to create a scenario in which constant CO_2 tax is applied, but the price of generated electricity by DGs are not considered. The effect of price of generated electricity by DGs with constant CO_2 emission tax can be seen from simulation results in Scenario 3. Comparing to the results from Scenario 2, it can be seen that in Scenario 3, DG units have lower shares in generation scheduling. Therefore it can be concluded that the applied CCE in this scenario is

not high enough to include all DG units at their maximum output in the generation scheduling. Also the decision to operate DG units at their maximum output, must take into consideration the price of their generated power.

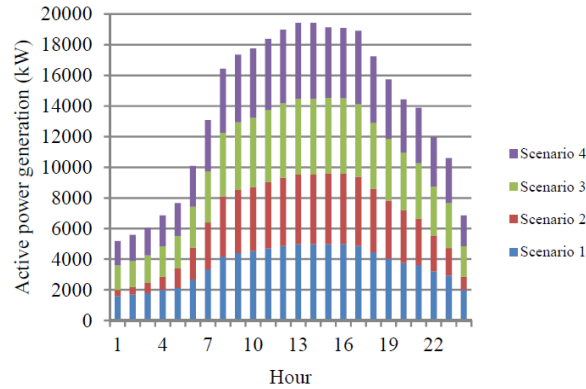


Figure 2.9: Injected power from the main grid in different scenarios.

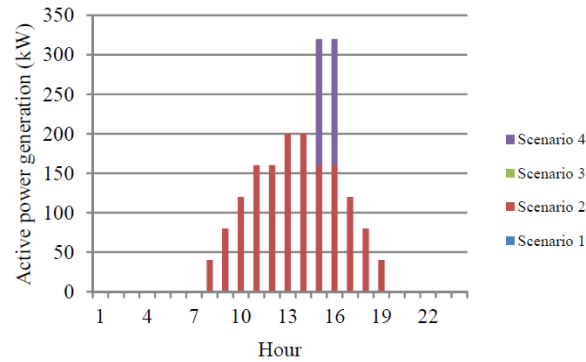


Figure 2.10: Generation scheduling of PVs on buses 4 and 25 in different scenarios.

Since the price of generated electricity by DGs is not considered in Scenario 2, it can be seen that operating cost decreases incredibly comparing to Scenario 1. In scenario 2, SO dispatches all DG units at their maximum output power to avoid the cost of CO_2 emission imposed by the injected power from the main grid. Applying price of generated electricity by DGs in scenario 3, forces SO to look for an optimal

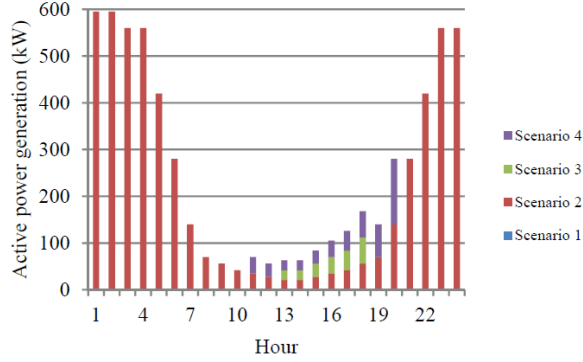


Figure 2.11: Generation scheduling of WTs on buses 7 and 30 in different scenarios.

point to decrease the operating cost, considering DG units cost. In this scenario, if CCE is too low, SO prefers to purchase power from the main grid to avoid the additional cost caused by DGs. So low CCE could not support integration of DGs in the micro-grid, economically. Increasing CCE can support utilizing DGs but in association with higher operating cost. Figure 2.12 also depicts that even though SO purchases more power from DGs, the operating cost of the network increases due to comparatively high electricity price of DGs.

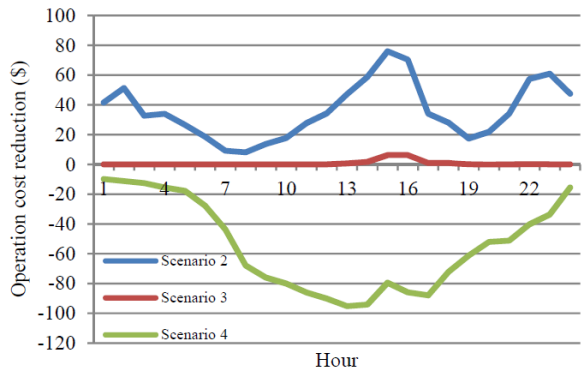


Figure 2.12: Operating cost reduction in different scenarios in comparison to scenario 1.

Figure 2.13 shows the CO_2 emission tax for Scenario 4. It can be seen that the CO_2 emission tax in scenario 4 follows the variations in loads. Increase in loads yields

increase in CO_2 emission tax. At time intervals 15 and 16, CO_2 emission tax is high enough for SO to operate PVs in Scenario 4. Also during time intervals 11 to 20, CO_2 emission tax is high enough for SO to operate WTs in Scenario 4.

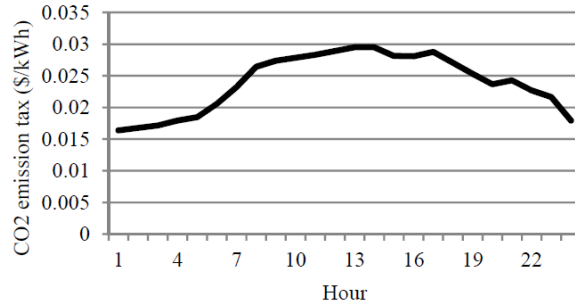


Figure 2.13: CO_2 emission tax in scenario 4.

Figure 2.14 shows that operation of DG units in the micro-grid can decrease ohmic loss. The ohmic loss reduction in Scenario 3 is the least among the other scenarios. The maximum active power loss reduction during the peak load in Scenario 2, 3, and 4 are 11.61%, 3.3%, and 11.07% of the maximum active power loss in Scenario 1, respectively.

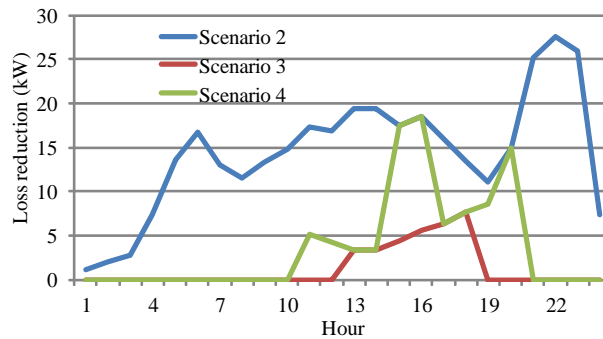


Figure 2.14: Active power loss reduction in different scenarios in comparison to scenario 1.

Comparing simulation results for all four scenarios, it can be concluded that applied CCE in Scenario 3 is not high enough to force SO to operate DG units at their maximum output. Whereas applying the same CCE in Scenario 2, ignoring the price of generated electricity by DGs, encourages SO to operate DGs at their maximum output. Increasing CO_2 emission tax could lower CO_2 emission by forcing SO to operate DGs at their maximum output, even it may increase operating cost of the micro-grid.

Results in this section, indicate the potential benefit of DGs in reduction of greenhouse gases emission. Next, we investigate uncertainty of WT generation, in order to take intermittency into the consideration.

2.5 Wind Energy Production

Production of wind energy depends on the geographical location and WT. Given a specific WT, the production of wind energy is highly correlated with the wind speed. Therefore the production of WT can be predicted based on the expected behavior of wind speed. Parametric model and non-parametric models are commonly used techniques to analyze the behavior of wind speed. Parametric models work with probability distribution function (pdf) but non-parametric models depend on mean and standard deviation (without having the pdf). The focus here is on a parametric model. Weibull distribution function is the most commonly used pdf to describe the behavior of wind speed [25]. The pdf and cumulative distribution function (cdf) of Weibull distribution are given as follows [26]:

$$f(v) = \left(\frac{k}{c}\right)\left(\frac{v}{c}\right)^{k-1}e^{-\left(\frac{v}{c}\right)^k}, \quad (2.8)$$

$$F(v) = 1 - e^{-\left(\frac{v}{c}\right)^k}, \quad (2.9)$$

where v represents the wind speed. c and k are parameters of Weibull distribution function called scale and shape parameter, respectively. Figure 2.15 depicts the pdf of Weibull distribution for different scale and shape parameters.

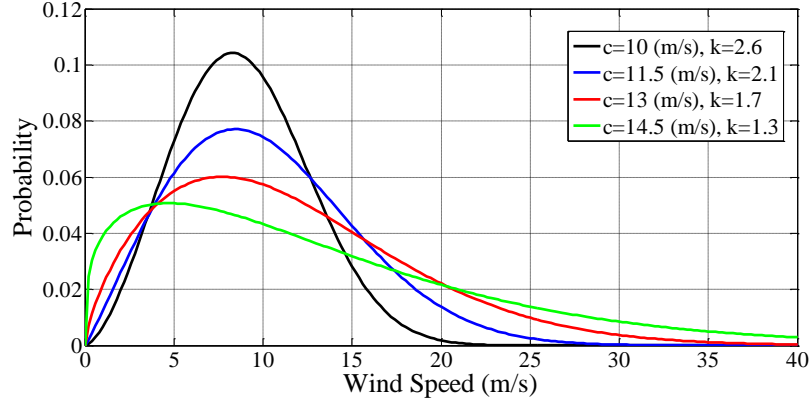


Figure 2.15: Weibull probability distribution function for wind speed.

Based on the pdf and the power curve of the WT, the output power of WT can be calculated. Figure 2.16 shows the typical power curve of a WT. In this figure, four operating regions can be recognized. Standby region (for the wind speed below cut-in speed v_{ci}) with zero output power, nonlinear power production region (for the wind speed between cut-in speed and rated speed v_r) with nonlinear function for output power, rated power region (for the wind speed between rated speed and cut-off speed v_{co}) with the rated output power P_r , and cut-off region (for the wind speed higher than cut-off speed) with zero output power.

The operating regions of a typical power curve of WT can be expressed as follows

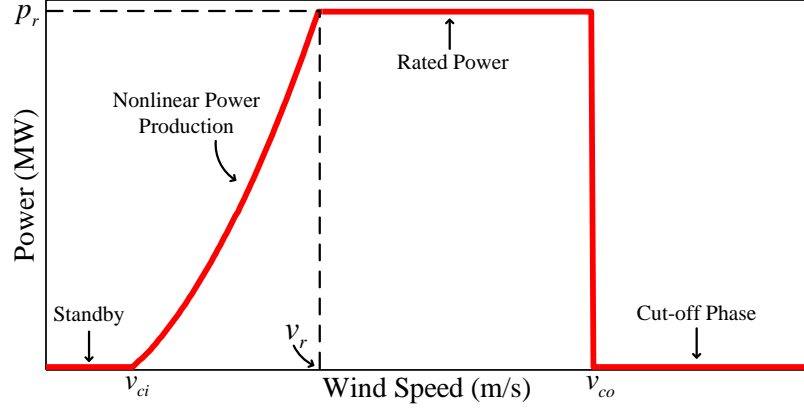


Figure 2.16: Typical power curve of WT.

[27]:

$$P(v) = \begin{cases} 0 & v < v_{ci} \text{ OR } v > v_{co}; \\ P_r(A + Bv + Cv^2) & v_{ci} \leq v \leq v_r; \\ P_r & v_r \leq v \leq v_{co}; \end{cases} \quad (2.10)$$

Calculation of coefficients A, B, and C, related to the nonlinear region, can be found in referee [27].

Another source of uncertainty in the micro-grid, is EV. Integration of EVs into the micro-grid may affect the optimal generation scheduling of the micro-grid. In the following section, the stochastic nature of EVs and its coordination with DGs are discussed.

2.6 Integration of EVs

The focus of the rest of this chapter is to evaluate the feasibility of using DGs and EVs in coordinated fashion. Integration of DGs and EVs has several advantages and

difficulties. For maximum utilization of renewable resources with intermittent nature, storage devices are inevitable. Super capacitor, flywheel, pumped storage, compressed air, battery, and superconducting magnetic technologies [28]- [30], are some examples of storage devices. Each of these storage devices has its advantages, disadvantages, and limitations. In addition, to have them in the system, extra investment must be done. Considering rapid increase in number of EVs, they can be used as distributed storage systems in grid operation.

In his 2011 State of the Union address, President Barack Obama set the goal for the U.S. to become the first country to have 1 million EVs on the road by 2015 [31]. Vehicle batteries could provide services to electricity sector (vehicle-to-grid). Quick battery reaction time has made vehicle-to-grid applications, an attractive solution to stabilize the fluctuations from intermittent sources (such as wind and solar). Integrating EVs into the EPSs, can provide distributed storages for SO without extra investment. However, uncontrolled EV charging/discharging may impose more burdens on power systems. Coordinated charging/discharging of EVs along with optimal scheduling of DGs can help SO to operate its system in an efficient, economic, and sustainable manner.

Reference [32] presented a framework and an optimization methodology for designing grid-connected systems that integrate plug-in EV chargers, DGs, and storage devices. In reference [33], by applying a non-cooperative game theoretical framework for charging and discharging of multiple plug-in hybrid EV batteries, energy consumption of a smart building was optimized. The optimized cost estimation was based on exogenously specified tariffs and market prices. As far as we searched in literature, the charging/discharging scheduling of EVs along with the operation of intermittent renewable resources, at system-wide level, is missing.

In the rest of this chapter, we present a new model in which market clearing prices

are endogenously determined. Potential suppliers include the main grid supply, a range of different DG technologies within the micro-grid, and EVs operated in vehicle-to-grid mode. We allow for supply uncertainties for renewable resources and also allow for uncertainties in EV availability for charging and discharging. Using a SOPF, we analyze the effects of operating DERs on social welfare considering emission taxes.

2.7 Stochastic Nature of EV Usage

In smart grid concept, EV can communicate with SO in real-time and can be charged at various charging flow rates. Therefore SO is able to perform centralized integration and control for EV charging. By applying new algorithms and automatic operation strategies for more precise and efficient load control, SO can save on operating cost while still satisfying customer's charging demand.

During an scheduled charging period, SO collects information from both the power grid and connected EVs and instructs the grid to charge each EV with a charging flow rate given by scheduling algorithm at each time interval. The charging flow rate is limited by EV charger's limit and also the power system delivery capacity.

In addition to power consumed by EVs, SO should also consider the basic daily power loads contributed by all other electronic appliances (e.g. refrigerators, coffee makers, washing machines, and etc) which are considered uncontrollable loads (loads which cannot be controlled by SO). Those loads are referred to as *base load* in this chapter. Values of base load should be counted towards the total power load and can be estimated from historical data.

The time of connection an EV to the micro-grid can be random. An EV can be connected to or disconnected from the micro grid at any time according to the customer's need. As stated in cutting edge framework [34], a customer will inform

SO with his/her desired departure time and final SOC of the EV battery, once the EV is connected to the micro-grid. Each *charging task* can be characterized by a 5-tuple (l, s_l, f_l, e_l, e'_l) , where l is the index for EV, s_l is the starting time, f_l is the desired finishing time, e_l is the initial SOC of the battery and e'_l is the desired SOC at finishing time.

For simplicity of problem formulation, we convert the charging time from *hour : minute* format to a number between 0 and 24. For example, suppose that an EV i is connected to the grid at 6:15 p.m. with an initial SOC of 0.6 and is scheduled to leave at 7:30 a.m. in the next day, with the battery fully charged. Then the corresponding charging task can be presented as $(i, 6.25, 19.5, 0.6, 1)$.

We define a charging/discharging schedule for a given charging/discharging task i as a vector $\Phi_i = [chr_{i,1}, dchr_{i,1}, \dots, chr_{i,t}, dchr_{i,t}, \dots, chr_{i,T}, dchr_{i,T}]$. Each entry of the vector specifies the charging and discharging flow rate at time interval t , where $chr_{i,t}$ and $dchr_{i,t}$ are the charging and discharging flow rate of the i th EV in time interval t , respectively. The charging/discharging schedule must satisfy the following constraints:

$$x_{i,t} = \begin{cases} e_i, & \forall i, t = \lfloor s_i \rfloor, \\ e'_i, & \forall i, t = \lceil f_i \rceil, \\ \frac{E_i[h_{i,t-1}chr_{i,t-1} - h_{i,t-1}'dchr_{i,t-1}]}{C_i} \\ + x_{i,t-1} & \text{otherwise,} \end{cases} \quad (2.11)$$

$$CHR_{i,t}' \leq chr_{i,t} \leq CHR_{i,t}, \quad (2.12)$$

$$DCHR_{i,t}' \leq dchr_{i,t} \leq DCHR_{i,t}, \quad (2.13)$$

where $x_{i,t}$ is the SOC of the i th EV at time interval t ; E_i and C_i are the charg-

ing/discharging efficiency and the battery capacity of the i th EV, respectively. Set of equations (2.11) guarantees that the EV is charged to the desired SOC at the end of charging/discharging scheduling. Note that in these equations $h_{i,t}$ and $h_{i,t}'$ give the actual charging and discharging time of each EV during each time interval, respectively. Equations (2.12) and (2.13) express the minimum and maximum limits for charging and discharging flow rate of each EV at each time interval. The value of $h_{i,t}$ and $h_{i,t}'$ must satisfy the following maximum limit (their minimum value is zero):

$$[h_{i,t} + h_{i,t}']_{max} = \begin{cases} 1, & \lfloor s_i \rfloor < t < \lfloor f_i \rfloor; \\ 1, & t = \lfloor s_i \rfloor, s_i = \lfloor s_i \rfloor; \\ 1, & t = \lfloor f_i \rfloor, f_i = \lfloor f_i \rfloor; \\ \lceil s_i \rceil - s_i & t = \lfloor s_i \rfloor, s_i \neq \lfloor s_i \rfloor; \\ f_i - \lfloor f_i \rfloor, & t = \lfloor f_i \rfloor, f_i \neq \lfloor f_i \rfloor; \\ 0, & \text{otherwise.} \end{cases} \quad (2.14)$$

The initial SOC of each EV depends on the traveled distance by each EV. Considering average daily travel distance and assuming that the SOC of an EV drops linearly with the traveled distance, the initial SOC can be expressed as follows [35]:

$$e_i = 1 - \frac{\alpha d}{d_R}, \quad (2.15)$$

where α is the number of days the EV has traveled since last charge, d is the daily traveled distance by the EV, and d_R is the maximum range of the EV. A typical value for d_R is 80 miles [36]. Considering normal distribution for the EV usage pattern, sc , the probability density function of the initial SOC, is given by the following equation [35]:

$$sc(e_i; \mu, \sigma) = \frac{1}{\frac{d_R}{\alpha}(1 - e_i)\sqrt{2\pi\sigma^2}} \times e^{-\frac{[\ln(1-e_i) - (\mu - \ln(\frac{d_R}{\alpha}))]^2}{2\sigma^2}}; \quad (2.16)$$

After modeling stochastic nature of renewable resources and EV usage patterns, next we provide and SOPF in order to achieve optimal generation scheduling of the micro-grid.

2.8 Stochastic Optimal Scheduling of Micro-Grid

SO as the only entity responsible to operate the micro-grid, must utilize the available resources in efficient, economic, and sustainable fashion while satisfying the demand and system constraints. To reach this goal, SO should run an OPF. Consider a micro-grid in which DGs, EVs, and several loads (base load) are connected. SO must decide how to schedule the output of available power sources (including DGs, the main grid power, and vehicle-to-grid services from EV). Figure 2.17 depicts flow of power in the system. Based on the objective function of SO, he/she decides on the dispatched power of the main grid and DGs. It also decides on the amount of charging/discharging flow rate of each EV and its time in a way that ensures the EV is ready when needed by the owner.

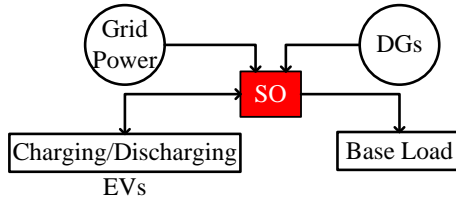


Figure 2.17: Flow of power in proposed algorithm.

The following equation presents the proposed objective function of SO. Note that

the optimization variables in this minimization are p_t^{grid} , $p_t^{DG_i}$, $chr_{l,t}$, $h_{l,t}$, $dchr_{l,t}$, and $h_{l,t}'$.

$$\begin{aligned}
\min \sum_{t=1}^T & [p_t^{grid} \times pr_t^r + \sum_{i=1}^M p_t^{DG_i} \times pr_{DG_i} \\
& + \sum_{l=1}^N pr_t^r \times chr_{l,t} \times h_{l,t} - \sum_{l=1}^N pr_t^r \times dchr_{l,t} \times h_{l,t}'] \\
& + \sum_{t=1}^T [CEF \times CCE \times (p_t^{grid} + \sum_{i=1}^M p_t^{DG_i})] \\
& + \sum_{t=1}^T [SEF \times CSE \times (p_t^{grid} + \sum_{i=1}^M p_t^{DG_i})] \\
& + \sum_{t=1}^T [NEF \times CNE \times (p_t^{grid} + \sum_{i=1}^M p_t^{DG_i})],
\end{aligned} \tag{2.17}$$

where N is the number of EVs in the network; and l is an index for EVs. SEF and CSE represent sulfur oxides Emission Factor (kg/kWh) and Cost of sulfur oxides Emission (\$/kg), respectively. NEF and CNE show nitrogen oxides Emission Factor (kg/kWh) and Cost of nitrogen oxides Emission (\$/kg), respectively. The first and second terms in the equation are for power generation cost, the third term captures battery wear, and the last term calculates the emission cost of the air pollutants from the grid network.

The proposed OPF in this section minimizes equation (2.17) and is subject to constraints (2.2)-(2.7) and (2.11)-(2.14).

2.9 Numerical Results

The following assumptions are considered during the simulations:

- The OPF is run for 24 hours a day. It means that the number of time interval

is 24.

- Constant CCE , SCE , and NCE (flat rate) are used.
- V_{min}^j and V_{max}^j are assumed to be 0.9 and 1 pu respectively, for all buses.
- Weibull distribution is used for wind speed.
- Normal distribution is used for EV usage pattern.

Figure 2.18 shows the test micro-grid [26]. As shown in the figure, three DGs are connected to the network. DG1 and DG2 are WTs with 1.5 MW capacity and DG3 is a natural gas micro-turbine with 1 MW capacity. Five groups of EVs are included in the network. Bus 1 is connected to the main grid.

For simulation we have used two different stochastic methods: Two points estimation; and Monte-carlo simulation. During simulation with two points estimation, we assume that the EVs are allowed to just charge, and the renewable DGs outputs are certain. For simulation with Monte-carlo method, we allow EVs to charge and/or discharge and we consider uncertainty in renewable DGs outputs and EVs usage patterns.

2.9.1 Simulation Using Two Points Estimation

To account for the uncertain nature of renewable resources we perform probabilistic load flow analysis using the two points estimation method. In the two points estimation method [37] we assume that we have mean and variance of the uncertain variables. Then for each of the uncertain variables we run the power flow twice for the value above the mean and the other below the mean. These two points may be symmetric about the mean or not. We investigate the symmetric one. While doing this for one uncertain variable we assume that the other uncertain variables are at

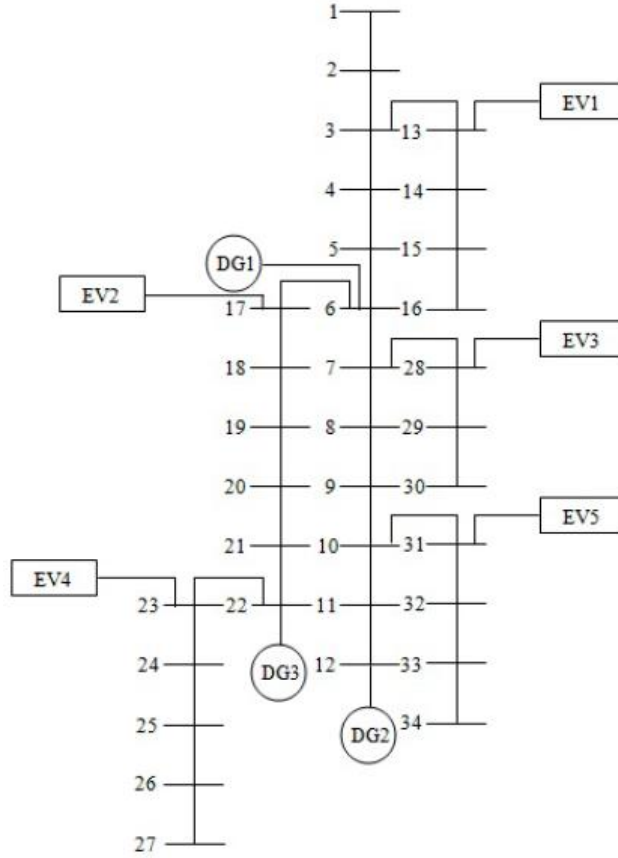


Figure 2.18: 34-bus Test system

their mean values. By doing this to each of the uncertain variables we obtain a set of outputs which are then further used to calculate the mean and the variance of the outputs.

In this part, we assume 40 EVs in each group and we use the electricity retail price and daily base load provided in section 2.4.

We set EV battery related parameters, including the charging rate limit and battery capacity, based on the specification of the Li-ion battery model of a modern EV [38]. Since most customers will charge their EVs during night time, we consider a charging scheduling period starting from 12:00 p.m. (noon) and ending at 12:00 p.m. (noon) in the next day. N charging tasks were generated for a scheduling pe-

Table 2.3: Simulation Settings

Mean of s_i	6 pm
Mean of f_i	7 am
Standard deviation of s_i	2 hours
Standard deviation of f_i	2 hours
E_i	0.9
C_i	16 kWh
P_i	4.4 kW
P'_i	0 kW

riod from 12 p.m. (noon) to 12 p.m. in the next day to simulate the overnight EV charging. To reflect the real-life commute pattern [39], the starting time, s_i , follows a normal distribution with a mean of $\mu = 6$ p.m. and a standard deviation of $\sigma = 2$ hours; the desired finishing time, f_i , follows a normal distribution with $\mu = 7$ a.m. and $\sigma = 2$ hours; and the initial SOC, e_i , is also a random variable uniformly distributed in the range $[0.5, 1]$. The desired SOC is set to 1 (fully charged) for each EV, i.e., $e'_i = 1, i \in \{1, \dots, N\}$. The charging efficiency is 0.9 for all EVs. The related simulation settings are summarized in Table 2.3:

Real wind speed data are taken from reference [40] and are converted to wind energy generation, as shown in Figure 2.19. The wind energy forecast error follows the error distribution given in reference [41].

The optimization variables in this OPF problem are p_t^{grid} , $p_t^{DG_i}$, $h_{i,t}$, and $chr_{i,t}$ for all time intervals. 200 EVs considered in this study are divided in five EV groups (40 EVs in each). Table 2.4 shows the emission factors that used in this study [42]. Note that the micro-turbine uses natural gas and emits air pollutants.

Since micro-turbine emits lower air pollutants than the grid (using coal), it is expected that SO prefers to use it more. Also locating micro-turbine in the micro-grid, causes lower power loss which means lower cost for SO. On the other side, using re-

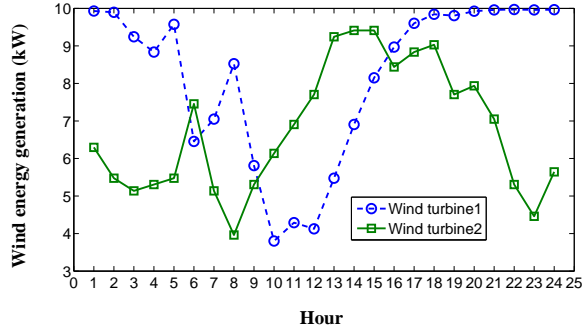


Figure 2.19: The WT energy generation.

Table 2.4: Emission Factors (lbs/MWh).

Fuel	CO_2	SO_x	NO_x
Conventional Coal	2425.5	13	6
Natural Gas	1254	0.1	1.7

newable resources like wind, causes zero cost in terms of air pollution. However, since the power production of these units are costly, SO has to decide on their scheduling, in an optimal way, to decrease the network operating cost.

Figure 2.20 shows the optimal scheduling of DGs in the network. It can be seen that DG3 (micro-turbine) has been scheduled to generate power with full capacity (1 MW) in all periods. The reason is that dispatching micro-turbine reduces overall emission cost. Also at periods 12 through 18, WTs are dispatched to minimize the overall cost.

EVs, as variable loads with flexibility in terms of charging flow rate and time of charging, are another parameter which should be taken in consideration by SO. Using OPF, SO must decide on optimal charging schedule (flow rate and time of charging) for each EV with particular pattern (starting and finishing time of charging, initial and desired SOC). Based on the available generation scheduling, the optimal charging

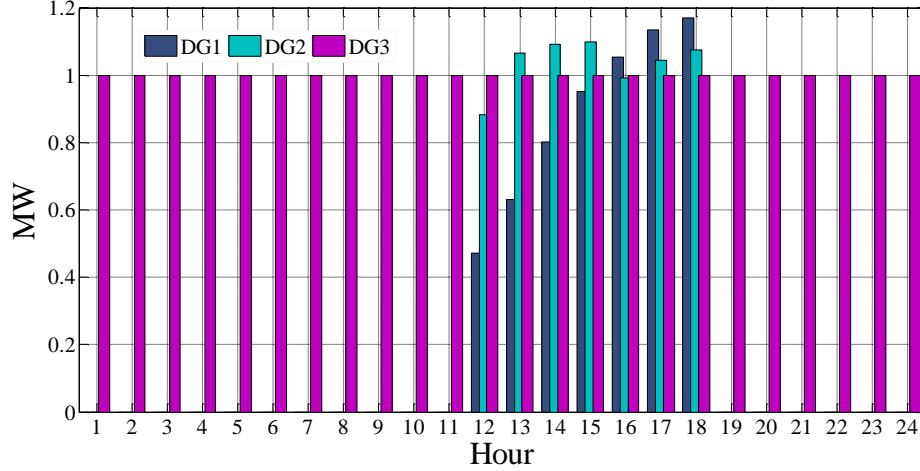
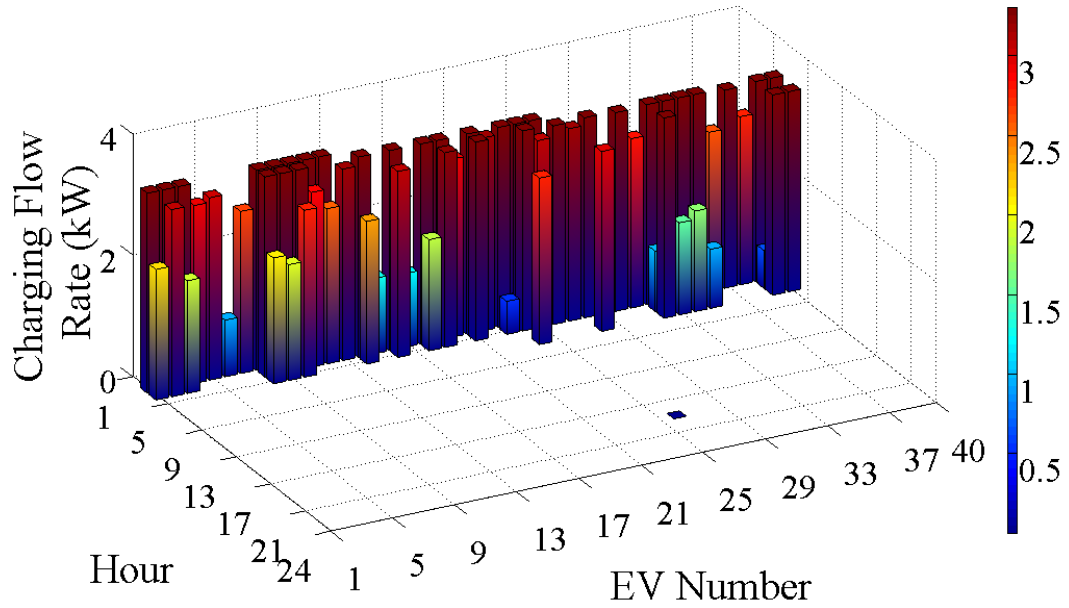


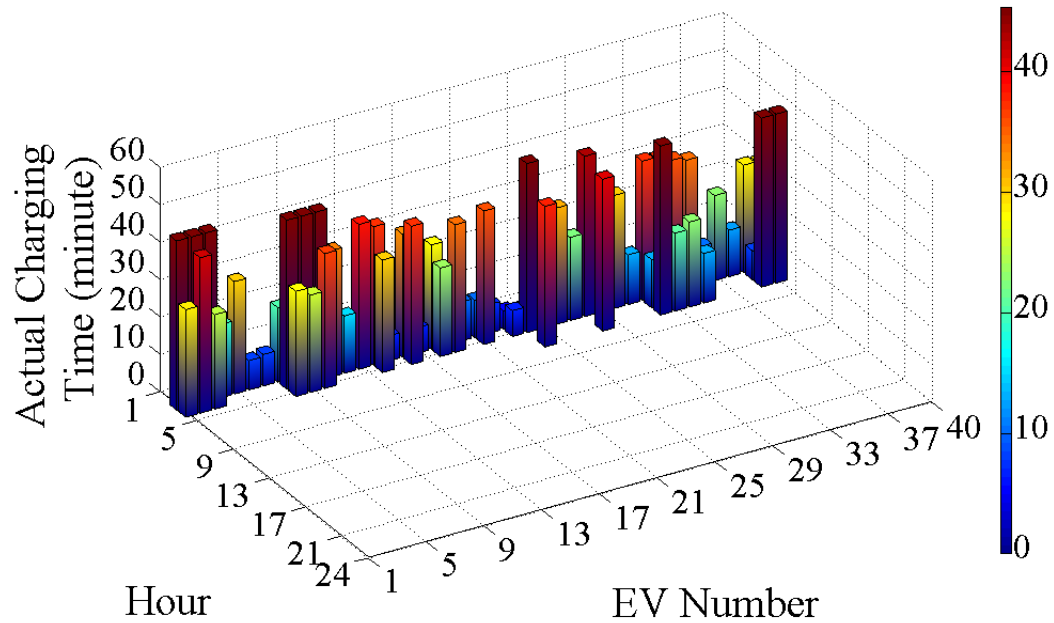
Figure 2.20: Generation scheduling of DGs

scheduling for EVs could be calculated. Figure 2.21 to 2.25 show the mean value of optimal charging scheduling for all EV groups. This optimal charging scheduling seems more meaningful when there are some renewable resources in the micro-grid. Since the emission cost has been applied in the objective function of the OPF, SO scheduled DGs generation and EVs charging in a way to decrease the emission cost as well as the power supply cost. Based on the OPF results, it can be seen that the scheduled charging for EVs are mostly during the off-peak periods or during DGs dispatching time intervals.

In order to quantify the impact of DGs on the operating cost of the micro-grid, we evaluate the operating cost for three scenarios. In the first scenario, all DGs are disconnected. In the second scenario, just micro-turbine is considered. Note that the operation of micro-turbine is associated with emission cost. In the third scenario, all DGs (micro-turbine and WTs) are considered. Note that scheduling results presented above are related to the third scenario. The mean value of the micro-grid operating cost of three scenarios are listed in Table 2.5, where cost reduction means the cost reduced from the first scenario.



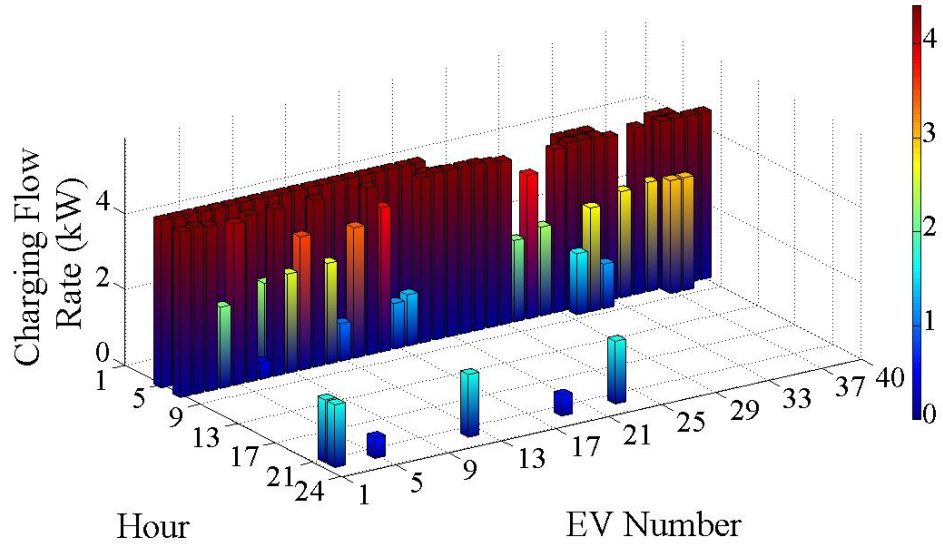
(a)



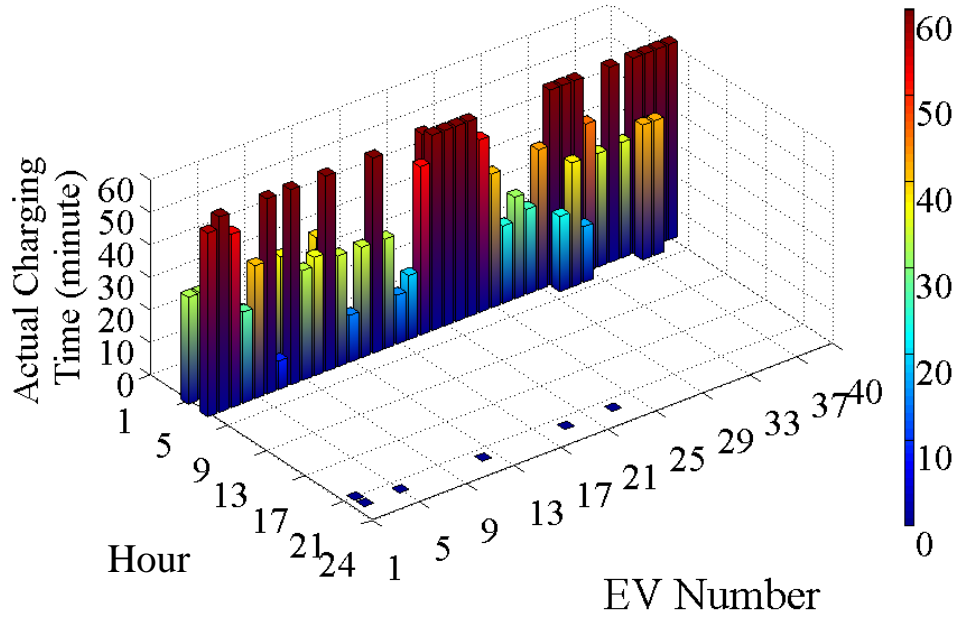
(b)

Figure 2.21: EV group 1 scheduling: (a) Mean value of charging flow rates; (b) Mean value of actual charging time.

From Table 2.5, it is clear that integrating DGs in the network (especially with low emitting resources like wind) and their optimized usage indeed decrease the micro-grid



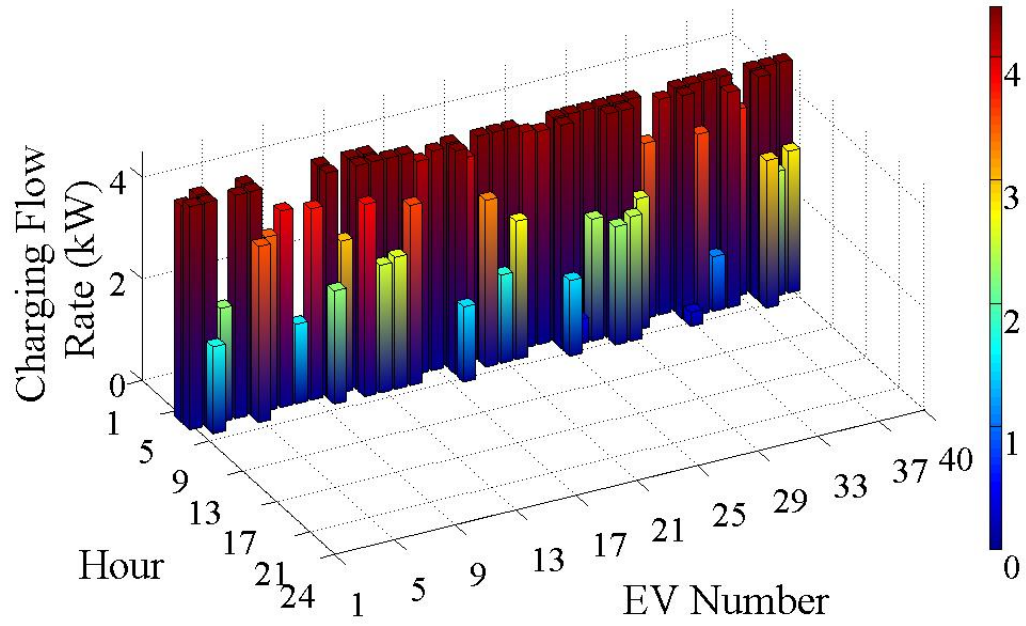
(a)



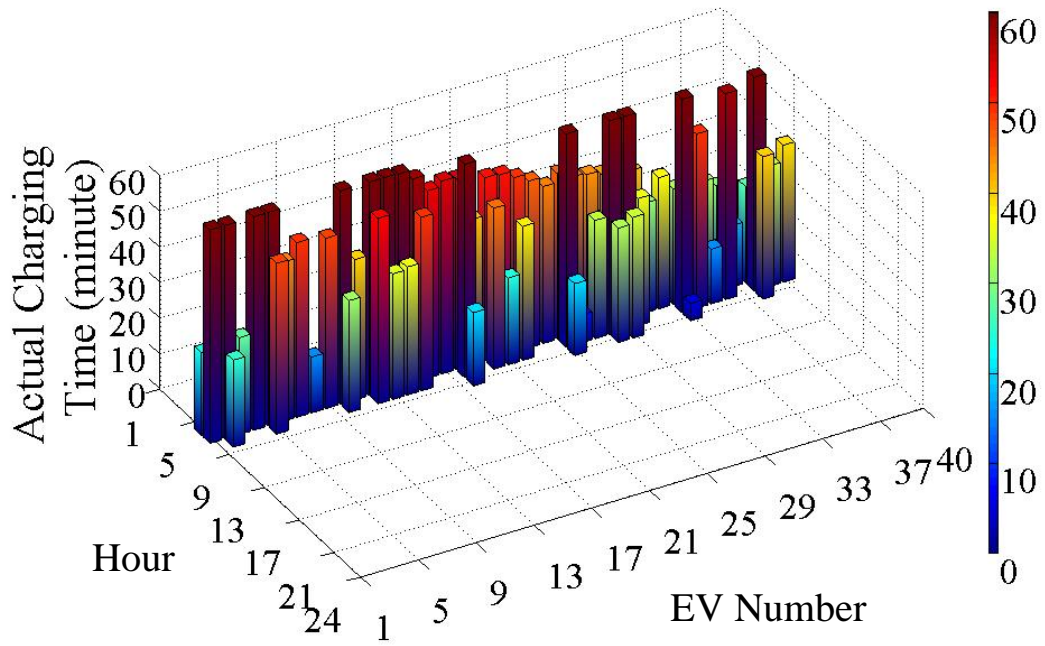
(b)

Figure 2.22: EV group 2 scheduling: (a) Mean value of charging flow rates; (b) Mean value of actual charging time.

operating cost.

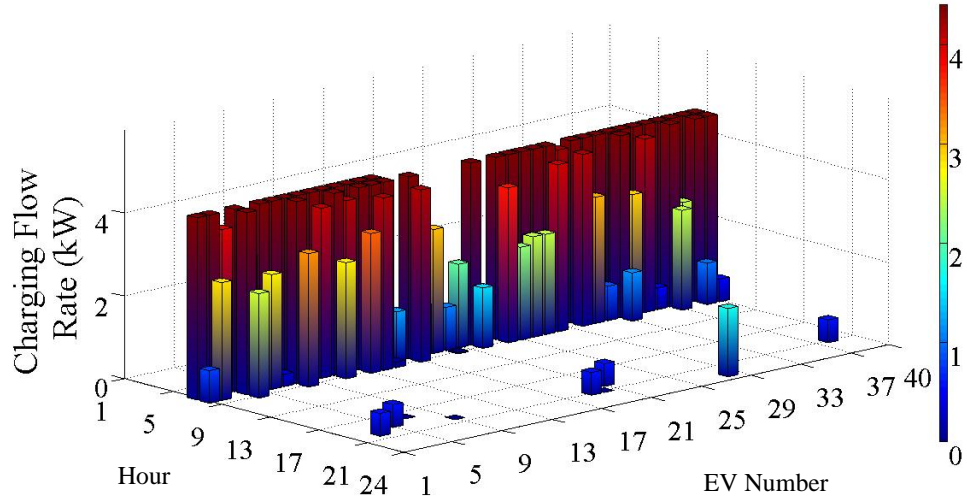


(a)

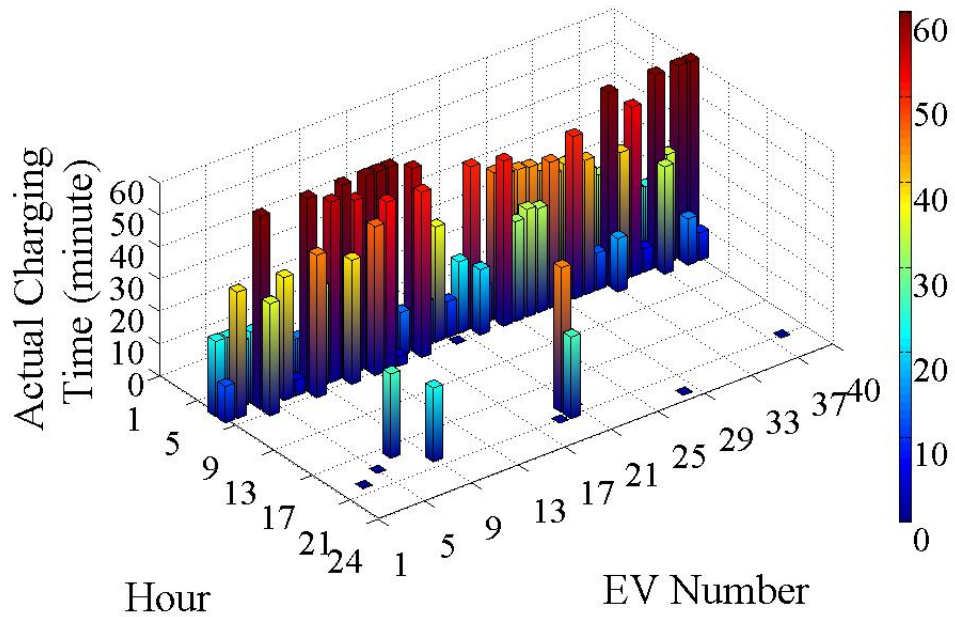


(b)

Figure 2.23: EV group 3 scheduling: (a) Mean value of charging flow rates; (b) Mean value of actual charging time.



(a)

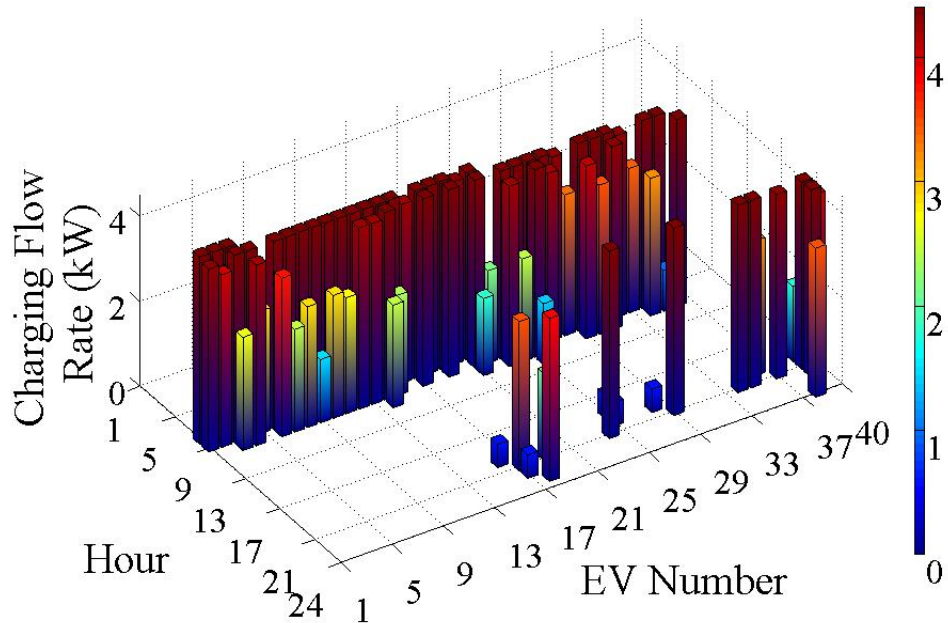


(b)

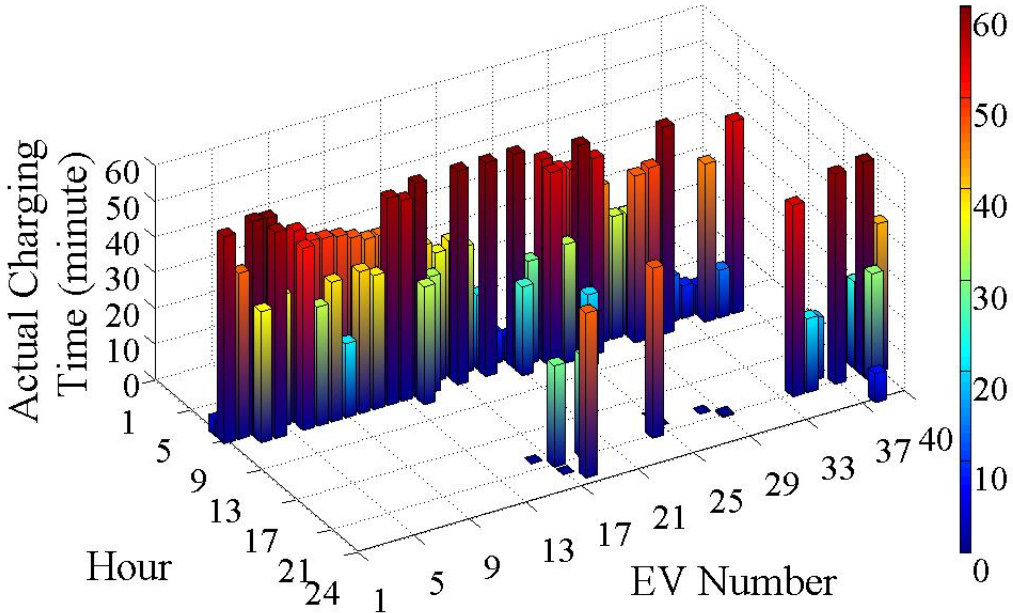
Figure 2.24: EV group 4 scheduling: (a) Mean value of charging flow rates; (b) Mean value of actual charging time.

2.9.2 Monte-Carlo Simulation

Due to the computational time, we have assumed 5 EVs in each group. For retail price of electricity, we have used the average March 2013 monthly price of New York



(a)



(b)

Figure 2.25: EV group 5 scheduling: (a) Mean value of charging flow rates; (b) Mean value of actual charging time.

Table 2.5: System Cost of Each Scenario.

Operating Scenario	Cost (\$)	Cost Reduction (%)
First Scenario	416,464.52	0
Second Scenario	401,761.92	3.5
Third Scenario	394,085.3	5.3

Independent System Operator (NYISO) for Upstate. To consider uncertainty in wind energy production and EV usage pattern, we use monte-carlo simulation. To generate samples, we use Weibull distribution for WTs. Note that normal distribution is used for EV usage pattern (initial SOC, starting time and finishing time of scheduling). Figure 2.26 depicts the flowchart of the monte-carlo simulation applied in the optimization of operation cost reduction.

We have considered two different wind patterns for two WTs in our simulation. For one WT we consider $c_1 = 11.1$ m/s and $k_1 = 2.17$ and for the other WT we assume $c_2 = 14$ m/s and $k_2 = 1.5$ as their scale and shape parameters [11]. Table 2.6 presents the information for EV usage pattern [26], [35], [43].

Table 2.6: Simulation Settings for Monte-Carlo Simulation.

Mean of s_i	6 pm
Mean of f_i	7 am
Standard deviation of s_i	2 h
Standard deviation of f_i	2 h
Mean of travelled distance	22.3 miles
Standard deviation of travelled distance	12.2 miles
E_i	0.9
C_i	16 kWh
T	24
$CHR_{i,t}, DCHR_{i,t}$	4.4 kW
$CHR_{i,t}', DCHR_{i,t}'$	0 kW

The optimization variables in this OPF problem are p_t^{grid} , $p_t^{DG_i}$, $h_{i,t}$, $chr_{i,t}$, $h_{i,t}'$,

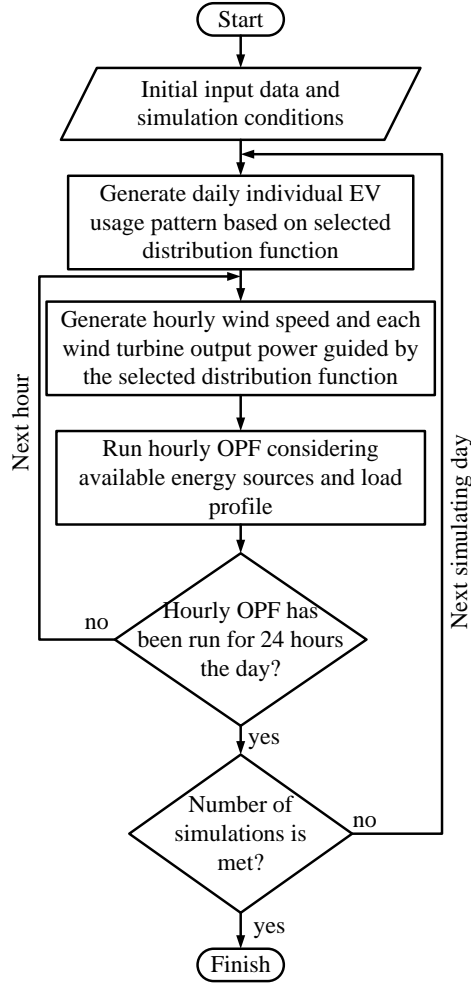


Figure 2.26: Flowchart of Monte-carlo simulation.

and $dchr_{i,t}$ for all time intervals. 25 EVs considered in this study are divided into five EV groups (5 EVs in each). Table 2.4 shows the emission factors that are used in this study [42].

Figure 2.27 and 2.28 show the mean value of daily charging and discharging scheduling of EVs, respectively. Figure 2.29 and 2.30 also show the mean value of actual charging and discharging time of EVs, respectively. From figures, it can be seen that the OPF tries to use EVs discharged power mostly during on-peak hours, in order to satisfy demand. Most of charging tasks of EVs also have been scheduled

during off-peak periods.

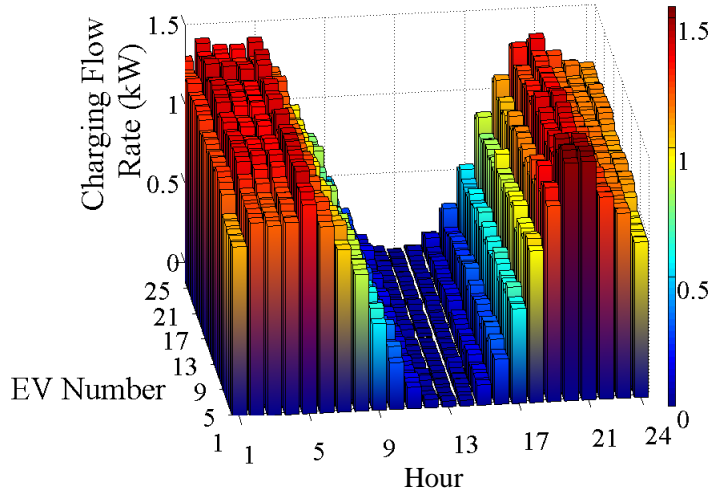


Figure 2.27: Mean value of daily charging flow rate of EVs.

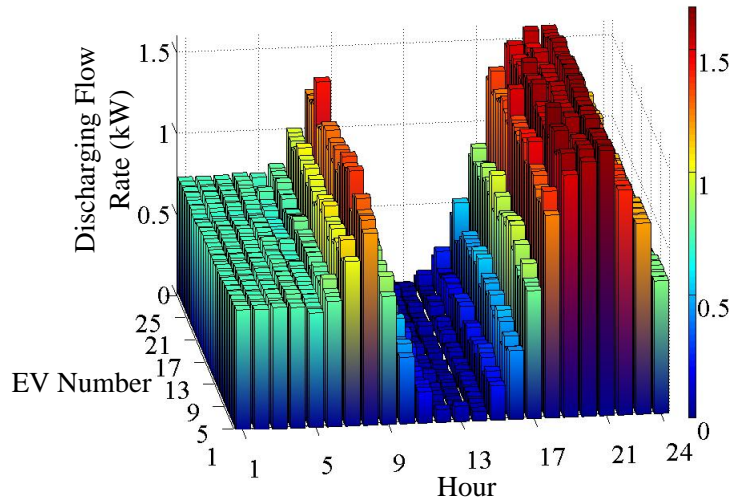


Figure 2.28: Mean value of daily discharging flow rate of EVs.

Since the marginal cost associated with WT production is zero, WTs are always dispatched at their maximum available power. The associated cost of power production from micro-turbine is assumed 3 cent per kWh. The nature of micro-turbine is

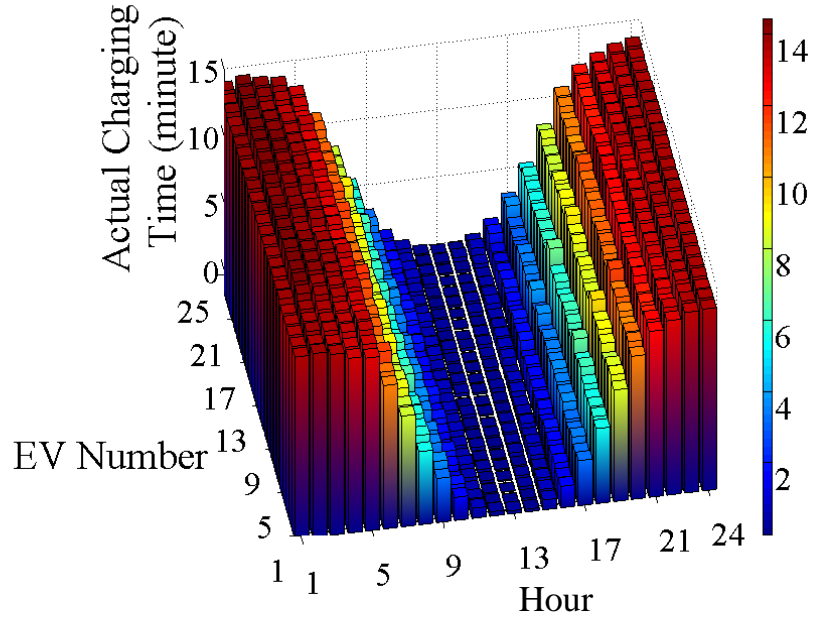


Figure 2.29: Mean value of daily actual charging time of EVs.

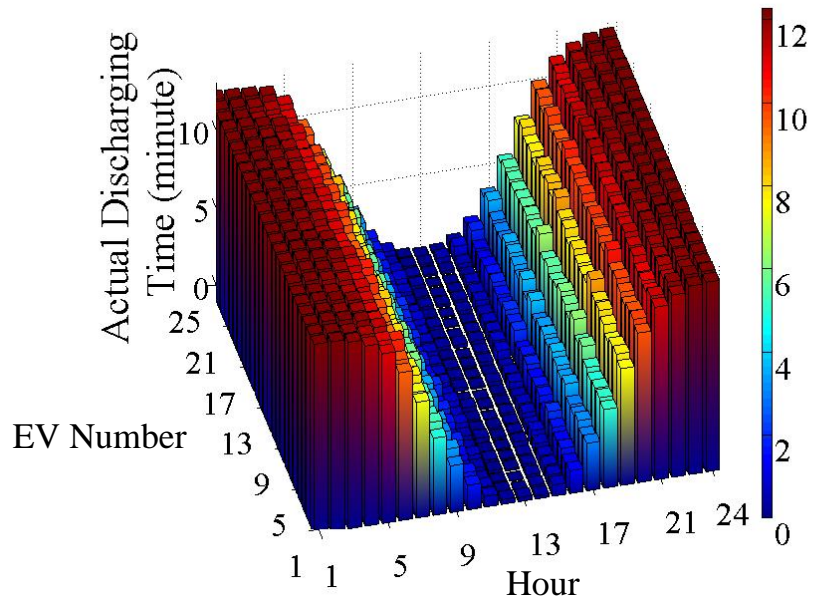


Figure 2.30: Mean value of daily actual discharging time of EVs.

deterministic. Since it is closer to the load center and is relatively cheaper than power from the main grid, it will be dispatched almost for all periods. Figure 2.31 and 2.32

show the mean value and standard deviation of DGs generated power.

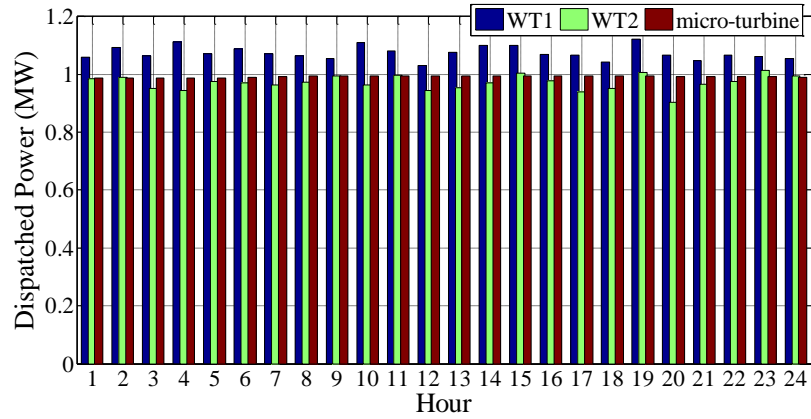


Figure 2.31: Mean value of daily DGs scheduling.

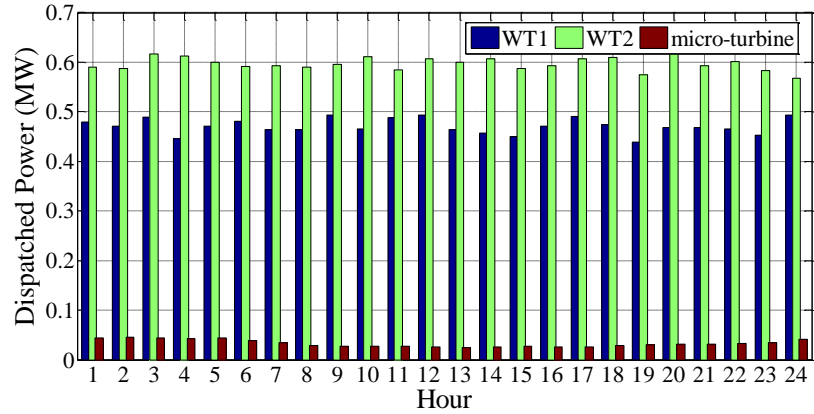


Figure 2.32: Standard deviation of daily DGs scheduling.

Figure 2.33 and 2.34 depict the variation of voltage magnitude of the system. These figures prove that the solution of proposed algorithm keeps the system safe and within its constraint. Mean value and standard deviation of daily operation cost correspond to our test system is \$63571 and \$15477, respectively.

Based on the simulation results, it can be inferred that the three key features of smart grid (efficiency, economics, and sustainability) can be improved by coordi-

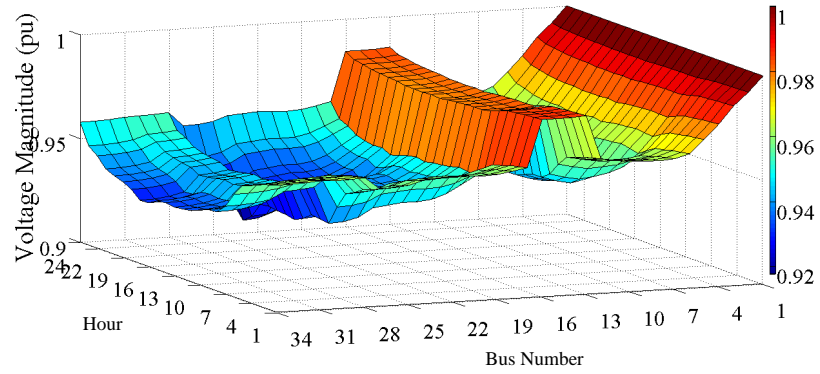


Figure 2.33: Mean value of daily voltage profile.

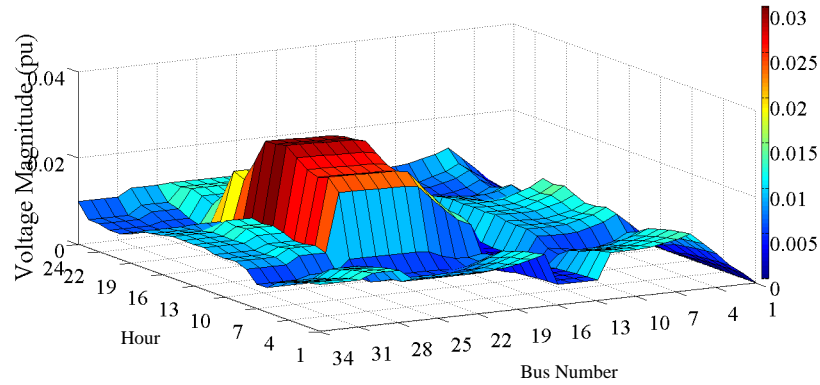


Figure 2.34: Standard deviation of daily voltage profile.

nated using of renewable resources and EVs. The proposed algorithm in this chapter utilized the renewable and less-polluting resources in an efficient way that decreases the operating cost of the system while satisfying all security constraints (voltage and current constraints) and EV owners comfort level.

2.10 Conclusion

This chapter presented a model based on different OPFs to minimize operating cost of a micro-grid, considering greenhouse gases emission cost. From simulation results,

it can be seen that, applying fixed emission tax structures as penalty factors, without considering the price of generated electricity by DGs, may not encourage operation of DG units. On the other hand applying high emission tax forces SO to operate DG units while it raises operating cost. Any increase in operating cost would yield higher prices for end users. Therefore policy makers need to consider the level of impact on end users, DG owners, and environmental concerns before the decisions are made. Integrating EVs in the micro-grid can help SO to utilize renewable energies in system operation. Results of the developed SOPF in this chapter clearly indicate that optimal coordinated DGs dispatch along with EVs charging/discharging scheduling, leads SO to operate the micro-grid in an economical, safe, and environmental friendly fashion. Therefore, one can conclude that DGs and EVs can have positive impacts on the system operation, if the optimal coordination is applied. In the following chapters, comprehensive modeling of EVs, different beneficial services from EVs, and systematic frameworks to engage them in the system operation are presented.

Chapter 3

EV Modeling

3.1 Introduction

Nowadays penetration of EVs is increasing rapidly. The market share of EVs is predicted to increase at a compound annual growth rate of 39% between 2012 and 2020 [44]. EV penetration level into the existing EPS can be increased significantly through intelligent coordination of their charging/discharging schedules [45]. This coordination can be done by an aggregator. An EV charging/discharging network is then defined as a cyber-physical system, which includes a power grid and a large number of EVs as well as aggregators that collect information and control charging procedures of connected EVs.

Exploiting maximum benefits of EVs through providing different possible services as well as charging EVs with minimum cost, require a precise operating model of EVs. This model should be simple to be implementable for large number of EVs and at the same time accurate enough to capture all cost terms associated with EVs operation. In this chapter, a model of EV is developed. All constraint including the initial and desired SOC, minimum and maximum SOC, arrival and departure time,

charger characteristics, and battery characteristics are considered in the model. The developed model then will be expanded to a large group of EVs, under an aggregator's control.

The main contribution of the research in this chapter is summarized as follows:

1. Modeling EV and defining an objective function to calculate the operating cost of the EV including battery degradation cost.
2. Approximating of the optimization problem with a linear program which improves the efficiency and scalability of the approach.

3.2 Optimization Horizon

We first discretize the parking time window into steps of τ , in hour, and use index k to refer to the corresponding time intervals in the EV's parking period. Based on this definition, the active and reactive power flow rates of the EV in time interval k are p_k and q_k in kW and kVAr, respectively. Next the SOC of the EV in time interval k is represented by x_k . Using the initial SOC as x_0 , the owner's desired SOC as x_f , and capacity u of the EV's battery, we calculate the SOC of the EV in each time interval as follows [46]:

$$\left\{ \begin{array}{l} x_1 = x_0 + \frac{\tau}{u}p_1; \\ x_2 = x_1 + \frac{\tau}{u}p_2; \\ \vdots \\ x_T = x_{T-1} + \frac{\tau}{u}p_T; \end{array} \right. \quad (3.1)$$

where T is the number of intervals during which EV is parked. Considering the arrival time h_0 and the departure time h_f , and for a given τ , the number of time intervals

when EV is parked would be as below:

$$T = \frac{h_f - h_0}{\tau}. \quad (3.2)$$

3.3 Battery Degradation

In this section, we introduce a model for battery degradation as a result of charging/discharging activity. To estimate the battery degradation, we have used the battery health model presented in reference [47] and is shown below:

$$\dot{d}_k(I_k, V_k) = \beta_1 + \beta_2 \|I_k\| + \beta_3 V_k + \beta_4 \|I_k\|^2 + \beta_5 V_k^2 + \beta_6 \|I_k\| V_k + \beta_7 V_k^3, \quad (3.3)$$

where I_k is the current (charging when $I_k \geq 0$ and discharging when $I_k < 0$), V_k is the battery cell terminal voltage at a given time instant k , d_k is the battery health in terms of energy capacity ($Amp \times hour \times sec^{-1}$), and β_1 to β_7 are constant values calculated from experimental results.

Based on information provided in reference [48], the battery cell has a constant nominal voltage, V , within the typical minimum and maximum SOC. Therefore, we can rewrite equation (3.3) in terms of p_k and in $Watt \times hour \times sec^{-1}$, as follows:

$$\dot{d}_k(p_k) = (\beta_1 V + \beta_3 V^2 + \beta_5 V^3 + \beta_7 V^4) + (\beta_2 + \beta_6 V) \|p_k\| + \frac{\beta_4}{V} \|p_k\|^2, \quad (3.4)$$

where $p_k = VI_k$. The battery degradation at a given time instant k , in terms of capacity loss, could then be expressed as shown below:

$$D_k(p_k) = \int_0^t \dot{d}_k(p_k) dt. \quad (3.5)$$

where t , in seconds, is the time duration in which the degradation amount is estimated.

Considering the unit price of the battery cell capacity ($\$/Wh$), ϑ , the cost of capacity loss, C , at a given time instant k , can be expressed as follows:

$$C_k(p_k) = t\vartheta D_k(p_k). \quad (3.6)$$

Next assume a battery is composed of n cells and the charged/discharged energy is divided equally into each cell. Then the capacity loss of the whole battery pack can be calculated using the equation below.

$$C_k(p_k) = t\vartheta \left[(\beta_2 + \beta_6 V) \|p_k\| + \frac{\beta_4}{nV} \|p_k\|^2 \right]. \quad (3.7)$$

For example, consider a 6.6 kVA EV charger with a 16 kWh Lithium-Ion battery pack used in the Mitsubishi's i MiEV. This battery pack is composed of 22 cell modules connected in series at nominal voltage of 330 V. Each cell module is composed of 4 cells with nominal voltage of 3.7 V and capacity of 50 Ah. Energy unit price ($\$/kWh$) for Lithium-Ion battery was assumed to be 1500 $\$/kWh$ based on the information in reference [50]. Using the values for β_1 to β_7 provided in reference [47], the battery degradation cost, in $\text{¢}/Sec$, can be calculated as follows:

$$C_k(p_k) = 1.22 \times 10^{-5} \|p_k\| + 2.56 \times 10^{-10} \|p_k\|^2. \quad (3.8)$$

Note that p_k in equation (3.8) is in *Watt*.

Considering values for V and β_1 to β_7 , one can approximate the battery degradation cost function, conservatively, to a linear function using the relation below:

$$C_k(p_k) \approx t\gamma \|p_k\|, \quad (3.9)$$

where $\gamma = \vartheta(\beta_2 + \beta_6 V + \frac{\beta_4}{nV} \bar{p})$. Notice that \bar{p} represents the maximum active power flow that could be used for charging/discharging the battery. For our example, linear approximated value of γ is $1.39 \times 10^{-5} \text{ ¢} \times \text{Watt}^{-1} \times \text{Sec}^{-1}$. Figure 3.1 shows the battery degradation cost per second before and after linear approximation.

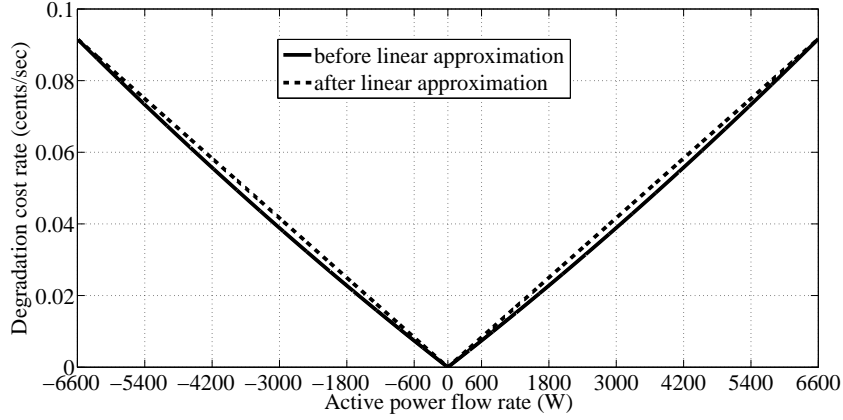


Figure 3.1: Degradation cost of a 16 kWh battery pack used in the Mitsubishi's i MiEV.

3.4 EV Operating Model

The maximum apparent power (in VA) exchanged between the EV charger and the grid is limited by the maximum apparent power of the charger's inverter. This limitation is defined as follows:

$$p_k^2 + q_k^2 \leq \bar{s}^2, \quad (3.10)$$

where \bar{s} is the maximum apparent power (kVA) of the inverter. This limit on the EV charger will be further analyzed in next chapter. Based on the sign of p_k and q_k , four operating regions can be defined as depicted in Figure 3.2.

We consider sets of non-negative prices for charging active power to be $[\rho_1, \rho_2,$

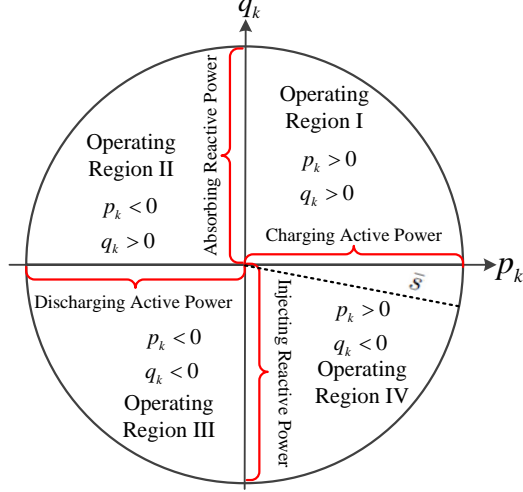


Figure 3.2: Operating regions of the EV.

$\dots, \rho_T]$ and for discharging active power to be $[\nu_1, \nu_2, \dots, \nu_T]$. The cost function f for operating the EV can then be defined as the summation over time of the costs associated with active power flow rates:

$$f = \sum_{k=1}^T f^c(p_k), \quad (3.11)$$

where

$$f^c(p_k) = \tau \left[\left(\frac{\rho_k}{\eta} + \gamma \right) p_k^+ + (\eta \nu_k - \gamma) p_k^- \right], \quad (3.12)$$

p_k^+ and p_k^- represent charging and discharging operation, respectively. $p_k^+ = p_k$ if p_k is non-negative and zero otherwise, and $p_k^- = p_k$ if p_k is negative and zero otherwise. η is the efficiency of the battery and γ is the degradation cost of the battery (expressed in \$/kWh). If the EV is charging active power, $p_k > 0$, then the owner cost is at a rate of $(\frac{\rho_k}{\eta} + \gamma)$ per unit time. If the EV is discharging active power, $p_k < 0$, then the owner income is at a rate of $(\eta \nu_k - \gamma)$ per unit time.

Based on the cost function presented above, an optimization problem can be

defined as follows:

$$\min_{p_k, x_k} f, \quad (3.13)$$

subject to

$$\text{equations in (3.1), and } x_T = x_f, \quad (3.14)$$

$$\underline{x} \leq x_k \leq \bar{x}, \quad (3.15)$$

$$\underline{p} \leq p_k \leq \bar{p}, \quad (3.16)$$

for all $k = 1, \dots, T$. Constraint (3.14) guarantees that by the end of the parking time, the battery meets the desired SOC.

To maintain long life of the EV battery, its SOC should be maintained within a certain range that is recommended by the manufacturer. The parameters \underline{x} and \bar{x} in (3.15) represent the minimum and maximum SOC of the EV battery, respectively. Constraint (3.16) represents the minimum and maximum limits for active power flow rate, \underline{p} and \bar{p} , respectively. Note that \underline{p} could be a negative value and then can be interpreted as the maximum discharging power. The battery active power limit is related to the SOC of the battery. The quantitative relationship between the maximum acceptable charging power of the EV battery and SOC of the battery can be described by SOC curve which is presented in reference [49]. We assume that for the acceptable range of SOC, the charger limit for active power is below the maximum acceptable charging power of the EV battery. Therefore, \bar{p} and \underline{p} are equal to maximum charging and discharging limit of the charger, respectively.

Our aim is to approximate the above optimization problem with a linear program. To accomplish that we first redefine parameters, mentioned above, in matrix forms as follows:

$$p = \begin{bmatrix} p_1, & p_2, & \dots, & p_T \end{bmatrix}^T, \quad x = \begin{bmatrix} x_1, & x_2, & \dots, & x_T \end{bmatrix}^T,$$

$$\rho = \left[\rho_1, \rho_2, \dots, \rho_T \right]^T, \nu = \left[\nu_1, \nu_2, \dots, \nu_T \right]^T,$$

$$e = \left[1, 0, \dots, 0 \right]_{T \times 1}^T,$$

D : $T \times T$ matrix with one on the first lower subdiagonal and zero elsewhere.

The function f^c in equation (3.12) discriminates between the cost of charging active power and the income received as a result of discharging active power. It is worth noting that at each time step k , the price of charging active power is higher than the price of discharging active power. In other words $\frac{\rho_k}{\eta} + \gamma > \eta\nu_k - \gamma$. Figure 3.3 shows the cost associated with active power flow from/to the EV in time step k . Considering the slope values, the cost function shown in Figure 3.3 is indeed convex piecewise linear. We also note from the figure that the function plotted in solid lines can also be considered as the pointwise maximum of the two linear functions $\tau(\frac{\rho_k}{\eta} + \gamma)p_k$ and $\tau(\eta\nu_k - \gamma)p_k$. We now rewrite the expression for f^c in a way so that

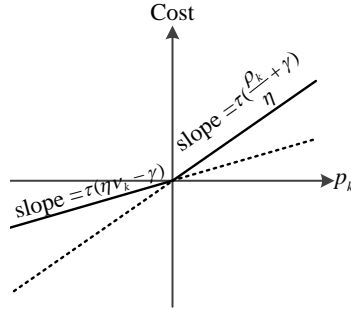


Figure 3.3: Associated cost of active power flow of an EV.

it facilitates the formulation of a linear program.

$$f^c(p_k) = \max \left\{ \tau \left(\frac{\rho_k}{\eta} + \gamma \right) p_k, \tau(\eta\nu_k - \gamma)p_k \right\}.$$

Now suppose c_k constitutes an upper bound for $f^c(p_k)$ at every k then $f^c(p_k) \leq c_k$.

This would imply

$$\tau \left(\frac{\rho_k}{\eta} + \gamma \right) p_k \leq c_k, \quad \tau(\eta\nu_k - \gamma)p_k \leq c_k,$$

for $k = 1, \dots, T$. Or equivalently

$$\tau \left(\frac{\rho}{\eta} + \gamma \right) \circ p \leq c, \quad \tau(\eta\nu - \gamma) \circ p \leq c,$$

where \circ denotes elementwise multiplication of vectors and

$$c = [c_1, c_2, \dots, c_T]^T.$$

Thus the function f in equation (3.11) is upper bounded by

$$\mathbf{1}^T c.$$

Using vector notation, we can rewrite the set of equations (3.1) in vector form as follows:

$$x = x_0 e + Dx + \frac{\tau}{u} p.$$

Furthermore, constraints (3.15)–(3.16) can be rewritten in vector notation as:

$$\underline{p}\mathbf{1} \leq p \leq \bar{p}\mathbf{1}, \quad \underline{x}\mathbf{1} \leq x \leq \bar{x}\mathbf{1}.$$

Next we replace the original optimization problem equation (3.13) with the following linear program:

$$\underset{p,x,c}{\text{minimize}} \quad \mathbf{1}^T c, \quad (3.17)$$

subject to

$$x = x_0 e + Dx + \frac{\tau}{u} p, \quad x_T = x_f, \quad (3.18)$$

$$\underline{p}\mathbf{1} \leq p \leq \bar{p}\mathbf{1}, \quad (3.19)$$

$$\underline{x}\mathbf{1} \leq x \leq \bar{x}\mathbf{1}, \quad (3.20)$$

Solving the optimization problem generates active power flow rates to or from the EV for $k = 1, 2, \dots, T$. Let us assume p_k^* for $k = 1, 2, \dots, T$ represents the optimal scheduled active power flow rate of the EV during the time interval k .

3.5 Aggregator Modeling and Optimization

As mentioned earlier, EV penetration level into the existing EPS can be increased significantly through intelligent coordination of their charging/discharging schedules. The EPS operation including EVs, can be studied from three point of views: SO; Aggregator; and EV owner. All mentioned participants needs to constantly exchange information through communication protocols [51]. Figure 3.4 shows different control and operation levels of the EPS for charging/discharging of EVs, as well as other possible ancillary services.

The responsibilities and objectives of each level can be listed as follows, according to the above control and operation levels:

- Upper level
 - SO is responsible for operating the EPS in safe, efficient, and reliable

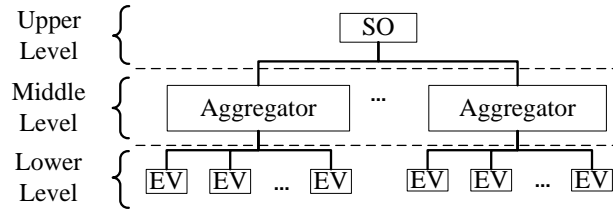


Figure 3.4: Control and operation levels of the EPS including EVs.

manner.

- SO announces the price of the electricity, as well as prices of ancillary services.
 - SO must determine the need for ancillary services and supply it from available sources.
- Middle level
 - Aggregator is responsible for charging EVs under its control. The/she must provide desired SOC for each individual EV by the end of its parking time.
 - Aggregator can participate in the ancillary service market as an ancillary service provider for the SO.
- Lower level
 - EV owners at this level are interested in charging their EVs by the end of their parking time.
 - If there is a need for permission to use EVs for participation in the ancillary market, then EV owners can decide on granting the permission to the aggregator.

After announcing the price of electricity, the aggregator must calculate the optimal schedule of charging/discharging of a group of EVs under his/her control. The optimal schedules must be calculated to minimize the aggregator's cost. We superscript $j = 1, \dots, J$ representing the ID of each EV under the aggregator's control. We also define a binary variable, α_k^j , for the EV ^{j} during time interval k , to indicate the connectivity of the EV to the grid. α_k^j is 1 if the EV is connected to the grid and 0 otherwise. The formulations developed in Section 3.4 are extended for all EVs to develop the aggregator's optimization problem. Considering an EV ^{j} , the following definitions will be used for the rest of the dissertation:

$$\begin{aligned}
p^j &= [p_1^j, p_2^j, \dots, p_T^j], \quad p = [p^1, p^2, \dots, p^J]^T, \\
x^j &= [x_1^j, x_2^j, \dots, x_T^j], \quad x = [x^1, x^2, \dots, x^J]^T, \\
\alpha^j &= [\alpha_1^j, \alpha_2^j, \dots, \alpha_T^j], \quad \alpha = [\alpha^1, \alpha^2, \dots, \alpha^J]^T, \\
c^j &= [c_1^j, c_2^j, \dots, c_T^j], \quad C = [c^1, c^2, \dots, c^J]^T, \\
\Gamma &= \left[\frac{[\rho]^T}{\eta^1} + \gamma^1, \frac{[\rho]^T}{\eta^2} + \gamma^1, \dots, \frac{[\rho]^T}{\eta^J} + \gamma^J \right]^T, \\
\Pi &= \left[[\nu]^T \eta^1 - \gamma^1, [\nu]^T \eta^2 - \gamma^2, \dots, [\nu]^T \eta^J - \gamma^J \right]^T, \\
\bar{p} &= \left[\bar{p}^1 \mathbf{1}_{1 \times T}, \bar{p}^2 \mathbf{1}_{1 \times T}, \dots, \bar{p}^J \mathbf{1}_{1 \times T} \right]^T, \\
\bar{x} &= \left[\bar{x}^1 \mathbf{1}_{1 \times T}, \bar{x}^2 \mathbf{1}_{1 \times T}, \dots, \bar{x}^J \mathbf{1}_{1 \times T} \right]^T, \\
\underline{x} &= \left[\underline{x}^1 \mathbf{1}_{1 \times T}, \underline{x}^2 \mathbf{1}_{1 \times T}, \dots, \underline{x}^J \mathbf{1}_{1 \times T} \right]^T,
\end{aligned}$$

$$\psi = \left[\frac{1}{\psi^1} \mathbf{1}_{1 \times T}, \frac{1}{\psi^2} \mathbf{1}_{1 \times T}, \dots, \frac{1}{\psi^J} \mathbf{1}_{1 \times T} \right]^T,$$

Assuming the initial SOC to be x_0^j , the desired SOC to be x_f^j , and the capacity of the battery to be ψ^j , we calculate the SOC of EV_{*j*} in each time interval as follows:

$$x_k^j = \alpha_{k-1}^j x_{k-1}^j + \alpha_k^j \frac{\tau}{\psi^j} p_k^j, \quad (3.21)$$

and

$$\begin{cases} x_k^j = x_0^j, & \text{for } k = \text{arrival time step} \\ x_k^j = x_f^j, & \text{for } k = \text{departure time step.} \end{cases} \quad (3.22)$$

The cost of charging/discharging of EV^{*j*} in time interval *k* can be expressed as:

$$f_c^j(p_k^j) = \max \left\{ \tau \left(\frac{\rho_k}{\eta^j} + \gamma^j \right) p_k^j, \tau (\eta^j \nu_k - \gamma^j) p_k^j \right\}.$$

Now suppose c_k^j constitutes an upper bound for $f_c^j(p_k^j)$ at every *k* then $f_c^j(p_k^j) \leq c_k^j$.

This would imply

$$\tau \left(\frac{\rho_k}{\eta^j} + \gamma^j \right) p_k^j \leq c_k^j, \quad \tau (\eta^j \nu_k - \gamma^j) p_k^j \leq c_k^j,$$

for all $k = 1, \dots, T$ and $j = 1, \dots, J$. Or equivalently

$$\tau \Gamma \circ p \leq C, \quad \tau \Pi \circ p \leq C.$$

Thus the cost function is upper bounded by $\mathbf{1}^T C$, which is linear with the optimization variables *C*.

We now rewrite the equation (3.21) for all EVs in matrix form as described below:

$$x = (I_J \otimes D)(\alpha \circ x) + \tau \alpha \circ \psi \circ p, \quad (3.23)$$

where I_J is the $J \times J$ identity matrix and \otimes denotes elementwise multiplication of vectors and Kronecker product.

Now we can extend cost function (3.17) for EVs under contract with the aggregator and the sum of those will be the aggregator's cost function. This function can then be defined as:

$$\underset{p,x,C}{\text{minimize}} \quad \mathbf{1}^T C, \quad (3.24)$$

subject to

$$-\alpha \circ \bar{p} \leq p \leq \alpha \circ \bar{p}, \quad (3.25)$$

$$\alpha \circ \underline{x} \leq x \leq \alpha \circ \bar{x}, \quad (3.26)$$

plus constraint 3.23 and constraint 3.22 for $j = 1, 2, \dots, J$.

3.6 Numerical Results

We have evaluated the performance of the proposed models using real electricity prices and real battery data. Specifically, the hourly electricity prices in the Central New York were obtained from the NYISO [52]. For the price of electricity, we have used a work day (February 12, 2015) price published by NYISO for Central zone. Since the market period for some markets in the NYISO territory is 10 minutes, the value of τ is 0.167 hour. In the absence of any market for discharging power by EVs, we have assumed the price of discharged power to the grid is equal to the price of the electricity.

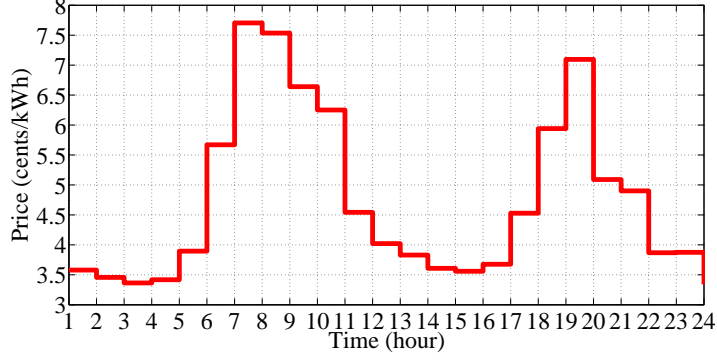


Figure 3.5: NYISO daily price of charging/discharging electrical power.

We have used the constant values of Lithium-Ion battery cell degradation, β_1 to β_7 provided in reference [47] and also presented in Table 3.1.

Table 3.1: Lithium-Ion battery cell degradation specifications.

β_1	1.14846×10^{-7}
β_2	3.9984×10^{-8}
β_3	1.3158×10^{-7}
β_4	5.5487×10^{-10}
β_5	4.9680×10^{-8}
β_6	1.1166×10^{-8}
β_7	6.5166×10^{-9}

For simulation purpose, we consider four types of EVs available in the market: Chevrolet Volt; Nissan LEAF; Mitsubishi i-MiEV; and Tesla. The battery specifications of all mentioned EVs can be obtained from the manufacturer data sheet. Energy unit price (\$/kWh) for Lithium-Ion battery was assumed to be 1500 \$/kWh based on information in reference [50]. Table 5.9 shows the battery characteristics and their chargers limit. Note that we have assumed $\underline{p} = -\bar{p}$ in our calculation.

To demonstrate the efficiency of our model, we perform the simulation first for

Table 3.2: EVs battery and charger specifications.

EV	Battery Capacity (kWh)	No. of Cells	Cell Nominal Voltage (V)	\bar{s} (kVA)	\bar{p} (kW)	γ (¢/kWh)
Chevrolet Volt	16.5	288	3.7	3.3	3.3	45.25
Nissan LEAF	24	192	3.75	6.6	6.6	45.86
Mitsubishi i-MiEV	16	88	3.7	3.3	3.3	46.94
Tesla	60	6831	3.7	11	11	44.03

single EV. We then extend our simulation to a group of 1000 EVs.

3.6.1 Single EV

In this part of the simulation, we have considered single Mitsubishi's i MiEV. The minimum and maximum SOC of the EV are assumed to be 20% and 90% respectively. We also assume that the EV is connected from 9 a.m. to 7 p.m. with initial SOC of 40% and desired SOC of 80%. We have assumed 40% for initial SOC just to indicate that EVs can be connected with initial SOC other than minimum value.

In order to show the effect of battery degradation cost on charging/discharging scheduling, we first ignore the degradation cost factor. Figure 3.6 demonstrates the optimal scheduling result, without considering the battery degradation effect. As can be seen from the figure, the EV is charging during off-peak periods, with lower prices, and discharging during on-peak periods, period with higher prices. The charging/discharging cost of the EV is \$25.9471.

Figure 3.7 shows the result of optimal charging/discharging schedule, including the battery degradation effect. As can be seen from the figure, no discharging was

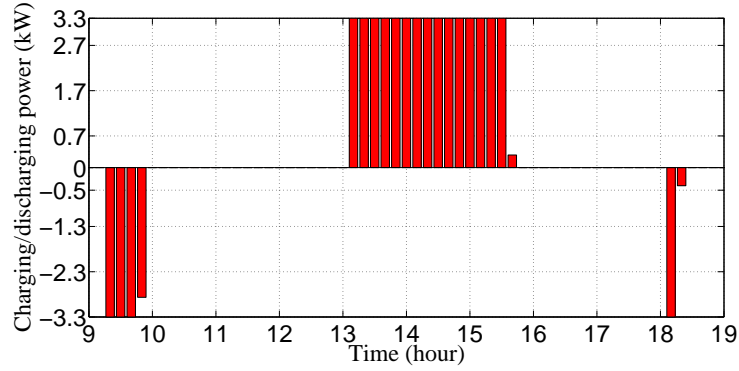


Figure 3.6: Charging/discharging schedule of a single EV ignoring the battery degradation effect.

scheduled. The reason is high degradation cost of the battery comparing to the price of discharging power. The charging/discharging cost of the EV is \$370.1007.

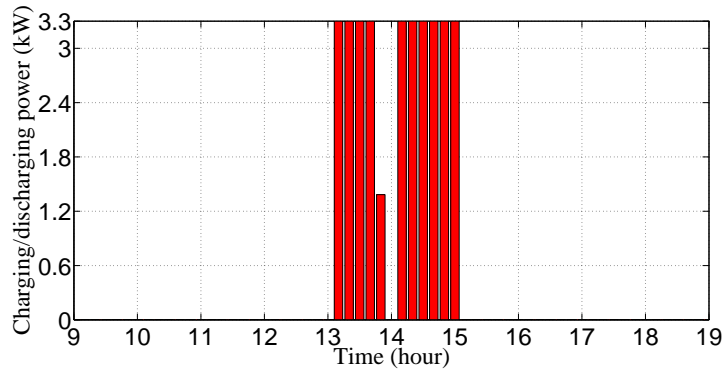


Figure 3.7: Charging/discharging schedule of a single EV including the battery degradation effect.

The charging/discharging cost including the battery degradation effect has been increased by \$344.1536 (1326.37%) comparing to the charging/discharging cost of the EV ignoring the battery degradation effect. This finding implies the necessity of taking battery degradation effect into consideration.

3.6.2 EV Usage Pattern Generation

In order to develop our simulations for a group of 1000 EVs, we need to generate realistic usage patterns of EVs. The initial SOC of each EV depends on the traveled distance by each EV. In this part, we consider the stochastic behaviour of EV usage presented in Section 2.7. Table 3.3 presents the information for EV usage pattern.

Table 3.3: Normal Distribution Function Settings for EVs Usage Patterns.

Mean of arrival time	9 a.m.
Mean of departure time	4 p.m.
Std. deviation of arrival time	2 hours
Std. deviation of departure time	2 hours
Mean of traveled distance	22.3 miles
Std. deviation of traveled distance	12.2 miles

Figure 3.8 shows the number of connected EVs, based on the generated patterns for all EVs under study ,in our simulation.

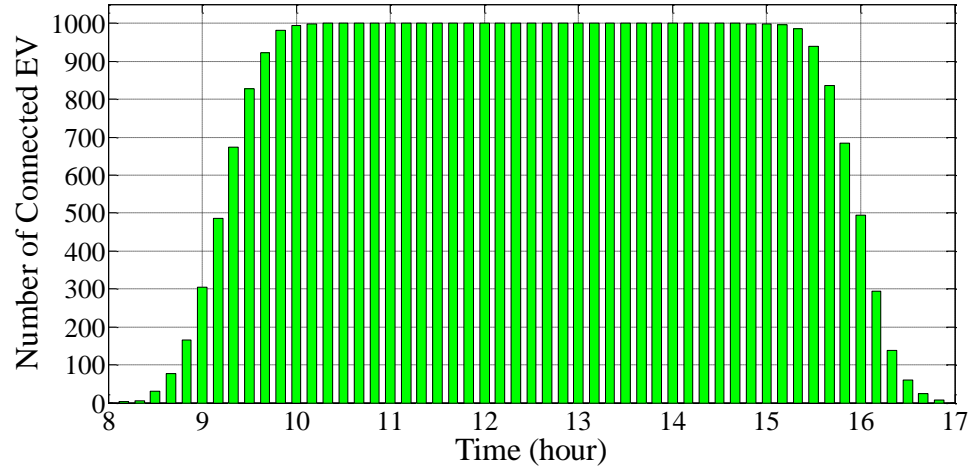


Figure 3.8: Number of connected EVs.

3.6.3 A Group of EVs

Figure 3.9 shows the share of different EV types used for simulations. Also Table 5.9 summarizes the specification of each EV type. Based on usage pattern of EVs

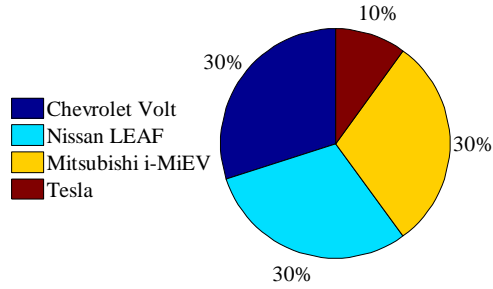


Figure 3.9: Percentage of different EVs in simulations.

and their connectivities according to Figure 3.8, the optimal charging/discharging schedule of the aggregator can be calculated as shown in Figure 3.10. Note that the battery degradation factor has been included in the calculation and that is the reason for the aggregator to not schedule any discharging activities. The aggregator cost due to charging activities for all connected EVs is \$453,695.78.

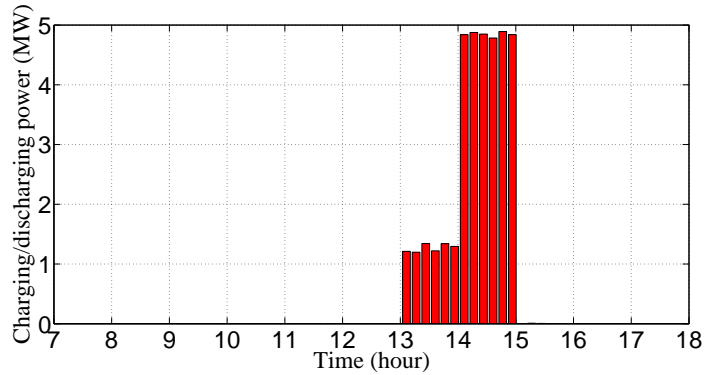


Figure 3.10: Aggregated charging/discharging schedule of a group of 1000 EVs.

3.7 Conclusion

In this chapter, we presented a linear model of the EV which includes charging and/or discharging modes of operation and the battery degradation factor. We defined a cost function for EV operation and then minimized the operating cost of the EV using linear programming. We then developed the the formulations to define the aggregator's operating cost. The optimal charging/discharging schedules of a group of 1000 EVs under the aggregator's control was calculated using linear programming, to minimize the aggregator's operating cost. Simulation results showed the scalability of developed framework. We also observed that the battery degradation effect on the operating cost is significant. Due to high battery degradation cost, the aggregator did not schedule any discharging activities. The developed model of EV operation in this chapter will serve as a foundation for modeling EVs services for grid operation in the following chapters.

Chapter 4

Reactive Power Service from EVs

4.1 Introduction

Reactive power is an important ancillary service needed by the SO to manage effects of inductive loads in power systems. Due to localized nature of reactive power, the relevant geographic market may be much smaller than a market for active power. Currently, generators are main sources of reactive power. However, the market with distributed RPSPs might be less concentrated than if only generation sources of reactive power were considered. Therefore, Federal Energy Regulatory Commission (FERC) suggested the use of competitive solicitations, in Order No. 784, to acquire ancillary services such as reactive power support and voltage regulation. Such competitive processes could elicit responses from a variety of resources, including generation, transmission, DR, and energy storage [53].

EV battery chargers are often composed of a voltage converter circuit. Such circuits can adjust injected/absorbed reactive power to/from the grid by controlling the magnitude and phase angle of the voltage generated by the AC-DC converter of the charger. Moreover reactive power service (injection/absorption) does not degrade

the battery [54]- [55]. Since EVs are scattered across the system (mostly near load centers) and parked for about 22 hours a day on an average [56], they have the potential to become distributed RPSPs when equipped with intelligent chargers.

In addition to fulfilling the technical requirements of EV as an RPSP [57]- [58], finding conditions for their optimal operation has been a challenge. In reference [59] the optimal combined frequency and voltage regulation, using a day-ahead command-based (contract-based) model and a day-ahead price-based model, was achieved by controlling both the active and reactive power flow rates of EVs. In the model proposed in reference [60], EV owners have to submit information regarding their preferred charging station, required charging energy, preferred parking interval, and arrival/departure times to the scheduling coordinator a day ahead. The coordinator schedules the charging activities and reactive power injection to the grid for each EV parked in the station, based on a multi-objective resource allocation problem. Clearly, this type of day-ahead information submission can be challenging for EV owners. Also, if SO requires more reactive power than anticipated, the coordinator will not be able to accommodate the additional service. In reference [61] a method used to generate the expected payment function of EVs, especially to include the lost opportunity costs, which was designed originally for DGs (e.g. reference [62]) rather than for EVs. It seems that this approach may not be appropriate since, as opposed to DGs, EVs demand active power as a load.

In this chapter we present a model of an EV as a load for active power in charging mode, as a generator for active power in discharging mode, and as an RPSP (injection/absorption). We first study the characteristics of EV for providing reactive power service. The developed model of EV in Chapter 3 is analyzed under various constraints such as limits on the current ripple in the DC-link capacitor of the EV charger. Next, we linearize the nonlinear constraints. We then develop a mathemati-

cal model to evaluate the cost of providing reactive power service by the EV. Finally, we introduce a novel algorithm to extract the reactive power supply function of the EV, as a step-wise accenting order function, with optimized cost for providing reactive power service. Solution guarantees that the flow of reactive power is consistent with all constraints on the EV.

The main contributions of this chapter are as follows:

1. Modeling EV as an RPSP and defining an objective function to calculate the operating cost of the EV under several constraints.
2. Approximation of the optimization problem with a linear program to improve the efficiency and scalability of the approach.
3. Inclusion of current ripple limitation of the DC-link capacitor as a constraint on optimal EV operation.
4. Evaluation of the cost and capability of reactive power service by an EV taking into consideration its load nature.
5. Development of reactive power supply function of the EV as a step-wise ascending order function.

4.2 Reactive Power Market: A Review

Provision of reactive power and payments to service providers are mainly based on bilateral agreements and contracts between transmission SOs and large generators. In this section, we review the current practices of providing reactive power in United States.

NYISO has contracts with eligible generators to provide reactive power service. The contracts provide a fixed payment plus a recovery payment for the lost opportunity costs. The reactive power charge is computed by dividing the anticipated annual cost of providing reactive power service, plus-or-minus any under/over collections from the previous year [63]. Projected 2013 NYISO reactive power service payments to generators is \$60.9M [64].

Generators managed by the California Independent SO are mandated to operate within a power factor band of 0.90 lag (consuming VAR) to 0.95 lead (producing VAR) [65]. Based on annual bilateral contracts, the generators are paid for providing the reactive power service to maintain the mandatory power factor range. The payment is based on the generator's capacity and operation.

The Independent SO of New England recovers the capacity cost (the fixed capital costs incurred by the installation and maintenance of the capability to provide reactive power support), the lost opportunity costs (the value of a generator's foregone opportunity to supply active power when providing reactive power support), the cost of energy consumed, and the cost of energy produced (the costs incurred by a generator dispatched out of economic merit to create reactive power capability) of qualified generators [66]. Independent SO of New England charges its customer on a monthly basis. The amount to be paid is determined by summing the hourly capacity cost component with the hour-specific lost opportunity costs, cost of energy consumed, and cost of energy produced by all generators providing reactive power supply.

Pennsylvania New Jersey Maryland Interconnection LLC treats reactive power supply and voltage control as a non-market, cost-of-service product. All generators and non-generation sources capable of providing reactive power are obligated to do so in accordance with the interconnection agreement. RPSPs receive a cost of service payment equal to their monthly revenue requirement for providing reactive power [67].

In territory managed by the Energy Regulatory Commission of Texas, all generation resources that have a gross generating unit rating greater than 20 MVA must provide reactive power service [68]. These service providers are dispatched to provide voltage support via an out-of-merit capacity deployment [69].

As discussed above, in most cases, SO contracts with RPSPs. In the absence of market mechanism for reactive power service, we think that reactive power ancillary services, in deregulated electricity markets, can be provided based on a two-stage approach, namely, reactive power procurement and reactive power dispatch, as proposed in reference [70]. Reactive power procurement is essentially a long-term issue, where SO signs seasonal contracts with possible service providers that would best suit its needs and constraints in the given season [71]. Reactive power dispatch, on the other hand, corresponds to the short-term allocation of reactive power, to meet the system need, from the contracted suppliers based on “real-time” operating conditions [72]. This chapter concentrates on defining a reactive power supply function of EVs that would allow us to engage them in reactive power dispatch activity using the framework explained in reference [73].

Figure 4.1 illustrates the schematic of the proposed procedure for short-term dispatch of reactive power that includes EVs as RPSP. The calculation of reactive power price components for procurement process has been explained in reference [70] and is out of the scope of this dissertation. SO determines the available sources for reactive power dispatch from the list of procured/contracted generators, the generating units available from the short-term energy market clearing, and the reactive power supply functions of the available EVs. The units are then dispatched using the OPF model, presented in reference [73], that minimizes total payments associated with reactive power dispatch, subject to appropriate system security constraints. It is worth emphasizing that the focus of this chapter is only calculating the reactive power supply

function of EVs, on a real-time basis, which can be incorporated into the OPF model mentioned above. Payments will be calculated after real-time operation, based on the actual usage and the dispatch requested by SO.

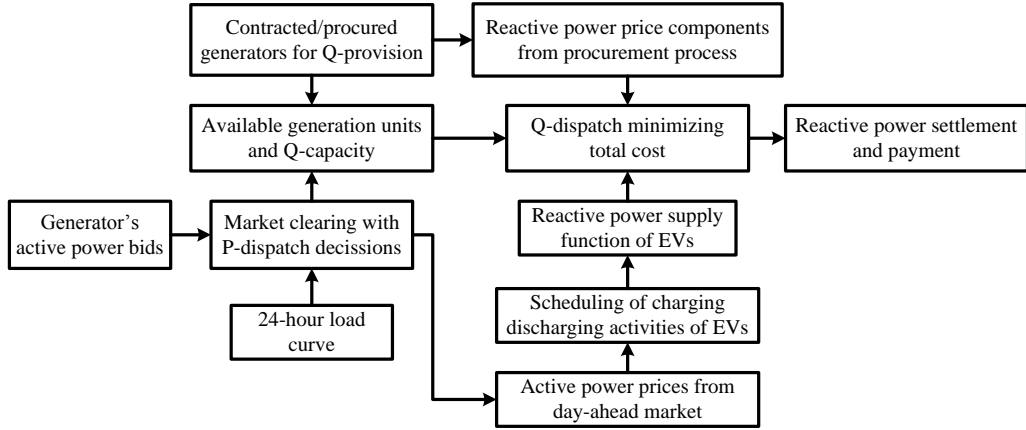


Figure 4.1: Short-term dispatch of reactive power services.

Figure 4.2 shows the information exchange between different entities in the short-term reactive power dispatch. As can be seen from the figure, an aggregator, representing aggregated EVs, is responsible for satisfying charging requirements of EVs and also submitting the reactive power supply function to SO.

Solving the optimization problem defined in Chapter 3, generates active power flow rates to/from the EV for $k = 1, 2, \dots, T$. Let us assume p_k^* for $k = 1, 2, \dots, T$ represents the optimal scheduled active power flow rate of the EV during the time interval k . Next, we discuss the EV's reactive power capability, during an optimized scheduled charging/discharging point.

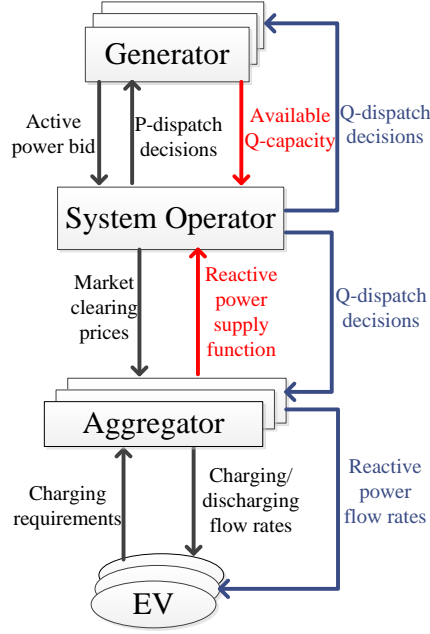


Figure 4.2: The information exchange between different entities in the short-term dispatch of reactive power services.

4.3 EV’s Characteristics for Reactive Power Service

Considering EV just as a pure demand of active power could not lead us to an efficient and cost-effective operation of power system. Based on the technological characteristics and location of EVs, we can include EVs in several potential activities rather than just charging active power. Table 4.1 summarizes these activities [54], [74]- [77]. From the table it can be seen that the services related to reactive power (reactive power regulation and motor starting) do not engage the battery. In fact, the DC-link capacitor C_{dc} in the charger of EV, enables it to provide reactive power support.

Figure 4.3 depicts a typical charger circuit of an EV. In this figure p_k and q_k rep-

Table 4.1: Potential Markets for V2G Services Offered by EV

Potential Markets of V2G	Duration of Service	Battery Degradation
Coordinated Charging	-	No
Peak Shaving	15 min - 2 h	Yes
Spinning Reserve	15 - 20 min	Yes
Active Regulation	1-5 min	Yes
Reactive Regulation	Seconds to 5 min	No
Renewable Transients	Seconds to 30 min	Yes
Motor Starting	Seconds	No

represent the active and reactive power flow rate of the charger at time interval k , L_c is the coupling inductor, v_i and i_i are the voltage and current of the grid side and V_o and I_o are the voltage and current of the battery side. Independently of the power converter topology, the battery chargers can be categorized as on-board or off-board [57]. The on-board charger placed inside the vehicle (for slow charging) and the off-board charger is placed outside of the vehicle (for fast charging). Based on the requested signal from SO for reactive power support, digital control system injects/absorbs the desired reactive power into/from the grid, by controlling the magnitude and the phase angle generated by the AC-DC converter part of the EV charger [58].

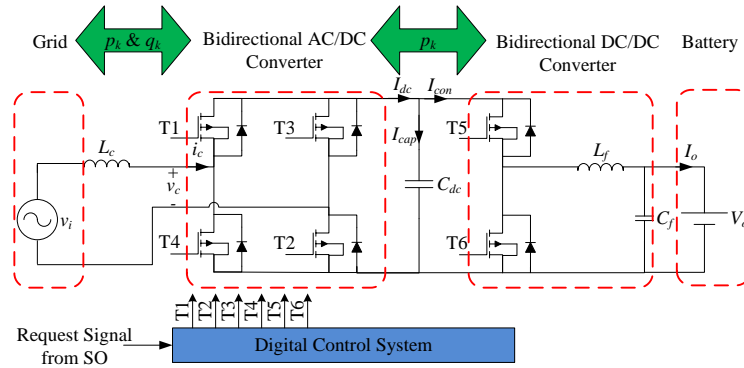


Figure 4.3: A typical circuit of EV charger.

Based on the directions of p_k and q_k , four operating regions for the EV can be defined as summarized in table 4.2 shown below.

Table 4.2: Operating Regions of EV Charger

Operating Region	Operating Range	Active Power	Reactive Power
Region I	$p_k \geq 0$ and $q_k \geq 0$	Charging	Absorption
Region II	$p_k \leq 0$ and $q_k \geq 0$	Discharging	Absorption
Region III	$p_k \leq 0$ and $q_k \leq 0$	Discharging	Injection
Region IV	$p_k \geq 0$ and $q_k \leq 0$	Charging	Injection

To evaluate the ability of the EV in providing reactive power service, we need to extract the capability curve of the EV. This capability curve can be calculated considering the limitations of the EV charger for providing reactive power service. In the following subsections, these limitations are presented.

4.3.1 Inverter Maximum Power

Maximum apparent power exchanged between the EV charger and the grid is limited by the maximum output power of the inverter. This limitation is defined as follow:

$$p_k^2 + q_k^2 \leq \bar{s}^2, \quad (4.1)$$

where \bar{s} is the maximum power of inverter.

4.3.2 Power Ripple in Charger

Due to single-phase conversion of AC power into DC power, we experience oscillating power between grid and charger [90]. It is worth to mention that the average power

is used for charging or discharging the battery.

Assuming that during time interval k , sinusoidal voltage at grid side (v_i in Figure 4.3) and default active power flow from the grid to the charger which causes charger voltage, v_c in equation (4.3), laggres grid voltage by δ , we have [90]:

$$v_i(t) = \sqrt{2}V_i \sin(\omega t), \quad (4.2)$$

$$v_c(t) = \sqrt{2}V_c \sin(\omega t - \delta), \quad (4.3)$$

where V_i and V_c are the rms values of grid voltage and charger voltage , respectively (V), ω is the angular frequency (rad/s), and δ is the lagging angel. Charger current, i_c in Figure 4.3, can be calculated using phasor analysis as follows:

$$i_c(t) = \sqrt{2}I_c \sin(\omega t - \theta), \quad (4.4)$$

where

$$I_c = \frac{\sqrt{(V_i - V_c \cos(\delta))^2 + (V_c \sin(\delta))^2}}{\omega L_c}, \quad (4.5)$$

$$\theta = \tan^{-1}\left(\frac{V_i - V_c \cos(\delta)}{V_c \sin(\delta)}\right). \quad (4.6)$$

Instantaneous power drawn from the grid, $p_i(t)$, can be calculated as below:

$$p_i(t) = v_i(t)i_c(t), \quad (4.7)$$

which must be equal to the summation of instantaneous power of the coupling inductor, $p_L(t)$, and instantaneous power that the charger receives, $p_c(t)$. After some

modification, we can calculate the instantaneous power of charger as follows:

$$p_c(t) = p_i(t) - p_L(t) = P_{avg} - p_{ripple}(t), \quad (4.8)$$

where

$$P_{avg} = V_i I_c \cos(\theta), \quad (4.9)$$

$$p_{ripple}(t) = -V_i I_c \cos(2\omega t - \theta) - \omega L_c I_c^2 \sin(2\omega t - 2\theta). \quad (4.10)$$

From equation (4.8), can be seen that the instantaneous power of charger has two terms, average power P_{avg} and ripple power $p_{ripple}(t)$. Defining $s = V_i I_c$, $q = V_i I_c \sin(\theta)$, $p = V_i I_c \cos(\theta)$, and some modification and phasor analysis, we can restate equation (4.10) as:

$$p_{ripple}(t) = P_{ripple} \cos(2\omega t + \beta), \quad (4.11)$$

where

$$P_{ripple} = \sqrt{s^2 + \left(\frac{\omega L_c}{V_i^2} s^2\right)^2 - 2\frac{\omega L_c}{V_i^2} s^2 q}, \quad (4.12)$$

and

$$\beta = \tan^{-1}\left(\frac{V_i I_c \sin(\theta) + \omega L_c I_c^2 \cos(2\theta)}{-V_i I_c \cos(\theta) + \omega L_c I_c^2 \sin(2\theta)}\right). \quad (4.13)$$

The oscillating component of the instantaneous power of charger $p_{ripple}(t)$ is stored in the DC-link capacitor of the charger and is used to to balance the power transfer between the grid and the charger [90]. It is worth to note that the stored energy in the DC-link capacitor can be calculated by integrating the ripple power between its minimum and maximum values. For a predefined average DC-link voltage V_{dc} and a DC-link peak-to-peak voltage ripple ΔV_{dc} the required capacitance can be calculated

as [90]:

$$C_{dc} = \frac{\sqrt{s^2 + \left(\frac{\omega L_c}{V_i^2} s^2\right)^2 - 2\frac{\omega L_c}{V_i^2} s^2 q}}{\omega V_{dc} \Delta V_{dc}}. \quad (4.14)$$

Neglecting the pulse width modulation (PWM) ripple components, instantaneous DC-link voltage can be expressed as [90]:

$$v_{dc}(t) = V_{dc} + \frac{\Delta V_{dc}}{2} \sin(2\omega t). \quad (4.15)$$

The current of DC-link capacitor can be calculated as:

$$i_{cap}(t) = C_{dc} \frac{dv_{dc}(t)}{dt} = \sqrt{2} I_{cap} \cos(2\omega t), \quad (4.16)$$

where I_{cap} is the rms value of the second harmonic current and defined as:

$$I_{cap} = \frac{1}{\sqrt{2}} \omega C_{dc} \Delta V_{dc}. \quad (4.17)$$

By calculating ΔV_{dc} from equation (4.14) and plugging it in equation (4.17), we can express the rms value of the second harmonic current as:

$$I_{cap} = \frac{\sqrt{s_k^2 + \left(\frac{\omega L_c}{V_i^2} s_k^2\right)^2 - 2\frac{\omega L_c}{V_i^2} s_k^2 q_k}}{\sqrt{2} V_{dc}}. \quad (4.18)$$

From equation (4.18), can be seen that for the same apparent power s_i , the rms of the second harmonic current has higher value for operating point in regions III and IV ($q < 0$) rather than for operating point in regions II and I ($q \geq 0$). Since the value of the term $\frac{\omega L_c}{V_i^2}$ is small (considering values for V_i and coupling inductor L_c in mH

range), we can use the following approximation for equation (4.18).

$$I_{cap} \approx \frac{\sqrt{s_k^2 - 2\frac{\omega L_c}{V_i^2} S_k^2 q_k}}{\sqrt{2}V_{dc}}, \quad (4.19)$$

and also by using Taylor series we have:

$$I_{cap} \approx \frac{s_k(1 - \frac{\omega L_c}{V_i^2} q_k)}{\sqrt{2}V_{dc}}. \quad (4.20)$$

For charging operation of charger ($p_k > 0$ and $q_k = 0$), the maximum rms value of the second harmonic current can be calculated as:

$$I_{cap}^{max} = \frac{\bar{s}}{\sqrt{2}V_{dc}}. \quad (4.21)$$

Based on equations (4.20) and (4.21), we can express the operation limit of the EV charger as:

$$s_k(1 - \frac{\omega L_c}{V_i^2} q_k) \leq \bar{s}. \quad (4.22)$$

One can infer that the union of constraints (4.1) and (4.22) for $q \geq 0$ is equal to the constraint (4.1). Similarly the union of constraints (4.1) and (4.22) for $q < 0$ is equal to the constraint (4.22). Recalling that $s_k = \sqrt{p_k^2 + q_k^2}$, we can formulate the operating limit of charger as:

$$\begin{cases} p_k^2 + q_k^2 \leq \bar{s}^2, & \forall q_k \geq 0; \\ (p_k^2 + q_k^2)(1 - \frac{\omega L_c}{V_i^2} q_k)^2 \leq \bar{s}^2, & \forall q_k < 0. \end{cases} \quad (4.23)$$

We define \bar{q} to represent the maximum value of reactive power injection by the

charge. \bar{q} can be calculated (by plugging $p_k = 0$ in equation (4.22)) as:

$$\bar{q} = \frac{\sqrt{1 + 4 \frac{\omega L_c}{V_i^2} \bar{s}} - 1}{2 \frac{\omega L_c}{V_i^2}}. \quad (4.24)$$

Figure 4.4 depicts the operating limit of the charger. As can be seen from the Figure 4.4, the operating limit is not symmetrical.

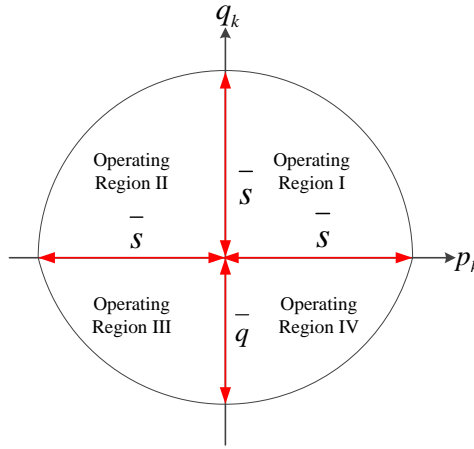


Figure 4.4: Operating limit of EV charger.

4.4 Reactive Power Capability of EV

The reactive power capability of an EV depends on the charger limits and the active power flow rate of the charger. Figure 4.5 demonstrates the EV's reactive power capability considering the optimal active power flow rate to be p_k^* . Assume q_k^* as the maximum reactive power flow rate corresponding to p_k^* (shown by blue dashed lines in the figure). The red solid line in the figure represents the maximum reactive power injection limit of the charger calculated using equation (4.24).

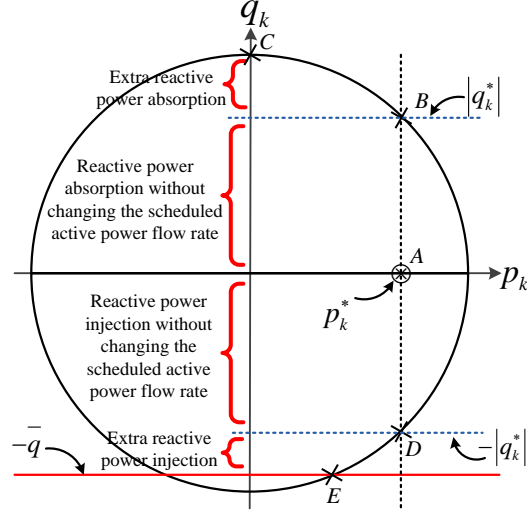


Figure 4.5: Reactive power capability of the EV: nonlinear approach.

Figure 4.5 shows four ranges of reactive power, q_k . Operating points on the dashed line AB provide a range of reactive power absorption without changing the scheduled active power flow rate of the charger. On the other hand, more reactive power absorption would result in moving the operating point of the charger on the circular section BC and causing change in scheduled active power flow rate. Similarly all operating points on the dashed line AD provide a range of reactive power injection without changing the scheduled active power flow rate. More reactive power injection will force the operating point of the charger to move on the circular section DE and reduce active power flow rate. Note that the maximum limit of reactive power absorption/injection is asymmetric. In Figure 4.5 one also can observe that the lower the active power flow rate p_k^* (charging/discharging), the bigger the range of reactive power q_k^* (injection/absorption) without changing the active power flow rate.

As explained above, in some ranges, provision of reactive power service results changes in scheduled active power flow rate. The change in scheduled active power flow rate, as solution of pre-defined optimization problem in Chapter 3, is termed as

perturbation of the optimal solution. This perturbation from optimal solution may increase the operating cost of the EV. In the following section, perturbations caused by reactive power service and associated costs are studied.

4.4.1 Nonlinear Approach

After calculating the optimal active power flow rates, p_k^* for $k = 1, 2, \dots, T$, the corresponding reactive power flow rates q_k^* to meet maximum apparent power of charger is calculated for $k = 1, 2, \dots, T$. As shown in Figure 4.5, during a time period k , any reactive power service from 0 to $|q_k^*|$ for absorption and from zero to $-|q_k^*|$ for injection, does not perturb the optimal scheduled active power flow rate. However, any increase in reactive power service above q_k^* by Δq_k , yields in perturbation of active power flow rate by Δp_k .

Since the optimal solution minimizes the cost function, any perturbation can increase the EV's operating cost. In the remainder of the chapter, the increment in total cost caused by the perturbation, will be called the imposed cost.

Any increase in reactive power service by Δq_k , moves the operating point, for example, from position ① to position ② as shown in Figure 4.6. The change in the operating cost of the EV can be explained as follows:

- If $p_k^* \geq 0$ then lower costs due to less active power consumption.
- If $p_k^* < 0$ then lower income for discharging less active power.

In order to meet the EV owner's desired SOC at the departure time, any change in active power flow rate at current time period k must be reschedulable during the remainder of its parking time, termed as *receding horizon* in our calculation. Therefore Δp_k , and corresponding Δq_k , is limited by maximum reschedulable active power flow rate in the receding horizon.

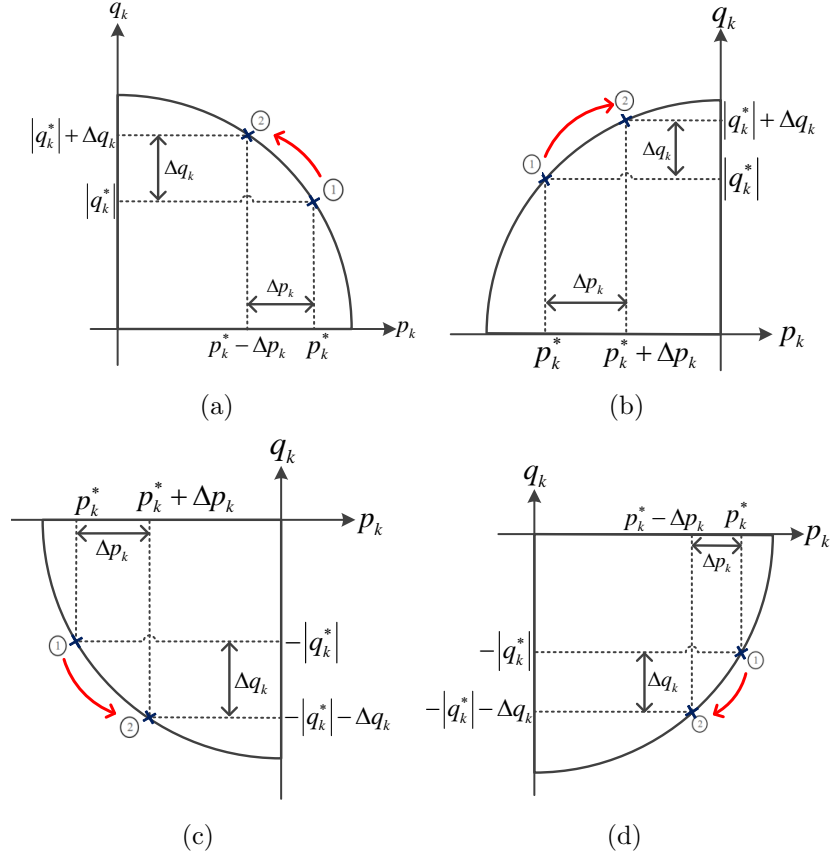


Figure 4.6: Perturbation in operating point due to a change in reactive power service for: (a) Region I; (b) Region II; (c) Region III; and (d) Region IV.

4.4.2 Linear Approach

The first step in the analysis is to approximate constraint (4.23) in such a way that the problem can be formulated as a set of linear equations. Since constraint (4.23) describes a convex set [91], we can use linear cuts to obtain a polyhedron, as depicted in Figure 4.7.

Since constraint (4.23) is asymmetric, we first divide the circular part into N arcs of angle θ , such that $N\theta = \pi$, to generate the linear cuts. The position of points on the upper semicircle can be calculated as $p_k^i = \bar{s} \cos(i\theta)$ and $q_k^i = \bar{s} \sin(i\theta)$ for $i = 1, \dots, N$. Images of these points represent the position of the points when q_k is

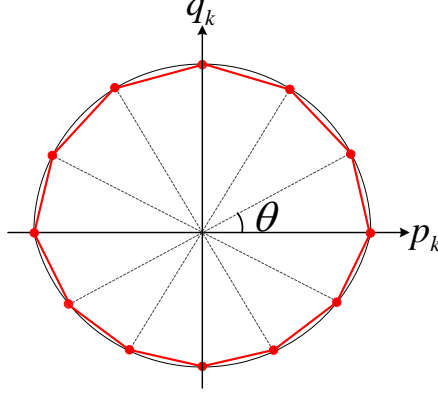


Figure 4.7: Linear cuts for constraint (4.23).

negative. Position of the points when q_k is negative can also be calculated using the equation below:

$$\begin{cases} p_k^{i+N} = \frac{1 - \sqrt{1 + 4 \frac{\omega L_c}{V_g^2} \bar{s} \sin(i\theta)}}{2 \frac{\omega L_c}{V_g^2}} \cot(i\theta), \\ q_k^{i+N} = \frac{1 - \sqrt{1 + 4 \frac{\omega L_c}{V_g^2} \bar{s} \sin(i\theta)}}{2 \frac{\omega L_c}{V_g^2}}, \end{cases} \quad (4.25)$$

for $i = 1, \dots, N$.

We have used $a_i q_k + b_i p_k + r_i = 0$ to represent the i^{th} side of the polyhedron corresponding to time interval k . The perpendicular distance from the origin to this line is given by

$$d_i = \frac{|r_i|}{\sqrt{a_i^2 + b_i^2}}$$

as shown in Figure 4.8. Therefore, any point (p_k, q_k) that falls below solid line in Figure 4.8 satisfies the following constraint.

$$\begin{bmatrix} \cos(i\theta) & \sin(i\theta) \end{bmatrix} \begin{bmatrix} p_k \\ q_k \end{bmatrix} \leq d_i.$$

Letting $i = 1, \dots, 2N$ and stacking the inequalities gives the following matrix repre-

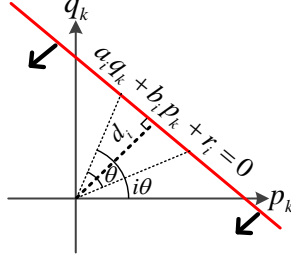


Figure 4.8: perpendicular distance to the i^{th} linear cut at time interval k .

senting points inside the polyhedron area.

$$\underbrace{\begin{bmatrix} \cos(\theta) & \sin(\theta) \\ \cos(2\theta) & \sin(2\theta) \\ \vdots & \vdots \\ \cos(2N\theta) & \sin(2N\theta) \end{bmatrix}}_A \begin{bmatrix} p_k \\ q_k \end{bmatrix} \leq \underbrace{\begin{bmatrix} d_1 \\ d_2 \\ \vdots \\ d_{2N} \end{bmatrix}}_d.$$

We now replace constraint (4.23) with the following constraint.

$$\begin{bmatrix} I_T \otimes A_1 & I_T \otimes A_2 \end{bmatrix} \begin{bmatrix} p \\ q \end{bmatrix} \leq \mathbf{1} \otimes d, \quad (4.26)$$

where I_T in constraint (4.26) is the $T \times T$ identity matrix, \otimes denotes the Kronecker product, and A_1 and A_2 denote the first and second columns of the matrix A , respectively.

To illustrate the reactive power capability of an EV, we have assumed that during the time interval k , the scheduled active power flow rate of the EV is p_k^* . We then calculate the maximum reactive power flow rate for absorption, q_k^+ , and for injection, q_k^- , when $p_k = p_k^*$, by considering the charger operating point on the corresponding linear cut boundary. Figure 4.9 demonstrates the reactive power capability of the EV,

by red solid lines $ABCDEF$. Three ranges for reactive power can be recognized from the figure. Any reactive power in the range $q_k^- \leq q_k \leq q_k^+$ can be provided without changing the scheduled active power $p_k = p_k^*$ (operating points on line CD). However any reactive power absorption in the range $q_k^+ \leq q_k \leq \bar{s}$ would result reduction of scheduled active power flow rate. To experience minimum reduction of p_k , the operating point should be on lines DE and EF . Similarly for any reactive power injection in the range $-\bar{q} \leq q_k \leq q_k^-$ the operating point should be on lines BC and AB .

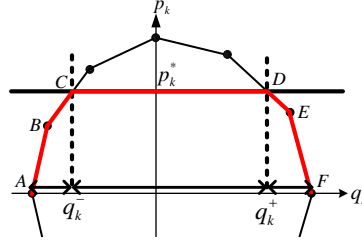


Figure 4.9: Reactive power capability curve of the EV at time interval k in linear approach.

As explained above, in some ranges, provision of reactive power service results changes in scheduled active power flow rate. The change in scheduled active power flow rate, which is solution of pre-defined optimization problem, is termed as perturbation in the optimal solution. This perturbation from optimal solution may increase the operation cost of the EV. In the following section, perturbations caused by reactive power service and associated costs are explained.

After calculating the optimal active power flow rates, p_k^* for $k = 1, 2, \dots, T$, the corresponding reactive power flow rates, q_k^+ and q_k^- , are calculated for $k = 1, 2, \dots, T$. As shown in Figure 4.9, during time period k , any reactive power service from 0 to q_k^+ for absorption and from zero to q_k^- for injection, does not perturb the optimal

scheduled active power flow rate. However, any increase in reactive power service above q_k^+ for absorption or beyond q_k^- for injection, by Δq_k , results in perturbation of active power flow rate by Δp_k .

Any increase in reactive power service by Δq_k , moves the operating point, for example, from position ① to position ② as shown in Figure 4.10. The change in the operating cost of the EV can be explained as follows:

- If $p_k^* \geq 0$ then lower costs due to less active power consumption.
- If $p_k^* < 0$ then lower income for discharging less active power.

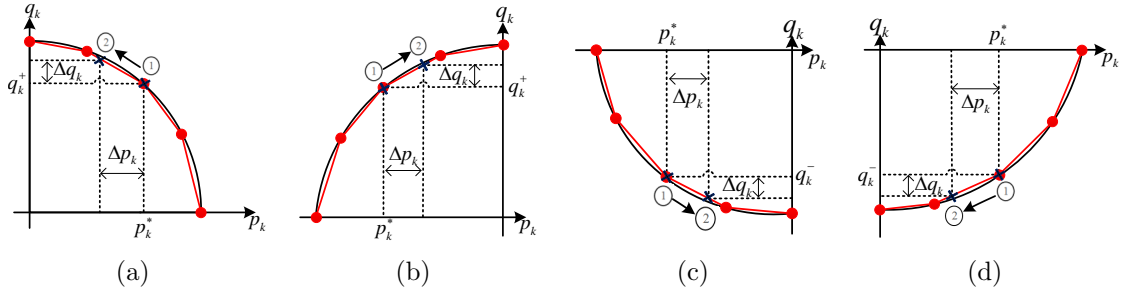


Figure 4.10: Perturbation in scheduled operating point by increase in reactive power service for (a) Region I; (b) Region II; (c) Region III; and (d) Region IV.

In order to satisfy constraint (3.18), any change in active power flow rate at current time period k must be reschedulable during the remainder of its parking time, termed as receding horizon in our calculation. Therefore Δp_k , and corresponding Δq_k , is limited by maximum reschedulable active power flow rate in the receding horizon.

4.5 Perturbation in Optimal Solutions

Let us assume that the change in active power flow rate at the current time period, k , is rescheduled during a time period r of the receding horizon. Any decrease in

charging power, when $p_k^* \geq 0$, must be compensated by increasing charging power at time period r if $p_r^* \geq 0$ or by decreasing discharging power if $p_r^* < 0$. Similarly, any decrease in discharging power, when $p_k^* < 0$, must be compensated by decreasing charging power at time period r if $p_r^* \geq 0$ or by increasing discharging power if $p_r^* < 0$. Table 4.3 summarizes changes in operation cost of the EV during current time period k and rescheduling that during time period r .

Table 4.3: Change in Operation Cost of EV due to Change in Active Power Flow Rate.

p_k^*	p_r^*	Δf_k^c	Δf_r^c
$p_k^* \geq 0$	$p_r^* \geq 0$	$-\tau(\frac{\rho_k}{\eta} + \gamma)\Delta p_k$	$\tau(\frac{\rho_r}{\eta} + \gamma)\Delta p_k$
$p_k^* \geq 0$	$p_r^* < 0$	$-\tau(\frac{\rho_k}{\eta} + \gamma)\Delta p_k$	$\tau(\eta\lambda_r^p - \gamma)\Delta p_k$
$p_k^* < 0$	$p_r^* \geq 0$	$\tau(\eta\lambda_k^p - \gamma)\Delta p_k$	$-\tau(\frac{\rho_r}{\eta} + \gamma)\Delta p_k$
$p_k^* < 0$	$p_r^* < 0$	$\tau(\eta\lambda_k^p - \gamma)\Delta p_k$	$-\tau(\eta\lambda_r^p - \gamma)\Delta p_k$

Therefore, the total change in the operation cost of the EV, f , can be calculated as follows:

$$\Delta f = \Delta f_k^c + \Delta f_r^c. \quad (4.27)$$

The marginal cost due to a deviation of Δp_k from optimal solutions, p_k^* and p_r^* , can be calculated by differentiating equations in third and fourth column of Table 4.3 with respect to Δp_k . Table 4.4 lists the marginal cost, MC_k , for deviation form p_k^* , and the marginal cost, MC_r , for deviation form p_r^* all in \$/kWh.

Therefore, the total marginal cost, MC_k^{total} , for deviation from optimal solutions can be calculated as follows:

$$MC_k^{total} = MC_k + MC_r. \quad (4.28)$$

Table 4.4: Marginal Cost of Deviation Caused by Δp_k in \$/kW.

p_k^*	p_r^*	MC_k	MC_r
$p_k^* \geq 0$	$p_r^* \geq 0$	$-\tau\left(\frac{\rho_k}{\eta} + \gamma\right)$	$\tau\left(\frac{\rho_r}{\eta} + \gamma\right)$
$p_k^* \geq 0$	$p_r^* < 0$	$-\tau\left(\frac{\rho_k}{\eta} + \gamma\right)$	$\tau(\eta\lambda_r^p - \gamma)$
$p_k^* < 0$	$p_r^* \geq 0$	$\tau(\eta\lambda_k^p - \gamma)$	$-\tau\left(\frac{\rho_r}{\eta} + \gamma\right)$
$p_k^* < 0$	$p_r^* < 0$	$\tau(\eta\lambda_k^p - \gamma)$	$-\tau(\eta\lambda_r^p - \gamma)$

Note that the marginal cost terms expressed in Table 4.4 are in \$/kW. Next we present marginal cost terms in \$/kVAr.

4.5.1 Nonlinear Approach

Considering the charger constraint, the optimal and non-optimal quantities are related as follows:

$$p_k^{*2} = \bar{s}^2 - q_k^{*2}, \quad (4.29)$$

$$p_k^2 = \bar{s}^2 - (|q_k^*| + \Delta q_k)^2. \quad (4.30)$$

By plugging equation (4.29) into equation (4.30), and simplifying it, Δp_k can be expressed as a function of Δq_k as follows:

$$\Delta p_k = \begin{cases} |p_k^*| - \sqrt{p_k^{*2} - \Delta q_k(\Delta q_k + 2q_k^*)}, & \forall q_k^* \geq 0; \\ |p_k^*| - \sqrt{p_k^{*2} - \Delta q_k(\Delta q_k - 2q_k^*)}, & \forall q_k^* \leq 0; \end{cases} \quad (4.31)$$

The marginal cost terms MCR_k^{total} in \$/kVAr, is then developed using the following equation:

$$MCR_k^{total} = MC_k^{total} \frac{\partial(\Delta p_k)}{\partial(\Delta q_k)} = MC_k^{total} \begin{cases} \frac{\Delta q_k + q_k^*}{\sqrt{p_k^{*2} - \Delta q_k(\Delta q_k + 2q_k^*)}}, & \forall q_k \geq 0; \\ \frac{\Delta q_k - q_k^*}{\sqrt{p_k^{*2} - \Delta q_k(\Delta q_k - 2q_k^*)}}, & \forall q_k < 0; \end{cases} \quad (4.32)$$

Therefore, based on the optimal scheduled active power flow rate at time period k , p_k^* , corresponding reactive power flow rate q_k^* , and the rescheduling time period r in the receding horizon, the marginal cost for providing different ranges of reactive power service, can be calculated using Table 4.4 and equation (4.32).

4.5.2 Linear Approach

Providing reactive power services in the ranges $-\bar{q} \leq q_k \leq q_k^-$ and $q_k^+ \leq q_k \leq \bar{s}$ will force the operating point to be on the linear boundaries. Therefore for cut i (where the operating point for the EV during time k falls), we can express q_k in terms of p_k as below:

$$q_k = -\frac{b_i}{a_i}p_k - r_i. \quad (4.33)$$

Now if we define $m_i = -\frac{b_i}{a_i}$, then from equation (4.33), it can be inferred that Δq_k is equal to $m_i \Delta p_k$. The marginal cost terms MCR_k^{total} in \$/kVAr, is then developed using the following equation:

$$MCR_k^{total} = \frac{\partial(\Delta p_k)}{\partial(\Delta q_k)} MCR_k^{total} = \frac{1}{m_i} MCR_k^{total}. \quad (4.34)$$

Therefore, based on the optimal scheduled active power flow rate at time period k , p_k^* , corresponding reactive power flow rates, q_k^+ for absorption and q_k^- for injection, and the rescheduling time period r in the receding horizon, the marginal cost for providing different ranges of reactive power service, can be calculated using Table 4.4 and equations (4.28) and (4.34).

In the following section, we provide a framework to find minimum marginal cost and calculate a reactive power supply function for the EV.

4.6 Calculation of Reactive Power Supply Function

The first step in the development of the framework is to calculate optimal scheduled active power flow rates, while minimizing the charging/discharging cost and provide desired SOC at the departure time. This effort provides information of the optimal scheduled active power flow rate, p_k^* , corresponding reactive power rate at optimal scheduled point, q_k^* , in nonlinear approach or the maximum reactive power flow rate for absorption, q_k^+ , and for injection, q_k^- , in linear approach, for $k= 1, 2, \dots, T$. Also x_k^* , SOC of the EV battery can be calculated using equation (3.1). Then during each time period k , the reactive power supply function is calculated. Next, we develop a framework to calculate the reactive power supply function, using above mentioned parameters value, to get minimum marginal cost of providing the service.

As explained before, any reactive power service from 0 to $|q_k^*|$ for absorption and from 0 to $-|q_k^*|$ for injection in nonlinear approach or any reactive power in the range $q_k^- \leq q_k \leq q_k^+$ in linear approach, does not result in perturbation of optimal solutions. Therefore, neglecting the switching losses, the cost of reactive power service for this ranges is zero. However, any reactive power service above q_k^* in nonlinear approach or any reactive power absorption above q_k^+ and any reactive power injection beyond q_k^- in linear approach, perturbs the scheduled active power flow rate during time period k . We define Δp_k , the deviation in scheduled active power from its scheduled value and Δx_k , the deviation in SOC of the battery from its scheduled value as a result of change in active power activity. We have used superscripts \uparrow for deviation in increase mode and \downarrow for deviation in decrease mode. Figure 4.11 shows an example of scheduled SOC of the EV battery. Note that SOC in each time interval must satisfy constraint (3.15).

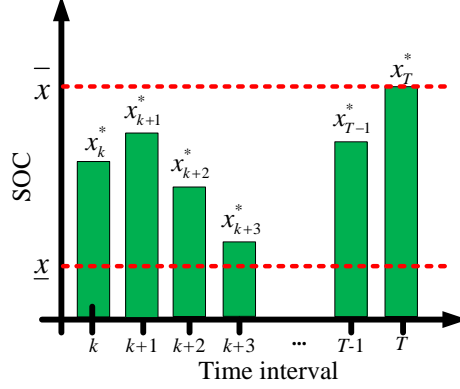


Figure 4.11: Scheduled SOC of the EV battery.

The following set of equations can be applied for all time intervals $k=1, 2, \dots, T$ of the optimization horizon.

$$\left\{ \begin{array}{l} \Delta x_k^\uparrow = \min \left\{ \bar{x} - x_k^*, (\bar{p} - p_k^*) \frac{\tau}{u} \right\}, \quad \text{if } p_k^* \geq 0; \\ \Delta x_k^\uparrow = \min \left\{ \bar{x} - x_k^*, \left| p_k^* \right| \frac{\tau}{u} \right\}, \quad \text{if } p_k^* < 0; \\ \Delta x_k^\downarrow = \min \left\{ x_k^* - \underline{x}, p_k^* \frac{\tau}{u} \right\}, \quad \text{if } p_k^* \geq 0; \\ \Delta x_k^\downarrow = \min \left\{ x_k^* - \underline{x}, (\bar{p} - \left| p_k^* \right|) \frac{\tau}{u} \right\}, \quad \text{if } p_k^* < 0; \end{array} \right. \quad (4.35)$$

Note that equation (4.35) guarantees that the perturbation in active power flow rates do not violate constraint (3.20).

Any decrease in optimal active power flow rate at current time period k , as a result of reactive power service, must be rescheduled, as listed in Table 4.5, to fulfill the desired SOC at the departure time.

Consider time interval k as the current time interval. $\overline{\Delta p_k}$ is defined as the maximum decrease in charging/discharging power at current time period k that is reschedulable in the receding horizon. In the receding horizon at the time period r , we define $p_r^{+\uparrow}$ as available charging power increment, $p_r^{+\downarrow}$ as available charging power

Table 4.5: Rescheduling Active Power Flow Rates in Receding Horizon Due to Perturbation in the Optimal Solution.

p_k^*	Perturbation in p_k^* due to reactive power service	Rescheduling strategy in the receding horizon
Charging	↓ charging power	↑ scheduled charging ↓ scheduled discharging
Discharging	↓ discharging power	↓ scheduled charging ↑ scheduled discharging

decrement, $p_r^{-\uparrow}$ as available discharging power increment, $p_r^{-\downarrow}$ as available discharging power decrement; $\overline{q_k^+}$ and $\overline{q_k^-}$ as maximum available reactive power service for absorption and injection, respectively. Figure 5.4 shows an example of optimal scheduled charging/discharging power activities. Red bars in the figure indicates the scheduled active power flow rate at each time period ($p_k^*, p_{k+1}^*, \dots, p_T^*$). Note that positive and negative values for active power flow rates represent charging and discharging activities, respectively. Also $p_r^{+\uparrow}$, $p_r^{+\downarrow}$, $p_r^{-\uparrow}$, and $p_r^{-\downarrow}$ are shown by yellow, green, blue, and purple arrows in the figure, respectively. The following set of equations can be recognized, from the figure, for the calculation of the maximum reschedulable power in receding horizon $\overline{\Delta p_r}$.

$$\overline{\Delta p_r} = \begin{cases} p_r^{+\uparrow} = \frac{\Delta x_r^{\uparrow} u}{\tau}, & \text{if } p_r^* \geq 0; \\ p_r^{+\uparrow} = 0, & \text{if } p_r^* < 0; \\ p_r^{+\downarrow} = \frac{\Delta x_r^{\downarrow} u}{\tau}, & \text{if } p_r^* \geq 0; \\ p_r^{+\downarrow} = 0, & \text{if } p_r^* < 0; \\ p_r^{-\uparrow} = \frac{\Delta x_r^{\downarrow} u}{\tau}, & \text{if } p_r^* \leq 0; \\ p_r^{-\uparrow} = 0, & \text{if } p_r^* > 0; \\ p_r^{-\downarrow} = \frac{\Delta x_r^{\uparrow} u}{\tau}, & \text{if } p_r^* \leq 0; \\ p_r^{-\downarrow} = 0, & \text{if } p_r^* > 0; \end{cases} \quad (4.36)$$

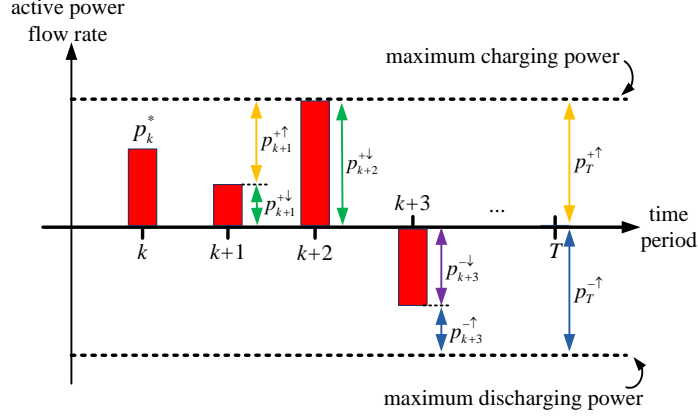


Figure 4.12: Reschedulable active power flow rate at current time period k and during receding horizon.

Deviation in p_k^* and consequently in Δx_k , will depend on the sign of p_k^* (charging/discharging). However, any perturbation in SOC of the EV battery during current time interval and receding horizon must comply with constraint (3.15). For example consider a case in which SOC of the battery in current time interval is 0.6 and in time interval r of the receding horizon is 0.3. Decreasing SOC of the battery at current time interval by 0.2 will decrease SOC of the battery in time interval r below \underline{x} . That means the time interval r can not accommodate the perturbation. In order to establish the reactive power supply function, the ability of all time intervals of the receding horizon to accommodate any perturbation must be investigated. We define three subsets in the receding horizon, namely set of reschedulable time intervals R , set of critical time intervals R' , and set of non-reschedulable time intervals R'' . Any $r \in R$ can accommodate any perturbation in current time interval k . Any $r \in R'$ has limited room to accommodate perturbation in current time interval k . And finally members of R'' can not accommodate any perturbation in current time interval k . In the following subsections, we present a procedure to establish sets R , R' , and R'' based on the sign of p_k^* .

4.6.1 $p_k^* \geq 0$

Any decrease in charging power during time interval k , Δp_k^\downarrow , will result in decrease in scheduled SOC during time interval k and in receding horizon ($k+1$, $k+2$, ..., and T) by $\Delta x_k^\downarrow = \frac{\tau \Delta p_k^\downarrow}{u}$. Figure 4.13 shows the flowchart of establishing three pre-defined sets of the receding horizon. The flowchart starts with the first time interval of receding horizon. This time interval will fall into R , if it can accommodate Δx_k^\downarrow , and $p_r^{+\uparrow} \neq 0$ when $p_r^* \geq 0$ or $p_r^{-\downarrow} \neq 0$ when $p_r^* < 0$. The time interval will fall into R' if it can not accommodate Δx_k^\downarrow , and $p_r^{+\uparrow} \neq 0$ when $p_r^* \geq 0$ or $p_r^{-\downarrow} \neq 0$ when $p_r^* < 0$. The time interval will fall into R'' otherwise. Note that when the flowchart reaches a time interval of receding horizon in which $x_r^* < x_k^*$ and $p_r^{+\uparrow} = 0$ if $p_r^* \geq 0$ or $p_r^{-\downarrow} = 0$ if $p_r^* < 0$, the time interval r and the remaining time intervals of the receding horizon will fall into R'' . The reason is that, the deviation in x_k^* will drop x_r^* below the minimum SOC (\underline{x}). Since $p_r^{+\uparrow} = 0$ if $p_r^* \geq 0$ or $p_r^{-\downarrow} = 0$ if $p_r^* < 0$, the scheduled charging/discharging power (p_r^*) and SOC of the EV battery (x_r^*) must remain unchanged. That will result in not changing any activity during time intervals of receding horizon occurring after time interval r .

4.6.2 $p_k^* < 0$

Any decrease in discharging power during time interval k , Δp_k^\downarrow , will result in increase in scheduled SOC during time interval k and in receding horizon ($k+1$, $k+2$, ..., and T) by $\Delta x_k^\uparrow = \frac{\tau \Delta p_k^\downarrow}{u}$. Figure 4.14 shows the flowchart of establishing three pre-defined sets of the receding horizon. The flowchart starts with the first time interval of receding horizon. This time interval will fall into R , if it can accommodate Δx_k^\uparrow , and $p_r^{+\downarrow} \neq 0$ when $p_r^* \geq 0$ or $p_r^{-\uparrow} \neq 0$ when $p_r^* < 0$. The time interval will fall into R' if it can not accommodate Δx_k^\uparrow , and $p_r^{+\downarrow} \neq 0$ when $p_r^* \geq 0$ or $p_r^{-\uparrow} \neq 0$ when $p_r^* < 0$.

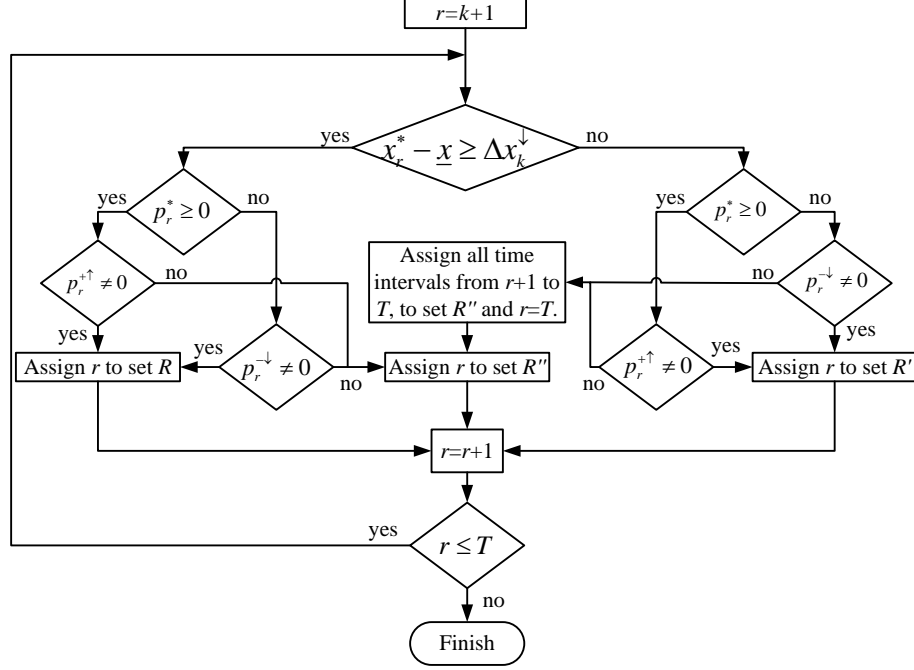


Figure 4.13: Classifying time intervals of the receding horizon when $p_k^* \geq 0$.

The time interval will fall into R'' otherwise. Similar to previous subsection, when the flowchart reaches a time interval of receding horizon in which $x_r^* > x_k^*$ and $p_r^{+↓} = 0$ if $p_r^* \geq 0$ or $p_r^{-↑} = 0$ if $p_r^* < 0$, the time interval r and the remaining time intervals of the receding horizon will fall into R'' .

Note that members of set R' , the critical time intervals, are arranged based on their occurrence in the receding horizon. For example, $r=10$ has higher priority than $r=15$. It is worth mentioning that, in case of scheduling the EV just for charging (when scheduled SOC of the EV battery is increasing in the optimization horizon) or just for discharging (when scheduled SOC of the EV battery is decreasing in the optimization horizon), the set R' is empty.

The maximum decrease in charging/discharging power at current time period k , $\overline{\Delta p_k}$, can then be calculated using Table 4.6.

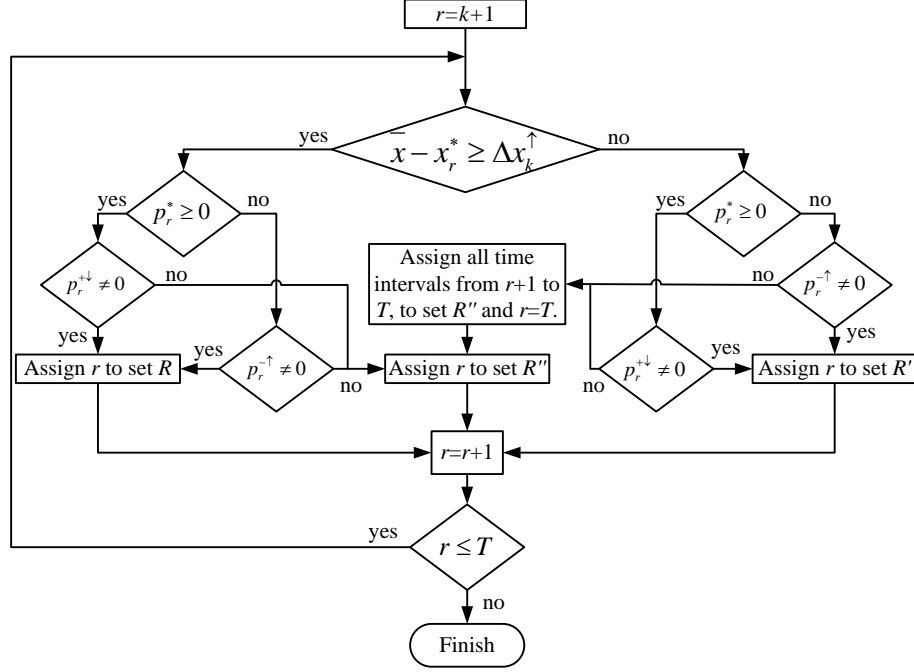


Figure 4.14: Classifying time intervals of the receding horizon when $p_k^* < 0$.

The marginal cost of perturbation at current time period k , MC_k , and the marginal cost of rescheduling at time period r of receding horizon, MC_r , are presented in Table 4.4. Rescheduling of active power flow rates in the receding horizon must be done in a way so that leads us to minimum total marginal cost, MC_k^{total} . Figure 4.15 presents a flowchart to perform the rescheduling task with the goal of minimizing total marginal cost. The flowchart starts with arranging $r \in R$, based on its MC_r , from the lowest to the highest. Since critical time intervals have limited rescheduling capacity and also to satisfy constraint (3.20), the rescheduling process starts with critical time intervals $r \in R'$. After rescheduling all critical time intervals, if the maximum decrease in charging/discharging power at current time period is still not met, the process continues with rescheduling charging/discharging power during time intervals $r \in R$. Note that rescheduling task during time intervals $r \in R$, starting with the lowest

Table 4.6: Maximum decrease in charging/discharging power at current time period k .

p_k^*	$\overline{\Delta p_k}$
$p_k^* > 0$	$\min \{p_k^*, \sum_{r \in R'} (p_r^{+\uparrow} + p_r^{-\downarrow}) + \sum_{r \in R} (p_r^{+\uparrow} + p_r^{-\downarrow})\}$
$p_k^* = 0$	0
$p_k^* < 0$	$\min \{ p_k^* , \sum_{r \in R'} (p_r^{+\downarrow} + p_r^{-\uparrow}) + \sum_{r \in R} (p_r^{+\downarrow} + p_r^{-\uparrow})\}$

marginal cost, guarantees the minimum total marginal cost.

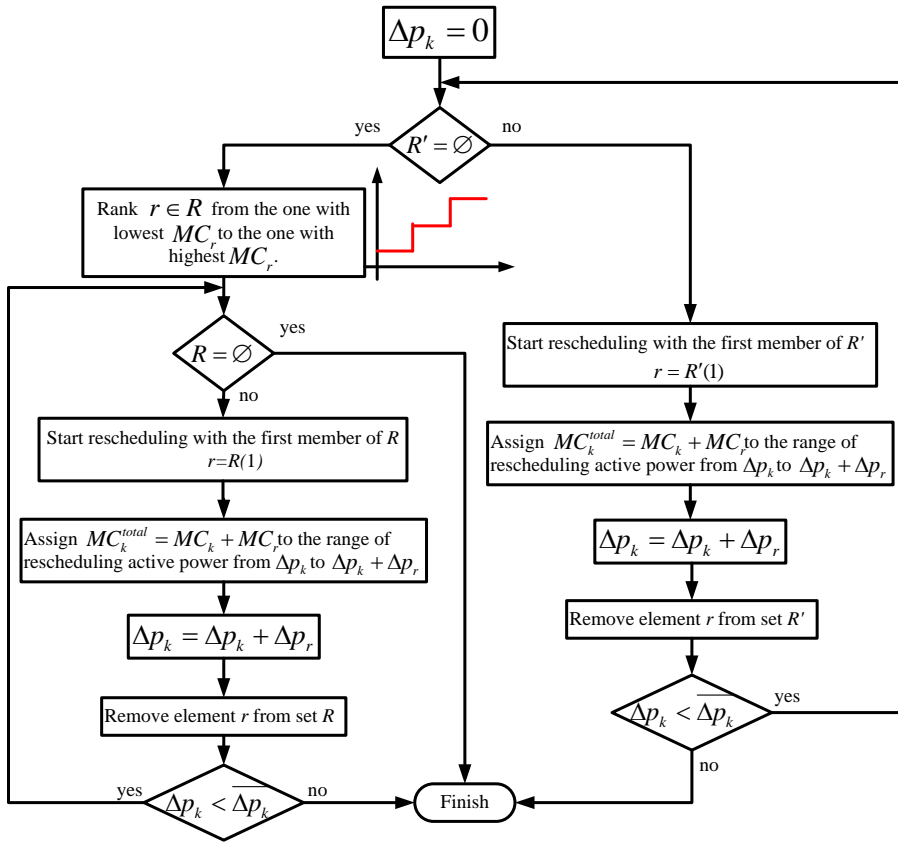


Figure 4.15: Flowchart of rescheduling of the receding horizon.

After calculation of MC_k^{total} , one can develop the MCR_r for different range of reactive power service.

4.6.3 Nonlinear Approach

Maximum available reactive power absorption and injection can be calculated as below.

$$\overline{q_k^+} = \sqrt{\overline{s}^2 - (|p_k^*| - \overline{\Delta p_k})^2}, \quad (4.37)$$

$$\overline{q_k^-} = \min \left\{ \overline{q}, \sqrt{\overline{s}^2 - (|p_k^*| - \overline{\Delta p_k})^2} \right\}. \quad (4.38)$$

Considering above explanation and reactive power capability of the charger, the reactive power supply function at current time period k can be calculated as follows:

- Any reactive power absorption from 0 to $|q_k^*|$ with zero cost;
- Any increase in reactive power absorption by Δq_k , beyond $|q_k^*|$ up to $\overline{q_k^+}$, would result in marginal cost of MCR_k^{total} calculated with equation (4.32);
- Any reactive power injection from 0 to $|q_k^*|$ with zero cost;
- Any increase in reactive power injection by Δq_k , beyond $|q_k^*|$ up to $\overline{q_k^-}$, would result in marginal cost of MCR_k^{total} calculated with equation (4.32);

Note that the range of reactive power service at time period k where $R = \left\{ \emptyset \right\}$ and $R' = \left\{ \emptyset \right\}$, is limited to 0 to $|q_k^*|$ with zero cost for absorption and 0 to $\min \left\{ |q_k^*|, \overline{q} \right\}$ with zero cost for injection. The reason for that is lack of reschedulable time intervals in the receding horizon.

4.6.4 Linear Approach

Maximum available reactive power for absorption, $\overline{q_k^+}$, and for injection, $\overline{q_k^-}$, can be calculated by equations (4.39) and (4.40). Note that $m^+ = m_i$ when the operating point $(|p_k^*| - \overline{\Delta p_k}, \overline{q_k^+})$ falls on the i^{th} linear cut boundary. Similarly $m^- = m_i$ when

the operating point $(|p_k^*| - \overline{\Delta p_k}, \overline{q_k^-})$ falls on the i^{th} linear cut boundary.

$$\overline{q_k^+} = m^+(|p_k^*| - \overline{\Delta p_k}), \quad (4.39)$$

$$\overline{q_k^-} = m^-(|p_k^*| - \overline{\Delta p_k}). \quad (4.40)$$

Considering above explanation and reactive power capability of the charger, the reactive power supply function at current time period k can be calculated as follows:

- Any reactive power absorption from 0 to q_k^+ with zero cost;
- Any increase in reactive power absorption by Δq_k , beyond q_k^+ up to $\overline{q_k^+}$, would result in marginal cost of MCR_k^{total} calculated using equation (4.34);
- Any reactive power injection from 0 to q_k^- with zero cost;
- Any increase in reactive power injection by Δq_k , beyond q_k^- up to $\overline{q_k^-}$, would result in marginal cost of MCR_k^{total} calculated using equation (4.34);

Note that the range of reactive power service at time period k where $R = \left\{ \emptyset \right\}$ and $R' = \left\{ \emptyset \right\}$, is limited to $q_k^- \leq q_k \leq q_k^+$ with zero cost due to the lack of reschedulable time intervals in the receding horizon.

4.7 Numerical Results

In this section, we perform simulations for nonlinear and linear approach separately. We have defined several scenarios in each case. In both cases, the minimum and maximum SOC for all EVs are assumed to be 0.2 and 0.9, respectively. We have used a work day (February 12, 2015) price published by NYISO for Central zone. From the price data, the on-peak periods can be recognized as 7 a.m. to 10 a.m. and 6 p.m.

to 8 p.m. Also the price of discharging active power has been assumed to be equal to the price of charging active power during corresponding time interval. Energy unit price (\$/kWh) for Lithium-Ion battery is assumed to be \$1500/kWh [50]. A multi-period security constrained unit commitment and dispatch model that co-optimizes to solve simultaneously for load, operating reserves, and regulation service is run by NYISO over fifteen minute intervals. Therefore, τ is assumed to be 0.25 hour in the calculation.

4.7.1 Nonlinear Approach

For simulation purpose, an EV with a 6.6 kVA charger, 95% battery efficiency, and 16 kWh battery capacity is considered [90]. Based on the specifications of the charger, the maximum injected reactive power, \bar{q} , can be calculated using equation (4.24) and the value is 6.11 kVAr. The 16 kWh battery pack used for simulation is similar to the battery used in Mitsubishi's i MiEV. This battery pack is composed of 22 cell modules connected in series at nominal voltage of 330 V. Each cell module is composed of 4 cells with nominal voltage of 3.7 V and capacity of 50 Ah. Using the values for β_1 to β_7 from reference [47], the battery degradation factor γ , in ¢/kWh, is equal to 49.97 ¢/kWh.

We have defined two scenarios. In scenario 1, we include the degradation cost of the battery, equation (3.9), due to charging/discharging activities. In scenario 2 we ignore the degradation effect on the battery because of two reasons: First to demonstrate the effect of the battery degradation by comparing simulation results in scenario 1; Second, to incorporate discharging activities in the simulations. Table 4.7 lists the simulation settings used in each scenario.

Assuming τ equal to 0.25 hour, the optimization horizon, in each scenario, includes

Table 4.7: Simulation settings in each scenario.

	h_0	h_f	x_0	x_f
Scenario 1	6 a.m.	11 a.m.	0.2	0.9
Scenario 2	6 p.m.	11 p.m.	0.3	0.9

20 time intervals ($T=20$).

4.7.1.1 Scenario 1

Figure 4.16 shows the optimal charging/discharging activities of the EV in scenario 1. Since the battery degradation cost is higher than price of electricity, no discharging activity has been scheduled in the optimization horizon. Also one can observe from the figure that during the on-peak periods, no charging activities have been scheduled.

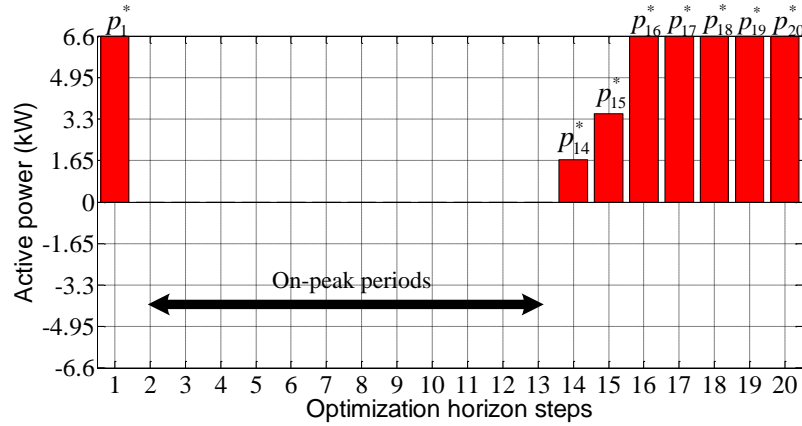


Figure 4.16: Optimal scheduled charging/discharging activities in scenario 1.

Since EV is scheduled for charging in the optimization horizon, SOC of the EV battery is accenting during optimization horizon, as depicted in Figure 4.17.

For any time interval $k=2, 3, \dots, 13$ in which the scheduled charging/discharging

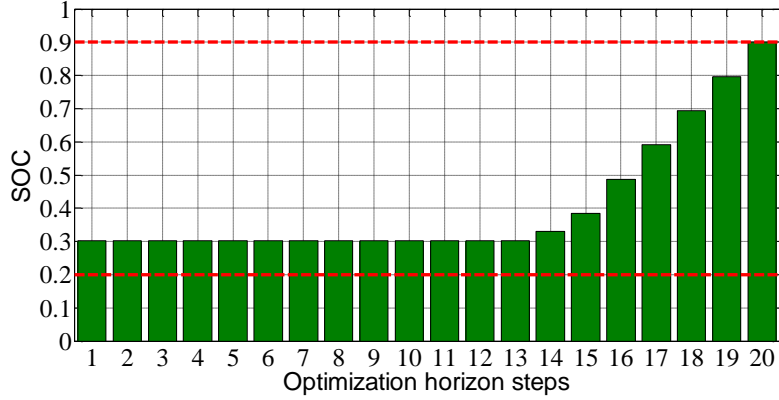


Figure 4.17: Scheduled SOC of the EV battery in scenario 1.

power is zero, the entire range of reactive power service can be provided by the EV with zero marginal cost. Therefore the reactive power supply function of the EV for those time intervals is as demonstrated by the red line in Figure 4.18.

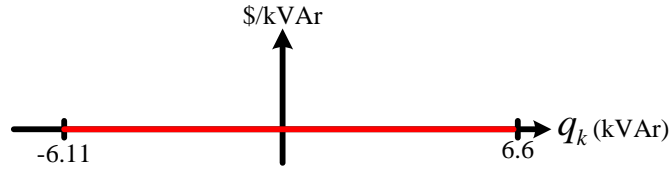


Figure 4.18: Reactive power supply function of the EV in scenario 1 and time interval $k=2, 3, \dots, 13$.

During other time intervals in which the charging/discharging power is non-zero, the marginal cost of reactive power service is different for different ranges of reactive power service. Consider time interval $k=1$ as current time interval. The receding horizon includes $r=2, 3, \dots, 20$. Scheduled active power during current time interval, p_k^* , is equal to 6.6 kW. Therefore $q_k^*=0$ kVAr. Any decrease in charging power during current time interval k must be rescheduled in the receding horizon ($r=2, 3, \dots, 20$) by increasing charging power or decreasing discharging power. Since SOC of the EV

battery is accenting during the receding horizon we can conclude that $R' = \{\emptyset\}$. Also using flowchart shown in Figure 4.13, one can conclude that $R = \{2, 3, \dots, 15\}$ and $R'' = \{16, 17, 18, 19, 20\}$.

Figure 4.19 shows the ranked reschedulable active power $r \in R$, starting from the lowest marginal cost MC_r , in the set R of the receding horizon. The maximum decrease in charging/discharging power at current time period $\overline{\Delta p_1}$, calculated from Table 4.6, is shown in the figure with black solid line. One can conclude that any decrease in charging power of current time interval, caused by reactive power service, can be rescheduled during time intervals 14 and 15, equally. Therefore, considering the marginal cost of decreasing charging power at current time interval, MC_1 , equal to $\text{¢}13.9846/\text{kW}$, the total marginal cost of rescheduling active power, MC_1^{total} , can be calculated using Table 4.4 and is equal to $\text{¢}0.1529/\text{kW}$.

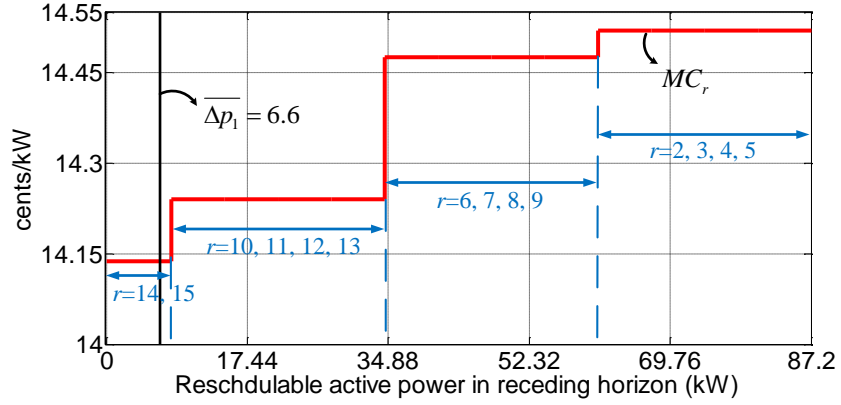


Figure 4.19: Reschedulable active power in receding horizon of time interval $k=1$.

Using equation (4.32), the marginal cost of providing reactive power service during current time interval $k=1$, MCR_1 , is calculated and is shown in Figure 4.20. Note that positive and negative value for reactive power in the figure represent absorption

and injection of reactive power, respectively.

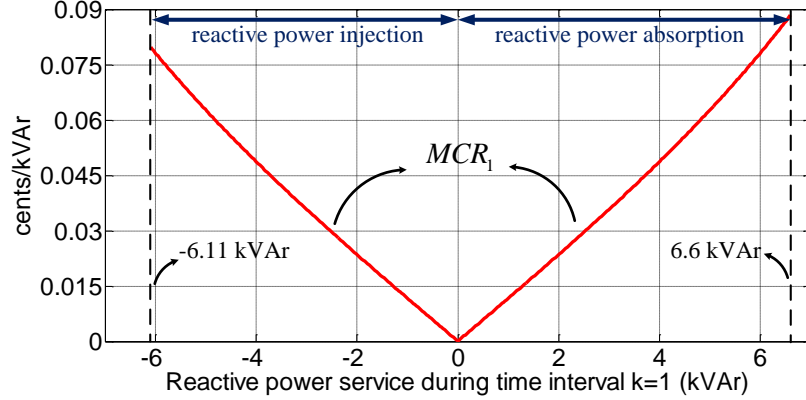


Figure 4.20: Reactive power supply function during time interval $k=1$ in scenario 1.

Now we consider $k=14$ as current time interval. p_{14}^* is equal to 1.69 kW and accordingly, q_{14}^* will be equal to 6.38 kVAr. Also $R = \{15\}$, $R' = \{\emptyset\}$, and $R'' = \{16, 17, \dots, 20\}$. Therefore any decrease in charging power during time interval 14, caused by providing reactive power service above 6.38 kVAr, can be rescheduled just in time interval 15. Using Table 4.6 and 4.4, we have $\overline{\Delta p_{14}}=1.69$ kW and $MC_{14}^{total}=\zeta_0/\text{kW}$. The reactive power supply function during time interval $k=14$ is equal to zero from 0 to $q_{14}^*=6.38$ kVAr, zero from 0 to $\max\{-\bar{q}, -q_{14}^*\}=-6.11$ kVAr, and zero from $q_{14}^*=6.38$ kVAr to 6.6 kVAr (since MC_{14}^{total} is equal to 0). Therefore the cost of reactive power service is equal to zero for the entire range of reactive power service (Figure 4.18).

During time interval $k=15$, $p_{15}^*=3.5$ kW and accordingly $q_{15}^*=5.59$ kVAr. From Figure 4.16 one can observe that $R = \{\emptyset\}$, $R' = \{\emptyset\}$, $R'' = \{16, 17, \dots, 20\}$, and therefore $\overline{\Delta p_{15}}$ is equal to zero. Hence the reactive power supply function during this time interval is zero for any reactive power service from -5.59 kVAr to 5.59 kVAr.

In scenario 1, during on-peak periods, the optimal active power was scheduled to

zero. That means the reactive power service can be provided, from zero to 6.6 kVAr for absorption and from 0 to 6.11 kVAr for injection, without any cost. The cost of reactive power service provided by the EV is relatively lower during on-peak periods, compare to off-peak periods. This opportunity can be a win-win situation for both, EV owner and SO, since the need for reactive power during on-peak periods is most likely higher.

4.7.1.2 Scenario 2

Figure 4.21 shows the optimal charging/discharging activities of the EV in scenario 2. Since the battery degradation cost is ignored and the initial SOC battery is 0.3 in this scenario, discharging activities are scheduled in time intervals 2, 3, 4, and 5. In time interval 1, although it is on-peak period, charging activity is scheduled to take advantage of energy arbitrage. Figure 4.22 shows SOC of the EV battery during the optimization horizon.

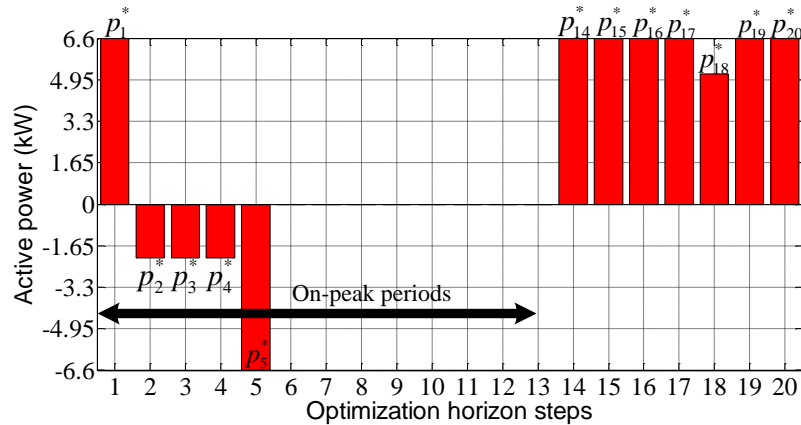


Figure 4.21: Optimal scheduled charging/discharging activities in scenario 2.

For time intervals 6 to 13, in which the scheduled charging/discharging power is zero, the entire range of reactive power service can be provided by the EV with zero

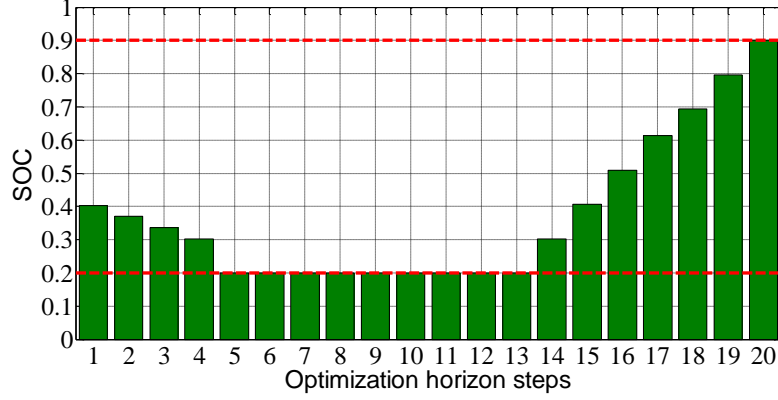


Figure 4.22: Scheduled SOC of the EV battery in scenario 2.

marginal cost (Figure 4.18).

Consider time interval $k=1$ as current time interval. Scheduled active power during current time interval, p_k^* , is equal to 6.6 kW. Therefore $q_k^*=0$ kVAr. Any decrease in charging power of current time interval k must be rescheduled in receding horizon ($r=2, 3, \dots, 20$) by increasing charging power or decreasing discharging power. The receding horizon is divided into three sets as $R = \{\emptyset\}$, $R' = \{2, 3, 4, \dots, 13\}$, and $R'' = \{14, 15, \dots, 20\}$. Since the set of reschedulable time intervals is empty, the rescheduling task has to be performed during critical time intervals in set R' . Note that the time intervals in set R' is ranked based on their occurrence in the receding horizon. Figure 4.23 shows the ranked reschedulable active power, starting from the first element of set R' . The maximum decrease in charging/discharging power at current time period $\overline{\Delta p_1}$, calculated from Table 4.6, is shown in the figure with black solid line. One can conclude that any decrease in charging power of current time interval, caused by reactive power service, can be rescheduled starting from time interval 2 up to 2.13 kW, then time interval 3 up to 2.13 kW, then time interval 4 up to 2.13 kW, and finally time interval 5 up to 0.21 kW.

Therefore, considering the marginal cost of decreasing charging power at current

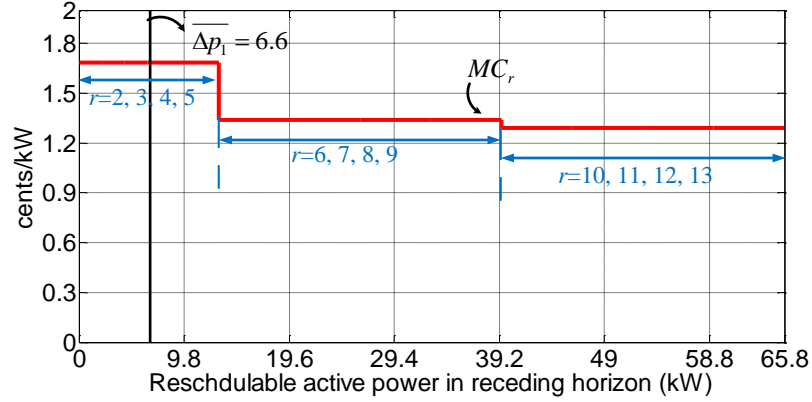


Figure 4.23: Reschedulable active power in receding horizon of time interval $k=1$.

time interval, MC_1 , equal to $\text{¢}1.5634/\text{kW}$, the total marginal cost of rescheduling active power, MC_1^{total} , can be calculated using Table 4.4 and is equal to $\text{¢}0.1219/\text{kW}$. Using equation (4.32), one can calculate the marginal cost of providing reactive power service during current time interval $k=1$, MCR_1 , is calculated and results are in Figure 4.24.

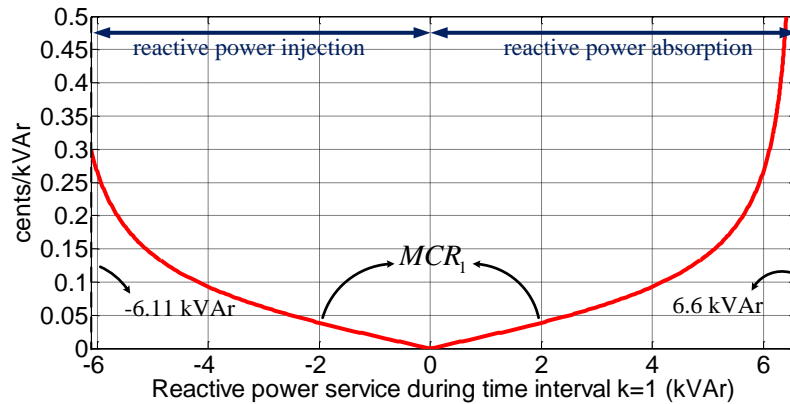


Figure 4.24: Reactive power supply function during time interval $k=1$ in scenario 2.

Now we consider $k=2$ as current time interval. p_2^* is equal to -2.13 kW and accordingly, q_2^* will be equal to 6.24 kVAr . Also using the flowchart presented in Figure

4.14, one can conclude $R = \{\emptyset\}$, $R' = \{3, 4\}$, and $R'' = \{5, 6, \dots, 20\}$ in the receding horizon. Therefore any decrease in discharging power during time interval 2, caused by providing reactive power service above 6.24 kVAr, can be rescheduled in time intervals 3 and then 4, by increasing their discharging power. Using Table 4.6, we have $\overline{\Delta p_2}=2,13$ kW. Also MC_r for $r=3$ and 4, is calculated to be $\text{ç}1.6853/\text{kW}$ using Table 4.4. Considering $MC_2=\text{ç}1.6853/\text{kW}$ for current time interval, one can conclude that $MC_2^{total}=\text{ç}0/\text{kW}$. The reactive power supply function during time interval $k=2$ is equal to zero from 0 to $q_2^*=6.24$ kVAr, zero from 0 to $\max\{-\bar{q}, -q_2^*\}=-6.11$ kVAr, and zero from $q_2^*=6.24$ kVAr to 6.6 kVAr (since MC_2^{total} is equal to 0). Therefore the cost of reactive power service is equal to zero for the entire range of reactive power service (Figure 4.18).

During time interval 4 ($k=4$), p_4^* is equal to -2.13 kW and accordingly, q_4^* will be equal to 6.24 kVAr. However, $R = \{\emptyset\}$, $R' = \{\emptyset\}$, and $R'' = \{5, 6, \dots, 20\}$ in the receding horizon. Therefore, any decrease in discharging power during time interval 4, caused by providing reactive power service above 6.24 kVAr, can not be rescheduled in the receding horizon. Hence the reactive power is equal to zero from 0 to $q_4^*=6.24$ kVAr and zero from 0 to $\max\{-\bar{q}, -q_4^*\}=-6.11$ kVAr. Similarly during time interval 5, where p_5^* is equal to -6.6 kW and accordingly q_5^* is equal to 0, $R = \{\emptyset\}$, $R' = \{\emptyset\}$, and $R'' = \{6, 7, \dots, 20\}$ in the receding horizon. Therefore the EV is not able to provide any reactive power service during time interval 5.

Let us consider $k=17$ as current time interval. $p_{17}^*=6.6$ kW and $q_{17}^*=0$ kVAr. $R = \{\emptyset\}$, $R' = \{18\}$, and $R'' = \{\emptyset\}$ in the receding horizon. Since $\overline{\Delta p_{17}}=1.4$ kW, it can be rescheduled in time interval $r=18$ by increasing the charging power. MC_r and MC_k is equal to $\text{ç}1.0197/\text{kW}$ and $\text{ç}1.0182/\text{kW}$, respectively. Therefore, the total marginal cost, MC_{17}^{total} , is equal to $\text{ç}0.0015/\text{kW}$. Figure 4.25 shows the reactive power

supply function during time interval 17. Considering the value of $\overline{\Delta p_{17}}$, the reactive power service provided by the EV is limited to 4.06 kVAr absorption/injection.

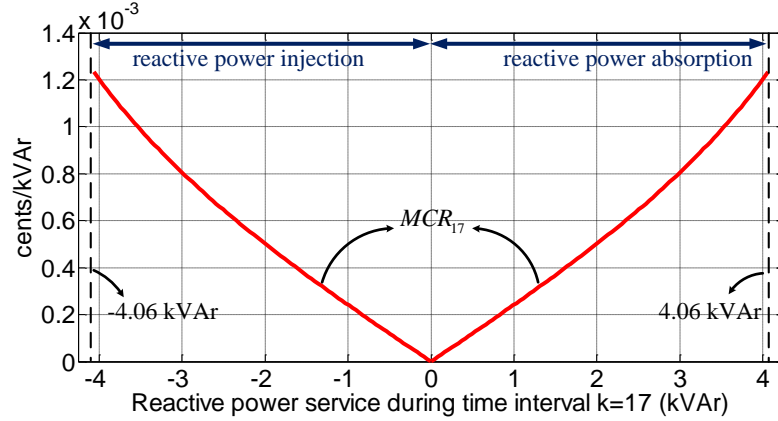


Figure 4.25: Reactive power supply function during time interval $k=17$ in scenario 2.

In scenario 2, as a result of ignoring the battery degradation cost, discharging activities have been scheduled during some on-peak periods. Higher initial SOC and longer parking time before the on-peak periods (which gives the EV an opportunity for energy arbitrage) result in more discharging activities during on-peak periods. Therefore, provision of reactive power service during those periods with discharging activities is incorporated with relatively higher marginal cost. However, for those time intervals of on-peak periods in which the EV is not scheduled for discharging, the reactive power service can be provided, from zero to 6.6 kVAr in absorption and from 0 to 6.11 kVAr in injection, without any cost. As mentioned before, ignoring the battery degradation cost would not be practical at this time. But improvement in battery technology can decrease battery degradation cost and then would allow discharging to be economically viable under certain conditions. Simulation results in scenario 2 clearly demonstrate efficient functionality of our framework during discharging and charging activities.

4.7.2 Linear Approach

We have defined two scenarios for simulations. In the first scenario, we have considered single EV and then expanded the number of EVs to 1000 in the second scenario. We have assumed that all of EVs considered for simulations are under one aggregator control and participating in the reactive power service.

4.7.2.1 Scenario 1

In this scenario, a Mitsubishi i-MiEV with 3.3 kVA charger and a 16 kWh Lithium-Ion battery pack is considered. Based on the specifications of the charger, the maximum injected reactive power, \bar{q} , can be calculated using equation (4.24) and the value is 3.23 kVA. The arrival time and departure time are assumed to be 4 p.m. and 11 p.m., respectively, in this scenario. Considering $\tau=0.25$ hour, the optimization horizon includes 27 intervals. The initial and desired SOC are assumed to be 0.2 and 0.9, respectively. Figure 4.26 shows the optimal charging/discharging scheduling in scenario 1.

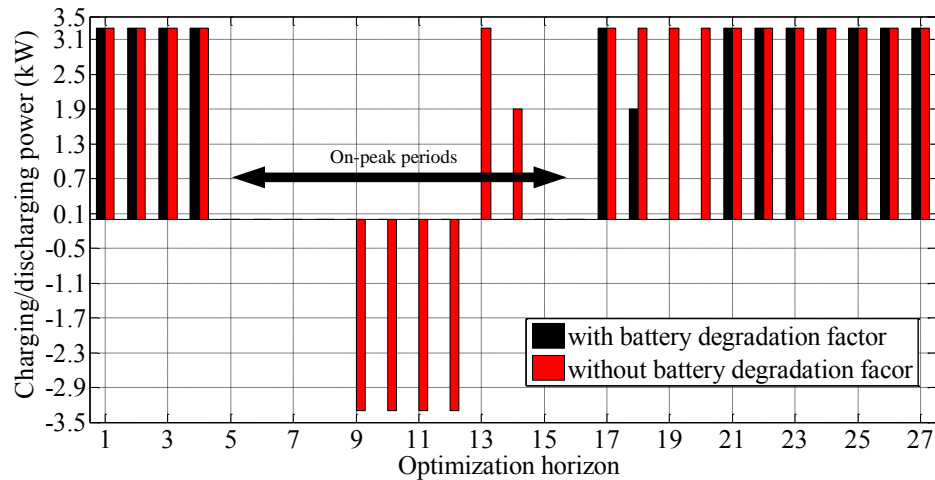


Figure 4.26: Optimal scheduled charging/discharging activities in scenario 1.

To highlight the impact of battery degradation factor on the operation of EV, we have included the optimal scheduling results with and without the battery degradation factor in Figure 4.26, with black and red bars, respectively. Since the battery degradation cost is higher than price of electricity, no discharging activity has been scheduled in the optimization horizon, when we consider the battery degradation factor. Also it can be seen that the charging activities are scheduled during off-peak periods. However, ignoring the battery degradation factor results in scheduling of discharging activities during on-peak periods, when the price is high.

For any time interval in which the scheduled charging/discharging power is zero, the entire range of reactive power service, from 0 to \bar{s} for absorption and from 0 to \bar{q} for injection, can be provided by the EV with zero marginal cost.

Let us consider $k=4$ as current time interval, when $p_4^*=3.3$ kW, accordingly $q_4^+=q_4^-=0$, and the receding horizon includes intervals 2, 3, ..., and 27. First we perform our analysis for the case in which the battery degradation factor is considered. In this case, $R = \{5, 6, 7, \dots, 15, 16, 18, 19, 20\}$, $R' = \{\emptyset\}$, and $R'' = \{17, 21, \dots, 27\}$. $\overline{\Delta p_4}$ is equal to 3.3 kW and Figure 4.27 shows the ranked reschedulable active power in $r \in R$, starting from the lowest marginal cost MC_r , in the set R of the receding horizon to accommodate $\overline{\Delta p_4}$.

Now, considering the marginal cost of decreasing charging power at current time interval, MC_4 , equal to $\text{¢}12.99/\text{kW}$, the total marginal cost of rescheduling active power, MC_4^{total} , can be calculated using Table 4.4. Using equation (4.34), the marginal cost of providing reactive power service during current time interval $k=4$, MCR_4 , is calculated and is shown in Figure 4.28. Note that positive and negative value for reactive power in the figure represent absorption (red solid line) and injection (blue solid line), respectively.

One can observe that the marginal cost of reactive power service during $k=4$, an

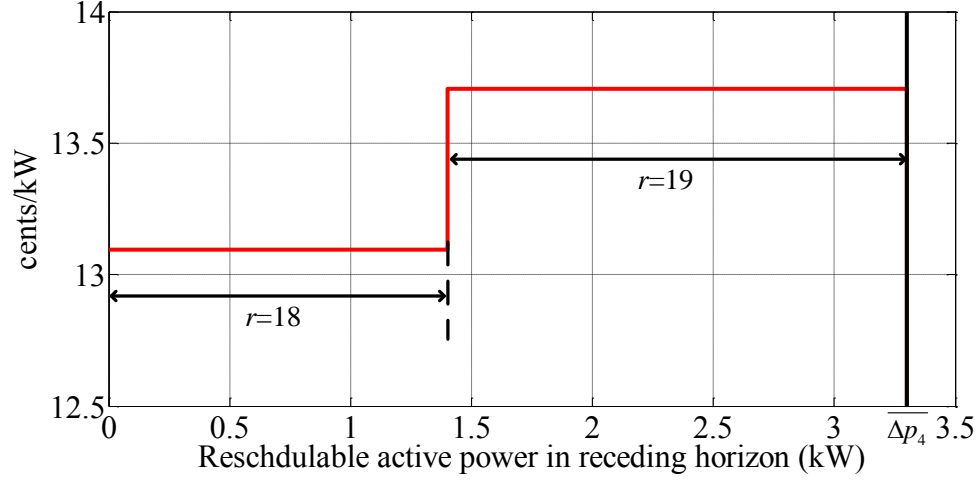


Figure 4.27: Reschedulable active power in receding horizon of time interval $k=4$, in scenario 1 considering the battery degradation factor.

off-peak period, comparing to those time intervals during on-peak periods in which the entire range of reactive power service can be provided by zero marginal cost, is relatively high.

During time interval $k=18$, when $p_{18}^*=1.9$ kW, accordingly $q_{18}^+=2.62$ kVAr and $q_{18}^-=-2.56$ kVAr, $\overline{\Delta p_{18}}=1.9$ kW, and the receding horizon includes intervals 19, 20, \dots , and 27. Therefore any reactive power service in the range $-2.56 \leq q_{18} \leq 2.62$, which does not perturb p_{18}^* , can be provided with zero marginal cost. In the receding horizon we find $R = \{19, 20\}$, $R' = \{\emptyset\}$, and $R'' = \{21, 22, \dots, 27\}$. Any perturbation in p_{18}^* , due to reactive power service, can be rescheduled during time interval $r=19$. Since $MC_{18}=\zeta-13.09/\text{kW}$ and $MC_{19}=\zeta+13.09/\text{kW}$, the total marginal cost, MC_{18}^{total} , is equal to zero. Therefore, any reactive power service above q_{18}^+ and below q_{18}^- can be provided with zero marginal cost. That will result in a reactive power supply function with zero marginal cost for the entire range of reactive power service, $-\bar{q} \leq q_{18} \leq \bar{s}$. It should be noted that for any time interval $k=21, 22, \dots, 27$, since in their receding horizon $R = R' = \{\emptyset\}$, the EV will not be able to provide any reactive power service.

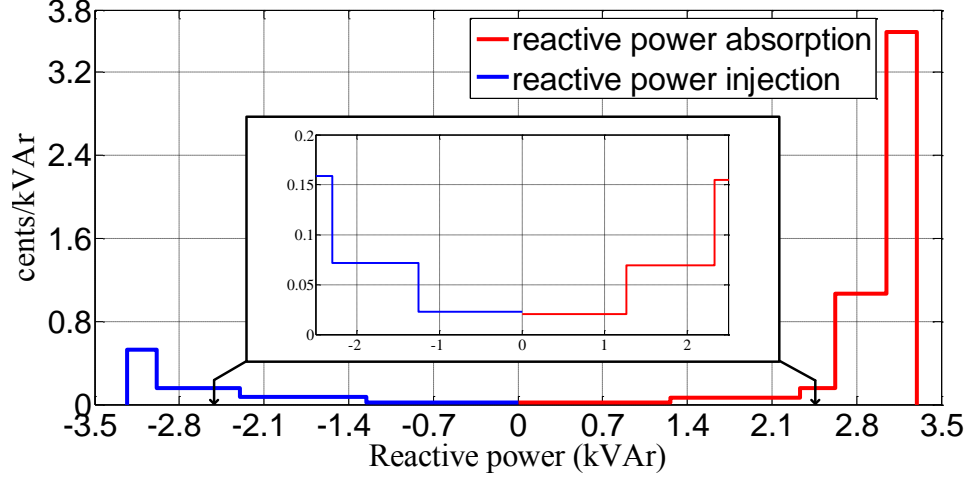


Figure 4.28: Reactive power supply function during time interval $k=4$ in scenario 1 considering the battery degradation factor.

Now we repeat our analysis neglecting the battery degradation cost. Considering $k=4$ as current time interval, when $p_4^*=3.3$ kW, $q_4^+=q_4^-=0$, and $\overline{\Delta p_4}=3.3$ kW. In the receding horizon $R = \{5, 6, 7, 8\}$, $R' = \{9, 10, 11, 12\}$, and $R'' = \{13, 14, \dots, 27\}$. Note that since R' is not empty in this case, the rescheduling procedure starts with the first time intervals of set R' , which is $r=9$. Since $\overline{\Delta p_4}$ can be accommodated in time interval 9, therefore the rescheduling procedure can be done in this time interval. Considering $MC_4=\zeta-1.26/\text{kW}$ and $MC_9=\zeta 1.6/\text{kW}$, the total marginal cost, MC_4^{total} , is equal to $\zeta 0.34/\text{kW}$. Using equation (4.34), the marginal cost of providing reactive power service during current time interval $k=4$, MCR_4 , is calculated and is shown in Figure 4.29.

Now consider $k=9$ as current time interval, when $p_9^*=-3.3$ kW (discharging), $q_9^+=q_9^-=0$, and $\overline{\Delta p_9}=3.3$ kW. In the receding horizon $R=\{13, 14, 17\}$, $R'=\{18, 19, \dots, 27\}$, and $R''=\{10, 11, 12, 15, 17\}$. The rescheduling procedure starts with the first time intervals of set R' , which is $r=18$. $\overline{\Delta p_9}$ can be accommodated in time interval 18, therefore the rescheduling procedure can be done in this time interval.

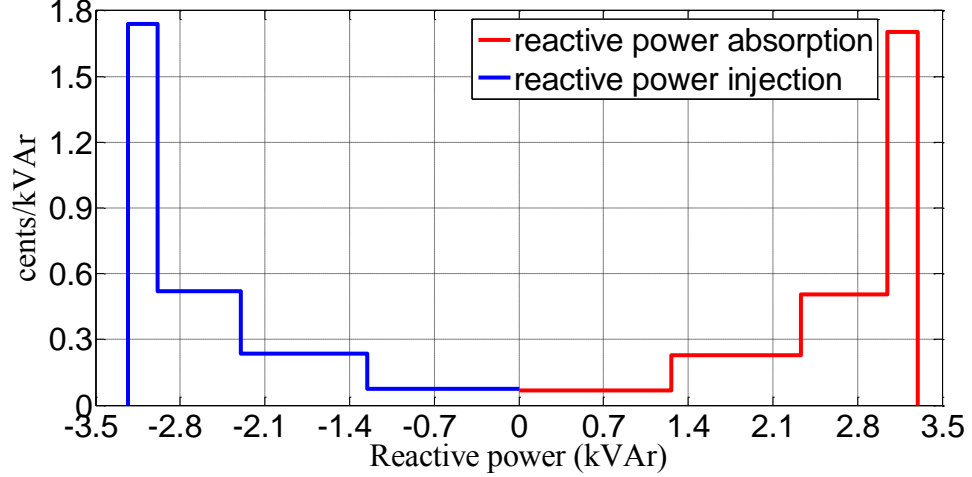


Figure 4.29: Reactive power supply function during time interval $k=4$ in scenario 1 neglecting the battery degradation factor.

Considering $MC_9 = \text{¢}1.6/\text{kW}$ and $MC_{18} = \text{¢}-1.36/\text{kW}$, the total marginal cost, MC_9^{total} , is equal to $\text{¢}0.24/\text{kW}$. Using equation (4.34), the marginal cost of providing reactive power service during current time interval $k=9$, MCR_9 , is calculated and is shown in Figure 4.30.

For any time interval $k=17, 18, \dots, 27$, since in their receding horizon $R = R' = \{\emptyset\}$, the EV will not be able to provide any reactive power service.

4.7.2.2 Scenario 2

In the second scenario, we have considered a fleet of 1000 EVs under one aggregator control. Table 5.9 summarizes the specification of EVs. The minimum and maximum SOC of all EVs are assumed to be 0.2 and 0.9 respectively.

To generate 1000 usage patterns for EVs, we have used a normal distribution function as described in Chapter 3. Table 4.9 presents the information used for EV usage pattern generation. Notice that the data in Table 4.9 represents day time when EVs are parked and connected to the system.

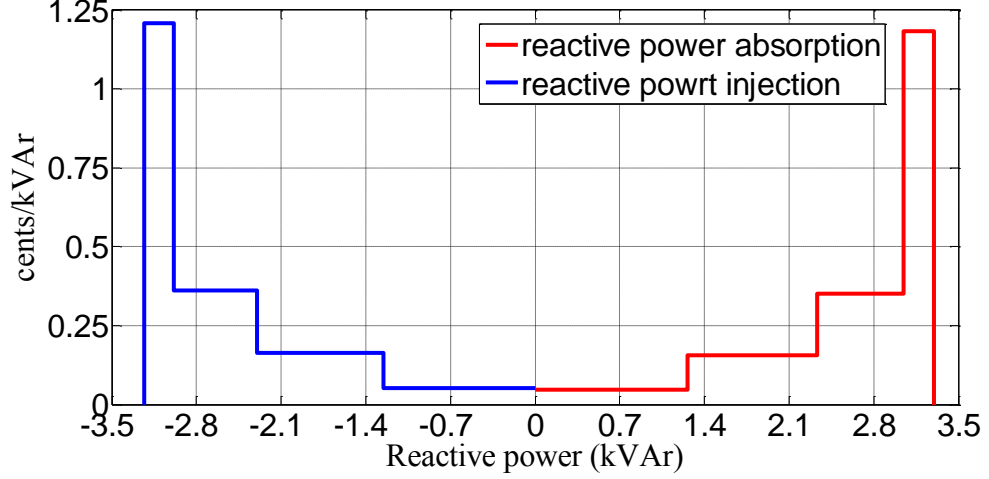


Figure 4.30: Reactive power supply function during time interval $k=9$ in scenario 1 neglecting the battery degradation factor.

Table 4.8: EVs specifications.

EV	no.	battery capacity (kWh)	\bar{s} (kVA)	\bar{q} (kVAr)	γ ($\text{¢}/\text{kWh}$)
Chevrolet Volt	300	16.5	3.3	3.23	45.25
Nissan LEAF	300	24	6.6	6.33	45.86
Mitsubishi i-MiEV	400	16	3.3	3.23	46.94

Considering the simulation settings in Table 4.9, EVs will be connected from 7 a.m. to 6 p.m. and our focus will be on this time window. Therefore the optimization horizon in second scenario includes 45 time intervals. Figure 4.31 shows the optimal aggregated charging/discharging scheduling in scenario 1. Since the battery degradation cost is higher than price of discharging power back to the grid, no discharging activities have been scheduled. As can be seen in the figure, most of the charging activities are scheduled during off-peak periods.

During on-peak periods, when scheduled active power flow rates are zero, the

Table 4.9: Normal Distribution Function Settings for EV's Usage Patterns.

Mean of arrival time	9 a.m.
Mean of departure time	4 p.m.
Std. deviation of arrival time	2 hours
Std. deviation of departure time	2 hours
Mean of traveled distance	40.3 miles
Std. deviation of traveled distance	6.2 miles

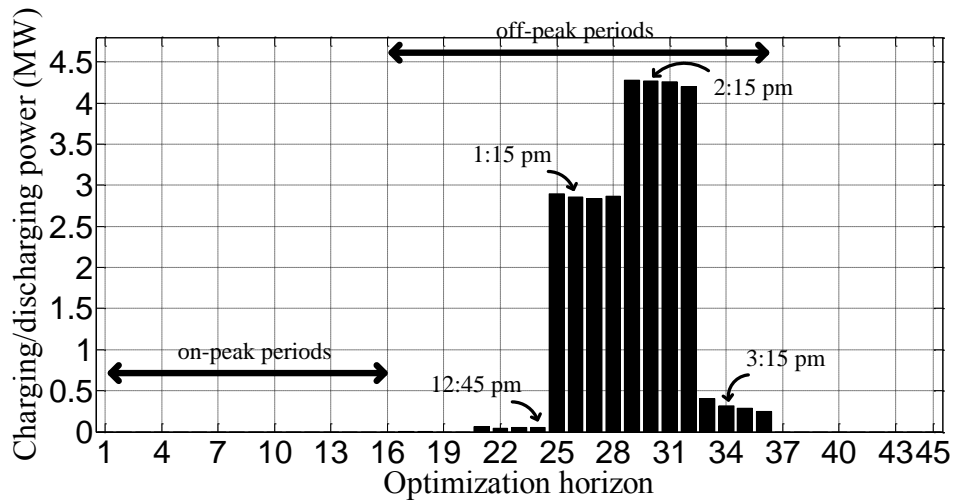


Figure 4.31: Optimal aggregated scheduled charging/discharging activities in scenario 2.

entire range of reactive power service can be offered with zero marginal cost. For example, during time interval $k=16$ (10 a.m.), any reactive power absorption from 0 to 4.29 MVar, and any reactive power injection from 0 to 4.16 MVar can be provided with zero marginal cost. For the sake of demonstration, we have picked four time intervals to show the reactive power supply function of the aggregator, $k=24$ (12:45 p.m.), $k=26$ (1:15 p.m.), $k=30$ (2:15 p.m.), and $k=34$ (3:15 p.m.).

Fig 4.32 to Fig 4.35 shows the reactive power supply function during those time intervals. From figures, once can observe that during off-peak periods when most

of charging activities are scheduled, the aggregator still has significant capacity to provide reactive power service. Also it is clear that a vast range of the capacity for reactive power service can be offered with a marginal cost lower than $\text{¢}0.1/\text{kVAr}$.

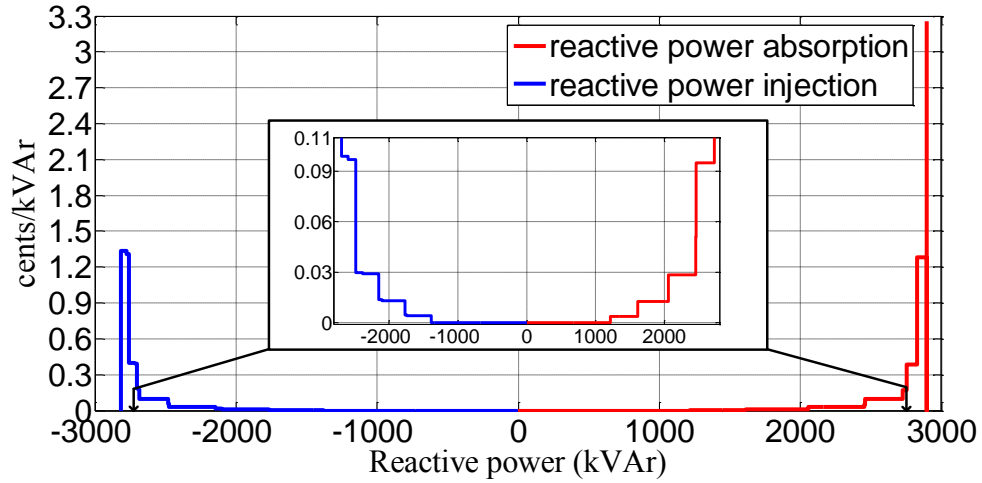


Figure 4.32: Reactive power supply function of the aggregator during time interval $k=24$ in scenario 2.

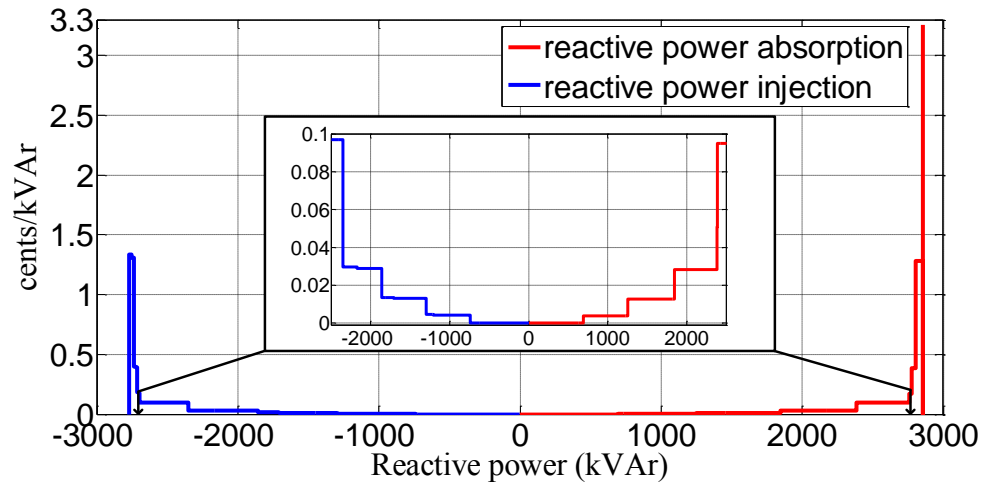


Figure 4.33: Reactive power supply function of the aggregator during time interval $k=26$ in scenario 2.

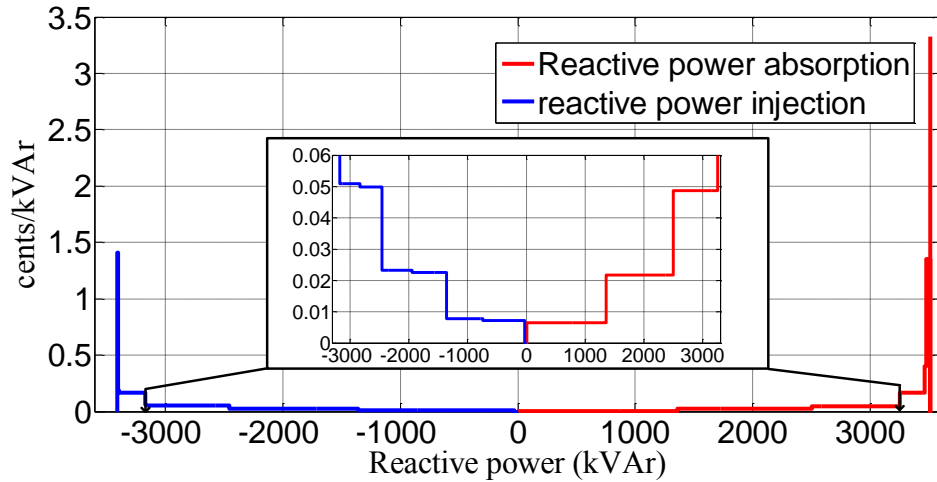


Figure 4.34: Reactive power supply function of the aggregator during time interval $k=30$ in scenario 2.

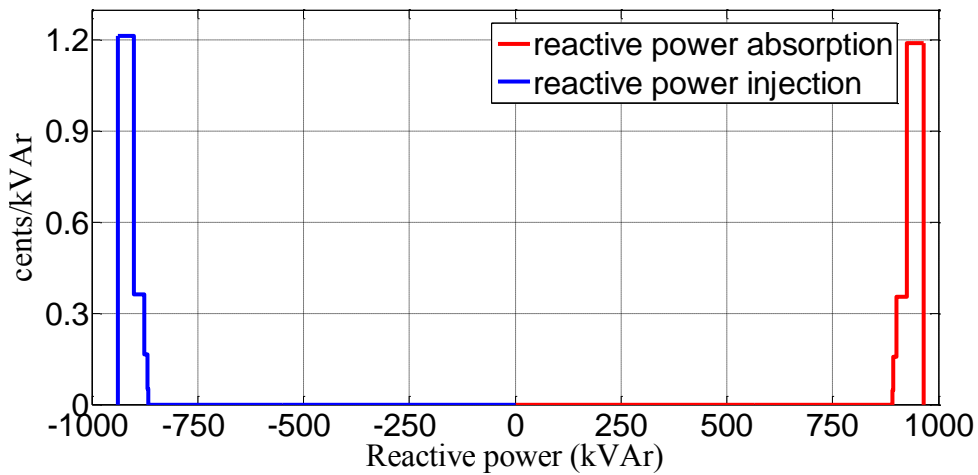


Figure 4.35: Reactive power supply function of the aggregator during time interval $k=34$ in scenario 2.

In scenario 2, similar to scenario 1, during on-peak periods, the entire range of reactive power service can be offered with zero marginal cost. In this case, the range of reactive power service offered by the aggregator, during on-peak periods, is up to 4.29 MVar for absorption and 4.16 MVar for injection. Since the need for reactive power service is most likely high during on-peak periods, providing reactive power

service by aggregated EVs would be a win-win situation for the aggregator and SO. The aggregator can have a revenue stream while no charging activities are scheduled, and SO can use this low-cost reactive power service to improve the power system operation.

4.8 Conclusion

Since reactive power support from an EV could be provided in a short response time and has very little, if any, affect on the vehicle's battery, it becomes a high promise for ancillary service. In this chapter, we presented a novel structure to calculate optimal conditions for active/reactive power service by the EV while minimizing the total operating cost for the EV owner. After estimating optimal operating points of an EV, we have developed an algorithm to calculate the reactive power supply function of the EV on a real-time basis. The calculated supply function is in step-wise ascending order. Results indicate the EV's capability to provide reactive power service, especially during on-peak periods, with low marginal cost. Since the need for reactive power service is most likely high during on-peak periods, providing reactive power service by aggregated EVs could be a win-win situation for both, the aggregator and SO. As shown, the developed methodology for calculating operating cost as well as reactive power supply function can be easily applied to a large group of EVs.

Chapter 5

Frequency Regulation Service from EVs

5.1 Introduction

Climate Change 2014 Synthesis Report suggests renewables will have to grow from their current 30% share to 80% of the power sector by 2050. In the longer term, the report states that fossil fuel power generation without carbon capture and storage technology would need to be phased out almost entirely by 2100 [78]. For wider adoption, intermittent nature of renewable sources needs to be overcome first.

According to reference [79], the highest value ancillary service for EVs is frequency regulation. Frequency regulation is the use of on-line generation, storage, or load that is equipped with AGC and that can change output quickly (MW/min) to track the moment-to-moment fluctuations in customer loads and to correct for the unintended fluctuations in generation [80].

According to reference [81], as the penetration of renewable energy sources in the system increases, frequency regulation requirements as well as need for faster ramping

resources will increase. This need has been recognized by FERC. On October 20, 2011, FERC issued a final ruling establishing a two-component market-based compensation scheme (capacity payment and performance-based payment) for providing frequency regulation service [82]. Considering rapid response and large instantaneous power, EVs can provide a fast response when the mismatch between load and generation is large and happens in short duration [83].

Various DR strategies for ancillary services by EVs have been reported in literature [84]- [87]. But so far no framework has been developed which could be easily implemented, scalable for large number of EVs, and fulfill FERC order 755. In this chapter, we present a systematic three-level optimization framework, from aggregator's prospective, to estimate the optimal operating conditions of EVs for frequency regulation service. The framework schedules EVs for charging/discharging activities with minimum cost, calculates bidding components (capacity and associated cost function) for frequency regulation service, and assigns each connected EVs, optimally, to provide the service.

The main contribution of the research in this chapter is summarized as follows:

1. Evaluating the EV's capability to provide frequency regulation service.
2. Developing a framework to estimate the supply function of the service provided by EV, complying with FERC Order 755.
3. Calculation of the service cost function in step-wise ascending order.
4. Developing a multi-level optimization approach, from aggregator's stand point, to engage a large group of EVs in the frequency regulation market.

5.2 Frequency Regulation: A Review

Frequency regulation, sometimes referred to as secondary frequency control, is a required ancillary service for which participating generation capacity follows the power commands from the SO [93]. The regulation power command is referred as AGC signal which is used to regulate grid frequency and maintain scheduled power exchanges between control areas [94]. This signal is usually updated every 2-10 seconds and indicates the new requested power output of participating generators, whether the power setpoint should be raised or lowered [80]. A common name for secondary frequency regulation in the seven U.S. electric energy regions managed by Independent System Operators (ISOs) or Regional Transmission Organizations (RTOs) is “regulation”, or “regulation-up” and “regulation-down”. While secondary frequency control can serve to restore frequency following a contingency or the loss of a large block of load, it cannot serve to limit the magnitude of the initial frequency swing following such an event [94].

In general, frequency regulation is performed by a subset of various power plants which have the capability to respond to an AGC signal, by dedicating a small portion of their power capacity to AGC [95]. A comprehensive literature survey of research on AGC is presented in reference [96]. Research in AGC covers different areas, such as determination of the area control error (ACE) [97], methods of calculating the frequency bias factor in frequency control [98], and effects of the intermittent renewable generations on AGC [99]– [101]. Optimal allocation of AGC signal to each participating generator is another critical aspect of AGC, since it can minimize the cost and improve the quality of frequency regulation service.

After the advent of deregulation, there has been much effort to form competitive markets for frequency regulation. These markets are usually for capacity reserves

and have been called regulation, balancing, load-following, frequency control or even combined with spinning reserve markets [102]. Figure 5.1 sectionizes operation of power system in different operational phases. In phase 1, based on the day-ahead load forecast, committed generators are selected using unit commitment process. An hourly-based economic dispatch is run in phase 2 to dispatch committed generators optimally, based on an objective function. In phase 3, the match between load and generation is achieved applying AGC, to minimize ACE.

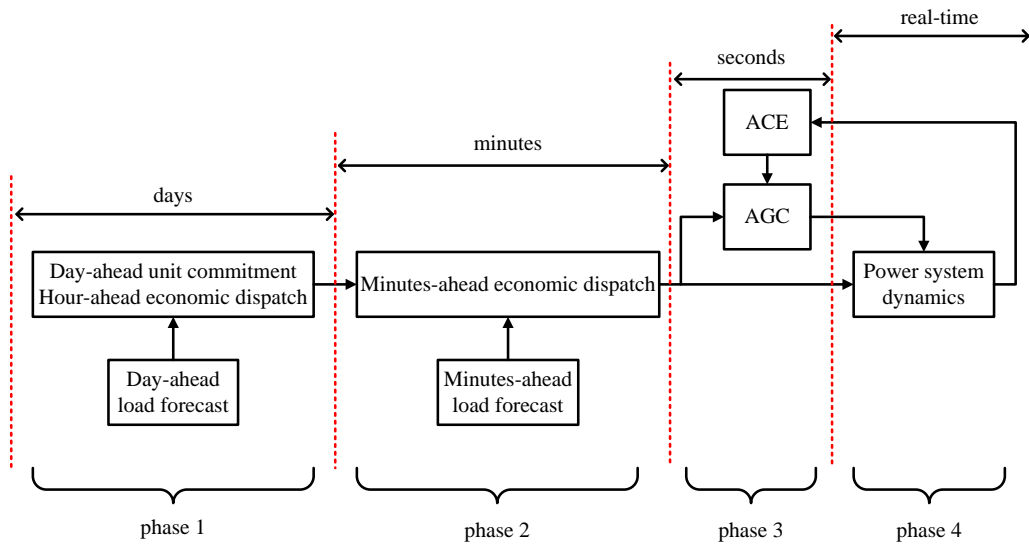


Figure 5.1: Sequential phases in power system operation.

Procurement of regulation service can be done through a market mechanism. A comprehensive survey of regulation market in the U.S. can be found in reference [103]. Based on the survey, four factors complicate understanding of the business practice manuals (BPMs) of ISOs/RTOs: “First, the business practices in question are extremely complex, covering the operations of multiple interconnected markets operating at multiple time scales. Second, the BPMs are lengthy documents written in highly legalistic language, which hinders their readability. Third, the BPMs are

continually being updated to include changes in rules of operation. Fourth, with one exception (Midwest ISO), the ISOs/RTOs do not include in their BPMs the precise forms of the optimization problems (objective functions plus constraints) that are used to determine their price, commitment, and dispatch solutions for energy and reserve.” Therefore, in this chapter, we consider the framework presented in reference [104], to allocate AGC signal optimally among participants in the regulation market. Figure 5.2 summarizes the framework, in which the SO receives the ACE. Then considering the available committed generator and regulation service provider’s bids, the SO assigns the AGC signal optimally, to minimize service cost and ACE. The formulation of optimal allocation of AGC signal was presented in references [104]– [105] and is out of the scope of this dissertation.

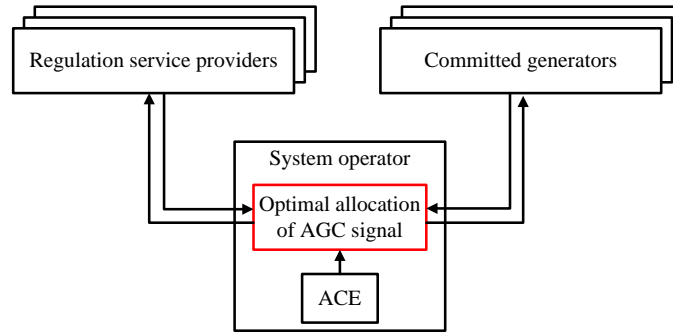


Figure 5.2: Schematic of optimal allocation of AGC signal.

Considering the characteristics of energy storage systems, high power and low energy, they are a suitable candidate satisfying FERC 755 requirements. The rapidly controllable power from energy storage devices can be valuable for frequency regulation, as discussed in reference [106]. Since EVs are equipped with battery and the charging flow rate of EVs can be controlled continuously, they can be considered as distributed energy storage units when vehicle-to-grid is available [107]. Involving

EVs in AGC has been studied in references [108] and [109]. However, evaluation of economic value and estimation of the bidding functions for regulation service by EVs, in a systematic way, is missing in the literature.

In order to estimate the supply function of the service, we first study the capability of an EV in provision of frequency regulation.

5.3 EV's Capability for Regulation Service

An EV can participate in regulation up service by decreasing its scheduled charging demand or increasing its discharging power. The regulation down service can also be provided from the EV by increasing its charging demand or decreasing its discharging power. Assuming p_k^* to be the optimal operating point of EV in time step k , Figure 5.3 demonstrates the frequency regulation service that needs to be provided by the EV to fulfil the service requirement.

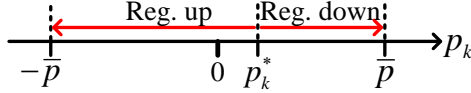


Figure 5.3: Frequency regulation service from EV in time step k .

Provision of regulation service results in changing the scheduled active power flow rate. The change in scheduled active power flow rate, which is the solution of pre-defined optimization problem in Chapter 3, is termed as perturbation in the optimal solution. This perturbation may increase the operation cost of the EV. Let us consider time interval k as current time period. Any regulation service during time interval k results in perturbation of active power flow rate by Δp_k . In order to satisfy constraint (3.18), any change in active power flow rate at current time period k must

be reschedulable during the remainder of its parking time, termed as receding horizon in our calculation. Therefore Δp_k is limited by maximum reschedulable active power flow rate in the receding horizon. Let us assume that the change in active power flow rate at the current time period, k , is rescheduled during a time period r of the receding horizon. In the following subsection, perturbations caused by regulation services and associated costs are discussed.

5.3.1 Perturbation in Optimal Solutions due to Regulation-Up Service

Any decrement in charging power, when $p_k^* \geq 0$, or increment in discharging power, when $p_k^* < 0$, to provide regulation-up service during time interval k , is rescheduled in the receding horizon. Table 5.1 summarizes changes in operation cost of the EV during current time period k and rescheduling time period r .

Table 5.1: Change in Operation Cost of EV due to Provision of Regulation-Up Service.

p_k^*	p_r^*	Δf_k^c	Δf_r^c
$p_k^* \geq 0$	$p_r^* \geq 0$	$-\tau(\frac{\rho_k}{\eta} + \gamma)\Delta p_k$	$\tau(\frac{\rho_r}{\eta} + \gamma)\Delta p_k$
$p_k^* \geq 0$	$p_r^* < 0$	$-\tau(\frac{\rho_k}{\eta} + \gamma)\Delta p_k$	$\tau(\eta\lambda_r^p - \gamma)\Delta p_k$
$p_k^* < 0$	$p_r^* \geq 0$	$-\tau(\eta\lambda_k^p - \gamma)\Delta p_k$	$\tau(\frac{\rho_r}{\eta} + \gamma)\Delta p_k$
$p_k^* < 0$	$p_r^* < 0$	$-\tau(\eta\lambda_k^p - \gamma)\Delta p_k$	$\tau(\eta\lambda_r^p - \gamma)\Delta p_k$

The marginal cost due to a deviation of Δp_k from optimal solutions, p_k^* and p_r^* , can be calculated by differentiating equations in third and fourth column of Table 5.1 with respect to Δp_k . Table 5.2 lists the marginal cost, MC_k , for deviation form p_k^* , and the marginal cost, MC_r , for deviation form p_r^* all in \$/kWh.

Table 5.2: Marginal Cost of Deviation Caused by Δp_k During Regulation Up Service (\$/kW).

p_k^*	p_r^*	MC_k	MC_r
$p_k^* \geq 0$	$p_r^* \geq 0$	$-\tau(\frac{\rho_k}{\eta} + \gamma)$	$\tau(\frac{\rho_r}{\eta} + \gamma)$
$p_k^* \geq 0$	$p_r^* < 0$	$-\tau(\frac{\rho_k}{\eta} + \gamma)$	$\tau(\eta\lambda_r^p - \gamma)$
$p_k^* < 0$	$p_r^* \geq 0$	$-\tau(\eta\lambda_k^p - \gamma)$	$\tau(\frac{\rho_r}{\eta} + \gamma)$
$p_k^* < 0$	$p_r^* < 0$	$-\tau(\eta\lambda_k^p - \gamma)$	$\tau(\eta\lambda_r^p - \gamma)$

5.3.2 Perturbation in Optimal Solutions due to Regulation-Down Service

Any increment in charging power, when $p_k^* \geq 0$, or decrement in discharging power, when $p_k^* < 0$, to provide regulation-down service during time interval k , is rescheduled in the receding horizon. Table 5.3 summarizes changes in operation cost of the EV during current time period k and rescheduling time period r .

Table 5.3: Change in Operation Cost of EV due to Provision of Regulation-Down Service.

p_k^*	p_r^*	Δf_k^c	Δf_r^c
$p_k^* \geq 0$	$p_r^* \geq 0$	$\tau(\frac{\rho_k}{\eta} + \gamma)\Delta p_k$	$-\tau(\frac{\rho_r}{\eta} + \gamma)\Delta p_k$
$p_k^* \geq 0$	$p_r^* < 0$	$\tau(\frac{\rho_k}{\eta} + \gamma)\Delta p_k$	$-\tau(\eta\lambda_r^p - \gamma)\Delta p_k$
$p_k^* < 0$	$p_r^* \geq 0$	$\tau(\eta\lambda_k^p - \gamma)\Delta p_k$	$-\tau(\frac{\rho_r}{\eta} + \gamma)\Delta p_k$
$p_k^* < 0$	$p_r^* < 0$	$\tau(\eta\lambda_k^p - \gamma)\Delta p_k$	$-\tau(\eta\lambda_r^p - \gamma)\Delta p_k$

The marginal cost due to a deviation of Δp_k from optimal solutions, p_k^* and p_r^* , can be calculated by differentiating equations in third and fourth column of Table 5.3 with respect to Δp_k . Table 5.4 lists the marginal cost, MC_k , for deviation from p_k^* , and the marginal cost, MC_r , for deviation from p_r^* , all in \$/kWh.

The total marginal cost, MC_k^{total} , for deviation from optimal solutions (due to

Table 5.4: Marginal Cost of Deviation Caused by Δp_k During Regulation Down Service (\$/kW).

p_k^*	p_r^*	MC_k	MC_r
$p_k^* \geq 0$	$p_r^* \geq 0$	$\tau(\frac{\rho_k}{\eta} + \gamma)$	$-\tau(\frac{\rho_r}{\eta} + \gamma)$
$p_k^* \geq 0$	$p_r^* < 0$	$\tau(\frac{\rho_k}{\eta} + \gamma)$	$-\tau(\eta\lambda_r^p - \gamma)$
$p_k^* < 0$	$p_r^* \geq 0$	$\tau(\eta\lambda_k^p - \gamma)$	$-\tau(\frac{\rho_r}{\eta} + \gamma)$
$p_k^* < 0$	$p_r^* < 0$	$\tau(\eta\lambda_k^p - \gamma)$	$-\tau(\eta\lambda_r^p - \gamma)$

provision of regulation-up/down service) can be calculated as follows:

$$MC_k^{total} = MC_k + MC_r. \quad (5.1)$$

Therefore, based on the optimal scheduled active power flow rate at time period k , p_k^* , and the rescheduling time period r in the receding horizon, the marginal cost for providing regulation services can be calculated using Table 5.2 and 5.4 and equation (5.1). In the following section, we provide a framework to find minimum marginal cost and calculate the bidding components for the EV to participate in the regulation market.

5.4 Bidding Strategy for Single EV

The bid from the EV must contain the offered capacity of power (kW) for the regulation service along with an energy cost function [82]. In this section we present a framework to calculate the optimal bidding components for a single EV. The first step in the development of the framework is to calculate optimal scheduled active power flow rates, while minimizing the charging/discharging cost and providing desired SOC at the departure time. This effort provides information of the optimal scheduled ac-

tive power flow rate, p_k^* , and scheduled SOC of the EV battery, x_k^* , for $k= 1, 2, \dots, T$. Then during each time period k , the bidding components are calculated.

We define Δp_k , the deviation in the active power from its scheduled value and Δx_k , the deviation in the SOC of the battery from its scheduled value, x_k^* , as a result of change in active power activity. We define x_r^* as the scheduled SOC of the battery at time interval r of the receding horizon. We also use superscripts \uparrow for deviation in increase mode and \downarrow for deviation in decrease mode.

In order to meet constraint (3.20), Δx_k is limited to Δx_k^\uparrow and Δx_k^\downarrow . Table 5.5 lists the reschedulable SOC, during time interval k , for increasing and decreasing modes.

Table 5.5: Reschedulable deviation in the SOC of the battery.

p_k^*	Δx_k^\uparrow	Δx_k^\downarrow
$p_k^* \geq 0$	$\min \{ \bar{x} - x_k^*, (\bar{p} - p_k^*) \frac{\tau}{u} \}$	$\min \{ x_k^* - \underline{x}, (\underline{p} + p_k^*) \frac{\tau}{u} \}$
$p_k^* < 0$	$\min \{ \bar{x} - x_k^*, (p_k^* + \bar{p}) \frac{\tau}{u} \}$	$\min \{ x_k^* - \underline{x}, (\underline{p} - p_k^*) \frac{\tau}{u} \}$

Therefore, reschedulable active power flow rate in each time interval, is limited to the reschedulable SOC of the battery during the corresponding time interval. We consider time interval k as the current time interval, and r representing a time interval of the receding horizon. During time interval r of the receding horizon, we define $p_r^{+\uparrow}$ as available charging power increment, $p_r^{+\downarrow}$ as available charging power decrement, $p_r^{-\uparrow}$ as available discharging power increment, $p_r^{-\downarrow}$ as available discharging power decrement. Figure 5.4 shows an example of optimal scheduled charging/discharging power activities. Red bars in the figure indicates the scheduled active power flow rate at each time period $(p_k^*, p_{k+1}^*, \dots, p_T^*)$. Note that positive and negative values for active power flow rates represent charging and discharging activities, respectively. Also $p_r^{+\uparrow}$, $p_r^{+\downarrow}$, $p_r^{-\uparrow}$, and $p_r^{-\downarrow}$ are shown by yellow, green, blue, and purple arrows in

the figure, respectively.

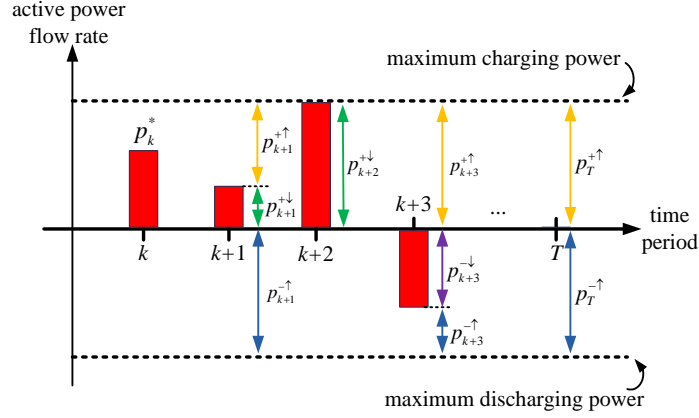


Figure 5.4: Reschedulable active power flow rate at current time period k and during receding horizon.

Considering Figure 5.4, Table 5.6 can be developed to calculate the reschedulable power during time interval r of the receding horizon.

Table 5.6: Reschedulable power during time interval r of receding horizon.

p_r^*	$p_r^{+\uparrow}$	$p_r^{+\downarrow}$	$p_r^{-\uparrow}$	$p_r^{-\downarrow}$
$p_r^* > 0$	$\frac{\Delta x_r^+ u}{\tau}$	$\frac{\Delta x_r^- u}{\tau}$	0	0
$p_r^* < 0$	0	0	$\frac{\Delta x_r^- u}{\tau}$	$\frac{\Delta x_r^+ u}{\tau}$
$p_r^* = 0$	$\frac{\Delta x_r^+ u}{\tau}$	0	$\frac{\Delta x_r^- u}{\tau}$	0

Deviation in p_k^* and consequently in x_k^* , will depend on the type of service (regulation-up/regulation-down). We define three subsets in the receding horizon, namely set of reschedulable time intervals R , set of critical time intervals R' , and set of non-schedulable time intervals R'' regulation service. Any $r \in R$ can accommodate any perturbation in current time interval k . Any $r \in R'$ has limited room to accommo-

date perturbation in current time interval k . And finally members of R'' can not accommodate any perturbation in current time interval k . In the following subsections, we present a procedure to establish sets R , R' , and R'' for regulation-up and regulation-down services during time interval k .

5.4.1 Regulation-Up

Perturbation in the scheduled SOC, as the result of regulation-up service, is in decreasing direction (Δx_k^\downarrow). Figure 5.5 shows the flowchart of establishing three pre-defined subsets of the receding horizon.

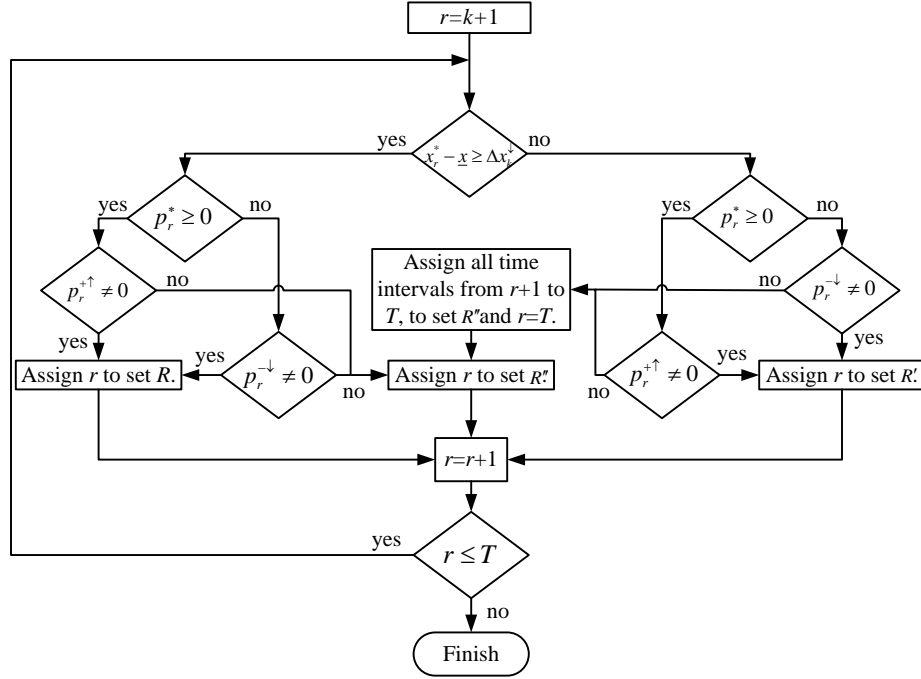


Figure 5.5: Classifying time intervals of the receding horizon for provision of regulation-up service.

The flowchart starts with the first time interval of the receding horizon. This time interval will fall into R , if it can accommodate Δx_k^\downarrow , and $p_r^{+↑} \neq 0$ when $p_r^* \geq 0$ or

$p_r^{-\downarrow} \neq 0$ when $p_r^* < 0$. The time interval will fall into R' if it can not accommodate Δx_k^\downarrow , and $p_r^{+\uparrow} \neq 0$ when $p_r^* \geq 0$ or $p_r^{-\downarrow} \neq 0$ when $p_r^* < 0$. The time interval will fall into R'' otherwise. Note that when the flowchart reaches a time interval of the receding horizon in which $x_r^* - \underline{x} < \Delta x_k^\downarrow$ and $p_r^{+\uparrow} = 0$ if $p_r^* \geq 0$ or $p_r^{-\downarrow} = 0$ if $p_r^* < 0$, the time interval r and the remaining time intervals of the receding horizon will fall into R'' . The reason is that, the deviation in x_k^* will drop x_r^* below the minimum SOC (\underline{x}).

5.4.2 Regulation-Down

Perturbation in the scheduled SOC, as the result of regulation-down service, is in increasing direction (Δx_k^\uparrow). Figure 5.6 shows the flowchart of establishing three pre-defined subsets of the receding horizon.

The flowchart starts with the first time interval of receding horizon. This time interval will fall into R , if it can accommodate Δx_k^\uparrow ($\bar{x} - x_r^* \geq \Delta x_k^\uparrow$), and $p_r^{+\downarrow} \neq 0$ when $p_r^* \geq 0$ or $p_r^{-\uparrow} \neq 0$ when $p_r^* < 0$. The time interval will fall into R' if it can not accommodate Δx_k^\uparrow ($\bar{x} - x_r^* < \Delta x_k^\uparrow$), and $p_r^{+\downarrow} \neq 0$ when $p_r^* \geq 0$ or $p_r^{-\uparrow} \neq 0$ when $p_r^* < 0$. The time interval will fall into R'' otherwise. Similar to previous subsection, when the flowchart reaches a time interval of receding horizon in which $\bar{x} - x_r^* < \Delta x_k^\uparrow$ and $p_r^{+\downarrow} = 0$ if $p_r^* \geq 0$ or $p_r^{-\uparrow} = 0$ if $p_r^* < 0$, the time interval r and the remaining time intervals of the receding horizon will fall into R'' .

Note that members of set R' , the critical time intervals, are arranged based on their occurrence in the receding horizon. For example, $r=10$ has higher priority than $r=15$. It is worth mentioning that, in case of scheduling the EV just for charging or just for discharging, the set R' is empty.

The maximum power available for regulation-up and regulation-down services

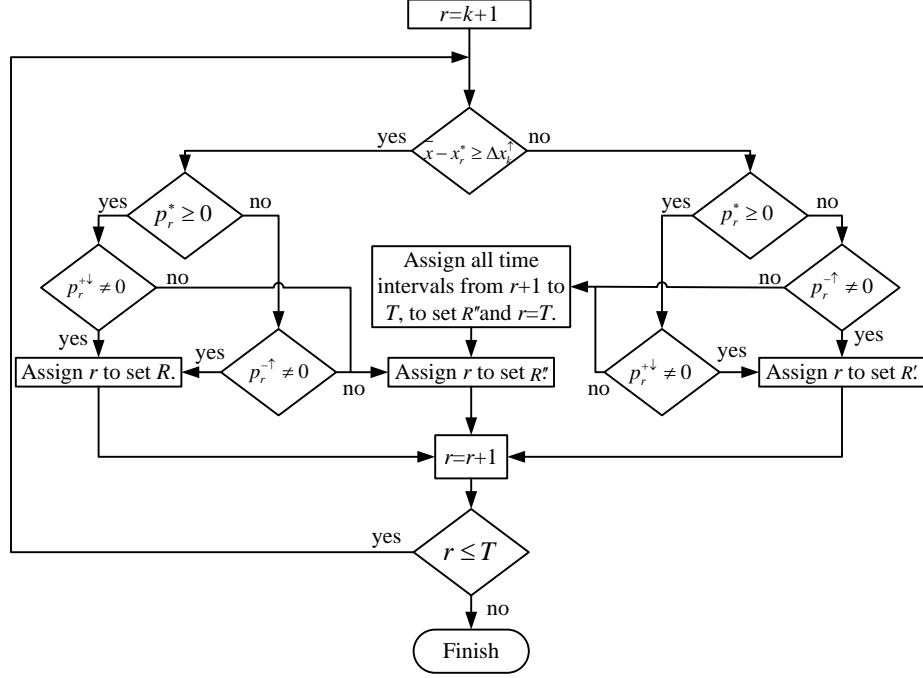


Figure 5.6: Classifying time intervals of the receding horizon for provision of regulation-down service.

during current time interval k , $\overline{\Delta p_k^{up}}$ and $\overline{\Delta p_k^{down}}$ respectively, are calculated using the following equations.

$$\begin{cases} \overline{\Delta p_k^{up}} = \min \left\{ \Delta x_{k\tau}^{\downarrow u}, \sum_{r \in R'} (p_r^{+\uparrow} + p_r^{-\downarrow}) + \sum_{r \in R} (p_r^{+\uparrow} + p_r^{-\downarrow}) \right\}; \\ \overline{\Delta p_k^{down}} = \min \left\{ \Delta x_{k\tau}^{\uparrow u}, \sum_{r \in R'} (p_r^{+\downarrow} + p_r^{-\uparrow}) + \sum_{r \in R} (p_r^{+\downarrow} + p_r^{-\uparrow}) \right\}; \end{cases} \quad (5.2)$$

The marginal cost of perturbation at current time period k , MC_k , and the marginal cost of rescheduling at time period r of receding horizon, MC_r , are presented in Table 5.2 and 5.4. Rescheduling of active power flow rates in the receding horizon must be done in a way so that it leads to minimum total marginal cost, MC_k^{total} . Figure 5.7 and 5.8 present flowcharts to perform the rescheduling task with the goal of minimizing total marginal cost of providing regulation-up and regulation-down service,

respectively. The flowcharts start with arranging $r \in R$, based on its MC_r , from the lowest to the highest. Since critical time intervals have limited rescheduling capacity and also to satisfy constraint (3.20), the rescheduling process starts with critical time intervals $r \in R'$. After rescheduling all critical time intervals, if the maximum power for regulation up/down at current time period is still not met, the process continues with rescheduling charging/discharging power during time intervals $r \in R$. Note that rescheduling during time intervals $r \in R$, starting with the lowest marginal cost, guarantees the minimum total marginal cost.

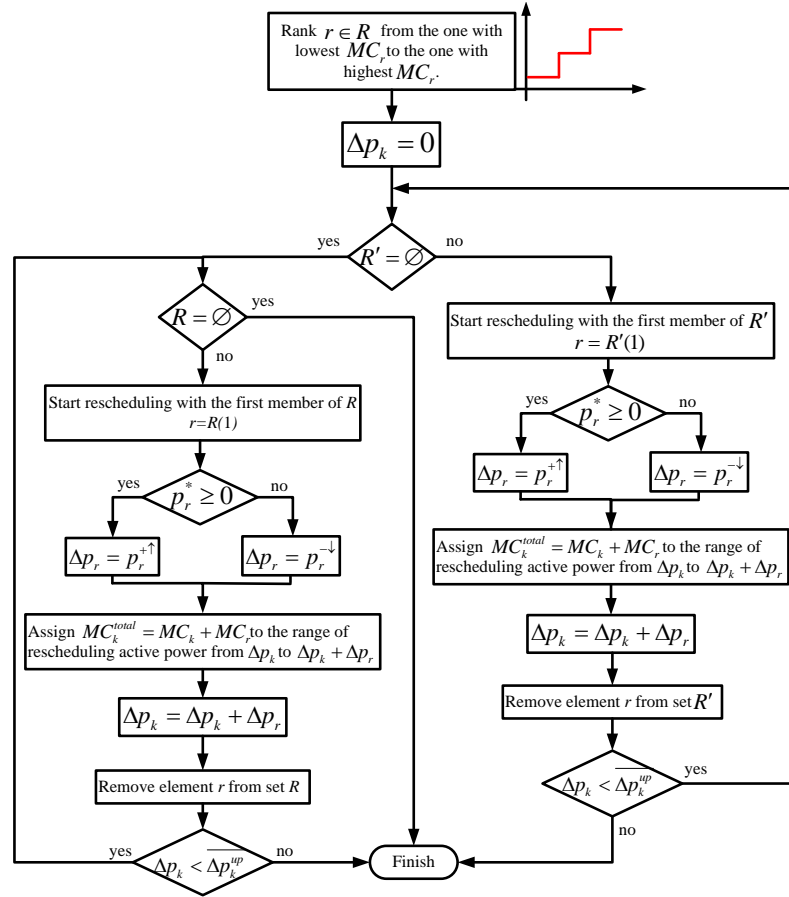


Figure 5.7: Flowchart of rescheduling during the receding horizon for providing regulation-up service.

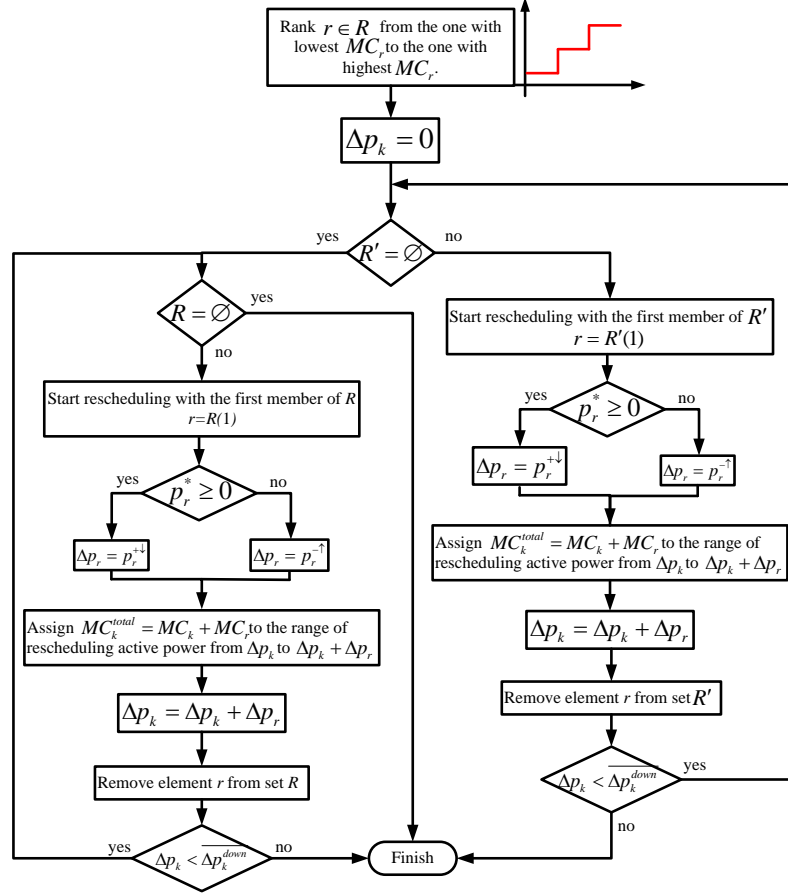


Figure 5.8: Flowchart of rescheduling during the receding horizon for providing regulation-down service.

Notice that the marginal cost assigned for each range of regulation services in Figure 5.7 and 5.8 is the cost of providing the services for that range.

After developing the framework for providing the regulation services from a single EV, we extend the framework to take care of a group of EVs. At this level, an aggregator would be responsible for this task.

5.5 Bidding Strategy for an Aggregator

In this section, we extend the framework for single EV to a group of EVs, from the aggregator's stand point. The aggregator is responsible for the EVs under his/her control. Also EV owners have granted the permission to the aggregator to participate in the regulation market.

The aggregator is responsible to provide required charging energy for each EV in order to provide the desired SOC at the departure time. This task should be accomplished with minimum cost. The aggregator is allowed to submit optimal bid for regulation services. After submitting the bid, if an AGC signal is allocated to the aggregator, he/she must satisfy the signal in an optimized way. To perform aggregator's tasks optimally, we present a framework consists of three hierarchical optimization levels, as displayed in Figure 5.9 and discussed below.

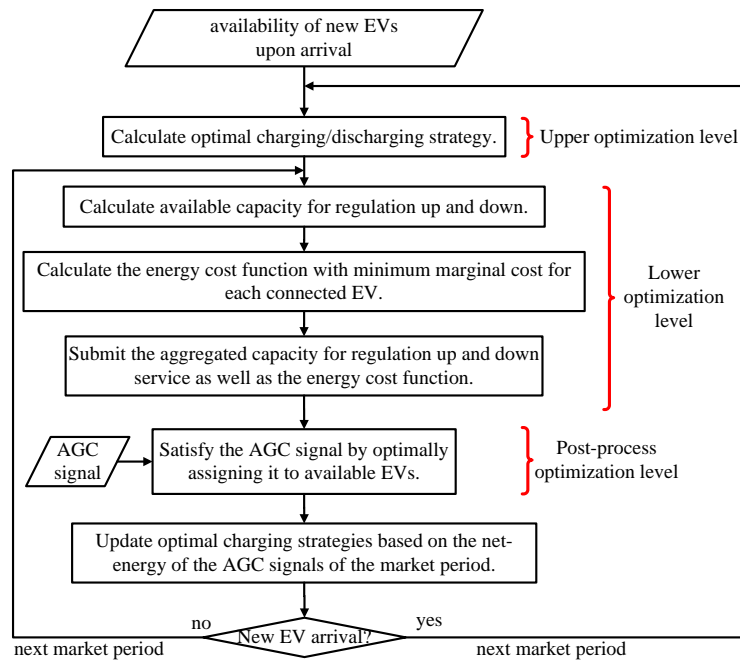


Figure 5.9: Flowchart of the aggregator's bidding strategy calculation for regulation service.

5.5.1 Upper Optimization Level

The aggregator's cost function is defined by the summation of all EV's cost functions, as defined in equation (3.12). The cost function is minimized by solving the linear optimization problem (3.17) for each EV. The optimal active power scheduling is calculated for each connected EV.

5.5.2 Lower Optimization Level

At this level, during each time interval, the available capacity for regulation-up and regulation-down service ($\overline{\Delta p_k^{up}}$ and $\overline{\Delta p_k^{down}}$) is calculated for each connected EV using equation (5.2). Also the cost function of providing services for each connected EV is calculated using flowcharts presented in Figure 5.7 and 5.8. It should be emphasized that the cost function at this level is calculated with minimum marginal cost for providing the service. To build the aggregated cost function, the aggregator must define the regulation service range from the lowest cost to the highest.

5.5.3 Post-process Optimization Level

As shown in Figure 5.10, after receiving the allocated AGC signal from the SO, the aggregator must assign a portion of the signal to each participating EV in order to satisfy the signal. To perform this task in an optimal fashion, the aggregator must provide the service (either regulation-up or regulation-down service), starting with the EV which has the lowest marginal cost, until the AGS signal is met.

Since the optimization problem in upper optimization level is solved using linear programming, the developed multi-level framework can be performed in a real-time fashion efficiently.

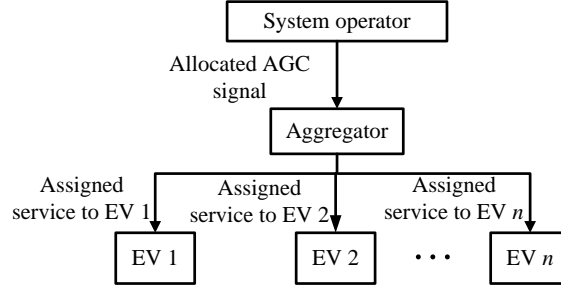


Figure 5.10: Post-process optimization level.

5.6 Numerical Results

We have defined two scenarios for simulations. In the first scenario, we have considered an EV and then expanded the number of EVs to 1000 in the second scenario. We have assumed that all of EVs considered for simulations are under one aggregator control and participating in the regulation service. Energy unit price (\$/kWh) for Lithium-Ion battery is assumed to be \$1500/kWh [50]. The minimum and maximum SOC for all EVs are assumed to be 0.2 and 0.9, respectively. We have used a work day (February 12, 2015) price published by NYISO for Central zone. This price data is the same price data used in simulations of Chapter 4. Since NYISO runs operating reserves and regulation service market over fifteen minute intervals, τ is assumed to be 0.25 hour in the calculation.

5.6.1 Scenario 1

In this scenario, a Mitsubishi i-MiEV with 3.3 kVA charger and a 16 kWh Lithium-Ion battery pack is considered. As explained in Section 4.7, the battery degradation factor γ , in ¢/kWh , is equal to $\text{¢}46.94/\text{kWh}$. The arrival time and departure time are assumed to be 4 p.m. and 11 p.m., respectively, in this scenario. Considering $\tau=0.25$ hour, the optimization horizon includes 27 intervals. The initial and desired

SOC are assumed to be 0.2 and 0.9, respectively. To highlight the impact of battery degradation factor on the operation of EV, we have defined two cases in this scenario: Case 1 in which the battery degradation is consider; and Case 2 in which the battery degradation is ignored.

Optimal charging/discharging scheduling in Scenario 1 is the same as optimal scheduling results in 4.7.2.1. Figure 5.11 repeats the optimal charging/discharging scheduling in this scenario.

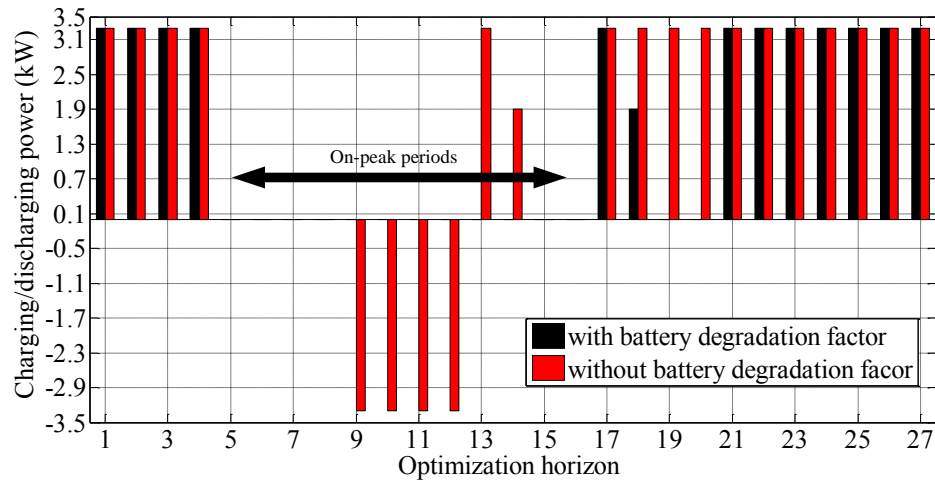


Figure 5.11: Optimal scheduled charging/discharging activities in scenario 1.

We have performed the proposed framework for three time intervals in each case, including $k=4$, $k=9$, and $k=18$ in Case 1 and $k=4$, $k=9$, and $k=14$ in Case 2. Table 5.7 and 5.8 list the three subsets R , R' , and R'' of receding horizons in each case. From tables, one can observe that scheduling discharging activity in Case 2, results in changing the subsets of the receding horizons. For example, during time interval $k=4$, the subset R' for regulation-up service in case 1 is empty. However, in case 2, the subset R' contains time interval 12 because of the scheduled discharging activities in Case 2.

Table 5.7: Subsets R , R' , and R'' of receding horizon in Scenario 1 and Case 1.

	Case 1		
	$k=4$	$k=9$	$k=18$
$\overline{\Delta p_k^{up}}$ (kW)	6.6	3.3	5.2
$\overline{\Delta p_k^{down}}$ (kW)	0	3.3	1.4
$\{R\}$ for reg. up	5, ..., 16, 18, 19, 20	10, ..., 16, 18, 19, 20	19, 20
$\{R\}$ for reg. down	\emptyset	17, 18, 21, ..., 26	21, ..., 27
$\{R'\}$ for reg. up	\emptyset	\emptyset	\emptyset
$\{R'\}$ for reg. down	\emptyset	27	\emptyset
$\{R''\}$ for reg. up	17, 21, ..., 27	17, 21, ..., 27	21, ..., 27
$\{R''\}$ for reg. down	5, ..., 27	10, ..., 16, 19, 20	19, 20

Table 5.8: Subsets R , R' , and R'' of receding horizon in Scenario 1 and Case 2.

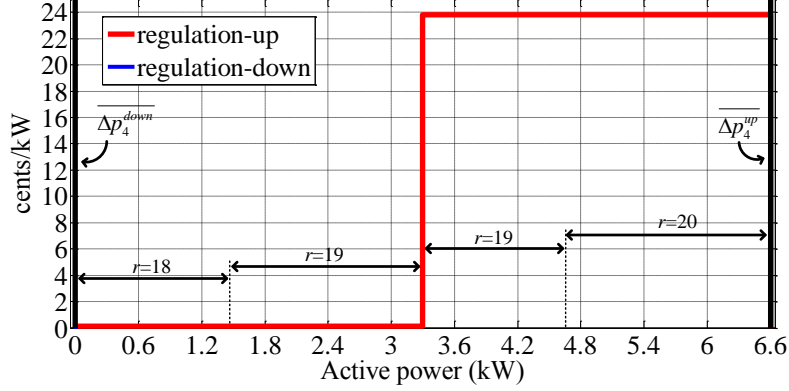
	Case 2		
	$k=4$	$k=9$	$k=14$
$\overline{\Delta p_k^{up}}$ (kW)	6.6	0	5.2
$\overline{\Delta p_k^{down}}$ (kW)	0	6.6	1.4
$\{R\}$ for reg. up	5, ..., 11, 14, 15, 16	\emptyset	15, 16
$\{R\}$ for reg. down	\emptyset	13, 14, 17, ..., 25	17, ..., 27
$\{R'\}$ for reg. up	12	\emptyset	\emptyset
$\{R'\}$ for reg. down	\emptyset	26, 27	\emptyset
$\{R''\}$ for reg. up	13, 17, ..., 27	10, ..., 27	17, ..., 27
$\{R''\}$ for reg. down	5, ..., 27	10, 11, 12, 15, 16	15, 16

The effect of battery degradation cost on the regulation-up and regulation-down cost function is clearly visible in simulation results. Figure 5.12 shows the regulation

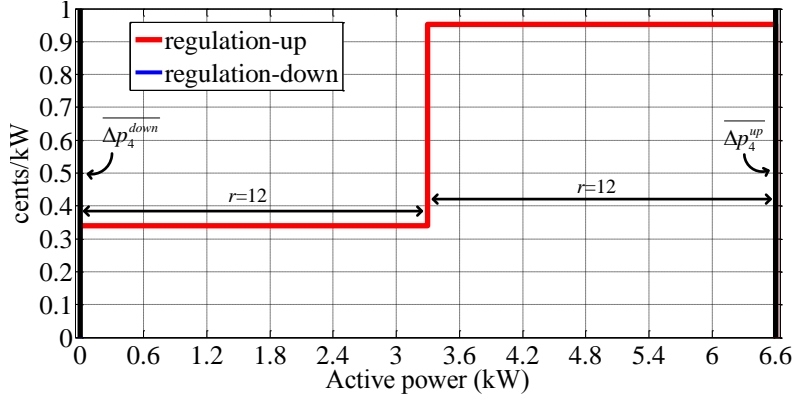
service cost function during $k=4$ for both cases. Regulation-down service is not available from the EV since $\overline{\Delta p_4^{down}}=0$. As can be seen in Figure 5.12 (a), in Case 1, perturbation in p_4^* due to provision of regulation-up service from 0 to 1.4 kW, from 1.4 to 4.7 kW, and from 4.7 kW to 6.6 kW is rescheduled during $r=18$, $r=19$, and $r=20$, respectively. From Figure 5.12 (b), it can be observed that in Case 2, the rescheduling task is performed during time interval $r=12$, since this time interval is a critical time interval. Also comparing the cost range of regulation services shows that in Case 1, for the range of regulation-up service in which the EV is being discharged, the cost of service is high (¢24/kW). That is because of the degradation cost of the battery caused by discharging activity. However this cost in Case 2, when the battery degradation is ignored, is less than ¢1/kW.

Figure 5.13 demonstrates the regulation service cost function during $k=9$ for both cases. In case 1, the values for $\overline{\Delta p_9^{up}}$ and $\overline{\Delta p_9^{down}}$ are equal and is 3.3 kW. In Case 1, the perturbation in p_9^* caused by regulation-up service is rescheduled during time intervals $r=18$ and $r=19$, as shown in Figure 5.13 (a). The perturbation caused by regulation-down service is rescheduled at time interval $r=17$, because this time interval falls in subset R' . The cost associated with regulation-up service is very high since the service is provided by discharging the EV. In Case 2, the EV is not able to provide regulation-up service ($\overline{\Delta p_9^{up}}=0$). The rescheduling task for providing regulation-down service in this case, is performed at time interval $r=26$.

Figure 5.14 shows the result during time interval $k=18$ for Case 1. $\overline{\Delta p_{18}^{up}}$ and $\overline{\Delta p_{18}^{down}}$ are 5.2 kW and 1.4 kW, respectively. The perturbation caused by regulation-up service from 0 to 3.3 kW and from 3.3 kW to 5.2 kW is rescheduled at time intervals $r=19$ and $r=20$, respectively. The spike in regulation-up cost function, from 0 to ¢13.1/kW is due to the battery degradation cost for discharging activity. The perturbation caused by regulation-down service (from 0 to 1.4 kW) is rescheduled at



(a)

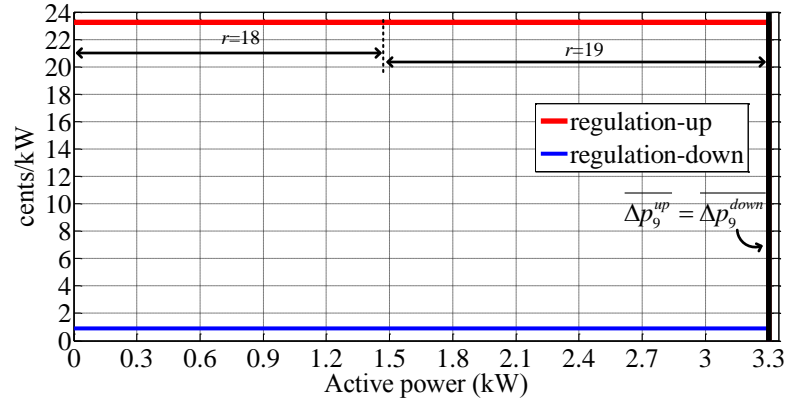


(b)

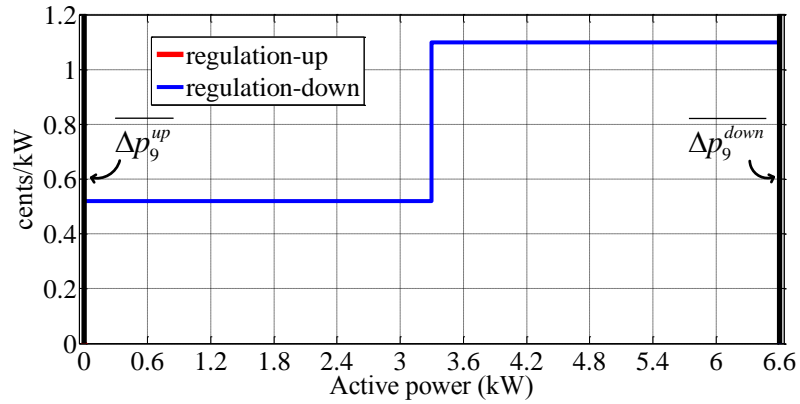
Figure 5.12: Regulation services in Scenario 1 during time interval $k=4$ for (a) Case 1 and (b) Case 2 .

time intervals $r=25$.

Figure 5.15 shows the result during time interval $k=14$ for Case 2. $\overline{\Delta p_{14}^{up}}$ and $\overline{\Delta p_{14}^{down}}$ are 5.2 kW and 1.4 kW, respectively. The perturbation caused by regulation-up service from 0 to 3.3 kW and from 3.3 kW to 5.2 kW is rescheduled at time intervals $r=15$ and $r=16$, respectively. Notice that the regulation-up cost function from 1.9 kW to 5.2 kW, although the service is provided by discharging the battery, is relatively low. That is because of ignoring the battery degradation factor. The perturbation caused by regulation-down service (from 0 to 1.4 kW) is rescheduled at time intervals $r=17$.



(a)



(b)

Figure 5.13: Regulation services in Scenario 1 during time interval $k=9$ for (a) Case 1 and (b) Case 2 .

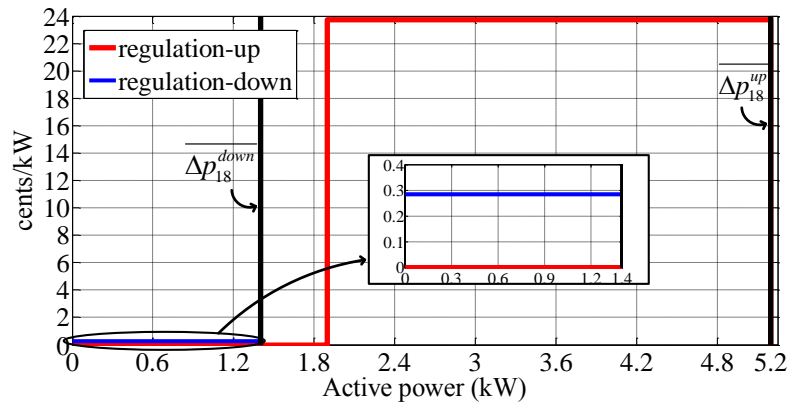


Figure 5.14: Regulation services in Scenario 1 during time interval $k=18$ for Case 1.

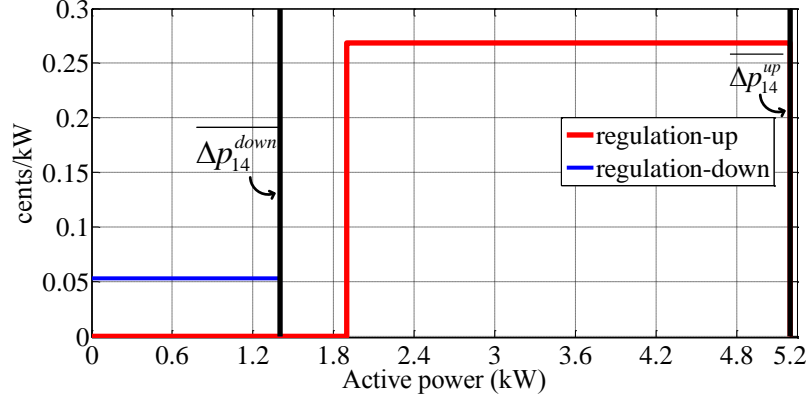


Figure 5.15: Regulation services in Scenario 1 during time interval $k=14$ for Case 2.

From the results in Scenario 1, one can observe that ignoring the battery degradation effect significantly impacts the regulation service cost function. However, improvement in battery technologies would eventually lower the battery degradation cost in the future.

5.6.2 Scenario 2

In the second scenario, we have considered a fleet of 1000 EVs under one aggregator control. Table 5.9 summarizes the specification of EVs. The minimum and maximum SOC of all EVs are assumed to be 0.2 and 0.9 respectively.

Table 5.9: EVs specifications.

EV	no.	battery capacity (kWh)	\bar{p} (kW)	\underline{p} (kW)	γ (¢/kWh)
Chevrolet Volt	300	16.5	3.3	-3.3	45.25
Nissan LEAF	300	24	6.6	-6.6	45.86
Mitsubishi i-MiEV	400	16	3.3	-3.3	46.94

To generate 1000 usage patterns for EVs, we have used a normal distribution function as described in 4.7.2.2.

5.6.2.1 Upper Optimization Level

The optimal charging/discharging scheduling in this scenario is the same as the optimal scheduling in 4.7.2.2. Figure 5.16 repeats the optimal aggregated charging/discharging scheduling.

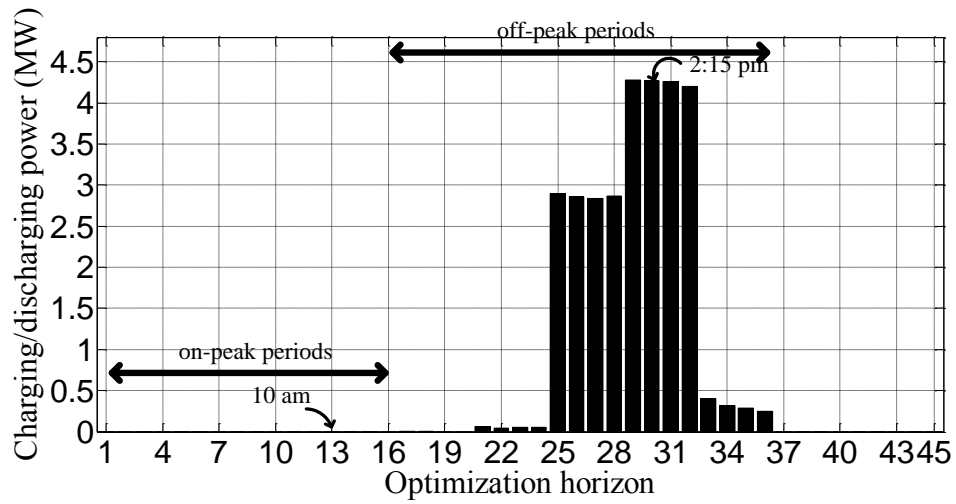


Figure 5.16: Optimal aggregated scheduled charging/discharging activities in scenario 2.

5.6.2.2 Lower Optimization Level

Figure 5.17 demonstrates the available regulation services and its cost function from the aggregated EVs at 10 a.m. (which is $k=13$ in the optimization horizon). Although there are number of EVs connected to the charging facilities at 10 a.m., one of on-peak periods, no charging/discharging activities have been scheduled. But 3.955 MW power is available for regulation services ($\overline{\Delta P_{13}^{up}} = \overline{\Delta P_{13}^{down}} = 3.95$ MW). The

price of regulation-up service is relatively higher because this service is provided by discharging participating EVs batteries.

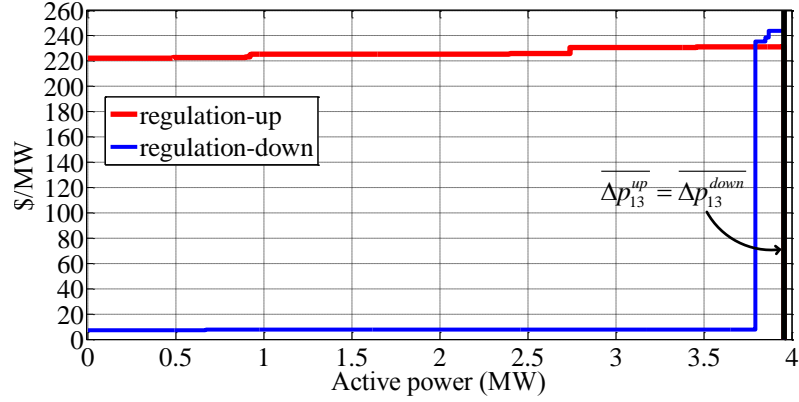


Figure 5.17: Regulation services in Scenario 2 at 10 a.m.

Figure 5.17 shows the results at 2:15 p.m. ($k=30$ in the optimization horizon), during off-peak periods. Since 2:15 p.m. is an off-peak period, most of the charging activities have been scheduled at this time. Scheduling more EVs for charging, the less regulation-down service is expected. As can be seen from the figure, although there is not any capacity available for regulation-down service ($\overline{\Delta P_{30}^{down}}=0$), 1.23 MW capacity is available for regulation-up service ($\overline{\Delta P_{30}^{up}}=1.23$ MW).

5.6.2.3 Post-Process Optimization Level

At this stage, the aggregator receives the allocated AGC signal from the SO. To satisfy the allocated AGC signal, either for regulation-up or regulation-down service, the aggregator must assign a portion of the service to each connected EV appropriately. Table 5.10 and 5.11 lists the results of post-process optimization level. For example, at 10 a.m. the regulation-up service from 0 to 1.77 kW is assigned to EV 5 (the perturbation in the scheduled power of the EV is rescheduled at $r=31$ of its receding

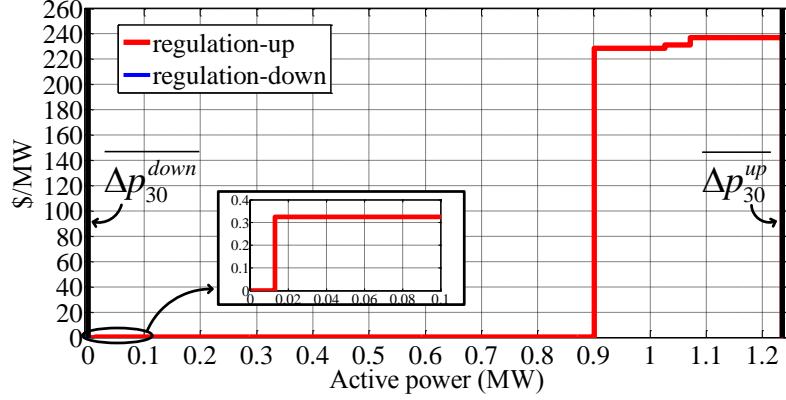


Figure 5.18: Regulation services in Scenario 2 at 2:15 p.m.

horizon).

Table 5.10: Post-process optimization results for assigning AGC signal at 10 a.m.

Service	From (kW)	To (kW)	Assigned EV no.	Rescheduling interval of the receding horizon r
Regulation-up	0	1.177	5	31
	1.177	4.477	7	31
	⋮			
	3946.7	3950	930	18
Regulation-down	0	2.611	586	37
	2.611	5.911	596	34
	⋮			
	3949.3	3950	586	29

Power capacity available to provide regulation services, from the aggregated EVs, are highest during on-peak periods. Any regulation services which is provided by discharging EVs, the associated cost is relatively high due to the high battery degradation cost. In the future it is expected that battery technologies will improve and the battery degradation factor would decrease. The less the battery degradation factor is, the more economical regulation services can be provided by EVs.

Table 5.11: Post-process optimization results for assigning AGC signal at 2:15 p.m.

Service	From (kW)	To (kW)	Assigned EV no.	Rescheduling interval of the receding horizon r
Regulation-up	0	0.655	39	32
	0.655	3.955	5	34
	\vdots			
	1229.8	1230	609	35

5.7 Conclusion

In this chapter, we presented a novel multi-level optimization framework for an aggregator, responsible for a group of EVs, to decide on the bid components of regulation services. In the upper optimization level, optimal charging/discharging activities of aggregated EVs are calculated. The objective function at this level is the charging/discharging cost of aggregated EVs. The objective function is minimized using linear programming. In the lower optimization level, bidding components (capacity and cost function) of regulation services, for aggregated EVs are calculated. The components are calculated in an optimal fashion, to minimize the cost of the service. In the post-process optimization level, when the aggregator receives the allocated AGC signal, participating EVs are assigned optimally to satisfy the signal. The proposed framework is scalable for a large group of EVs and easy to implement in a real-time manner. It should be noted that the framework does not lower the EV owners comfort level.

Chapter 6

DGs Integration and Micro-Grid

6.1 Introduction

Improvement in renewable generation technologies and environmental concerns along with restructuring of the electricity market make Distributed Generators (DGs) an attractive solution to meet the electricity demand. However integrating DGs into the distribution Electric Power System (EPS) could challenge the operation of it. These challenges could be listed as: voltage rise effect, power quality, protection, and stability [110].

Challenges related to protection can be identified as: Protection of the generation equipment from internal faults; Protection of the distribution network from fault currents supplied by the DG; Anti-islanding or loss-of-main source protection; and Impact of DG on existing distribution system protection.

The focus of this chapter is on islanding issue. Islanding can be defined as a condition in which a portion of the utility system containing both load and DG, remains energized while being isolated from the remainder of the EPS [111]. Under islanding conditions, the magnitude and frequency of the voltage at the point of

common coupling (PCC) tend to drift from the rated grid values as a function of the generation-load imbalance. As addressed in standards like IEC 62116, IEEE 1547, and IEEE 929, DG is required to be disconnected from the grid in case of islanding. The main issues engaged with islanding are [112]:

- Safety issues to utility workers and the public since a portion of the EPS remains energized while it is not expected to be;
- The islanded system may be inadequately grounded by the DG interconnection;
- Instantaneous reclosing could cause out-of-phase between DGs and the EPS;
- Loss of control over voltage and frequency in the islanded system;
- Excessive transient voltage and current stresses upon reconnection to the grid;
- Uncoordinated protection in the EPS;

This chapter engages with IEEE 1547 requirement for anti-islanding which is, loss of grid connection must be detected by DGs within 2 seconds and must lead to immediate trip of the DGs from the EPS.

From the DG's perspective, many anti-islanding schemes have been reported in technical literature to satisfy the standard requirement, which can be grouped in two wide categories: Communication based; and Local detection. Figure 6.1 demonstrates these two categories and corresponding subcategories.

Communication based schemes are known as remote techniques integrating the EPS and the DG facility. They are more reliable than local detection schemes but they are more costly due to installation, recurring operation, and maintenance. Local detection schemes are based on the measurement of some parameters (voltage, current, and frequency) at the DG facility. Local detection schemes are classified as

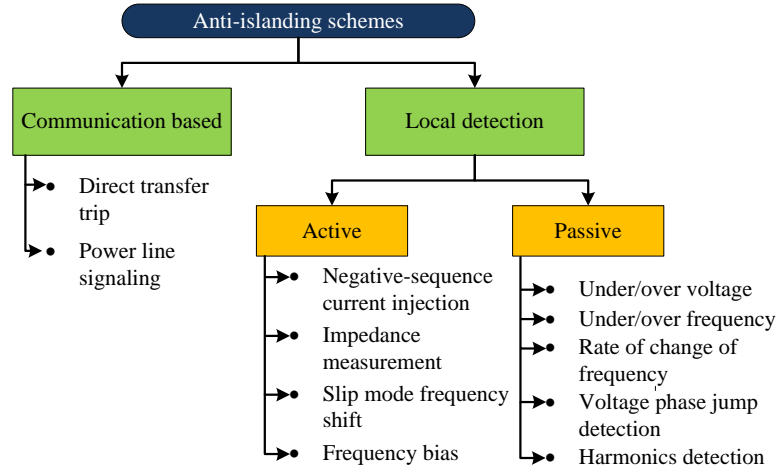


Figure 6.1: Anti-islanding schemes.

passive (based exclusively on the measured parameters) and active (intentionally introducing disturbance at the output and observing its effect on measured parameters) techniques [113].

Unfortunately, local detection anti-islanding schemes are not 100% reliable as they present an inherent operation region, characterized by small power imbalances in an island system, where they are not able to detect islanding condition in a timely manner [114]. The corresponding system operating conditions are called non-detection zone (NDZ) and the islanding detection failure is named unintentional islanding [115]. From a utility stand point, understanding the behavior of NDZs is very important because they may violate the standard requirements for unintentional islanding.

Considering the substantial growth in DG sources that are requesting to be connected to the distribution EPS, the time frame to assess the risk of islanding of units by a utility is getting shorter, typically caused by regulated timelines imposed on utilities. When PV systems are involved, the time scale is often uncomfortably shorter [116]. To avoid extra cost, extra time, and excessive level of pessimism in assessing the risk of unintentional island, a useful tool which could be used not only for

risk-of-islanding study, but also for utility's evaluation of DG interconnection impacts, seems crucial.

Several screening procedures have been reported in literature [117]- [118], as a utility interconnection acceptance process of DG. Most of the screening procedures are based on the FERC Small Generator Interconnection Procedure (SGIP) or Mid-Atlantic Distributed Resources Initiative (MADRI) procedures. These screening procedures are based on a singular or over-simplified parameters and may be no definitive technical basis for the criteria level of screen [118]. The purpose of a screening procedure is to determine additional measures or if more in-depth evaluation is necessary or not. As can be implied, screening tools do not provide in-depth analysis of the distribution feeder and interconnected DGs. Increasing penetration of DGs results in tighter screening criteria. Therefore, an analytical toll which can perform in-depth and sufficiently rigorous islanding analysis, could help utilities to assess the risk of islanding in more reliable fashion and also facilitate DGs interconnections in safer manner.

In this chapter, we present a framework, which can be used by utility companies, to assess the risk of unintentional islanding of interconnected DGs with the distribution EPS. The proposed framework can also provide a platform for other studies at the distribution level, such as voltage flicker. The proposed framework is simple to implement and fast, which means savings in cost and time of islanding studies. Since PV is a dominant type of DG technology being interconnected to the EPS in the United States in recent years and deployment of PV systems continues to increase rapidly, the focus of results demonstrated in this chapter is on PV interconnection. However the framework is not dependent on DG technology and can be used for other kinds of DG technology. The framework is also independent of the kind of anti-islanding schemes used in DGs (active/passive) and can be used for any islanding case studies

in radial distribution feeder systems.

The main contribution of the research in this chapter is summarized as follows:

1. Developing an algorithm to detect nodes connectivities in radial distribution feeder;
2. Developing an algorithm to model radial distribution feeder independent of node and/or branch numbering;
3. Developing a procedure to identify NDZ of interconnected DGs in a radial distribution feeder, in a systematic and efficient manner.

6.2 Screening Procedure: A Review

Interconnection procedures vary depending on state or federal jurisdiction, and implementation practices vary by utility. Most procedures allow for expedited interconnection without additional technical studies if the proposed interconnection passes a series of technical screening. In this section, a quick review of different screening procedures used in the United States, at the time of this writing, is presented.

In California a screening procedure, as outlined in their state regulated Rule 21, is used to determine the level of review process required for interconnected systems. There is no specified system capacity limit. However for systems larger than 1 MW, a system stabilization function and telemetering could be required. In California, additional study is required for those DG units that satisfies at least one of the following criteria: the unit injects power into the grid, its rating is greater than 500 kW, and the total generation connected to the line section is less than 15% of the line section's peak load [119]. The 15% threshold was then adopted in the FERC SGIP and is used as a model for developing their interconnection procedures [120].

The FERC SGIP process has been revised in 2003 [121]. The review process first examines total penetration by capacity and determines whether penetration level is less than 15% of the line-section peak load or not. For typical distribution circuits in the United States, minimum load is approximately 30% of peak load [120]. Based on this generalization, the 15% penetration level, which is one half of the 30%, was selected as a conservative penetration level for general screening purposes.

To understand the rationale behind the FERC SGIP criterion, we consider the island voltage as V_I , the feeder nominal voltage as V_N , the PV output active power as P , and the load power at nominal voltage as P_N . Therefore we have [116]:

$$\frac{V_I}{V_N} = \sqrt{\frac{P}{P_N}}. \quad (6.1)$$

From equation (6.1), one can imply that any ratio of the PV power to the minimum feeder load greater than 0.77 results in island voltage greater than 0.88 p.u. (the IEEE 1547 low voltage limit [10]). Or for PV penetration higher than 77%, the voltage of the island will be above the minimum limit. Therefore by limiting the DG penetration below 77% or roughly 3/4 of the feeder minimum load, the risk of islanding would be zero.

The scope of the MADRI procedures include DG systems under 10 MVA that are not interconnected under federal jurisdiction [122]. The MADRI procedures are organized into four levels. Level 1 is for certified inverter-based systems that are below 10 kVA. Level 2 is for certified inverter-based systems that are below 2 MVA or systems that did not pass the level 1 review. Level 3 is for systems that are below 10 MVA and do not qualify for or did not pass level 1 or the level 1 or level 2 reviews. Level 4 is for systems that do not qualify for level 1 or level 2 review and do not inject power to the grid. The MADRI procedures follows FERC SGIP criteria for screening

phase of each level. For example, in level 1, for interconnection to a radial distribution circuit, aggregated generation on circuit including the proposed DG system must be less than 15% of the line section annual peak load.

The Interstate Renewable Energy Council (IREC) recommended interconnection procedures provide four review paths, following FERC SGIP criteria: Simplified path for certified DG systems up to 25 kVA; Expedited path for certified DG systems up to 2 MVA; Standard path for certified DG systems between 2 MVA and 10 MVA; and the last review path includes all DG systems that do not qualify for last three paths [123].

In 2012, SANDIA published a guideline, specifically to assess the risk of unintentional islanding of a proposed DG system [117]. The guideline, based on a four-step procedure, indicates when the risk of islanding may not be negligible. Figure 6.2 demonstrates the screening procedure.

The SANDIA screening procedure is based on an assumption that inverters are utilizing positive feedback based active anti-islanding. Therefore, for cases in which there are PVs that do not utilize positive feedback based active anti-islanding, the procedure is not applicable. The reason that the SANDIA guideline recommends 2/3 instead of 3/4 as the threshold for DG penetration level is essentially to provide a comfortable margin of error to account for reduced-voltage behavior of the load, while continuing to use a standard threshold [117]. Also mismatch in reactive power generation and consumption guarantees that inverter-based DG will deviate in frequency after a loss of main [125]. The VAR mismatch recommended by the SANDIA report, to eliminate the risk of islanding, is more than 1%.

As explained above, all of screening procedures are used to avoid unnecessary in-depth supplementary study to assess the risk of unintentional islanding in a DG system. However, considering the rapid growth rate of DG penetration, it is expected

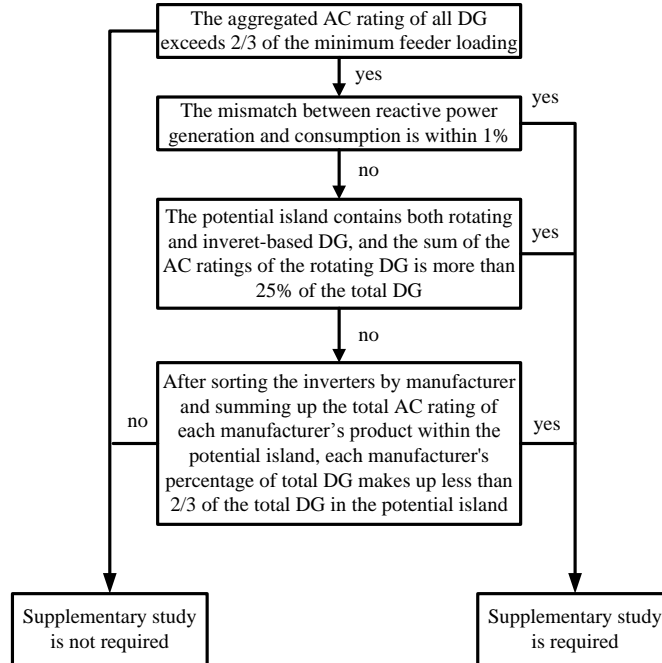


Figure 6.2: SANDIA screening procedure.

that the simplified screening tools will not be able to address the risk of unintentional islanding of the EPS with many DGs. In that case, in-depth supplementary study seems necessary. To reduce the time and cost of DG system installations, the study should be effective and easy to implement. In this work we developed a framework for in-depth evaluation of risk of unintentional islanding of a DG system, which can be generalized and easy to implement. We start with distribution feeder modeling.

6.3 Distribution Feeder Modeling

Since most of DGs are connected to distribution feeders, providing an accurate model of the feeder is the first step of our framework. Considering the size of the feeders and number of elements in the feeders, this step could be complicated, time consuming, and not easy to implement. This task could be more challenging considering chaotic

IDs for sections and nodes. In this section we present a novel and simple algorithm to detect distribution feeder topology, nodes conductivities, and all pathes from substation to end nodes of the feeder. The proposed algorithm, which can be used for a radial feeder with any size and number of element, is based on graph theory.

To have a better understanding of proposed algorithm, first we provide some definitions of graph theory. A graph G consists of two sets:

- A set $V = V(G)$ whose elements are called vertices, points, or nodes of G .
- A set $E = E(G)$ of unordered pairs of distinct vertices called edges of G .

Vertices u and v are said to be adjacent or neighbors if there is an edge $e = \{u, v\}$. In such a case, u and v are called the end points of e , and e is said to connect u and v . Also, the edge e is said to be incident on each of its end points u and v . The degree of a vertex v in a graph G , written $\deg(v)$, is equal to the number of edges in G which contain v , that is, which are incident on v .

Since distribution systems have radial nature, we can consider the distribution feeder as a tree graph G which is connected and has no loop. Therefor the distribution feeder can be treated as a connected directed tree graph. A finite tree with n vertices must have $n-1$ edges. A vertex coloring, or simply a coloring of G is an assignment of colors to the vertices of G such that adjacent vertices have different colors. We say that G is m -colorable if there exists a coloring of G which uses m colors. Algorithm 1 gives an algorithm by Welsh and Powell [124] for coloring of a graph G .

Based on the degree of a node, we define four types of nodes: Source Node; End node; Junction node; and Interconnected node. Source node is the node representing the substation on the feeder. End node is a node in the graph with degree of one. If the distribution system has a single feeder, then the source node will have a degree of one but we should notice that it is not an end node. Junction node is a node with the

Algorithm 1 Welsh-Powell algorithm

- 1: Order the vertices of G according to decreasing degree.
 - 2: Assign the first color C_1 to the first vertex and then, in sequential order, assign C_1 to each vertex which is not adjacent to a previous vertex which was assigned C_1 .
 - 3: Repeat step 2 with a second color C_2 and the subsequence of noncolored vertices.
 - 4: Repeat step 3 with a third color C_3 , then a fourth color C_4 , and so on until all vertices are colored.
 - 5: Exit.
-

degree of 3 or more. These nodes send power to more than one downstream nodes. Since distribution system is modeled as directed tree, it should be mentioned that there is just only one way from each node to its upstream node (which receive power from) otherwise we would have loop. Interconnected node is a node with the degree of 2.

The data that are available and commonly used in all utility companies, are the substation node ID and line data. In order to detect conductivities of nodes and generate the accurate topology of the feeder, we use a coloring algorithm which was discussed in Section 6.3. The algorithm starts with the substation node or source node. We refer this node as the first level of the graph. The degree of the source nodes is equal to the number of feeders (branches) coming out of the node. The algorithm will go through all branches coming out of the source node, till faces the end node. Whenever the algorithm reaches a junction node, it increases the level. So each junction node will increase its level. We can consider the number of level as the color of each junction node and assign 1 to the color of source node. There are three states for position of interconnected nodes. They could be between level 1 (source node) and a junction node level, between two junction nodes levels, or after the last junction node level (between junction node and end node). If they are between the level 1 and a junction node level, we will assign color 1 to them. If they are between

two junction nodes levels, we will assign the color of the upper junction node level to them. If they are after the last junction node, we will assign the color of the last junction node level to them. After this step, we have leveled the network and assigned a color to all nodes. Assigning a color to each node helps us to find the topology of the feeder regardless of node IDs.

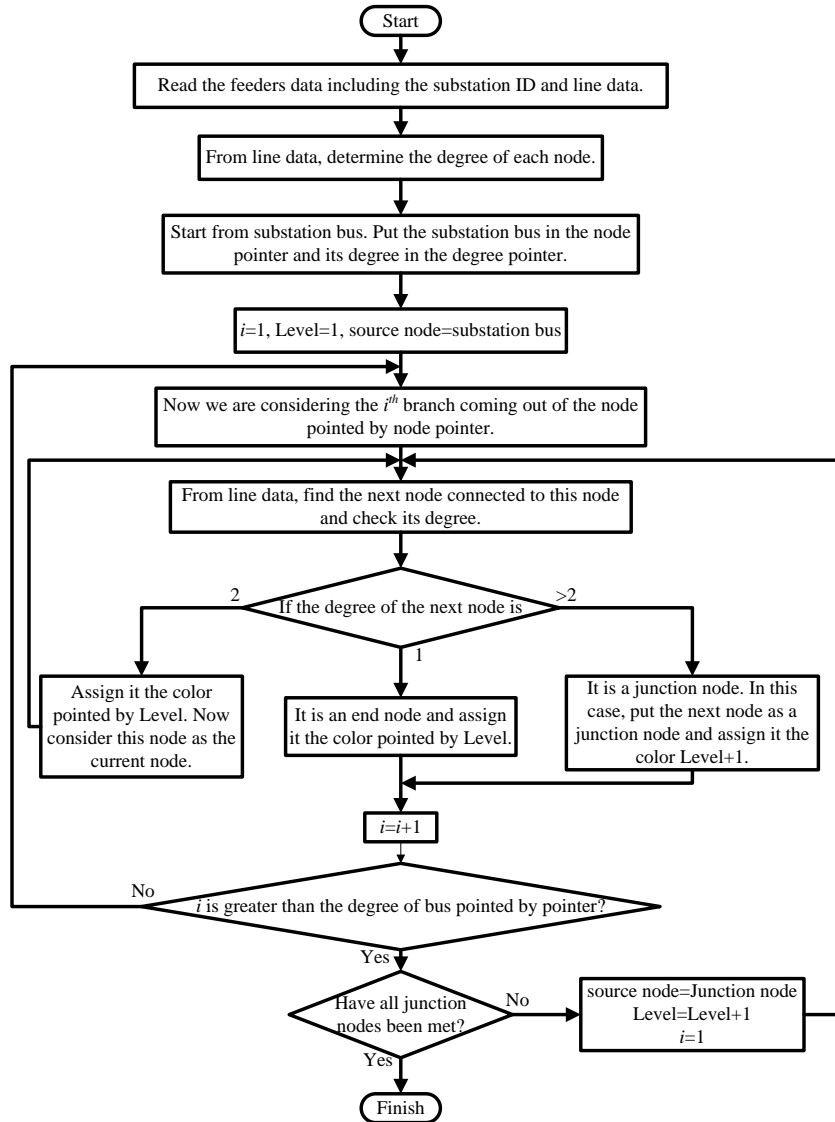


Figure 6.3: Flowchart of assigning color to each node.

Figure 6.4, as an example, shows a leveled graph. All nodes in each level shown by dashed black border for level 1, dashed red border for level 2, dashed green border for level 3, and dashed blue border for level 4, have been assigned the same color of their containing level.

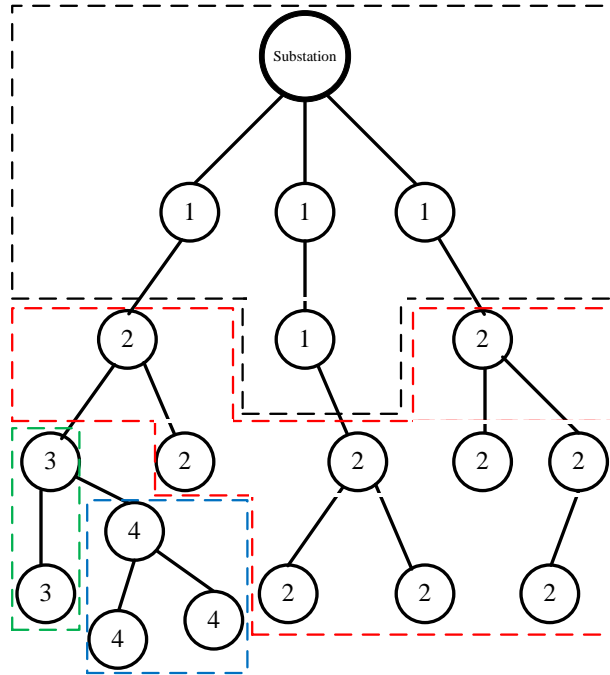


Figure 6.4: Leveled graph using proposed algorithm.

After leveling the graph and assigning a color to each node, we introduce an algorithm, as shown in Figure 6.5, to detect the conductivities of nodes and find the path from each end node to the source node. The number of paths in a graph is equal to the number of end nodes of the graph. The key point here is when the algorithm reaches a junction node. When the algorithm reaches an interconnected node, there is just one way to continue, however when it reaches a junction node, there are more than one way to continue. Just one branch from junction node conducts the

algorithm to the upper level (color with lower number) node. So in this situation, the algorithm checks the color of all adjacent nodes which have been assigned in the previous step. The algorithm will continue by the adjacent node which has a color with lower number.

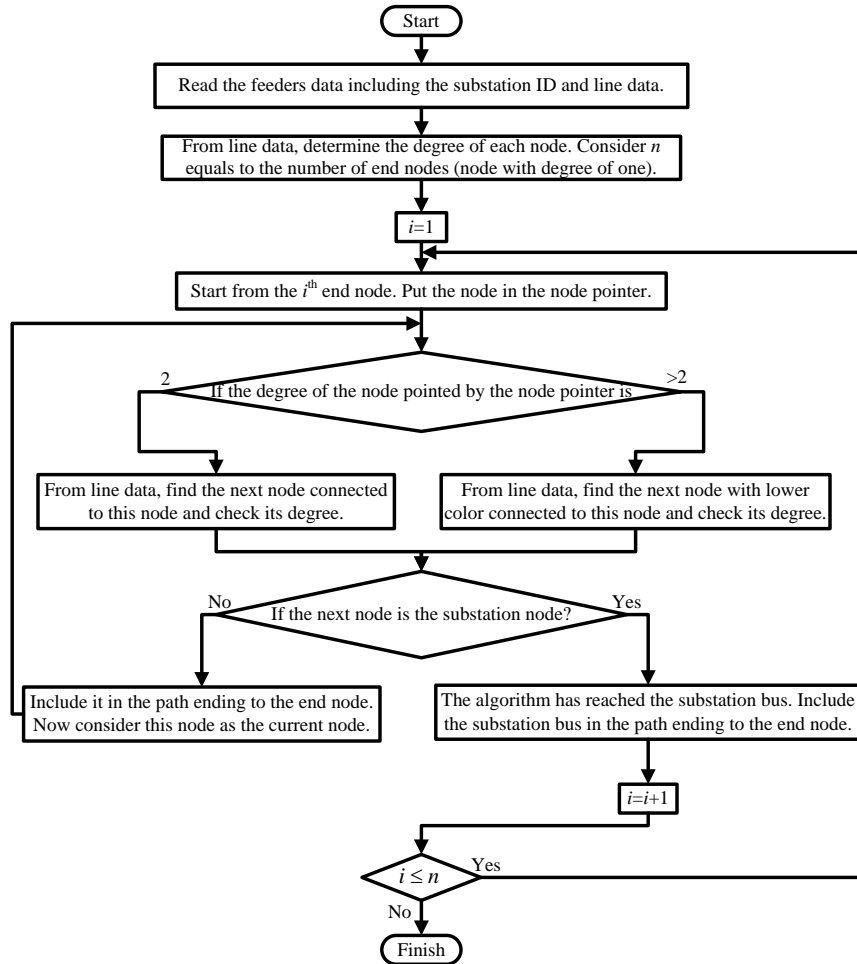


Figure 6.5: Flowchart of tracking all paths from each end node to the source node.

Figure 6.4, demonstrates two paths, shown by black and red arrows, of the leveled graph. Note that each path starts from an end node and finishes at the source node. When the algorithm reaches a junction node, it will be directed to the node of higher

level (with lower assigned color).

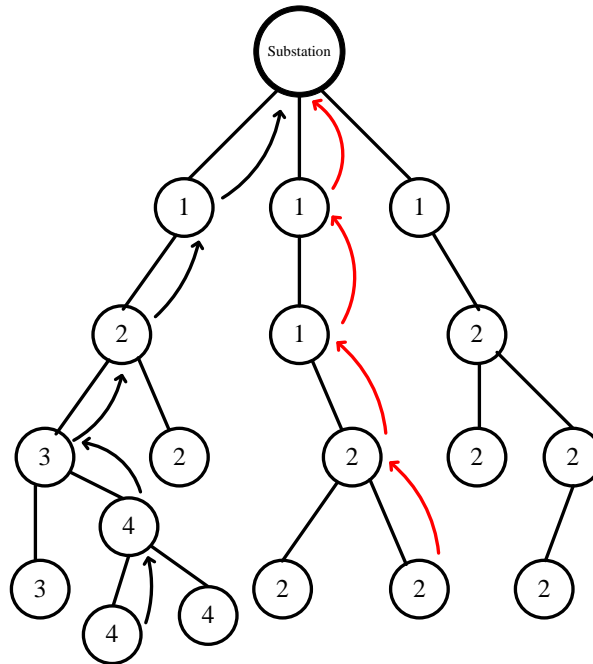


Figure 6.6: Finding path in a graph using proposed algorithm.

By this point, we have configured the topology of the feeder. Now we can create the feeder model in a software platform. Due to the MATLAB/SIMULINK ability in modeling and simulations, we have chosen MATLAB/SIMULINK as our software platform. To model each node, we have used the Three-phase VI Measurement block. Also we have modeled each section with a Three-phase Mutual Induction block. The input parameters for a Three-phase Mutual Induction block are the zero and positive sequence impedance of the line. These information can be easily obtained from line data. After modeling the feeder, it is time to connect our DG units. In the next section we present the used DG model.

6.4 PV Modeling

Amongst all DG technologies, PV systems have attracted considerable attention and investment in several countries, [126], such that a significant penetration of PV energy into the EPS is anticipated, [127]. In this section, we discuss a generic model of PV for islanding study.

Figure 6.7 shows the schematic diagram of a three-phase (3ph) PV system. As shown in the figure, a PV system includes a PV generator (consisting of many PV panels) along with a boost DC/DC converter connected to the DC side of 3ph DC/AC converter, LC low-pass filter which is connected to the AC side of the 3ph DC/AC converter, and an isolation transformer to connect the rest of the system to the grid. We focus on the DC/AC converter as a Voltage-Sourced Converter (VSC). Each leg of a 3ph VSC consists of two semiconductor valves corresponding to a phase. The valves in each leg are switched in a complementary manner, based on the carrier-based Pulse-Width Modulation (PWM) strategy or state-vector modulation strategy [127]. Magnitude and phase angle of the voltage at AC side are controllable through the switching strategy. Variables m_d and m_q are the d - and q -axis components of the PWM modulation waveforms.

For simulation of power system transients, the VSC can be modeled in different ways. Circuit-based models of semiconductor switches with different degrees of complexity and switched or topological models which ignore the switching transient phenomena [127]. For faster simulations, especially if a fairly complex network is to be simulated, the switched model of the VSC can be replaced by an equivalent dynamic average-value model [128]- [129]. In such a model, which is known as averaged model, instead of applying switching scheme, terminal variables of the VSC are approximated by their respective per-switching-cycle moving average values [127].

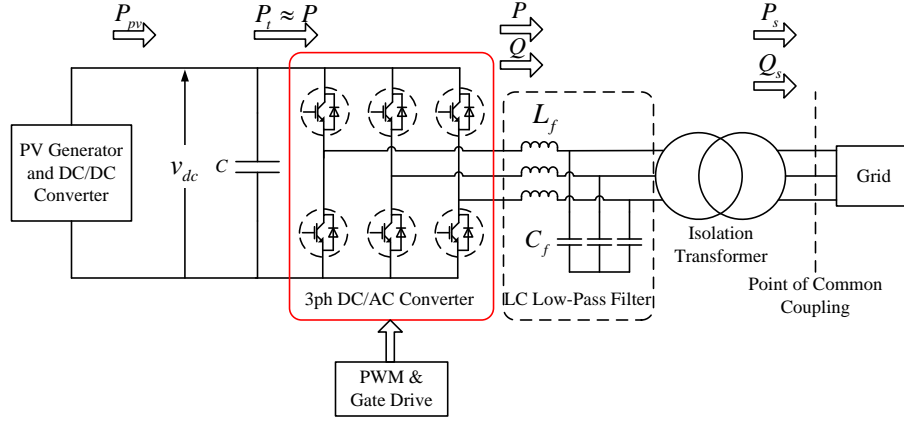


Figure 6.7: Diagram of a grid-connected PV system.

Based on the averaged model, an algebraic relationship can be developed between AC and DC variables in an orthogonal reference frame (the $\alpha\beta$ or dq frame). In the rest of the report indexes $t, s, d, q, \alpha, \beta, a, b,$ and c refer to terminal of the VSC, point of common coupling, d component of dq frame, q component of dq frame, α component of $\alpha\beta$ frame, β component of $\alpha\beta$ frame, phase A, phase B, and phase C, respectively. Also parameters $v, i, \rho, P, Q,$ and m represent voltage, current, reference angle, nominal value, active power, reactive power, and PWM modulation waveform, respectively.

The power balance between DC and AC side terminals of the VSC can be presented as follows [127]:

$$v_{dc}i_{dc} = v_{ta}i_{ta} + v_{tb}i_{tb} + v_{tc}i_{tc}. \quad (6.2)$$

$$i_{dc} = \frac{v_{ta}i_{ta} + v_{tb}i_{tb} + v_{tc}i_{tc}}{v_{dc}}. \quad (6.3)$$

Notice that in equations (6.2) and (6.3) the VSC power loss has been ignored. We

co-operate in a nested control architecture, [127]. Assuming a fixed input DC power at DC side of the VSC, the variation in sun irradiations and its effect on DC-link voltage could be ignored, for islanding studies purpose. Also based on current practises in utilities, PVs are not allowed to do voltage regulation, instead the voltage and frequency is imposed by the grid. Therefore, for islanding studies, the real and reactive power control scheme plays an important role. This control scheme is explained in the following subsection.

6.4.1 Real and Reactive Power Control Scheme

The goal of this control loop is to regulate P_s and Q_s . However, based on the diagram presented in Figure 6.7, P_s and Q_s are related to P and Q (active and reactive power before filter stage). Neglecting the active power loss in filter stage, we can express $P_s \approx P$ and $Q_s \approx Q + Q_f$ (where Q_f is the reactive power of the filter stage). On the other side, P and Q must be controlled by two respective reference values, P_{ref} and Q_{ref} . As mentioned before, current practices in utilities do not allow DGs to support reactive power in distribution EPS. P_{ref} could be interpreted as the input DC power in DC side of the VSC.

The real and reactive power control could be achieved based on either the voltage-mode control strategy or the current-mode control strategy, [127]. In the voltage-mode control method, P and Q are controlled, respectively, by the phase angle and the amplitude of the VSC terminal voltage, relative to the grid voltage, [130]. The voltage-mode control has been mainly utilized in high voltage or high power applications such as flexible AC transmission systems, [131] and [132]. The voltage-mode control strategy is easy to implement in practice, however, it is vulnerable to large currents due to lack of closed loop regulation on the AC side of the VSC, [127]. In the current-

mode control method, first the AC-side current of the VSC is controlled by a dictated control scheme through the terminal voltage of the VSC. Then both real and reactive power are controlled by the phase angle and the amplitude of the line current of the VSC, with respect to the grid voltage, [133]. The advantages of the current-mode scheme are robustness against overload conditions, variations in parameters of the VSC and AC system, superior dynamic performance, and higher control precision, [134]. This chapter is engaged with the current-mode control.

Figure 6.9 shows a schematic diagram of a current-controlled real/reactive power controller in dq -frame, [133]. The feedback and feed-forward signals are first transformed to the dq frame and then processed by compensators to produce the control signals in dq frame. Finally, the control signals are transformed to the abc frame and fed to the VSC (Figure 6.8). i_{td}^r and i_{tq}^r in Figure 6.9, are reference values of the VSC current in dq frame. Also we consider v_{td}^r and v_{tq}^r as the d - and q - components of the VSC voltage respecting to the reference values.

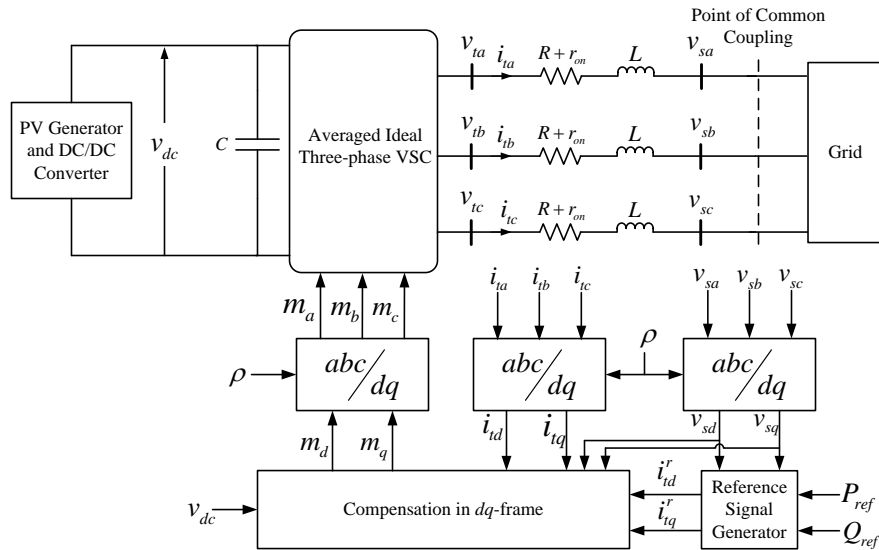


Figure 6.9: Schematic diagram of a current-controlled real/reactive power controller in dq -frame.

The active and reactive power P and Q can be expressed as follows, [133]:

$$P = \frac{3}{2}(v_{sd}i_{td} + v_{sq}i_{tq}). \quad (6.5)$$

$$Q = \frac{3}{2}(v_{sq}i_{td} - v_{sd}i_{tq}). \quad (6.6)$$

Considering the synchronization scheme, $v_{sq} = 0$, P and Q could be rephrased as follows, [127]:

$$P = \frac{3}{2}v_{sd}i_{td}. \quad (6.7)$$

$$Q = -\frac{3}{2}v_{sd}i_{tq}. \quad (6.8)$$

We can observe the linear relationship between P and i_{td} , and between Q and i_{tq} from equations (6.7)-(6.8). Having v_{sd} approximated by the nominal grid voltage amplitude, we can have the d - and q - component of the VSC current respecting to the reference values as follows:

$$i_{td}^r = \left(\frac{3}{2}v_{sdn}\right)^{-1}P_{ref}. \quad (6.9)$$

$$i_{tq}^r = -\left(\frac{3}{2}v_{sdn}\right)^{-1}Q_{ref}. \quad (6.10)$$

Considering a steady-state operating condition, in which $\omega(t) = \omega_0$, we can have

$$L\frac{di_{td}}{dt} = L\omega_0i_{tq} - (R + r_{on})i_{td} + v_{td} - v_{sd}, \quad (6.11)$$

$$L\frac{di_{tq}}{dt} = -L\omega_0i_{td} - (R + r_{on})i_{tq} + v_{tq} - v_{sq}. \quad (6.12)$$

Based on the VSC model in dq frame, and equations (6.11)-(6.11), v_{td} and v_{tq} can be

expressed as equations (6.13)-(6.14), [133].

$$v_{td} = \frac{v_{dc}}{2} m_d. \quad (6.13)$$

$$v_{tq} = \frac{v_{dc}}{2} m_q. \quad (6.14)$$

According to equations (6.9)-(6.14), Figure 6.10 shows a block representation of the d - and q -axis current controllers of the VSC system, [133].

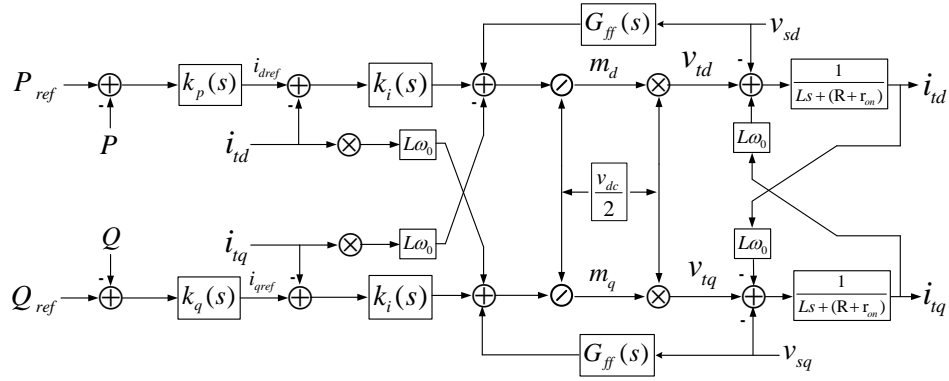


Figure 6.10: Control block diagram of a current-controlled VSC system.

Blocks $K_p(s)$ and $K_q(s)$, in their simplest form, can be the proportional integrator compensator. Due to strong linear relationship between P and i_{td} , and between Q and i_{tq} , $K_p(s)$ and $K_q(s)$ may be omitted, [127]. Procedures to tune compensator $K_i(s)$ and feed-forward filter $G_{ff}(s)$, are explained comprehensively by [133]. It is worth noting that the control, feed-forward, and feedback signals are DC quantities in the steady state.

After understanding the feeder and DG model, next we present operational conditions in which the potential risk of island is high.

6.5 Islanding Conditions

All grid-connected PV inverters are supposed to have over/under frequency protection (OFP/ UFP) and over/under voltage protection (OVP/UVP) to force the PV inverter from supplying power to the utility grid if the frequency or amplitude of the voltage at its PCC falls outside of pre-defined limits. Considering the PV output active and reactive power as P and Q , respectively, and the load active and reactive power as P_L and Q_L , respectively, Figure 6.11 shows the schematic diagram of the distribution feeder under study. As can be seen from the figure, the mismatch between generation and consumption in the feeder, shown by $\Delta P + j\Delta Q$, is compensated by the Grid.

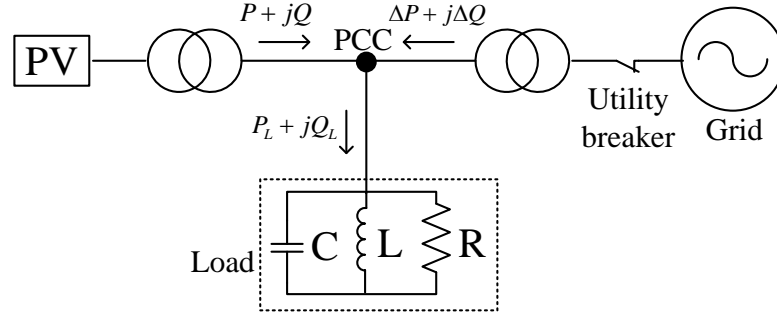


Figure 6.11: Schematic diagram of the distribution feeder under study.

The following equations can be developed from Figure 6.11.

$$P_L = P + \Delta P, \quad (6.15)$$

$$P_L = \frac{V_{PCC}^2}{R}, \quad (6.16)$$

$$Q_L = Q + \Delta Q, \quad (6.17)$$

$$Q_L = \frac{3V_{PCC}^2}{2\pi fL} \left[1 - \left(\frac{f}{f_0} \right)^2 \right], \quad (6.18)$$

where V_{PCC} and f are the magnitude of voltage and frequency at PCC and f_0 is the resonant frequency of the load. Therefore, from equations (6.15) to (6.18), one can infer that in loss of main, V_{PCC} and f depend on the load characteristics if P and Q are known.

The quality factor of the load, Q_f , is defined as follows:

$$Q_f = R\sqrt{\frac{C}{L}}. \quad (6.19)$$

Therefore, the frequency at PCC can be calculated using the following equation [135].

$$f = \frac{1}{2\pi\sqrt{LC}} \left(\sqrt{\left(\frac{Q_L}{Q_f P_L}\right)^2 + 4} - \frac{Q_L}{Q_f P_L} \right). \quad (6.20)$$

The behavior of the system at the time of utility disconnection will depend on ΔP and ΔQ at the instant before the breaker opens to form the island. If $\Delta P \neq 0$, the amplitude of V_{PCC} will change, and the OVP/UVP can detect the change and prevent islanding. If $\Delta Q \neq 0$, the load voltage will show a sudden shift in phase, and then the inverter's control system will cause the frequency of the inverter output current, and thus the frequency of V_{PCC} , to change until $\Delta Q = 0$ (that is, until the load's resonant frequency is reached). This change in frequency can be detected by the OFP/UFP [136]. Notice that increasing Q_f , forces f_0 to converge to f and that means the islanding detection becomes difficult.

If $\Delta P = \Delta Q = 0$ when the utility disconnects, there will be insufficient change in the voltage amplitude or frequency at PCC to activate any of the standard OVP/UVP or OFP/UFP devices. In reality, ΔP and ΔQ do not have to be exactly equal to zero for this to occur because the magnitude of the utility voltage can be expected to deviate slightly from nominal values, and therefore the thresholds for the OVP/UVP

and OFP/UFP devices cannot be set arbitrarily small or the PV inverter will be subject to nuisance trips [136].

Any values of ΔP and ΔQ which result in remaining the island energized more than 2 seconds, is recognized as NDZ. However, providing NDZ in terms of ΔP and ΔQ might not give us a transparent view of the feeder operational condition. Therefore, in this chapter, we define NDZ based on the load fraction (LF) and power factor (PF) of the feeder. LF denotes the load fraction of the feeder, as percentage of the feeder peak load. Figure 6.12 demonstrates NDZ in LF-PF plane with dotted area. Notice that defining NDZ in LF and PF helps utilities to evaluate the risk of island of calculated NDZ based on the history of operating load characteristics of the feeder under study.

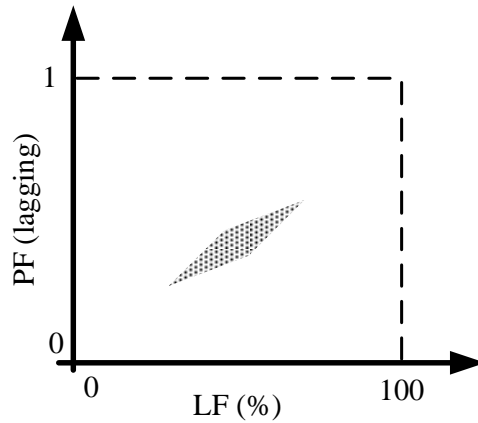


Figure 6.12: Mapping of the NDZ in LF-PF space.

Next we present a procedure to calculate NDZ, in terms of LF and PF, based on the feeder and PVs model.

6.6 Study Procedure

In this section, we develop a procedure, step by step, to perform a risk of islanding study, on a radial distribution feeder. The procedure starts by generating the feeder and PVs model. Notice that to generate the feeder model, we can use the feeder's data base available from commonly-used softwares, for example CYME. Using Algorithm 1 and flowcharts in Fig 6.3 and 6.5, one can detect the feeder conductivities and generate the feeder topology. Developed PV model can then be connected to its connecting node.

The next step is selecting a location where loss of main is occurring. Therefore, based on the formed island, its load and containing DGs, one can find the balance point at which the active/reactive power generation matches the active/reactive power consumption. We denote this balance point by LF^* and PF^* and calculate as follows:

$$LF^* = \frac{\sqrt{P^2 + (Q + Q_{cap})^2}}{\sqrt{P_L^2 + Q_L^2}}, \quad (6.21)$$

$$PF^* = \frac{P}{\sqrt{P^2 + (Q + Q_{cap})^2}}, \quad (6.22)$$

where Q_{cap} stands for reactive power injection by capacitor bank. Notice that in equations (6.21) and (6.22), we use the aggregated DG plants generation capacity (P and Q) and peak load of the feeder (P_L and Q_L).

After calculating the balance point (LF^* , PF^*), a batch-mode coarse-resolution sweep is run over the expected range of LF and PF. For all pairs of LF and PF in the batch, a simulation is run in which an island is formed, by applying loss of main, and the resulting run-on time of all DG plants in the island is recorded. Notice that the run-on time of a DG plant is defined as the time from occupance of loss of main to the plant disconnection. The NDZ is defined as the range of loads over which the

run-on times of the DG plant are longer than the IEEE 1547 limit of 2 sec. Once any NDZ is located, batches utilizing finer resolution are run to determine the peak run-on time values and refine the prediction of the shape of the NDZ in the LF-PF plane. Finally, once the NDZ location has been determined with suitable confidence and the maximum run-on times are known, utility engineers confer to decide whether the NDZ is such that the risk of islanding is negligible, or whether it represents a realistic loading scenario and additional mitigation is needed.

It is worth to emphasize that the proposed framework in this chapter is not dependent on the islanding detection schemes. The developed PV model is equipped with OVP/UVP and OFP/UFP relays. If the PV plant utilizes an active anti-islanding scheme and the algorithm of its detection scheme is provided by the PV manufacturer, then OVP/UVP and OFP/UFP relays will be operated based on the anti-islanding detection response. However, in the absence of active anti-islanding, the OVP/UVP and OFP/UFP relays in the PV model will be operated based on the voltage magnitude and the frequency at PCC.

6.7 Numerical Results

As mentioned earlier, we use MATLAB/SIMULINK as our main software platform. The feeder data we have used for simulations was accessible through CYME software. The data base includes nodes, loads, transformers, and lines/sections data of the feeder. We first exported the feeder data from CYME and imported to the MATLAB/SIMULINK software platform for our simulations. We have tested our islanding study procedure on two actual cases in National Grid USA territories. Each case includes an operating radial distribution feeder and several PV plants inservice. It is worth noting that both cases are based on actual islanding study projects defined in

Table 6.1: Voltage and frequency trip set-points of the PV plants.

Element	Pickup Range	Time Delay
Under Voltage	0.5 pu	160 ms
Under Voltage	0.88 pu	2 s
Over Voltage	1.1 pu	1 s
Over Voltage	1.2 pu	160 ms
Under Frequency	57 Hz	160 ms
Over Frequency	60.5 Hz	160 ms

National Grid USA operating region in Northeastern U.S. For each case, we run each scenario for 2.1 seconds, after occurring loss of the main feeder protective device. If any DG plant remains connected more than 2 seconds after loss of main, that will be recognized as a potential island risk. To consider the effect of all loads on the feeder, we locate the loss of source right at the substation. However, the loss of source can be defined by the user at any point of the feeder. Table 6.1 lists the settings for OVP/UVP and OFP/UFP relays used in protection scheme of DG facilities.

In current practices, DGs are operating at constant PF. In order to achieve maximum advantage of the DG, they are usually operating at unity PF. That means the reactive power injection/absorption by the DG is zero. Therefore, in our simulations, we have assumed that all DG plants are operating at unity PF. The only sources of reactive power in test distribution feeders are capacitor banks.

6.7.1 Case 1

In Case 1 a four-wire multi-grounded neutral overhead distribution feeder operated at 13.2 kV, as shown in Figure 6.13, has been considered. Note that the voltage levels for step down transformers in the figure are in kV. The feeder contains 1438 nodes, 1437 branches, 2 fixed shunt capacitor banks, and 4 transformers. The feeder's measured

peak daytime load during the past twelve months was approximately 9.469 MVA, and the daytime minimum load was measured to be approximately 3.0 MVA, which is slightly less than 1/3 of the peak load. Two PV plants, PV plant 1 and PV plant 2, are connected to the feeder. PV plant 1 is composed of 6 inverter modules, each with 500 kW capacity. The total capacity of PV plant 1 is 3 MW. PV plant 2 is composed of 4 inverter modules, each with 500 kW capacity. The total capacity of PV plant 2 is 2 MW. Both PV plants are connected to the feeder with a step up 0.32/13.2 kV transformer. In the absence of any information regarding any active anti-islanding for each plant, we have assumed that each plant utilizes passive anti-islanding protection with set-points presented in Table 6.1.

Figure 6.14 shows the run-on time over a range of LF and PF. Black bars indicate that for corresponding PF and LF, all PV plants have been disconnected within 2 seconds. Red bars indicate that for corresponding PF and LF, at least one PV plant has not been disconnected within 2 seconds. Therefore, red bars are identifying unintentional islanding situations.

Figure 6.15 shows the NDZ of each PV plant. Black plus symbols demonstrate the NDZs regarding PV plant 1 and red cross symbols represent NDZs related to PV plant 2. From this figure, the range of LF and PF in which each PV plant remains connected, can be defined. Considering these ranges, and also the daytime minimum load of the feeder, it can be concluded that the risk of unintentional islanding of interconnected PV plants is high and additional protection scheme (such as direct transfer trip) is required.

We define the high-voltage side of each PV plant's transformer connection to the utility feeder as its PCC. To illustrate the behaviour of each PV plants in their NDZs, we consider a point from their NDZs with $LF=0.6$ and $PF=0.9802$. Figure 6.16 demonstrates the frequency at PCC of PV plants for defined LF and PF . From

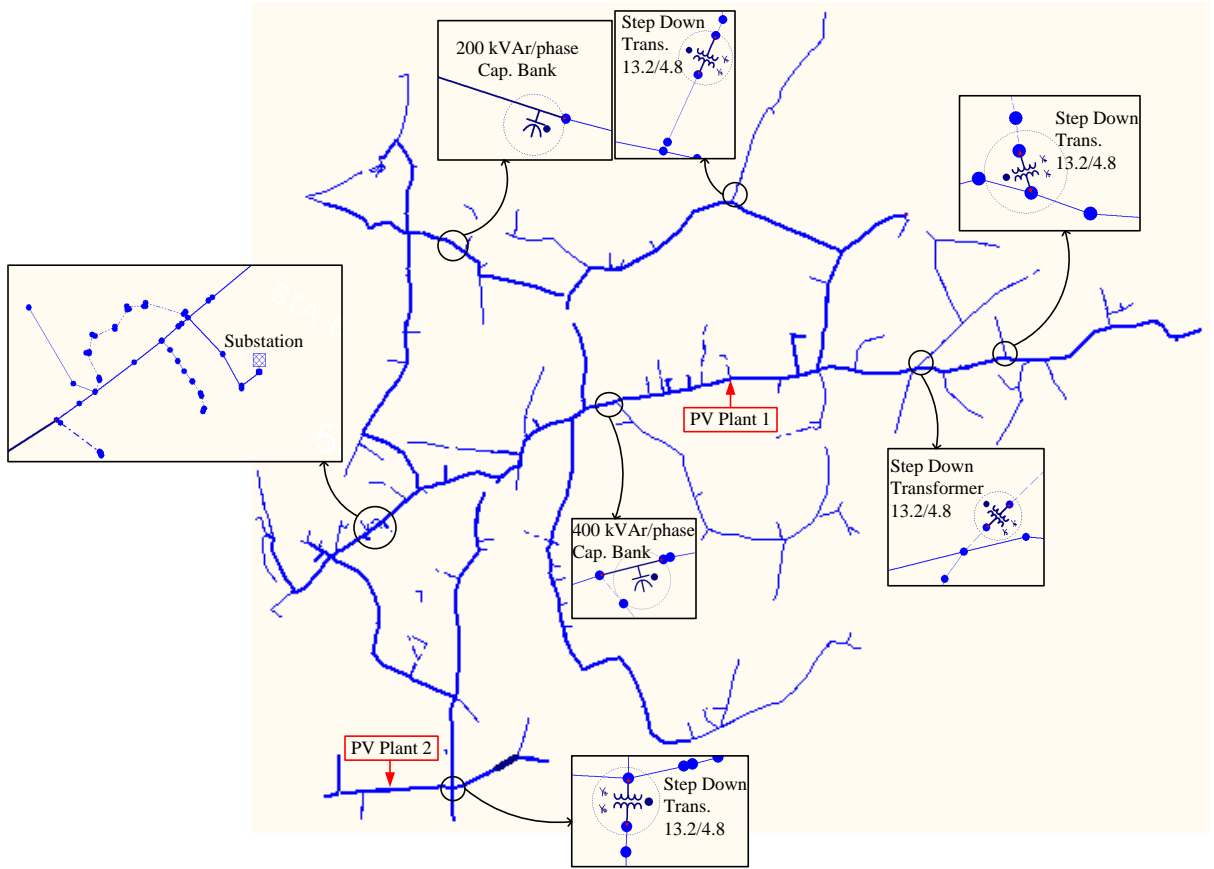


Figure 6.13: Feeder single line diagram in Case 1.

the figure, one can observe that the range of frequency, after occurrence of loss of main, for both PV plants, are not in the range to actuate the OFP/UFP relay.

Figure 6.17 and 6.18 show the voltage at PCC of PV plant 1 and PV plant 2, after occurrence of loss of main, respectively. From these figures also one can conclude that the range of voltages are not in the range to actuate the OVP/UVP relay.

6.7.2 Case 2

In Case 2 a four-wire multi-grounded neutral overhead distribution feeder operated at 13.2 kV, as shown in Figure 6.19, has been considered. The feeder contains 1614

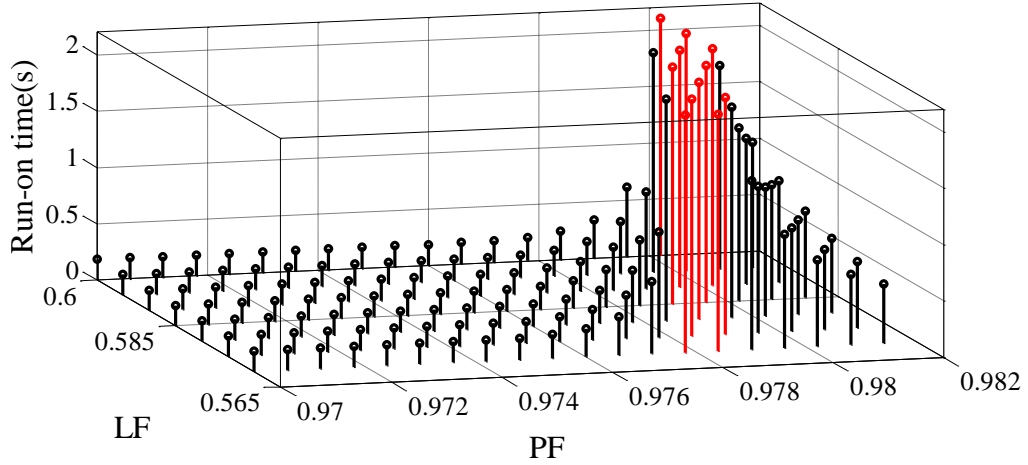


Figure 6.14: Run-on time in Case 1.

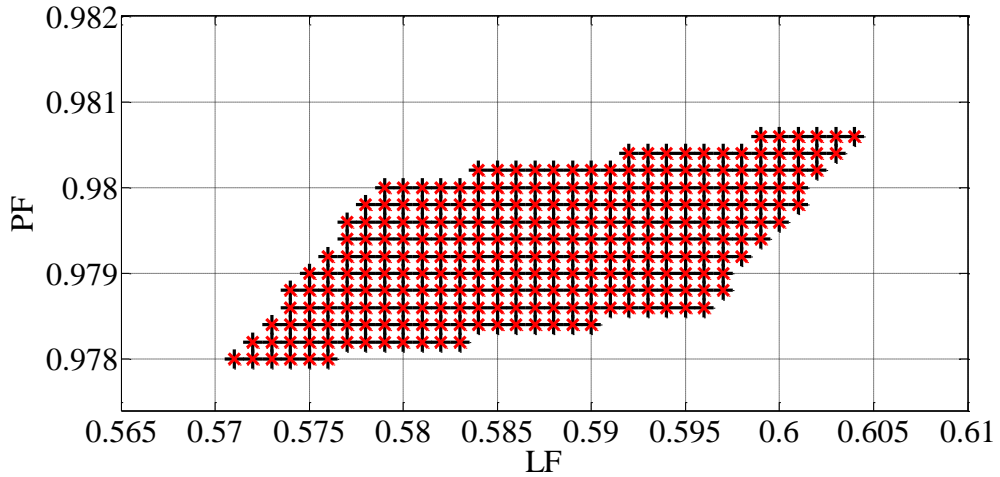


Figure 6.15: NDZ of PV plants in Case 1.

nodes, 1613 branches, 5 fixed shunt capacitor banks, and 10 transformers. Table 6.2 and 6.3 lists the specifications of transformers and capacitor banks. Two PV plants, PV plant 1 and PV plant 2, are connected to the feeder. The feeder's measured peak and minimum daytime load during the past twelve months were approximately 6.584 MVA and 2.97 MVA, respectively. PV plant 1 is composed of 4 inverter modules, each with 500 kW capacity. The total capacity of PV plant 1 is 2 MW. PV plant 2

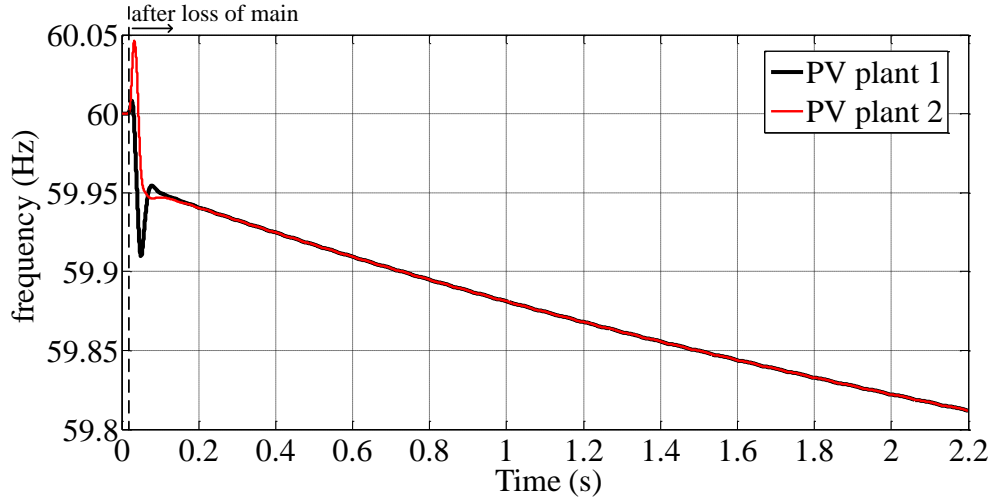
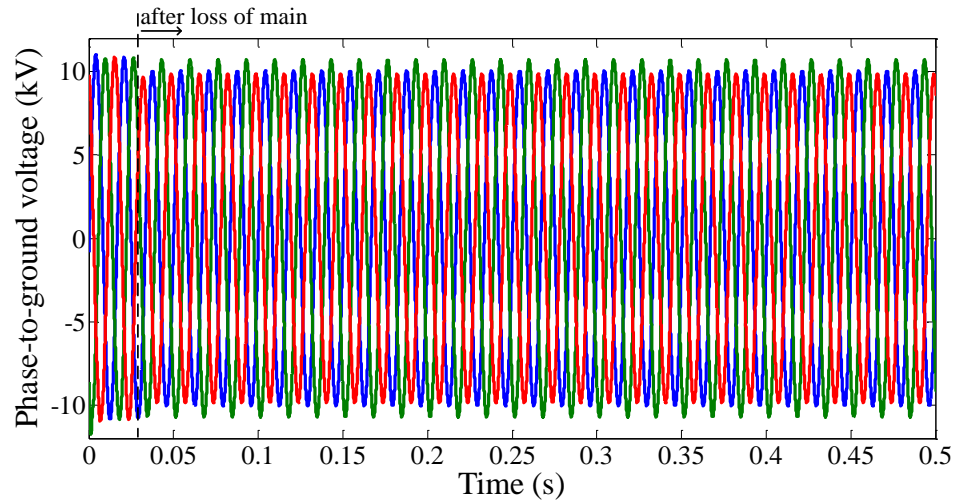


Figure 6.16: Frequency at PCC of PV plants in Case 1, with $LF=0.6$ and $PF=0.9802$.

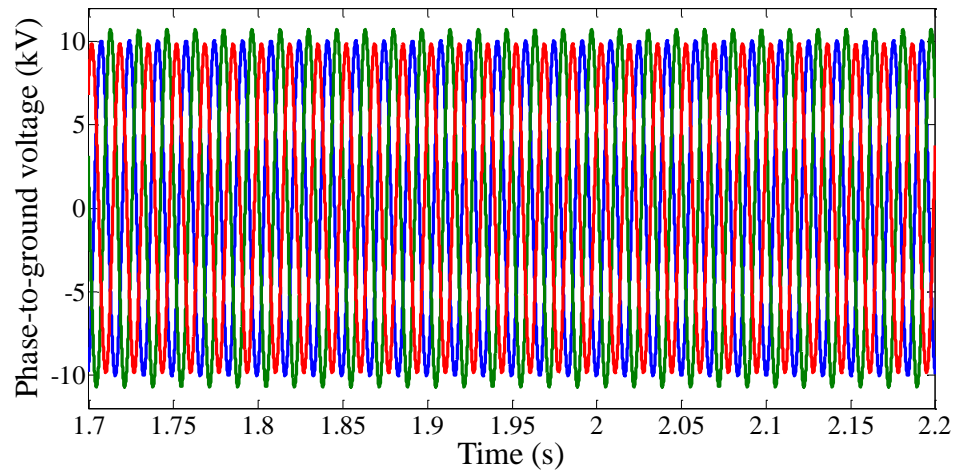
is composed of 6 inverter modules, each with 500 kW capacity. The total capacity of PV plant 2 is 3 MW. Both PV plants are connected to the feeder with a step up 0.48/13.2 kV transformer with the PCC at the 13.2 kV connection to the utility. In the absence of any information regarding any active anti-islanding for each plant, we have assumed that each plant utilizes passive anti-islanding protection with set-points presented in Table 6.1.

Figure 6.20 shows the run-on time over the expected range of LF and PF. Black bars indicate that for corresponding PF and LF, all PV plants have been disconnected within 2 seconds. Red bars indicate that for corresponding PF and LF, at least one PV plant has not been disconnected within 2 seconds. Therefore, red bars are identifying unintentional islanding situations.

Figure 6.21 shows the NDZ of each PV plant. Black plus symbols demonstrate the NDZs regarding PV plant 1 and red cross symbols represent NDZ related to PV plant 2. From this figure, the range of LF and PF in which each PV plant remains energizing the grid, can be defined. Considering the range of LF in the

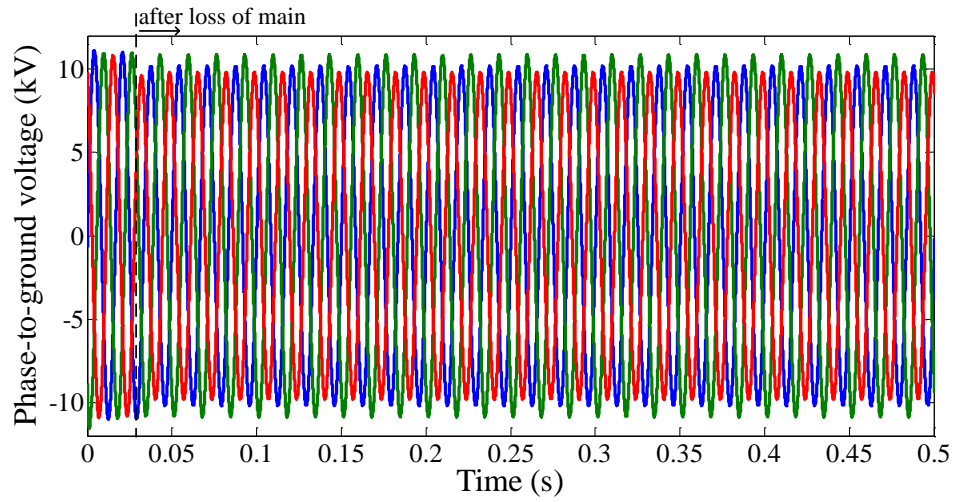


(a)

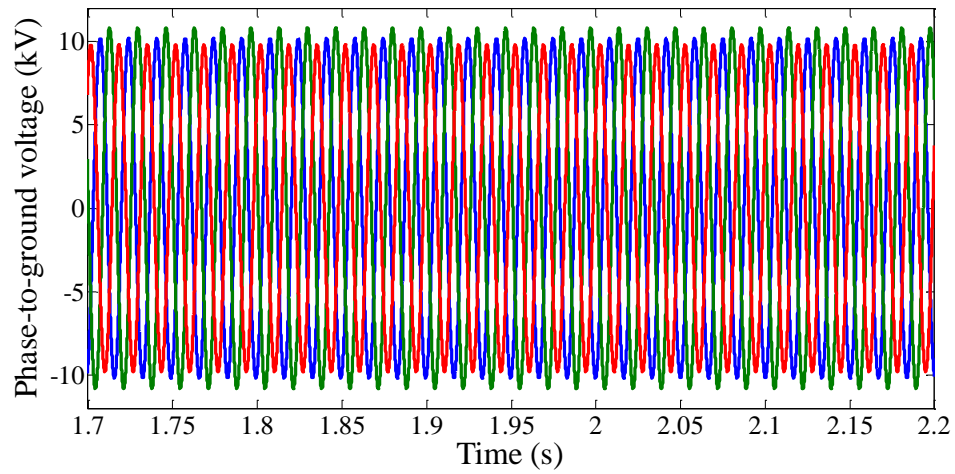


(b)

Figure 6.17: Three-phase voltage (phase A with blue, phase B with green, and phase C with red) at PCC of PV plant 1 in Case 1, with $LF=0.6$ and $PF=0.9802$: (a) For time window form 0 to 0.5 second; (b) For time window form 1.7 to 2.2 second .



(a)



(b)

Figure 6.18: Three-phase voltage (phase A with blue, phase B with green, and phase C with red) at PCC of PV plant 2 in Case 1, with $LF=0.6$ and $PF=0.9802$: (a) For time window form 0 to 0.5 second; (b) For time window form 1.7 to 2.2 second .

Table 6.2: Transformers specifications of feeder in Case 2.

Transformer	Capacity (kVA)	Primary Voltage (kV)	Secondary Voltage (kV)
Trans. 1	50	13.2	4.8
Trans. 2	50	13.2	4.8
Trans. 3	90	13.2	4.8
Trans. 4	167	13.2	4.8
Trans. 5	250	13.2	4.8
Trans. 6	50	13.2	4.8
Trans. 7	167	13.2	4.8
Trans. 8	100	13.2	4.8
Trans. 9	100	13.2	4.8
Trans. 10	50	13.2	4.8

Table 6.3: Capacitor banks specifications of feeder in Case 2.

Capacitor Bank	Capacity in Phase A (kVAr)	Capacity in Phase B (kVAr)	Capacity in Phase C (kVAr)
Cap. 1	50	0	0
Cap. 2	50	50	0
Cap. 3	100	0	0
Cap. 4	50	0	0
Cap. 5	100	100	100

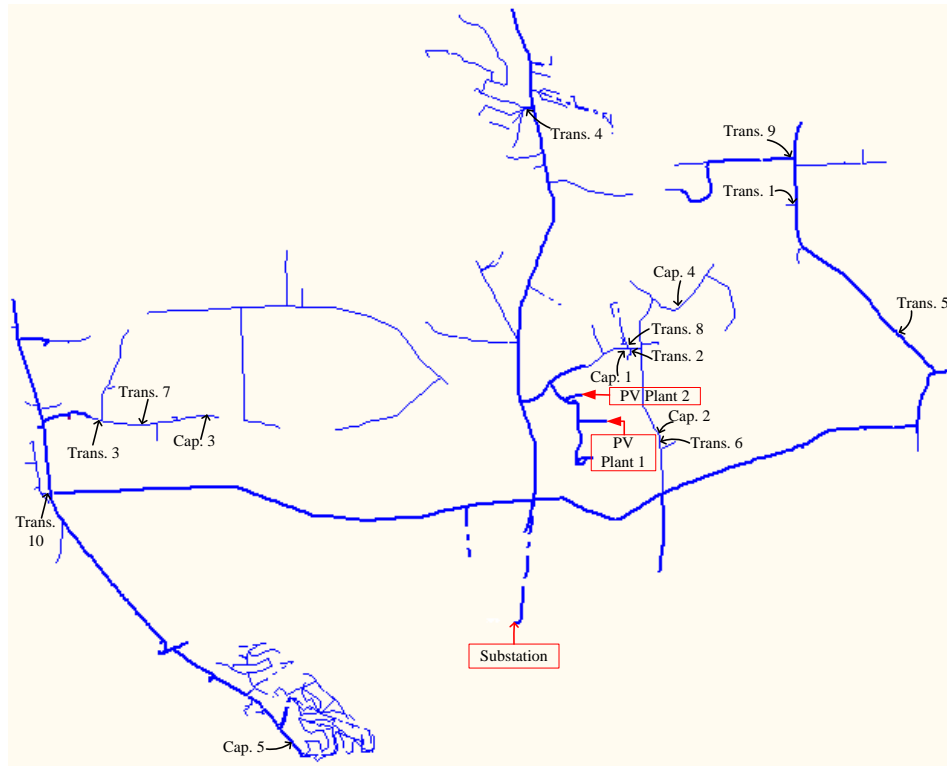


Figure 6.19: Feeder single line diagram in Case 2.

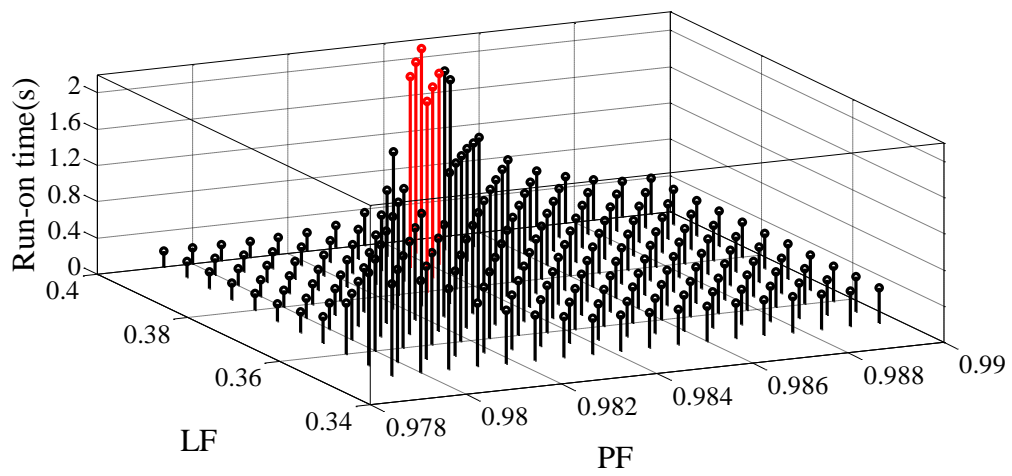


Figure 6.20: Run-on time in Case 2.

figure and day time minimum load of the feeder (0.45), it can be concluded that the risk of unintentional islanding of both PV plants is zero. Therefore, no further action regarding islanding protection is required.

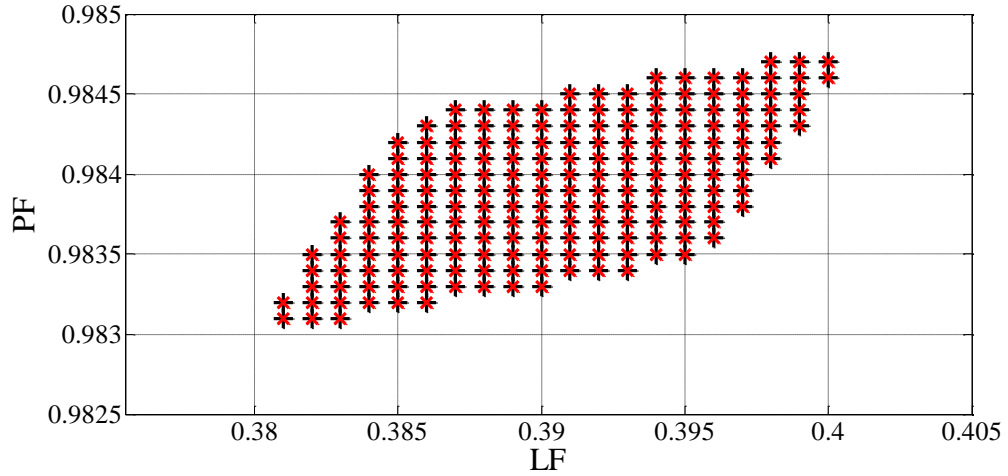


Figure 6.21: NDZ of PV plants in Case 2.

Similar to the previous case study, we define a loading condition for the feeder, from the detected NDC, and demonstrate the behaviour of each PV plant after occurrence of loss of main. The loading condition is assumed to be $LF=0.4$ and $PF=0.9848$. Figure 6.22 shows that the frequency at PCC of each PV plant is in the safe range.

Figure 6.23 and 6.24 show the voltage at PCC of PV plant 1 and PV plant 2, after occurrence of loss of main, respectively. From these figures one can observe that the range of voltages are not in the range to actuate the OVP/UVP relay.

In summary, a screening procedure for risk-of-islanding can lead to margins where risk needs further time-based transient condition analysis. The developed analytical tool then can model the radial distribution feeder and its loading characteristics profile, in order to drive better accuracy of the islanding risk. Choosing LFs and PFs

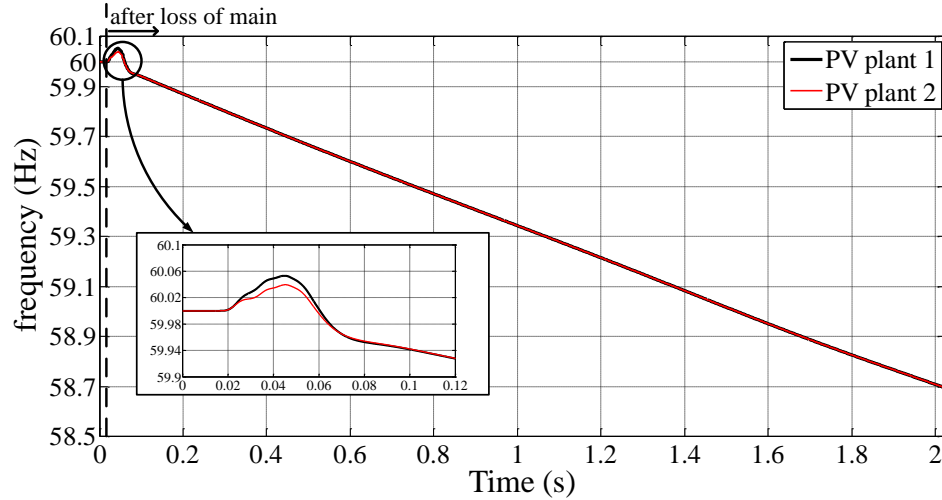
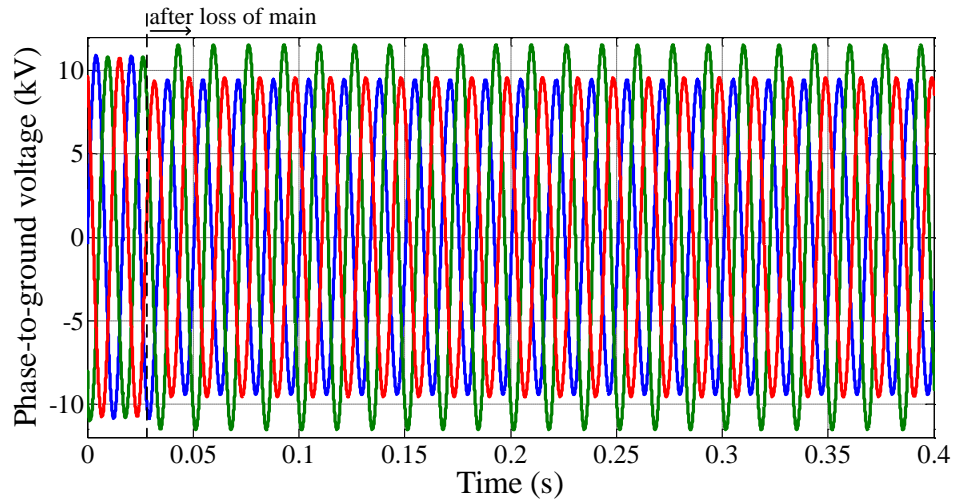


Figure 6.22: Frequency at PCC of PV plants in Case 2, with $LF=0.4$ and $PF=0.9848$.

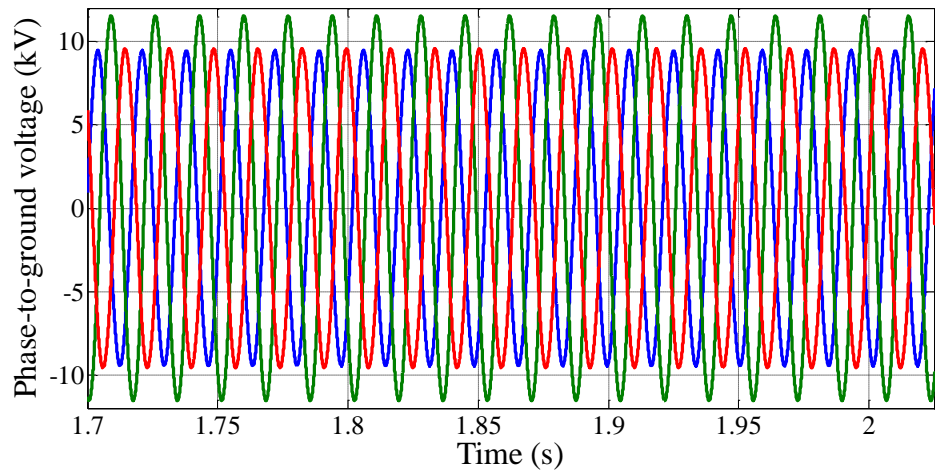
for operating conditions of the feeder's loading characteristics will drive specific case risk analysis where there are NDZs.

6.8 Conclusion

Considering the rapid growth in penetration of DGs in distribution EPS, it is crucial for the utility companies to ensure that connected DGs preclude any unintentional island risk to the grid. Several screening procedures have been reported in the literature which based on a singular or over-simplified parameters and may offer no definitive technical basis for the criteria level of screening. In this chapter, we presented a novel framework, from a utility stand point, to study the risk of unintentional islanding of interconnected DGs in a systematic manner. The framework can help utility companies to avoid extra cost, extra time, and excessive level of pessimism in assessing the risk of unintentional island. Simulation results of real case studies clearly indicate the simplicity, efficiency, and accuracy of the framework.

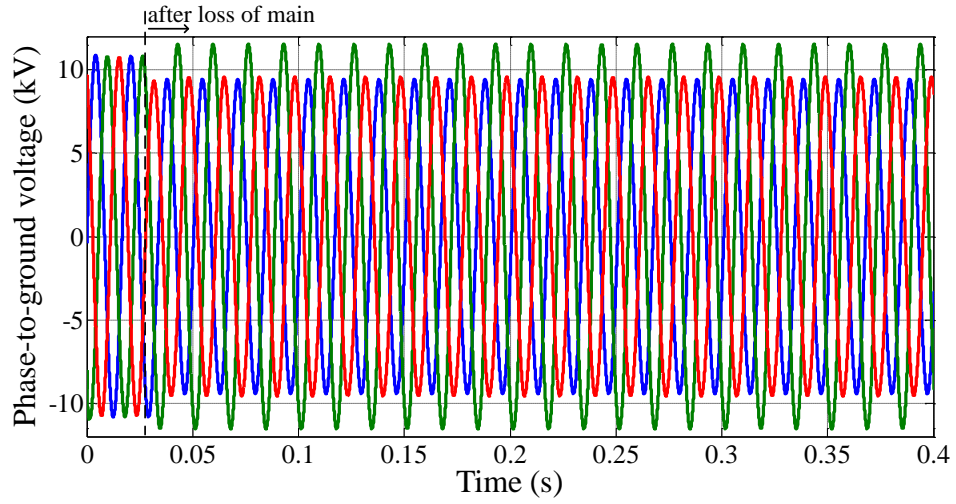


(a)

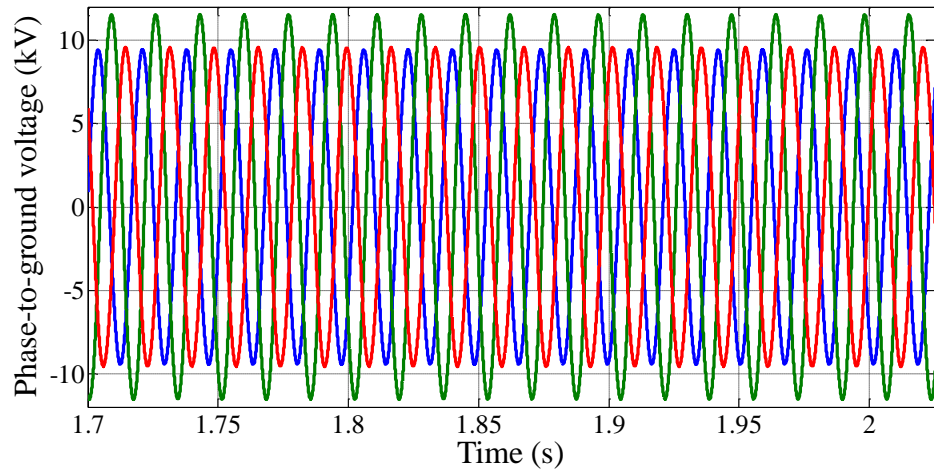


(b)

Figure 6.23: Three-phase voltage (phase A with blue, phase B with green, and phase C with red) at PCC of PV plant 1 in Case 2, with $LF=0.4$ and $PF=0.9848$: (a) For time window form 0 to 0.4 second; (b) For time window form 1.7 to 2.025 second .



(a)



(b)

Figure 6.24: Three-phase voltage (phase A with blue, phase B with green, and phase C with red) at PCC of PV plant 2 in Case 2, with $LF=0.4$ and $PF=0.9848$: (a) For time window form 0 to 0.4 second; (b) For time window form 1.7 to 2.025 second .

Chapter 7

Conclusion and Future Work

High penetration of DGs along with integration of EVs are increasingly observed worldwide. In smart grid context, these new participants can have positive and negative impacts on the system operation. This dissertation demonstrates the positive impacts of optimal coordinated DG's generation and EV's charging/discharging schedulings on the micro-grid operation. In this way, an optimization problem defined to maximize the social welfare using an SOPF, considering the stochastic nature of renewable energy resources and EV usage pattern.

By providing a comprehensive operating model of EV, the dissertation investigated other possible services form EVs which can have positive impacts on grid operation and also monetary gains for EV owners. Those services include reactive power support and frequency regulation services. A framework was developed in this dissertation to calculate reactive power supply function of EV as a step-wise ascending order function. The framework is practical which consider realistic constraints of EV's charger (current ripple on DC-link capacitor) and battery degradation factor. The frame work is easy to be implemented for a large group of EVs in a real-time basis. In addition to reactive power support, a multi-level approach was presented in the

dissertation to engage EVs in frequency regulation services. Complying with FERC Order 755, the approach calculates optimal bidding components including available capacity and energy cost function for the service. Simulation results clearly showed the opportunity for EV owners to generate revenue streams through providing reactive power support and frequency regulation services, without lowering their comfort level.

In this dissertation, a procedure, which can be used by utility companies, is developed to assess the risk of unintentional islanding of interconnected DGs into the distribution EPS. The developed procedure is simple to implement and fast, which means savings in cost and time of islanding studies. The procedure is not dependent on DG technology and can be used for other kinds of DG technology. The procedure is also independent of the kind of anti-islanding schemes used in DGs (active/passive) and can be used for any islanding case studies in radial distribution feeder.

Methodologies and results presented in this dissertations open new research horizons from different perspectives. The developed frameworks for exploiting reactive power support and frequency regulation services from EVs are from aggregator's perspective. However, studying the EV's participation in those services from the SO's stand point could be an exciting research area. Due to the location of EVs in the EPS (near to load centers) and low cost of providing the services, they might have significant impacts on the system operation cost.

Another possible interesting research area can be defined based on results provided regarding islanding studies. In the case of high DG penetration, studying NDZ with fixed DG output power (usually at maximum level) and variable LF and PF may not be enough. The reason is that a fraction of DG output power can lead to a reasonably high risky LF and PF in order to have match between load and generation. Therefore, the NDZ has to be explored in three domains: LF; PF; and DG output power. To explore the NDZ in three domains, running simulation for more samples

is inevitable. That means the time of simulation will increase. To overcome this challenge, appropriate stochastic modeling and analysis which are fast to implement and accurate enough, are necessary.

Glossary

ACE Area Control Error. 126

AGC Automatic Generation Control. 7

cdf Cumulative Distribution Function. 24

DER Distributed Energy Resources. 5

DG Distributed Generator. 2

DR Demand Response. 3

EPS Electric Power System. 3

ERCOT Electric Reliability Council of Texas. 3

EV Electric Vehicle. 3

FERC Federal Energy Regulatory Commission. 7

IREC Interstate Renewable Energy Council. 159

ISO Independent System Operator. 126

MADRI Mid-Atlantic Distributed Resources Initiative. 156

NDZ Non-Detection Zone. 155

NYISO New York Independent System Operator. 43

OPF Optimal Power Flow. 5

PCC Point of Common Coupling. 3

pdf Probability Distribution Function. 24

PJM Pennsylvania-New Jersey-Maryland Interconnection. 1

PLL Phase Locked Loop. 169

PV Photovoltaic. 3

PWM Pulse Width Modulation. 81

RPSP Reactive Power Service Provider. 6

RTO Regional Transmission Operator. 126

SGIP Small Generator Interconnection Procedure. 156

SO System Operator. 3

SOC State of Charge. 8

SOPF Stochastic Optimal Power Flow. 5

WT Wind Turbine. 3

Bibliography

- [1] W. A. Wolf, “Great achievements and grand challenges,” *Nat. Acad. Eng. Bridge*, vol. 30, no. 3/4, p. 6, 2000.
- [2] C. S. Leung and P. Meisen, “How electricity consumption affects social and economic development by comparing low, medium, and high human development countries,” Global Energy Network Institute, 2005. Available: <http://www.geni.org/globalenergy/issues/global/qualityoflife/HDI-vs-Electricity-Consumption-2005-07-18.pdf>.
- [3] M. G. Simoes, R. Roche, E. Kyriakides, S. Suryanarayanan, B. Blunier, K. D. McBee, P. H. Nguyen, P. F. Riberio, and A. Miraoui, “A comparison of smart grid technologies and progresses in Europe and the U.S.,” *IEEE Transactions on Industry Applications*, vol. 48, no. 4, pp. 1154–1162, 2012.
- [4] United States Department of Energy, “2010 Smart Grid System Report,” Report to Congress, 2012.
- [5] Smart Grid Consumer Collaborative, “Smart grid economic and environmental benefits, a review and synthesis of research on smart grid benefits and costs,” October 2013. Available: <http://smartgridcc.org/wp-content/uploads/2013/10/SGCC-Econ-and-Environ-Benefits-Full-Report.pdf>.

- [6] P. Siano, "Demand reponse and smart grid - A survey," *Renewable and Sustainable Energy Review*, vol. 30, pp. 461–478, 2014.
- [7] R. Miceli, "Energy management and smart grid," *Energies*, vol. 6, no. 4, pp. 2262–2290, 2013.
- [8] A. Vejdani, "Smart integration," *IEEE Power and Energy Magazine*, vol. 6, no. 6, pp. 71-79, 2008.
- [9] H. Zareipour, K. Battacharya, and C. Canizares, "Distributed generation: current status and challenges," In Proc. of *Annual North American Power Symposium*, pp. 1-8, 2004.
- [10] P1547 Standard Series for Interconnecting Distributed Resources with Electric Power Systems, IEEE 1547 Working Group, 2003.
- [11] T. Ackerman, "Electricity market regulations and their impact on distributed generation," In Proc. of *Electric Utility Deregulation and Restructuring and Power Technologies*, pp. 608-613, 2000.
- [12] A. P. S. Melipoulos, "Distributed energy source: needs for analysis and design tools," In Proc. of *IEEE Vancouver Summer Meeting*, pp. 548-550, 2001.
- [13] C. Mingyong, A. Xin, and L. Zhili, "Study on low-carbon generation scheduling of distribution containing microgrid," In Proc. of *5th International Conference on Critical Infrastructure*, pp. 1-4, 2010.
- [14] D. Pudjianto and G. Strbac, "Investigation of regulatory, commercial, economic and environmental issues in microgrid," *International Journal of Distributed Energy Resources*, vol. 2, no. 3, pp. 245-259, 2006.

- [15] A. G. Tsikalakis and N. D. Hatziargyriou, "Environmental benefits of distributed generation with and without emissions trading," *Energy Policy*, vol. 35, no. 6, pp. 3395-3409, 2007.
- [16] F. A. Mohamed and H. N. Koivo, "System modeling and online optimal management of microgrid using multiobjective optimization," In Proc. of *International Conference on Clean Electrical Power*, pp. 148-153, 2007.
- [17] C. A. Hernandez-Aramburo, T. C. Green, and N. Mugniot, "Fuel consumption minimization of a microgrid," *IEEE Transaction on Industry Applications*, vol. 41, no. 3, pp. 673-681, 2005.
- [18] Emission of greenhouse gases report, Energy Information Administration, DOE/EIA-0573(2008), December 2009.
- [19] "Getting warmer: US CO₂ emission from power plants emissions rise 5.6% in 2010," Environment Integrity Project, 2011. Available: http://www.environmentalintegrity.org/documents/CO2Report_2011RJD21811final.pdf.
- [20] J-H. Choi, J-C. Kim, and S-I. Moon, "Integration operation of dispersed generations to automated distribution network for network reconfiguration," In Proc. of *Power Technology*, 2003.
- [21] Annual energy outlook 2011, Energy Information Administration, DOE/EIA-0383(2010), December 2010.
- [22] S. Braithwait, D. Hansen, and M. O'Sheasy, "Retail electricity pricing and rate design in evolving market," *Edison Electric Institute*, 2007.
- [23] Available: <http://www.eia.gov/oiaf/1605/coefficients.html>.

- [24] Available: http://www.irrcinstitute.org/pdf/irrc_trucost_0906.pdf.
- [25] M. R. Haghifam and M. Omidvar, "Wind farm modeling in reliability assessment of power system," In Proc. of *International Conference on Probabilistic Methods Applied to Power Systems*, pp. 1-5. 2006.
- [26] T. Jin and Z. Tian, "Uncertainty analysis for wind energy production with dynamic power curves," In Proc. of *IEEE 11th International Conference on Probabilistic Methods Applied to Power Systems*, pp. 745–750, 2010.
- [27] P. Giorsetto and K.F. Utsurogi, "Development of a new procedure for reliability modeling of wind turbine generators," *IEEE Transactions on Power Apparatus and Systems*, vol. PAS-102, no. 1, pp. 134–143, 1983.
- [28] C. Abbey and G. Joos, "Supercapacitor energy storage for wind energy applications," *IEEE Transactions on Industrial Applications*, Vol. 43, pp.769–776, 2007.
- [29] S.L. Ye and B. Sun, "Application of flywheel battery in solar power system," In Proc. of *International Conference on Energy and Environment Technology*, pp.533–536, 2009.
- [30] Y. Liu and C. Jiang, "A review on technologies and methods of mitigating impacts of large-scale intermittent renewable generations on power system," *Research Journal of Applied Sciences, Engineering and Technology*, vol. 5, no. 9, pp.2765–2770, 2013.
- [31] Jerry Mitlitski (2011-02-18), "Raising the Volt-Age: Is Obama's Goal of 1 Million Electric Vehicles on U.S. Highways by 2015 Realistic?," *Scientific American*, Retrieved 2012-05-11.

- [32] S. J. Gunter, K. K. Afridi, and D. J. Perreault, "Optimal design of grid-connected PEV charging systems with integrated distributed resources, *IEEE Transactions on Smart Grid*, vol. 4, no. 2, pp. 956–967, 2013.
- [33] H. K. Nguyen and J. B. Song, "Optimal charging and discharging for multiple PHEVs with demand side management in vehicle-to-building," *Journal of Communications and Networks*, vol. 14, no. 6, pp.662–671, 2012.
- [34] S. Kabisch, A. Schmitt, M. Winter, and J. Heuer, "Interconnections and communications of electric vehicles and smart grids," *Smart Grid Communications*, pp. 161–166, 2010.
- [35] K. Qian, C. Zhou, M. Allan, and Y. Yuan, "Modeling of load demand due to EV battery charging in distribution systems, *IEEE Transactions on Power System*, vol. 26, no. 2, pp. 802–810, 2011.
- [36] A. Mendoza and J. Argueta, "Performance characterization, GM EV1 Panasonic lead acid battery," *Southern California EDISON*, April, 2000.
- [37] M. Aien, R. Ramezani, and S. M. Ghavami, "Probabilistic load flow considering wind generation uncertainty," *Engineering Technology and Applied Science Research*, vol. 1, no. 5, pp. 126–132, 2011.
- [38] Chevy Volt Specifications, <http://www.chevrolet.com/volt/>
- [39] Summary of Travel Trends, 2009 National Household Travel Survey, U.S. Department of Transportation, 2009.
- [40] Wind speed data, online. Available: <http://www.windenergy.org/datasites/0000-aeiwtc/>.

- [41] Y.V. Makarov, R.T. Guttromson, Z. Huang, K. Subbarao, P.V. Etingov, B.B. Chakrabarti, and J. Ma, “Incorporating wind generation and load forecast uncertainties into power grid operations,” *Wind Energy Management System EMS Integration Project*, 2009, online. Available: http://www.pnl.gov/main/publications/external/technical_reports/PNNL-19083.pdf.
- [42] EPA Cross-State Air Pollution Rule, *Air Quality Technical Advisory Committee*, 2011.
- [43] S. B. Peterson, J. F. Whitacre, and J. Apt, “The economics of using plug-in hybrid electric vehicle battery packs for grid storage,” *Journal of Power Sources*, vol. 195, pp. 2377–2384, 2010.
- [44] Electric Vehicle Market Forecasts, [Online]. Available: http://www.pikeresearch.com/research/electric_vehicle_market_forecasts.
- [45] M. A. Ortega-Vazquez, F. Bouffard, and V. Silva, “Electric vehicle aggregator/system operator coordination for charging scheduling and services procurement,” *IEEE Transactions on Power Systems*, vol. 28, no. 2, pp. 1806–1815, 2013.
- [46] C. Jin, J. Tang, and P. Ghosh, “Optimizing electric vehicle charging with energy storage in electricity market,” *IEEE Transactions on Smart Grid*, vol. 4, no. 1, pp. 311–320, 2013.
- [47] J. C. Forman, “Minimally invasive characterization of lithium phosphate battery electrochemical and health models using fisher information and optimal experimental design,” Ph.D. dissertation, Department of Mechanical Engineering, University of Michigan, Ann Arbor, MI, 2012.

- [48] K. W. E. Cheng, B. P. Divakar, H. Wu, K. Diang, and H. Fai Ho, "Battery-management system (BMS) and SOC developement for electric vehicles," *IEEE Transactions on Vehicular Technology*, vol. 60, no. 1, pp. 76–88, 2011.
- [49] Y. Cao, S. Tang, C. Li, P. Zhang, Y. Tan, Z. Zhang, and J. Li, An optimized EV charging model considering TOU prices and SOC curve, *IEEE Transactions on Smart Grid*, vol. 3, no. 1, pp. 388-393, 2012.
- [50] R. Carnegie, D. Gotham, D. Nderitu, and P. V. Preckel, "Utility scale energy storage systems: benefits, applications, and technologies," *State Utility Forecasting Group*, 2013. Available: <http://www.purdue.edu/discoverypark/energy/assets/pdfs/SUFG/publications/SUFG\%20Energy\%20Storage\%20Report.pdf>.
- [51] C. Jin, J. Tang, and P. Ghosh, "Optimizing electric vehicle charging with energy storage in the electricity market," *IEEE Transactions on Smart Grid*, vol. 4, no. 1, pp. 311–320, 2013.
- [52] Availabale: www.nyiso.com.
- [53] Federal Energy Regulatory Comission, Reactive Power Staff Report, April 2014. Available: <http://www.ferc.gov/legal/staff-reports/2014/04-11-14-reactive-power.pdf>.
- [54] M. Ehsani, M. Falahi, and S. Lotfifard, "Vehicle to grid services: Potential and applications," *Energies*, vol. 5, no. 10, pp. 4076–4090, 2012.
- [55] M. C. Kisacikoglu, B. Ozpineci, and L. M. Tolbert, "Reactive power operation analysis of a single-phase EV/PHEV bidirectional battery charger," In Proc. of

- IEEE 8th International Conference on Power Electronics and ECCE Asia*, pp. 585–592, 2011.
- [56] C. Guille and G. Gross, “A conceptual framework for the vehicle-to-grid (V2G) implementation,” *Energy Policy*, vol. 37, no. 11, pp. 4379–4390, 2009.
- [57] V. Monterio, J. G. Pinto, B. Exposto, H. Goncalves, J. C. Ferreira, C. Couto, and J. L. Afonso, “Assessment of a battery charger for electric vehicles with reactive power control,” In Proc. of *38th Annual Conference on IEEE Industrial Electronics Society*, pp. 5142–5147, 2012.
- [58] T. Noda, Y. Kabasawa, K. Fukushima, K. Nemoto, and S. Uemura, “A method for compensating customer voltage drops due to nighttime simultaneous charging of EVs utilizing reactive power injection from battery chargers,” *Electrical Engineering in Japan*, vol. 184, no. 1, pp. 19–29, 2013.
- [59] C. Wu, H. Mohsenian-Rad, J. Huang, and J. Jatskevich, “PEV-based combined frequency and voltage regulation for smart grid,” In Proc. of *IEEE Power and Energy Society Innovative Smart Grid Technologies*, pp. 1–6, 2012.
- [60] B. Jiang and Y. Fei, “Decentralized scheduling of PEV on-street parking and charging for smart grid reactive power compensation,” In Proc. of *IEEE Power and Energy Society Innovative Smart Grid Technologies*, pp. 1–6, 2013.
- [61] H. Feshki Farahani, H. A. Shayanfar, and M. S. Ghazizadeh, “Modeling of stochastic behavior of plug-in hybrid electric vehicle in a reactive power market,” *Electrical Engineering*, vol. 96, no. 1, pp. 1–13, 2012.

- [62] J. Zhong and K. Bhattacharya, "Toward a competitive market for reactive power," *IEEE Transactions on Power Systems*, vol. 17, no. 14, pp. 1206–1215, 2002.
- [63] NYISO, New York Independent System Operator Ancillary Service Manual, March 2013.
- [64] NYISO. Available: http://www.nyiso.com/public/webdocs/markets_operations/market_data/pricing_data/rate_schedule_2/2013/2013_OATT_MST_Schedule-2-VSS_Rates_FINAL.pdf.
- [65] CaISO, California Independent System Operator Tariff Sections-section 8, Oct. 2013.
- [66] NEISO, ISO New England Manual for Tariff Accounting, Oct. 2010.
- [67] PJM, Open Access Transmission Tariff Accounting, Sept. 2013.
- [68] ERCOT, ERCOT Protocols-Section 6: Ancillary Services, Sept. 2010.
- [69] ERCOT, An introductory guide to how the ERCOT facilitates the competitive power market, 2005.
- [70] E. Ismaeil, K. Bhattacharya, C. Canizares, M. F. Anjos, and J. Pan, "A procurement market model for reactive power services considering system security," *IEEE Transactions on Power Systems*, vol. 23, no. 1, pp. 137–149, 2008.
- [71] K. Bhattacharya and J. Zhong, "Reactive power as an ancillary service," *IEEE Transactions on Power Systems*, vol. 16, no. 2, pp. 294–300, 2001.

- [72] E. Ismaeil, K. Bhattacharya, and C. Canizares, “A unified framework for reactive power management in deregulated electricity markets,” In Proc. of *IEEE-PES Power Systems Conference and Exposition*, pp. 901–907, 2006.
- [73] C. Canizares, E. Ismaeil, K. Bhattacharya, H. Haghghat, J. Pan, and C. Tang, “Re-defining the reactive power dispatch problem in the context of competitive electricity markets,” *IET Generation, Transmission & Distribution*, vol. 4, no. 2, pp. 162–177, 2010.
- [74] S. Rahman and Y. Teklu, “Role of the electric vehicle as a distributed resource,” In Proc. of *IEEE Power Engineering Society Winter Meeting*, pp. 23–27, 2000.
- [75] W. Kempton and J. Tomic, “Vehicle-to-grid power fundamentals: Calculating capacity and net revenue,” *Journal of Power Sources*, vol. 144, no. 1, pp. 268–279, 2005.
- [76] W. Kempton and J. Tomic, “Vehicle-to-grid power implementation: From stabilizing the grid to supporting large-scale renewable energy,” *Journal of Power Sources*, vol. 144, no. 1, pp. 280–294, 2005.
- [77] K. Clement, E. Haesen, and J. Driesen, “Coordinated charging of multiple plug-in hybrid electric vehicles in residential distribution grids,” In Proc. of *IEEE/PES Power Systems Conference and Exposition*, pp. 1–7, 2009.
- [78] IPCC Fifth Assessment Synthesis Report, *Climate Change 2014 Synthesis Report*, November, 2014.
- [79] W. Kempton, V. Udo, K. Huber, K. Komara, S. Letendre, S. Baker, D. Brunner, and N. Pearre, “A test of vehicle-to-grid (V2G) for energy storage and frequency regulation in the PJM system,” University of Delaware, Newark, Report, 2008.

- [80] B. J. Kirby, “Frequency regulation basics and trends,” Oak Ridge National Laboratory, Technical Report, 2004.
- [81] A. D. Papalexopoulos and P. E. Andrianesis, “Performance-based pricing of frequency regulation in electricity markets,” *IEEE Transactions on Power Systems*, vol. 29, no. 1, 2014.
- [82] Federal Energy Regulatory Commission. Order No. 755. Frequency Regulation Compensation in the Organized Wholesale Power Markets, Oct. 20, 2011. Available: <http://www.ferc.gov>.
- [83] J. Zhong, L. He, C. Li, Y. Cao, J. Wang, B. Fang, L. Zeng, and G. Xiao, “Coordinated control for large-scale EV charging facilities and energy storage devices participating in frequency regulation,” *Applied Energy*, vol. 123, pp. 253–262, 2014.
- [84] E. Sortomme and M. A. El-Sharkawi, “Optimal charging strategies for unidirectional vehicle-to-grid,” *IEEE Transactions on Smart Grid*, vol. 2, no. 1, pp. 131–138, 2011.
- [85] S. Shao, M. Pipattanasomporn, and S. Rahman, “Demand response as a load shaping tool in an intelligent grid with electric vehicles,” *IEEE Transactions on Smart Grid*, vol. 2, no. 4, pp. 624–631, 2011.
- [86] S. Shao, M. Pipattanasomporn, and S. Rahman, “Grid integration of electric vehicles and demand response with customer choice,” *IEEE Transactions on Smart Grid*, vol. 3, no. 1, pp. 543–549, 2012.

- [87] J. Soares, H. Morais, T. Sousa, Z. Vale, and P. Faria, “Day-ahead resource scheduling including demand response for electric vehicles,” *IEEE Transactions on Smart Grid*, vol. 4, no. 1, pp. 596–605, 2013.
- [88] F. C. Lu and Y. Y. Hsu, “Reactive power/voltage control in a distribution substation using dynamic programming,” *IEE Proceedings-Generation, Transmission and Distribution*, vol. 142, no. 6, pp. 639–645, 1995.
- [89] M. C. Kisacikoglu, B. Ozpineci, and L. M. Tolbert, “Examination of a PHEV bidirectional charger for V2G reactive power compensation,” In Proc. of *25th Annual IEEE Applied Power Electronics Conference and Exposition*, pp.458–465, 2010.
- [90] M. C. Kisacikoglu, B. Ozpineci, and L. M. Tolbert, “EV/PHEV bidirectional charger assessment for V2G reactive power operation,” *IEEE Transactions on Power Electronics*, vol.28, no.12, pp. 5717–5727, 2013.
- [91] S. Boyd and L. Vandenberghe, “Convex optimization,” *Cambridge University Press*, Cambridge, U. K., 2004.
- [92] H. Mohsenian-Rad and A. Leon-Garcia, “Optimal residential load control with price prediction in real-time electricity pricing environment,” *IEEE Transactions on Smart Grid*, vol. 1, no. 2, pp. 120–133, 2010.
- [93] J. Aho, L. Y. Pao, P. Fleming, and E. Ela, “Controlling wind turbines for secondary frequency regulation: an analysis of AGC capabilities under new performance based compensation policy,” In Proc. of *13th International Wind Integration Workshop*, pp. 1–6, 2014.

- [94] N. Jaleeli, L. Vanslyck, D. Ewart, L. Fink, and A. Hoffmann, "Understanding automatic generation control," *IEEE Transactions on Power Systems*, vol. 7, no. 3, pp. 1106–1122, 1992.
- [95] D. C. H. Prowse, P. Koskela, T. A. Grove, and L. R. Larson, "Experience with joint AGC regulation," *IEEE Transactions on Power Systems*, vol. 9, no. 4, pp. 1974–1979, 1994.
- [96] I. Ibraheem, P. Kumar, and D. P. Kothari, "Recent philosophies of automatic generation control strategies in power systems," *IEEE Transactions on Power Systems*, vol. 20, no. 1, pp. 346–357, 2005.
- [97] J. Kumar, K. H. Ng, and G. Sheble, "AGC simulator for price-based operation, part 1: a model," *IEEE Transactions on Power Systems*, vol. 12, no. 2, pp. 527–532, 1997.
- [98] M. Scherer, E. Iggland, A. Ritte, and G. Anderson, "Improved frequency bias factor sizing for non-interactive control," In Proc. of *Cigre Session 44*, pp. 1–6, 2012.
- [99] J. L. Rodriguez-Amenedo, S. Arnalte, and J. C. Burgos, "Automatic generation control of a wind farm with variable speed wind turbines," *IEEE Transactions on Energy Conversion*, vol. 17, no. 2, pp. 279–284, 2002.
- [100] Q. Liu and M. Ilic, "Enhanced automatic generation control (E-AGC) for future electric energy systems," In Proc. of *IEEE Power and Energy Society General Meeting*, pp. 1–8, 2012.

- [101] L. Wang and D. Chen, "Extended term dynamic simulation for AGC with smart grids," In Proc. of *IEEE Power and Energy Society General Meeting*, pp. 1–7, 2011.
- [102] C. C. Liu, A. Bose, and J. Cardell, "Agent modeling for integrated power systems," Power Systems Engineering Research Center, Publication 08-17, 2008.
- [103] J. Ellison, L. S. Tesfatsion, V. W. Loose, and R. H. Byrne, "Project report: a survey of operating reserve markets in U.S. ISO/RTO-managed electric energy regions," Sandia National Laboratories, SAND2012-1000, 2012.
- [104] D. Apostolopoulou, "Enhanced automatic generation control with uncertainty," Ph.D. dissertation, Department of Electrical and Computer Engineering, University of Illinois at Urbana-Champaign, Illinois, 2014.
- [105] D. Apostolopoulou, P. W. Sauer, and A. D. Dominguez-Garcis, "Automatic generation control and its implementation in real time," In Proc. of *47th International Conference on System Science*, pp. 2444–2452, 2014.
- [106] O. Leitmann, "Energy storage for frequency regulation on the electric grid," Ph.D. dissertation, Department of Electric Engineering and Computer Science, Massachusetts Institute of Technology, Cambridge, MA, 2012.
- [107] C. Guille and G. Gross, "A conceptual framework for the vehicle to grid (V2G) implementation," *Energy Policy*, vol. 37, no. 11, pp. 4379–4390, 2009.
- [108] H. Yang, C. Y. Chung, and J. Zhao, "Application of plug-in electric vehicles to frequency regulation based on distributed signal acquisition via limited communication," *IEEE Transactions on Power Systems*, vol 28, no. 2, 2013.

- [109] J. Zhong, L. He, C. Li, Y. Cao, J. Wang, B. Fang, L. Zeng, and G. Ziao, “Coordinated control of large-scale EV charging facilities and energy storage devices participating in frequency regulation,” *Applied Energy*, vol. 123, pp. 253–262, 2014.
- [110] J. A. Pecas Lopes, N. Hatziargyriou, J. Mutale, P. Djapic, and N. Jenkins, “Integrating distributed generation into electric power systems: A review of drivers, challenges and opportunities,” *Electric Power System Research*, vol. 77, pp. 1189–1903, 2007.
- [111] L. A. C. Lopes and Z. Yongzheng, “Islanding detection assessment of multi-inverter systems with active frequency drifting methods,” *IEEE Transactions on Power Systems*, vol. 23, no. 1, pp. 480–486, 2008.
- [112] H. G. Gonzales and R. Iravani, “Current injection for active islanding detection of electronically-interfaced distributed resources,” *IEEE Transactions on Power Delivery*, vol. 21, no. 3, pp. 1698–1705, 2006.
- [113] M. Yingram and S. Premrundeepracharn, “Investigation over/undervoltage protection of passive islanding detection method of distributed generations in electrical distribution systems,” In proc. of *International Conference on Renewable Energy Research and Applications*, pp. 1–5, 2012.
- [114] W. Xu, K. Mauch, and S. Martel, “An assessment of distributed generation islanding detection methods and issues for Canada,” CANMET Energy Technology Center, Varennes, Nat. Resources Canada, Technical Report 2004074.
- [115] D. Salles, W. Freitas, J. C. M. Vieira, and W. Xu, “Nondetection index of anti-islanding passive protection of synchronous distributed generators,” *IEEE Transactions on Power Delivery*, vol. 27, no. 3, pp. 1509–1518, 2012.

- [116] M. E. Ropp and A. Ellis, “Guidelines document for helping utility protection engineers determine when additional anti-islanding studies are prudent,” In Proc. of *IEEE 38th Photovoltaic Specialists Conference*, pp. 748–752, 2012.
- [117] M. Ropp and A. Ellis, “Suggested guidelines for assessment of DG unintentional islanding risk,” SANDIA Report, SAND2012-1365, 2012.
- [118] P. Sheaffer, “Interconnection of distributed generation to utility systems: recommendations for technical requirements, procedures and agreements, and emerging issues,” The Regulatory Assistance Project, 2011.
- [119] R. Elliott, “The integration of distribution level generation & storage into the grid: problems and solutions,” State of California Public Utilities Commission Energy Division, 2014.
- [120] M. Coddington, A. Ellis, K. Lynn, A. Razon, T. Key, B. Kroposki, B. Mather, R. Hill, K. Nicole, and J. Smith, “Updating technical screens for PV interconnection,” In Proc. of *IEEE 38th Photovoltaic Specialists Conference*, pp. 1768–1773, 2012.
- [121] M. Coddington, A. Ellis, K. Lynn, A. Razon, T. Key, B. Kroposki, B. Mather, R. Hill, K. Nicole, and J. Smith, “Updating interconnection screens for PV system integration,” National Renewable Energy Laboratory, Technical Paper NREL/TP-5500-54063, 2012.
- [122] Available: http://sites.energetics.com/MADRI/pdfs/inter_modelsmallgen.pdf.
- [123] Connecting to the grid 6th edition 2009 - A guide to distributed generation interconnection issues, Interstate Renewable Energy Coun-

cil, Availabl: <http://irecusa.org/wp-content/uploads/2009/11/Connecting-to-the-Grid-Guide-6th-edition.pdf>.

- [124] D. J. A. Welsh and M. B. Powell, “An upper bound for the chromatic number of a graph and its application to timetabling problems,” *The Computer Journal*, vol. 10, no. 1, pp. 8586, 1967.
- [125] H. Zeineldin and J. Kirtley, ”Islanding operation of inverter-based distributed generation with static load models,” In Proc. of *IEEE Power and Energy Society General Meeting*, pp. 1–6, 2008.
- [126] M. Oprisan and S. Pneumaticos, “Potential for electricity generation from emerging renewable sources in Canada,” In Proc. of *IEEE EIC Climate Change Technology Conference*, pp. 1–9, 2006.
- [127] A. Yazdani, A. Rita Di Fazio, H. Ghoddami, M. Russo,, M. Kazerani, J. Jatskevich, K. Strunz, S. Leva, and J. Martinez, “Modeling guidelines and a benchmark for power system simulation studies of three-phase single-stage photovoltaic systems,” *IEEE Transactions on Power Delivery*, vol. 26, no. 2, pp. 1247–1264, 2011.
- [128] A. Nabavi-Niaki and M. R. Iravani, “Steady-state and dynamic models of unified power-flow controller (UPFC) for power system studies,” *IEEE Transactions on Power Systems*, vol. 11, no. 4, pp. 1937–1943, 1996.
- [129] S. Chiniforoosh, J. Jatskevich, A. Yazdani, V. Sood, V. Dinavahi, J. A. Martinez, and A. Ramirez, “Deffinitions and applications of dynamic average models for analysis of power systems,” *IEEE Transactions on Power Delivery*, vol. 25, no. 4, pp. 2655–2669, 2010.

- [130] O. Wasynczuk and N. A. Anwah, "Modeling and dynamic performance of a self-commutated photovoltaic inverter system," *IEEE Transactions on Energy Conversion*, vol. 4, no. 3, pp. 322–328, 1989.
- [131] L. Angquist and L. Lindberg, "Inner phase angle control of voltage source converter in high power applications," In Proc. of *IEEE Power Electronics Specialists Conference PESC*, pp. 293–298, 1991.
- [132] L. Xu, V. G. Agelidis, and E. Acha, "Development considerations of DSP-controlled PWM VSC-based STATCOM," *IEE Proceedings-Electric Power Application*, vol. 148, no. 5, pp. 449–455, 2001.
- [133] A. Yazdani and R. Iravani, "Voltage-sourced converters in power systems," John Wiley & Sons, Inc, 2010.
- [134] M. P. Kazmierkowski and L. Malesani, "Current-control techniques for three-phase voltage-source PWM converters: A survey," *IEEE Transactions on Industrial Electronics*, vol. 45, no. 4, pp. 691–703, 1998.
- [135] S. Wang, Q. Wei, and S. Cai, "Microgrid islanding detection method based on frequency-reactive power feedback," *International Journal of Grid and Distributed Computing*, vol. 6, no. 4, pp. 107–116, 2013.
- [136] W. Bower and M. Ropp, "Evaluation of islanding detection methods for utility-interactive inverters in photovoltaic systems," Sandia National Lab, SAND2002-3591, 2002.

MOHAMMAD NIKKHAH MOJDEHI's VITA

MAJOR:

Electrical Engineering

EDUCATION:

- Ph.D., May 2015, Syracuse University, USA (expected)
- M.S., January 2009, Iran University of Science and Technology, Iran
- B.S., May 2002, University of Guilan, Iran

PROFESSIONAL EXPERIENCE:

- Graduate Assistant, 20011-2015, Syracuse University, USA
- Student Intern and Research Assistant, 2014-2015, National Grid, USA
- Research Assistant, 2014, O'Brien & Gere , USA

PUBLISHED PAPERS:

- **M. Nikkhah Mojdehi** and P. K. Ghosh, "Minimization of energy usage and cost for EV during reactive power service," Accepted in *IEEE International Conference on Smart Energy Grid Engineering*, 2015.
- **M. Nikkhah Mojdehi** and P. K. Ghosh, "Optimal EVs aggregators bidding strategy to participate in unidirectional frequency regulation market," Accepted in *IEEE Conference on Technologies for Sustainability*, 2015.

- **M. Nikkhah Mojdehi**, M. Fardad, and P. K. Ghosh, “Energy and cost minimization of bidirectional frequency regulation service by EV following FERC Order 755,” Accepted in *IEEE Power and Energy Society General Meeting*, 2015.
- **M. Nikkhah Mojdehi** and P. K. Ghosh, “Estimation of the battery degradation effects on the EV operating cost during charging/discharging and providing reactive power service,” Accepted in *IEEE 81st Vehicular Technology Conference*, 2015.
- **M. Nikkhah Mojdehi** and P. K. Ghosh, “Modeling and revenue estimation of EV as reactive power service provider,” In Proc. of *IEEE Power and Energy Society General Meeting*, pp. 1–5, 2014.
- **M. Nikkhah Mojdehi**, P. K. Ghosh, and P. Wilcoxon, “Market equilibrium of distribution network with alternative energy resources,” In Proc. of *IEEE International Conference on Smart Grid Engineering, Canada*, pp. 1–7, 2013.
- C. Jin, **M. Nikkhah Mojdehi**, and P. K. Ghosh, “A methodology to design a stochastic cost efficient DER scheduling considering environmental impact,” In Proc. of *IEEE International Conference on Smart Grid Engineering*, pp. 1–6, 2012. **Best Paper Award**.
- **M. Nikkhah Mojdehi** and P. K. Ghosh, “Distributed generations scheduling in micro-grid considering CO_2 emission cost,” In Proc. of *IEEE Power and Energy Society General Meeting*, pp. 1–6, 2012.

SUBMITTED PAPERS:

- **M. Nikkhah Mojdehi** and P. K. Ghosh, “An on-demand compensation function for an EV as a reactive power service provider,” submitted for publication.
- **M. Nikkhah Mojdehi**, M. Fardad, and P. K. Ghosh, “Technical and economical evaluation of reactive power service from aggregated EVs,” submitted for publication.
- **M. Nikkhah Mojdehi**, and P. K. Ghosh, “A Framework to develop reactive power supply function of aggregated EVs,” submitted for publication.
- **M. Nikkhah Mojdehi**, and P. K. Ghosh “Optimization tools to minimize both energy usage and cost for EV during active and reactive power exchange with the distribution system,” submitted for publication.
- “A Procedure for Utilities to Assess Risk of Unintentional Islanding of Interconnected Distributed Generators at Distribution Feeder,” in preparation for submission.
- “A multilevel optimization approach for offering bidirectional frequency regulation service by EVs: aggregators perspective,” in preparation for submission.